Aston University

Some pages of this thesis may have been removed for copyright restrictions.

If you have discovered material in AURA which is unlawful e.g. breaches copyright, (either yours or that of a third party) or any other law, including but not limited to those relating to patent, trademark, confidentiality, data protection, obscenity, defamation, libel, then please read our Takedown Policy and contact the service immediately

MECHANISMS FOR TRIGGERING HIGH-VOLTAGE BREAKDOWN IN VACUUM

BRIAN MORELAND COAKER BEng, Wh.Sch.

Doctor of Philosophy

THE UNIVERSITY OF ASTON IN BIRMINGHAM

February 1995

This copy of the thesis has been supplied on condition that anyone who consults it is understood to recognise that its copyright rests with its author and that no quotation from the thesis and no information derived from it may be published without proper acknowledgement.

THE UNIVERSITY OF ASTON IN BIRMINGHAM

BRIAN MORELAND COAKER

Doctor of Philosophy, 1995

THESIS SUMMARY

The electrical and optical characteristics of a cylindrical alumina insulator (94% Al_2O_3) have been measured under ultra-high vacuum ($P < 10^{-8}$ mBar) conditions. A high-resolution CCD camera was used to make real-time optical recordings of DC prebreakdown luminescence from the ceramic, under conditions where DC current magnitudes were limited to less than 50μA. Two concentric metallized rings formed a pair of co-axial electrodes on the end-face of the alumina tube; a third 'transparent' electrode was employed to study the effect of an orthogonal electric field upon the radial conduction processes within the metallized alumina specimen. The wavelength-spectra of the emitted light was quantified using a high-speed scanning monochromator and photo-multiplier tube detector. Concurrent electrical measurements were made alongside the recording of optical-emission images. An observed time-dependence of the photon-emission is correlated with a time-variation observed in the DC current-voltage characteristics of the alumina.

Optical images were also recorded of pulsed-field surface-flashover events on the alumina ceramic. An intensified high-speed video technique provided 1ms frames of surface-flashover events, whilst 100ns frames were achieved using an ultra high-speed fast-framing camera. By coupling this fast-frame camera to a digital storage oscilloscope, it was possible to establish a temporal correlation between the application of a voltage-pulse to the ceramic and the evolution of photonic emissions from the subsequent surface-flashover event.

The electro-optical DC prebreakdown characteristics of the alumina are discussed in terms of solid-state photon-emission processes, that are believed to arise from radiative electron-recombination at vacancy-defects and substitutional impurity centres within the surface-layers of the ceramic. The physical nature of vacancy-defects within an alumina dielectric is extensively explored, with a particular focus placed upon the trapped electron energy-levels that may be present at these defect centres.

Finally, consideration is given to the practical application of alumina in the trigger-ceramic of a sealed triggered vacuum gap (TVG) switch. For this purpose, a physical model describing the initiation of electrical breakdown within the TVG regime is proposed, and is based upon the explosive destabilisation of trapped charge within the alumina ceramic, triggering the onset of surface-flashover along the insulator. In the main-gap prebreakdown phase, it is suggested that the electrical-breakdown of the TVG is initiated by the low-field 'stripping' of prebreakdown electrons from vacancy-defects in the ceramic under the influence of an orthogonal main-gap electric field.

Key words: vacuum, surface-flashover, alumina, luminescence

to my parents,

Ann and Moreland

ACKNOWLEDGEMENTS

The author would like to thank his supervisor, Professor Rodney Latham, for his consistent support and sound guidance throughout this programme of research. He appreciates the frequent discussions and daily assistance of his associate supervisor, Dr Ningsheng Xu. Further stimulus was provided by a supervisory team from EEV Limited, with external supervision and support from Mr Francis Jones of EEV Limited at Lincoln, and helpful discussions with Mr Ken Cook. Communications with Professor Ray Boxman, Professor Shinichi Kobayashi and Dr Yoshio Saito proved helpful and stimulating. The timely technical assistance of Messrs Andrew Abbot and Bernard Lawrence was most valuable.

In the provision of diagnostic instruments for experimental investigations, the author wishes to thank Anne Burns of Rees Instruments Limited for her invaluable assistance in the optical spectrometric investigation, and for the use of a Monolight high-speed scanning monochromator. He also thanks Dr Sayah Saied and Dr John Sullivan of Aston University for their kind assistance in the diagnostic spectroscopy of experimental materials. The comprehensive advice and support of John Rice, formerly of EEV Limited (Chelmsford), were invaluable in the procurement of a high-resolution CCD camera and accompanying lens optics.

Support from the Engineering Board of the Engineering and Physical Science Research Council (EPSRC) is gratefully acknowledged, and their provision of the high-speed video and fast-framing camera imaging equipment. Special thanks are due to Mr Peter Goodyer of the Rutherford-Appleton Laboratory for his extensive assistance in commissioning the camera apparatus. The efficient services of Dr Chris Jeynes and Dr Bill Gillin, of the EPSRC Central Facility for Ion Beam Technology at the University of Surrey were most valuable.

Finally, the author wishes to thank EEV Limited for their support and help in this work, with particular thanks to Messrs Graham Jex and Richard Keyse of EEV Limited, Lincoln, not least for the supply of metallized alumina specimens. He is grateful for the technical support provided by Mr Keith Welham at EEV Limited, Chelmsford, who performed the scanning-electron microscopy of experimental specimens.

The work described in this thesis was undertaken within the Engineering and Physical Sciences Research Council (EPSRC) Total Technology studentship scheme, award number 91302542.

CONTENTS

		Page
Title Page		1
Thesis Summary		2
Dedication		3
Acknowledgements		4
Table of Contents		5
Index of Figures and Tables		11
1.	**INTRODUCTION**	25
1.1	**Triggered vacuum gap switches**	25
1.2	**Physical mechanisms of insulator surface-flashover in vacuum**	27
1.2.1	Electron-stimulated gas desorption (ESD)	27
1.2.2	'Solid-state' mechanisms of insulator flashover	28
	1.2.2.1 Electron collision-ionisation	28
	1.2.2.2 Dielectric polarisation-relaxation	29
1.3	**Direction and scope of experimental investigation**	30
1.3.1	Technological background	30
1.3.2	Experimental trigger insulator regime	31
1.3.3	Experimental studies of surface-flashover	32
	1.3.3.1 DC prebreakdown experiments	32
	1.3.3.2 Pulsed-field breakdown experiments	32
	1.3.3.3 Surface analysis	33
1.3.4	Analysis of experimental findings	33
2.	**TRIGGERED VACUUM BREAKDOWN**	35
2.1	**Vacuum insulation**	35
2.1.1	'Ideal' Vacuum-insulated regimes	37
2.1.2	'Non-Ideal', Solid-Insulator Bridged Vacuum Gaps	38
2.2	**Prebreakdown electronic phenomena in a bridged vacuum gap**	40
2.2.1	Prebreakdown electron-emission into a vacuum gap	40
2.2.2	'Metallic' model of field electron-emission (FEE)	42
2.2.3	FEE due to non-metallic cathode inclusions	43
	2.2.3.1 Hot electron emission: I - Filamentary model of FEE	44
	2.2.3.2 Hot electron emission: II- Antenna Effect	45
2.3	**Vacuum gaps bridged by a solid-insulator**	46
2.3.1	Electronic charging of solid insulators	46

2.3.2 Optical luminosity from solid insulators 48

2.3.3 Triple junction phenomena 49

2.3.4 Modifications in stressed dielectrics after flashover 51

2.3.4.1 Surface melting and treeing on solid insulators 51

2.3.4.2 Insulator punch-through 52

2.3.4.3 Discoloration of stressed insulators 53

2.4 Charge injection and transport in solid dielectrics 53

2.4.1 Conduction through metallic surface layers 54

2.4.2 Charge transport in single-crystal dielectrics: I - Band Conduction 54

2.4.3 Charge transport in single-crystal dielectrics: II - Polaron 'Hopping' 55

2.4.4 Charge transport in polycrystalline dielectrics: I - Ionic Conduction 57

2.4.5 Charge transport in polycrystalline dielectrics: II - Exciton Hopping 59

2.4.6 Charge transport in mixed-phase materials 59

2.5 Surface-flashover of solid-insulators in vacuum 61

2.5.1 Electron-stimulated desorption (ESD) 61

2.5.2 Electron collision-ionisation 63

2.5.3 Explosive relaxation of trapped polarisation energy 67

2.6 Solid Insulator structure and modification 71

2.6.1 Solid insulator materials 71

2.6.2 Aluminium oxide (alumina) 71

2.6.3 Ferroelectric ceramic materials: I - Barium Titanate 73

2.6.4 Ferroelectric ceramic materials: II - PZT and PLZT 75

2.6.5 Optimised insulator structures 76

2.6.6 Dielectric material-engineering and modification 78

2.6.7 Optimisation of trigger insulator flashover properties 79

2.6.8 Optimised TVG structures 80

2.7 Triggered vacuum gap switches 81

2.7.1 Circuit description of the TVG switch 81

2.7.1.1 TVG operational modes 81

2.7.1.2 TVG switching performance 82

2.7.1.3 Delay characteristics of TVGs 85

2.7.2 Laser-triggered vacuum gap (LTVG) switches 86

2.7.3 Exploding-wire TVGs 87

2.7.4 Surface-discharge TVGs 88

2.7.4.1 Surface discharge trigger structures 88

2.7.4.2 Surface-discharge triggered vacuum switches 91
2.7.5 Technological basis for investigation - a commercial TVG 93

3. EXPERIMENTAL 96
3.1 Experimental trigger specimen modules 96
3.1.1 Metallized alumina modules 96
3.1.2 Confined electrode regime 98
3.1.3 'Bulk' dielectric alumina specimens 98
3.1.4 Encapsulated alumina modules 99
3.2 Analytical systems 101
3.2.1 Experimental system 101
3.2.2 Transparent Anode electrocathodoluminescence imaging 102
3.2.2.1 Transparent Anode specimen fixture 103
3.2.2.2 Electrode module fixture and connection 104
3.2.3 Pulsed power supplies 105
3.2.3.1 High-voltage 0-7kV power supply 105
3.2.3.2 Extra high-voltage 30kV power supply 106
3.2.4 Remote diagnostics 107
3.2.4.1 Video recording and image processing 107
3.2.4.2 High-speed videography 108
3.2.4.3 Fast frame imaging 111
3.2.4.4 Evaluation of imaging techniques 111
3.2.4.5 Optical spectrometry 112
3.3 Surface analysis techniques 114
3.3.1 Scanning electron microscopy (SEM) 114
3.3.2 Large area X-ray photoelectron spectroscopy (LAXPS) 116
3.3.2.1 Surface analysis of alumina ceramic 117
3.3.2.2 Analysis of collected efflux material 117
3.3.3 Microprobe Rutherford Backscattering Spectrometry (μ-RBS) 118
3.4 Surface engineering of trigger ceramics 119
3.4.1 Direct implantation of Cr ions into alumina 119
3.4.2 Implantation of B ions through TiN film 121

4. EXPERIMENTAL FINDINGS 124
4.1 Experimental findings 1 - DC characterisation 124
4.1.1 DC Prebreakdown electrical characteristics and optical imaging 124
4.1.1.1 Electro-optical observations of metallized 124

alumina specimens

4.1.1.2 Electro-optical observations of 'bulk' dielectric alumina modules 129

4.1.1.3 Electro-optical observations of ion-implanted alumina modules 131

4.1.2 Spectral nature of DC prebreakdown photon emission 132

4.1.2.1 High-speed optical spectrometry 133

4.1.2.2 High-resolution optical spectrometry 134

4.1.3 DC prebreakdown electron emission 136

4.1.3.1 Transverse prebreakdown electrical characteristics 136

4.1.3.2 Transverse electro-optical phenomena 139

4.1.3.3 Desorbed gas analysis 140

4.1.3.4 Electro-optical observations of confined alumina modules 141

4.2 Experimental findings II - pulsed field 146

4.2.1 Imaging of optical events on module end-face 146

4.2.1.1 Pulsed-field optical phenomena 146

4.2.1.2 Persistence of luminous centres in the alumina gap 148

4.2.1.3 Propagation of emitted 'jets' 150

4.2.1.4 Influence of body envelope upon jet propagation 152

4.2.1.5 Pulsed field optical emission from 'bulk' dielectric modules 154

4.2.2 Initiation of pulsed-field surface-flashover events 156

4.2.2.1 Temporal development of surface-flashover 156

4.2.2.2 Temporal development of luminous zones 158

4.2.2.3 Initiation of surface flashover luminosity 159

4.2.3 Orthogonal recording of surface-flashover events 162

4.2.3.1 Pulsed field optical phenomena 162

4.2.3.2 Pulsed-field optical emission along outer-diameter of alumina module 164

4.2.3.3 Development and propagation-velocity of jet phenomena 166

4.2.4 Spectroscopy of pulsed flashover events 168

4.2.4.1 Spectral nature of optical emissions 168

4.2.4.2 Current measured through auxiliary anode collector 169

4.2.5 Spatial correlation of DC and pulsed-field emissions 170

4.3 Experimental findings III - surface analysis 172

4.3.1 Surface topography of alumina module 172

4.3.2 Microstructure of metallized ceramic M-I region 173

4.3.3 Surface microtopography of alumina ceramic 174

4.3.4 Microfeatures at sites of localised optical emission phenomena 175

4.3.5 Species profiling of alumina trigger ceramic 178
4.3.5.1 XPS signature of alumina material 178
4.3.5.2 μ-RBS analysis of alumina ceramic 180
4.3.6 Collected efflux material from HV (5kV) flashover events 182
4.3.6.1 XPS spectrum of HV Nb foil collector 182
4.3.6.2 SEM analysis of HV Nb target 184
4.3.7 Collected efflux material from EHV (20kV) flashover events 185
4.3.7.1 Analysis of EHV Nb target 185
4.3.7.2 XPS spectrum of EHV Nb foil collector 185
4.3.7.3 SEM analysis of EHV alumina modules 189
4.4 Summary of experimental findings 192
4.4.1 DC prebreakdown luminosity 192
4.4.2 DC prebreakdown electron-emission 192
4.4.3 High-voltage pulsed-field optical emission 193
4.4.4 Extra-high voltage pulsed-field optical emission 193

5. DISCUSSION 194
5.1 Planar DC prebreakdown behaviour of alumina in vacuum 195
5.1.1 Origin of optical emission 195
5.1.1.1 Nature of 'doughnut' emission (λ=694nm) 196
5.1.1.2 Nature of localised bright-blue 'spots' (λ=325nm and λ=410nm) 197
5.1.2 Planar prebreakdown electrical characteristics 198
5.1.3 Physical processes of photon emission 200
5.1.3.1 Initiation of 'doughnut' emission 200
5.1.3.2 Persistence of the doughnut emission 201
5.1.3.3 Onset and persistence of bright-blue 'spots' (λ=410nm) 202
5.2 Transverse DC prebreakdown characteristics 203
5.2.1 Mechanisms of field-stripping of electrons 203
5.2.1.1 Contribution of planar emission to transverse current 204
5.2.2.2 Nature of electron-emission from planar bright-blue 'spots' 204
5.2.2 Desorbed gas analysis 206
5.3 Pulsed-field breakdown behaviour of alumina in vacuum 206
5.3.1 Properties of emitted 'jets' 207
5.3.1.1 Trajectory tracks and propagation velocity 207
5.3.1.2 Environmental interaction of jets 207
5.3.1.3 Nature of jet material 207
5.3.1.4 Nature of 'diffuse' emission phenomena 210
5.3.1.5 Electron exo-emission 210

5.3.2 Physical origin of jets 211
5.3.3 Nature of luminous centres within the dielectric 211
5.3.3.1 Nature of luminous centre emission 212
5.3.3.2 Electronic characteristics of pulsed-field breakdown events 212
5.3.4 Defect-initiated model of surface flashover 215
5.4 Surface-discharge initiation of triggered vacuum breakdown 217
5.4.1 Physical origins of 'Initiating Electrons' 218
5.4.2 Post-breakdown phenomena in the TVG trigger ceramic 220
5.4.3 Vaporisation phenomena in the trigger ceramic 220

6. CONCLUSIONS AND RECOMMENDATIONS 223
6.1 DC prebreakdown optical emission 223
6.2 Prebreakdown DC electronic characteristics 224
6.3 Optical emission from pulsed-field surface-flashover events 225
6.4 Pulsed-field electronic behaviour 226
6.5 Surface topography of flashover sites 226
6.6 Recommendations for further investigation 227
6.6.1 Temperature monitoring of alumina dielectric 227
6.6.2 Ultra high-speed optical spectrometry 227
6.6.3 High sensitivity fast-frame imaging 228
6.6.4 TVG main gap breakdown development 228

REFERENCES 230

APPENDICES 248
A UHV SYSTEM DESIGN 248
B 6kV PULSED POWER SUPPLY DESIGN 256
C 30kV PULSED POWER SUPPLY DESIGN 259
D PUBLICATIONS 263
"Electrical and Optical DC Vacuum Emission Phenomena from a Ceramic-Insulated Planar Electrode Configuration", *IEEE Trans. Plasma Sci.*, **21** (5), pp. 400-406, 1993 263
"Photon emission from an alumina insulator in vacuum subjected to DC electrical fields", *J.Phys.D: Appl. Phys.*, **27**, pp. 1448-1456, 1994 270
"High-speed optical imaging of explosive exoemission from an alumina ceramic in vacuum", in *XVI International Symposium on Discharges and Electrical Insulation in Vacuum*, Gennady A Mesyats, Editor, Proc. SPIE 2259, pp. 10-13, 1994 279

FIGURES AND TABLES

List of Figures

		Page
1.1	A schematic section of a surface-discharge-initiated triggered vacuum gap (TVG) switch	26
1.2	Illustrating the field distribution in the interelectrode region (a) before application of trigger pulse, and (b) with the introduction of a plasma-burst from the surface-discharge across the trigger region	26
1.3	Electron-stimulated desorption (ESD) of adsorbed gas from the surface of the solid insulator	27
1.4	(a) Uniform field charging, and (b) high-field electron collision-ionisation, leading to the surface-flashover of a solid insulator	28
1.5	High-energy electron-injection and growth of negative space-charge within a solid insulator	29
1.6	Waveform diagram showing delay-time, T_d, between surface-flashover breakdown of TVG trigger region, and initiation of main-gap current	31
1.7	Schematic representation of experimental metallized alumina module	32
2.1.1	Related measurements defining vacuum	36
2.1.2	Variation of static DC breakdown voltage (V_B) with pressure (P) for a fixed electrode spacing	37
2.1.3	Schematic arrangement of a sealed electronic vacuum tube	38
2.1.4	Illustrating the bridging of a vacuum gap by a solid insulator	38
2.1.5	Schematic illustration of pulsed-field flashover along a solid insulating spacer within an evacuated electrode gap	39
2.2.1	Illustrating the typical electrical behaviour of a plane vacuum-insulated electrode gap	40

2.2.2 Illustrating the influence of electrode separation upon the Fowler-Nordheim plots of the vacuum gap current-voltage characteristics 41

2.2.3 Illustrating the geometric enhancement of a macroscopic electric field, E_m, to a higher microscopic field value, E_l, at a microprotrusion on an electrode surface 43

2.2.4 Illustrating a conducting channel within the M-I-V regime of an insulating inclusion at the electrode surface, and enhancement of the microscopic electric field 44

2.2.5 Band diagram representation of electron-emission from a conducting channel formed in a M-I-V microregime 45

2.2.6 Illustrating the "antenna effect" associated with the M-I-M-V regime of a conducting microparticle embedded into the oxidised surface-layer of a metal electrode 45

2.3.1 Electrode-insulator geometries 47

2.3.2 Variation of secondary electron emission yield, δ, with incident electron-energy, E_i, for alumina ceramic 48

2.3.3 Optical emission spectrum from an alumina r.f. window 49

2.3.4 Equipotential plots through (a) ideal electrode-insulator-vacuum triple junction, and (b) with small void at the electrode-dielectric interface 50

2.3.5 Post-discharge 'treeing' on a sapphire insulator 52

2.3.6 Surface melting arising from the pulsed-field surface-flashover of an alumina ceramic 52

2.3.7 Surface treeing and grain-ejection following the pulsed-field surface-flashover of a polycrystalline ceramic 53

2.4.1 Schematic illustration of a planar insulator coated with a thin film of conducting island structures 54

2.4.2	Illustrating the energy-band representation of an insulator	55
2.4.3	Illustrating the self-trapped negative charge of a polaron lattice-site	56
2.4.4	Illustrating the potential-well associated with the lattice-distortion around a polaron electron-centre	56
2.4.5	(a) Potential-energy barriers to ionic transport, and (b) lowering of the barrier-height with the application of an electric field, **E**	58
2.4.6	A schematic diagram of the physical structure of a multiphase dielectric material	60
2.5.1	Illustrating the positive charging of an insulator surface due to the secondary-emission cascade of "hopping" electrons	62
2.5.2	Illustrating the evolution of ions and neutrals from the insulator surface due to the impact of prebreakdown "hopping" electrons	63
2.5.3	Optical emission spectrum from lucalox alumina (99.9% Al_2O_3)	64
2.5.4	Illustrating the sequence of prebreakdown events leading to the surface-flashover of a solid insulator in vacuum	65
2.5.5	Illustrating an exoelectron emission model; region **A**: bulk insulator, **B**: negative space-charge region, **C**: (neutral) boundary layer, **D**: positively-charged surface-layer	66
2.5.6	Schematic illustration showing (a) a slab of dielectric material with (b) attached electrodes, and normal incidence of a diagnostic electron-beam	67
2.5.7	Illustrating the electron "mirror" effect obtained by probing a charged dielectric sample with a low-voltage electron beam	68
2.5.8	Trapping of electrons (a) at the interface of the insulator surface and a contamination layer, (b) in the bulk of the grains of a freshly-annealed dielectric, and (c) in the grain-boundaries of an aged insulator	69

2.5.9 Illustrating the surface-flashover process resulting from the destabilisation of trapped charge, and leading to (a) surface decontamination, (b) melting of the dielectric grains, and (c) the ejection of grains from the insulator 70

2.6.1 Unit cell of α-alumina lattice structure 72

2.6.2 The variation of the permittivity of $BaTiO_3$ ceramic with temperature and grain-size 74

2.6.3 Unit cell of barium titanate ($BaTiO_3$) ceramic 74

2.6.4 Variation of relative permittivity, ε_r, across the compositional range of the $Pb(Zr_xTi_{1-x})O_3$ system 75

2.6.5 Variation of relative permittivity, ε_r, with temperature and electric field, for the $PbZrO_3$:$PbTiO_3$:La_2O_3 (PLZT) system 76

2.6.6 Optimised geometry of a high-voltage insulating spacer 77

2.6.7 Illustrating a non-intimate metal-ceramic M-I interface 78

2.6.8 Illustrating the reduction of electrical field-stress at an electrode triple-junction by the use of a graded-permittivity solid dielectric 78

2.6.9 A schematic illustration of two alternative interelectrode structures that have been used for a triggered vacuum gap 81

2.7.1 Operational modes of a TVG switch 82

2.7.2 Circuit representation of a typical capacitor-discharge application of a TVG switch 83

2.7.3 Waveform diagram representation of TVG switch closure 83

2.7.4 (a) Distributed switch and (b) distributed load switching arrays 84

2.7.5 Internal cross-section of a laser-triggered TVG switch 86

2.7.6 Internal structure of an exploding-wire triggered vacuum switch 88

2.7.7 Cross-sectional view of a trigger assembly 89

2.7.8 Simple triggered vacuum gap assemblies 90

2.7.9 Operational consistency of trigger assemblies using various insulator materials 90

2.7.10 A cross-section of a sealed triggered vacuum switch 92

2.7.11 Sectional diagram of (a) sealed miniature triggered vacuum switch, with (b) sintered carbon trigger film 93

2.7.12 The commercial TVG switch used for the present study, viewed from (a) the trigger / adjacent electrode assembly, and (b) the opposite main electrode 94

2.7.13 (a) Sectioned illustration of commercial triggered vacuum switch, with (b) circuit representation of three-electrode TVG 95

3.1.1 Experimental alumina modules, showing threaded trigger connection and adjacent copper electrode tag 96

3.1.2 End-elevation and sectioned axial views of the metallized alumina module 97

3.1.3 Outline form of 'confined' electrode modules 98

3.1.4 (a) Outline form and (b) schematic sectioned drawing of metallized 'bulk' alumina tube modules 99

3.1.5 (a) Demountable glass-bulbed alumina module, and (b) detail of encapsulated trigger specimen fixture 100

3.2.1 General arrangement of analytical UHV system 102

3.2.2 Schematic of electrode module and Transparent Anode 103

3.2.3 Arrangement of alumina module behind Transparent Anode, showing (a) front- and (b) side-views of module fixture 104

3.2.4 Front view of electrode module clamped within stainless steel fixture 104

3.2.5 Oscillograms of (a) open-circuit 6kV high-voltage (HV) pulse from pulsed PSU, and (b) breakdown pulse measured across alumina module 105

3.2.6 Oscillograms of (a) open-circuit 30kV extra high-voltage (EHV) pulse from pulsed PSU, and (b) breakdown pulse measured across electrode module 106

3.2.7 System schematic of electrode module and the Transparent Anode 107

3.2.8 (a) Front (port **1**) and (b) side (port **2**) views of the metallized alumina module 108

3.2.9 (a) High-speed imaging system, with (b) intensified CCD camera and processor 109

3.2.10 (a) General arrangement of fast-framing experimental system, incorporating (b) ultra high-speed camera head 110

3.2.11 (a) Experimental layout of optical imaging and spectroscopy system, with (b) detail of high-speed scanning monochromator 113

3.3.1 Electron micrographs showing (a) front-face of metallized alumina module, and (b) detail of metallized alumina M-I-M structure 114

3.3.2 General arrangement of a Scanning Electron Microscope (SEM) 115

3.3.3 (a) Back-scattered electron (BSE) and (b) secondary-electron (SE) images, showing M-I region of metallizing edge on alumina substrate 115

3.3.4 General arrangement of an X-ray photoelectron spectrometer 116

3.3.5 Experimental arrangement of alumina module with niobium foil collector 117

3.3.6 Schematic representation showing μ-RBS analysis of metallized alumina module 118

3.4.1 Illustrating the implantation of chromium (Cr) ions into alumina ceramic 120

3.4.2 Computed plots of longitudinal penetration of 1MeV Cr ions into Al_2O_3 substrate, modelled for (a) 10 and (b) 100 implanted Cr ions 120

3.4.3 Depth profiles of vacancy-production arising from implantation of 1MeV Cr ions into Al_2O_3 substrate, modelled for (a) 10 and (b) 100 implanted Cr ions 121

3.4.4 Implantation of boron ions into alumina ceramic through a TiN film 121

3.4.5 Computed plots of longitudinal penetration of 100keV B ions through 2000Å TiN film into Al_2O_3 substrate, modelled for (a) 50 and (b) 500 implanted B ions 122

3.4.6 Depth profiles of vacancy-production arising from implantation of 100keV B ions through 2000Å TiN film into Al_2O_3 substrate, for (a) 50 and (b) 500 implanted ions 122

4.1.1 (a) I-V characteristics of planar DC prebreakdown, recorded from i) initial measurements, and ii) following 30 minute exposure of the alumina module to +5kV. Corresponding images of (b) 'doughnut' emission (V_t = +2.5kV: *Image A*), and (c) localised bright-blue 'spots' (V_t = +4kV: *Image B*) from the 300μm-wide alumina region 126

4.1.2 Line-scans of pixel-intensity through the doughnut and bright-blue spot regions of Image B {Fig 4.1.1(c)} 127

4.1.3 (a) DC prebreakdown I-V characteristic of (b) 'dark' alumina module 128

4.1.4 (a) DC prebreakdown optical emission along the alumina cylinder (V_t = +10kV, I_t = 1.5μA), and (b) pixel-intensity line-scan through the cathode and anode luminosity regions 129

4.1.5 Images of (a) specimen outline, and optical events recorded for (b) a positive inner-electrode voltage (V_t) of +4kV (I_t = 1.2μA), and (c), (d) a negative inner-electrode voltage (V_t) of -4.5kV ($I_t = 3.8 \times 10^{-7}$A) 130

4.1.6 'Bulk' specimen planar I-V characteristics (positive and negative voltage-polarities) 131

4.1.7 (a) Planar V_t-I_t characteristics, with associated (b) planar spots on (c) metallized end-face of Cr-implanted alumina module 132

4.1.8 Optical spectrum of 'doughnut' and localised 'spot' emission observed on the end-face of the alumina specimen, for applied voltages (V_t) of +8kV and +10kV (200 spectral scans (averaged), 5nm half-power bandwidth) 133

4.1.9 Optical spectrum of 'doughnut' and localised 'spot' emission, for applied voltage (V_t) of +8kV (200 spectral scans (averaged), 5nm HPBW) 134

4.1.10 Spectral expansions of (a) UV / blue region, and (b) deep-red emission peak (1300 spectral-scans, 0.3nm HPBW) 135

4.1.11 Variation of transparent anode current (I_a) with transparent anode voltage (V_a); quiescent inner-ring voltage V_t = +3kV 137

4.1.12 (a) Transverse behaviour of transparent anode current, I_a, with inner ring voltage, V_t, for transparent-anode voltages {V_a} of +2.5kV, +5kV, +7.5kV and +10kV, and (b) associated planar I-V characteristics, showing the variation of inner electrode-ring current, I_t, with planar voltage, V_t, for transparent anode voltages {V_a} of 0V, +5kV and +10kV 138

4.1.13 Prebreakdown images for the three-electrode arrangement, with planar voltage only (V_t = +3kV), and (b) with application of transverse voltage (V_t = +3kV, V_a = +7kV); (c) schematic representation of three-electrode prebreakdown image 139

4.1.14 Schematic illustration of the confined module structure 141

4.1.15 Transverse I_a-V_a characteristic of confined main-gap, for a range of fixed planar voltage (V_t) values 142

4.1.16 Planar I_t-V_t characteristics, for a range of fixed main-gap (transverse) voltages (V_a) 143

4.1.17 Front view of confined alumina module 143

4.1.18 (a) Transverse and (b) planar prebreakdown images recorded from confined alumina modules 144

4.1.19 (a) Photographic and (b) schematic pictures of tracking along alumina cylinder of confined alumina module 145

4.2.1 (a) Captured image and (b) schematic illustration of pulsed breakdown event on front-face of alumina module {V_t = +4kV, 1ms framing period} 147

4.2.2 Spatial variation of observed optical-intensity along a radial line-scan through a luminous centre observed in the alumina gap between the electrode-rings 148

4.2.3 Composite series of four successive 1ms frames, showing (a) recorded images and (b) corresponding intensity profiles of the post-breakdown decay of a luminous centre in the alumina gap 149

4.2.4 Decay of peak measured-intensity of luminous centre with time 150

4.2.5 (a) Captured image and (b) schematic sketch of pulsed breakdown event on front-face of alumina module {V_t = +20kV} 151

4.2.6 (a) Outline of front end-face of 'confined' alumina module, and (b) millisecond image of pulsed flashover event 152

4.2.7 (a) Side view of 'confined' alumina module, with (b) composite millisecond image of pulsed flashover emission 153

4.2.8 Schematic illustration of observed jet behaviour within a confined electrode regime 154

4.2.9 (a) Front view of 'bulk' alumina module, with {(b) - (f)} consecutive 2ms frames of EHV pulsed breakdown event 155

4.2.10 (a) Front view of alumina module, with {(b) (c) (d)} 1μs frames of surface-flashover event (2μs interval between frames), and (e) final 1ms frame showing 'jet' emission 157

4.2.11 Waveform timing diagram, showing the exposure-times of the image channels with respect to the applied EHV pulse, V_t 158

4.2.12 Consecutive 500ns frames showing the initiation and development of a pulsed-field surface-discharge on the metallized end-face of the alumina module 159

4.2.13 Oscillogram of extra high-voltage breakdown pulse (V_t = +25kV, upper trace) and corresponding synchronisation pulse-edge (TTL, lower trace) marking capture of first frame 160

4.2.14 (a) Illuminated front-view of alumina module, and sequence of four consecutive 100ns frames {(b) - (e)} showing initiation of pulsed-field breakdown event 161

4.2.15 Captured 1ms frames of (a) optical activity associated with a pulsed-breakdown flashover event, viewed orthogonally to the end-face of the alumina specimen, and (b) emitted jets striking a tin oxide-coated glass target 162

4.2.16 Spatial variation of observed optical intensity along an emitted 'jet' 163

4.2.17 (a) Side view of alumina module, and (b) oscillogram associated with a pulsed flashover along the side of the alumina cylinder 164

4.2.18 Consecutive millisecond frames of photon-emission from a flashover event along the side of the alumina cylinder 165

4.2.19 Pixel-intensity line-scan of photon-emission from a flashover event 165

4.2.20 (a) Side view of alumina module, and (b) 1ms frame of flashover event 166

4.2.21 (a) Initial 5μs and (b) subsequent 1ms frames showing side profile of EHV pulsed breakdown event 167

4.2.22 Consecutive 50μs frames of propagating jets (inverted images) 168

4.2.23 Oscillogram of voltage-breakdown waveform (amplitude $V_t \approx +3kV$), together with the current-pulse waveform (I_a) recorded through a transparent anode 169

4.2.24 Outline view of alumina module front-face 170

4.2.25 (a) Pulsed breakdown event, and (b) corresponding voltage-pulse (V_t) oscillogram 170

4.2.26 Image of DC prebreakdown photon-emission (V_t = 3kV, I_t = 40μA) 171

4.3.1 Electron micrograph showing front face of metallized alumina module 172

4.3.2 Metallized alumina M-I regions at edges of (a) outer and (b) inner electrode rings 173

4.3.3 Oblique view across the inner electrode-ring and the 300μm alumina region towards the brazed outer electrode-ring 174

4.3.4 Surface detail of alumina region between the electrode rings 175

4.3.5 (a) Secondary electron image of alumina module, with (b) image of DC prebreakdown photon emission (V_t = +4kV, I_t = 1.5μA) 176

4.3.6 (a) Secondary electron (SE) image of alumina region, with (b) corresponding DC prebreakdown 'spots' at porous sites 176

4.3.7 Back-scattered electron (BSE) image of porous alumina region 177

4.3.8 Back-scattered electron (BSE) images of (a) upper and (b) lower pores observed in alumina region 177

4.3.9 Illustrating normal-incidence and glancing-angle X-ray beam geometries 178

4.3.10 X-ray photoelectron spectra of alumina ceramic, for (a) normal (0°) and (b) 85° glancing-angle beam incidence 179

4.3.11 RBS spectra of alumina ceramics 180

4.3.12 Normalised RBS spectra of alumina ceramics 181

4.3.13 X-ray photoelectron spectra of Nb foil collector, and exposed Nb target 182

4.3.14 Electron micrographs showing (a) surface of exposed Nb foil, and (b) collected microparticles of Al / Si material 184

4.3.15 Niobium foil {left} and exposed EHV Niobium target {right} 185

4.3.16 XPS spectra of (a) scarred and (b) unscarred regions of Nb target {binding energy range 0 - 600 eV} 186

4.3.17 XPS spectra of (a) scarred and (b) unscarred regions of Nb target {binding energy range 600 - 1100 eV} 187

4.3.18 Electron micrograph showing front face of "used" alumina module 189

4.3.19 Electron micrographs of eroded inner electrode-ring 190

4.3.20 Electron micrograph of eroded alumina region near outer electrode-ring 191

4.3.21 Glassy 'step' in eroded alumina region near outer electrode-ring 191

5.1 Illustrating the inhomogeneous structure of a polycrystalline alumina ceramic 194

5.2 Illustrating the energy levels associated with the photon-emission spectra recorded from a polycrystalline alumina ceramic 197

5.3 Electron energy diagram of the metal-insulator-metal (M-I-M) regime formed by a polycrystalline alumina ceramic bridging two electrodes in vacuum 199

5.4 Energy-band diagram, illustrating photon-emission by four solid-state mechanisms at defect-sites within an alumina insulator 201

5.5 Illustrating electron-energy levels for absorption and photon-emission processes at F and F^+ centres within an alumina insulator 205

5.6 The estimated physical parameters of an alumina efflux microparticle 208

5.7 Time-variation of efflux-microparticle temperature owing to radiative energy-loss 209

5.8	Examples of breakdown voltage-pulses recorded for surface-flashover events (a) on the front-face and (b) along the side of the alumina module	213
5.9	Schematic illustrations of (a) the metallized alumina trigger module, with (b) applied voltages and electric fields	214
5.10	Schematic illustration of enhanced-field polarisation and explosive charge-relaxation at a ceramic pore, leading to the vaporisation of jets of ceramic material	216
5.11	Illustrating jet emission by (a) collimated processes from deep pore structures, and (b) diffuse emission processes from shallow pores	217
5.12	A schematic temporal sequence showing the breakdown of the (a) trigger and (b) main-gap voltages in a TVG, with (c) a proposed cycle of electro-optical emission events from a porous region of the trigger ceramic	219
5.13	(a) An illustration of the effective shortening of the main interelectrode gap-spacing {d} of a TVG, that may occur as a result of (b) the introduction of a trigger-discharge plasma	222
6.1	A proposed experimental system for observing the temporal development of a triggered vacuum breakdown event	229

List of Tables

		Page
2.1	Electronic properties of various grades of alumina	73
2.2	Delay parameters of TVG modes	86
3.1	Performance comparison of optical imaging systems	112
4.1	Residual gas background during planar prebreakdown	141
4.2	XPS spectrum of niobium foil substrate	183
4.3	XPS spectrum of exposed HV niobium target	183
4.4	XPS spectrum of outer region of exposed EHV niobium target	188
4.5	XPS spectrum of scarred region in exposed EHV niobium target	188

1. INTRODUCTION

1.1 Triggered vacuum gap switches

Three-electrode triggered vacuum gap (TVG) closing switches are widely used in pulsed power switching applications, and have been successfully operated in the commutation of mega-ampère currents, with a switch closure period as low as 300ns [1]. More generally, TVG switches have been implemented in crowbar circuits which demand the clamping of several hundred kilo-ampère currents over a 100μs to 200μs period [2,3]. Thus, TVGs have been found to provide a high-speed, high-current switching capability, and present an alternative technique to more 'traditional' gas-filled switch technologies [4,5], such as thyratrons, ignitrons and trigatron (spark gap) switches.

Vacuum-insulation of two normally-open main electrodes has enabled TVGs to withstand high open-circuit voltages [6], whilst being capable of switching high currents with short time-delay (<1μs), over a wide range of operating voltages [7]. Various techniques have been used to initiate the triggered breakdown of the vacuum gap, in which an energetic plasma is injected into the main vacuum gap separating the two vacuum-insulated electrodes.

A common triggering method is the extraction of a trigger-discharge-plasma from the surface-flashover of a solid-insulator [1-11]. This trigger mechanism relies upon the electrical breakdown of a solid insulator within the evacuated envelope of the TVG. An experimental investigation of the *in vacuo* electrical behaviour of such solid insulators forms the basis of this thesis.

The solid trigger insulator is typically located within one of the main electrodes inside the TVG envelope, together with the auxiliary trigger electrode. Figure 1.1 illustrates the internal three-electrode structure of a surface-discharge-initiated TVG switch. In this type of device, surface-flashover of the solid insulator occurs under the influence of a fast-rising voltage-pulse, V_t, which is applied to the trigger electrode (the trigger-electrode and adjacent main-electrode bridged by the solid insulator). Breakdown of the trigger insulator is characterised by the collapse of the applied trigger voltage (V_t), and is accompanied by a surface-flashover discharge in the region of the insulator surface.

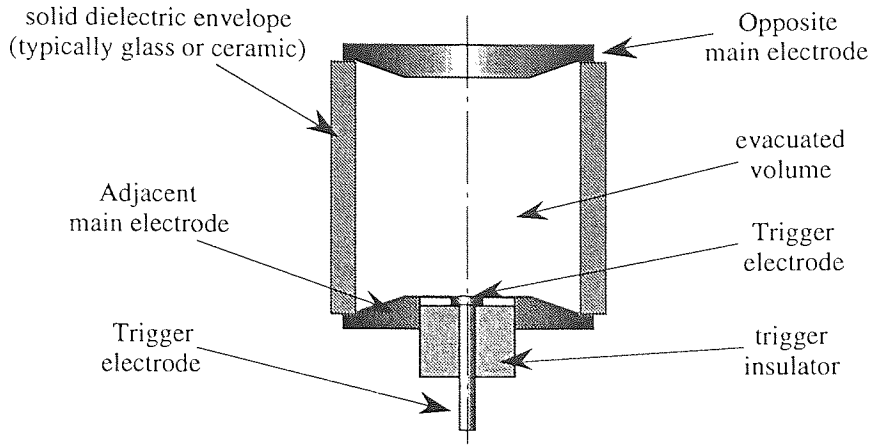

Fig. 1.1 A schematic section of a surface-discharge-initiated triggered vacuum gap (TVG) switch

Despite the widespread use of this "erosion" type of surface-discharge ignition of the TVG [5], there remains much debate concerning the precise nature of the physical mechanism(s) responsible for the phenomenon of insulator surface-flashover in vacuum [12]. A further important question is the mechanism by which energetic material, which is injected into the vacuum gap from this *trigger discharge*, subsequently gives rise to the electrical breakdown of the main vacuum-insulated gap. The associated plasma injection process is illustrated in Fig 1.2.

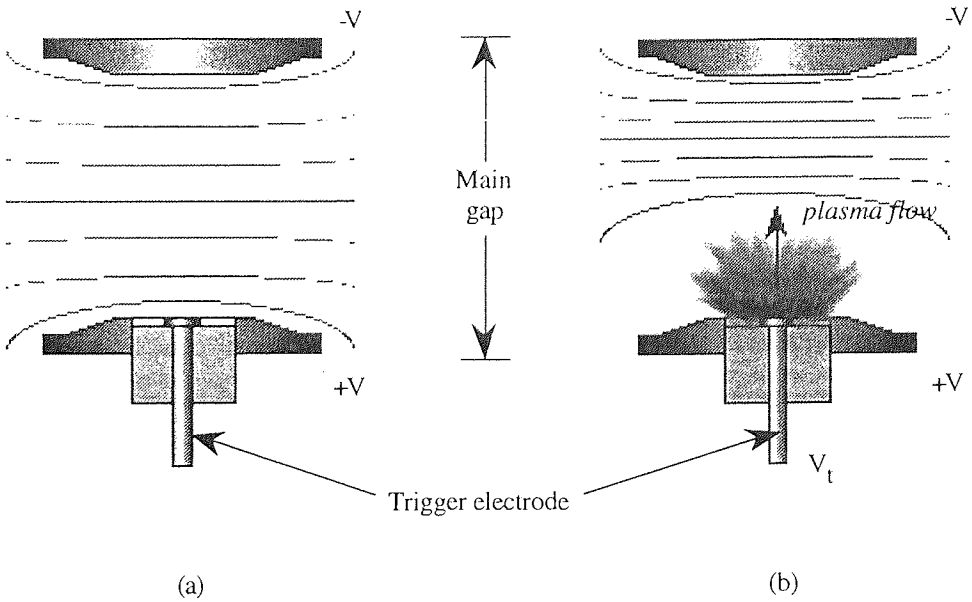

Fig. 1.2 Illustrating the field distribution in the interelectrode region (a) before application of trigger pulse, and (b) with the introduction of a plasma-burst from the surface-discharge across the trigger region (after Boxman [13])

The ultimate aim of this investigation is a precise description of the surface-flashover phenomenon as it occurs in the trigger regime, and the physical process(es) by which this surface-flashover discharge is believed to lead to the 'firing' of the triggered vacuum gap [13,14].

1.2 Physical mechanisms of insulator surface-flashover in vacuum

In order to understand the operational characteristics of a TVG switch, it is necessary to consider the physical mechanisms which are thought to be responsible for the pulsed-voltage surface-flashover of the trigger insulator. At present, these physical models fall into two broad categories.

1.2.1 Electron-stimulated gas desorption (ESD) The longest-standing model of insulator surface-flashover proposes that electrons are field-emitted from the cathode-insulator-vacuum triple-junction, and subsequently 'hop' along the insulator surface [15]. As a result, the layer of gas that had previously been adsorbed by the insulator is desorbed, as these hopping electrons strike the insulator surface. This electron-stimulated desorption (ESD) process, by which gas is desorbed from the insulator by the impacting electrons, is illustrated in Fig 1.3.

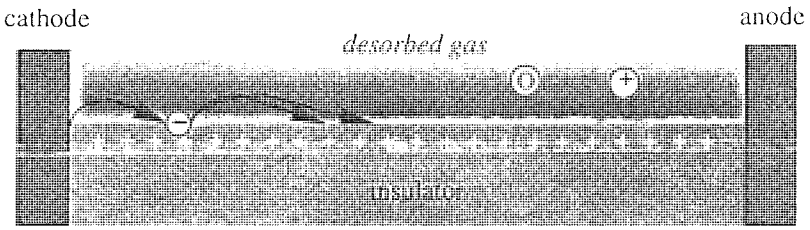

Fig. 1.3 Electron-stimulated desorption (ESD) of adsorbed gas from the surface of a solid insulator

In addition, the secondary-emission of further electrons from the insulator leads to an avalanching cascade of electrons along the insulator surface [16], which, in turn, results in the insulator surface becoming positively-charged [17]. Flashover then results from the ionisation of the desorbed gas by the electron avalanche, and the subsequent growth of a thin layer of dense plasma along the insulator surface [18,19]. However, the rapid formation-time of this plasma appears to conflict with observations of long delay-times preceding the DC surface-flashover of solid insulators [12]: such experimental findings have led to the emergence of a "new

generation" of solid-state physical models to describe the vacuum surface-flashover of a solid insulator.

1.2.2 'Solid-state' mechanisms of insulator flashover Two recent models describe alternative physical mechanisms which may lead to the creation of a surface-flashover plasma.

1.2.2.1 Electron collision-ionisation The first of these contemporary models suggests that the surface-flashover plasma results from the flow of 'solid-state' currents within the *surface layers* of the insulator [20-22]. These currents are assumed to be initiated by electron-injection processes associated with the cathode triple-junction [23,24], which lead to electron-impact ionisation of defect centres in the solid dielectric, and field-enhanced positive-charging within the insulator surface [17].

At a critical value of applied voltage, collision-ionisation within the insulator is sustained by cathode-injected electron-emission. Injected electrons and positive-ions then form a highly-conductive plasma within the surface-layers of the solid dielectric, through which flashover can occur. As will be discussed later in this thesis (Section 2.2.3), the surface-glow observed from these flashover events appears to correspond to transition radiation luminescence, resulting from the ionisation of impurity and vacancy defect centres within the insulator material [25], i.e. as illustrated in Fig 1.4 .

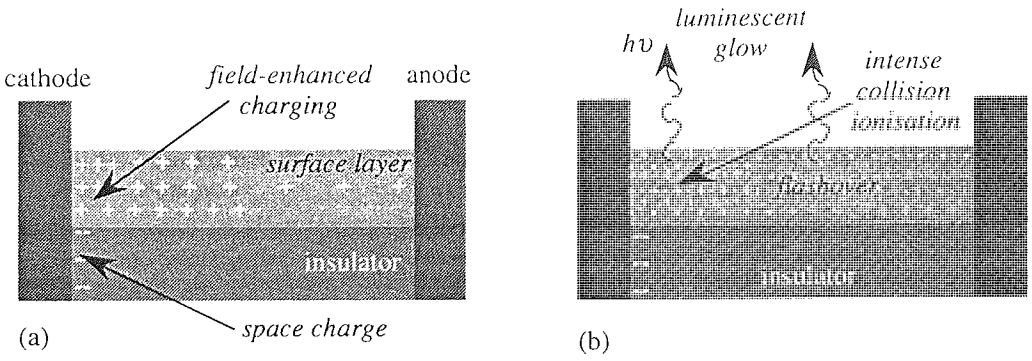

Fig. 1.4 (a) Uniform field charging, and (b) high-field electron collision-ionisation, leading to the surface-flashover of a solid insulator (after Jaitly & Sudarshan [20,24])

1.2.2.2 Dielectric polarisation-relaxation A second flashover model [26,27] describes the explosive depolarisation of trapped electronic charges within the *bulk* of the insulator. Initially, the solid dielectric becomes polarised under the influence

of an applied electric field [28,29]. An electronic space-charge is created within the dielectric medium as mobile electronic charges migrate in the electric field, and subsequently become trapped at defect centres within the insulator. Figure 1.5 illustrates the injection of electrons into an insulator, together with the formation of a distributed space charge, as the injected electrons migrate and are trapped by defect trapping centres.

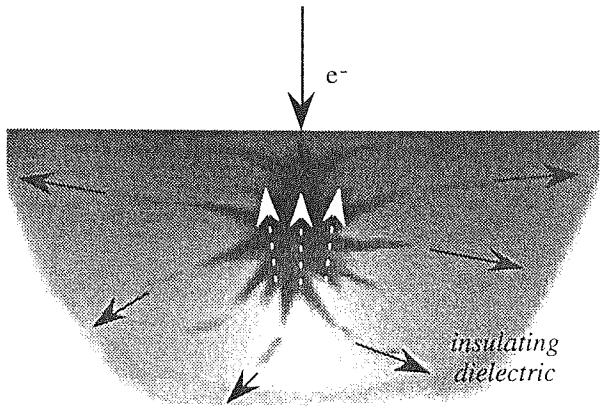

Fig. 1.5 High-energy electron-injection and growth of negative space-charge within a solid insulator (after Blaise & Le Gressus [28])

A polarisation energy is consequently induced in the trapped charge by the electric field; this polarisation energy can represent significant energy storage in the dielectric, particularly for a high density of trapping centres [30]. The charging process shown in Fig 1.5 ultimately leads to an equilibrium space charge within the dielectric. However, any perturbation of this equilibrium regime, such as a disturbance of the applied electric field, can lead to the spontaneous *detrapping* of the stored charge.

Such a rapid release and subsequent avalanching of trapped-charge is proposed as a mechanism for initiating the explosive depolarisation of the solid dielectric medium. As the dielectric relaxes from its polarised state, the polarisation energy associated with the trapped-charge is transferred to the phonon bath of the solid insulator. This energy transfer excites the lattice of the solid dielectric, producing a mechanical shock wave in the insulator material [31]. This shock wave leads to further mechanical perturbation of the dielectric lattice, and accelerates the depolarisation process. The increasing energy of the avalanching electrons ultimately reaches a threshold value approaching the band-gap of the solid-dielectric, whereupon the valence-band of the dielectric may be locally ionised to form an energetic microplasma [27].

1.3 Direction and scope of experimental investigation

Previous studies of surface-discharge trigger structures [32] have evolved broad 'design rules', outlining structures and materials that have been found to offer optimum TVG tube performance. However, there has been little investigation of the precise nature of the physical processes involved in the operation of these TVG devices. Furthermore, there remains much debate concerning the actual extent to which each of these physical processes influences the flashover performance of an insulator in vacuum. In the context of this thesis, this debate has been extended to consider the influence of the physical processes within the trigger insulator upon the switching performance of the TVG.

Thus, the underlying approach of the work described in this thesis is to present a physical description of the surface-discharge initiation mechanism which occurs in the 'firing' of a triggered vacuum gap switch. This physical approach is pursued through a coupling of experimental observations of TVG switching phenomena with the physical models of insulator surface-flashover outlined in Section 1.2.

1.3.1 Technological background Evaluations of the switching performance of surface-discharge TVGs show an inconsistency in the magnitude of the pulsed breakdown-voltage of the solid trigger-insulator. Further variation is observed in the time-delay, T_d, following the voltage breakdown of the trigger insulator, and the formation of the main-gap current, I_a, through the 'fired' TVG. These varying parameters cause the TVG switch to exhibit a shot-to-shot uncertainty in the overall time-delay measured between the application of a voltage-pulse, V_t, to the trigger-electrode, and the initiation of main-gap current through the TVG [33].

Figure 1.6 illustrates this TVG firing delay-time, with a measured delay, T_d, observed between the voltage-breakdown of the trigger region, and the subsequent flow of main-gap electrode current through the TVG switch. Uncertainty in the magnitude of this delay-time, δT_d, is known as *jitter* in the temporal firing characteristics of the TVG. In critical applications, this jitter in the firing delay-time of the TVG can be problematic, particularly where a circuit array of multiple TVG switches require precise simultaneous firing.

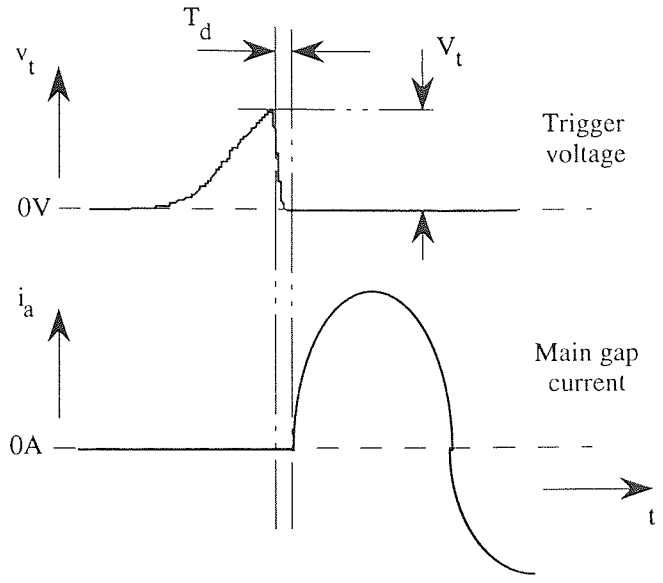

Fig. 1.6 Waveform diagram showing delay-time, T_d, between surface-flashover breakdown of TVG trigger region and initiation of main-gap current

To address the jitter observed in TVG operation, this work focuses on the characterisation of such a surface-flashover trigger structure, and describes the electronic and optical phenomena observed on the electrically-stressed trigger-insulator structure. This experimental evidence is then used as a basis for discussing the nature of the physical process(es) observed in the pulsed-field surface-flashover initiation of a TVG.

1.3.2 Experimental trigger insulator regime To facilitate an analytical study of the trigger insulator structure, experimental insulator modules were assembled. These modules replicated the metal-insulator-metal (M-I-M) structure of the trigger-electrode / trigger-insulator / adjacent main-electrode assembly of a commercial TVG switch, such as that depicted in Fig 1.1. The trigger- and adjacent-electrodes of the experimental modules were bridged by a trigger insulator formed from alumina (Al_2O_3) trigger ceramic. Although alumina has not found widespread use as a trigger-insulator material [32], it is widely-used as an 'engineering' ceramic [34], with electrodes readily applied to the alumina using a molybdenum / manganese metallization technique [35]. Figure 1.7 illustrates the structure of the experimental M-I-M modules used in this work.

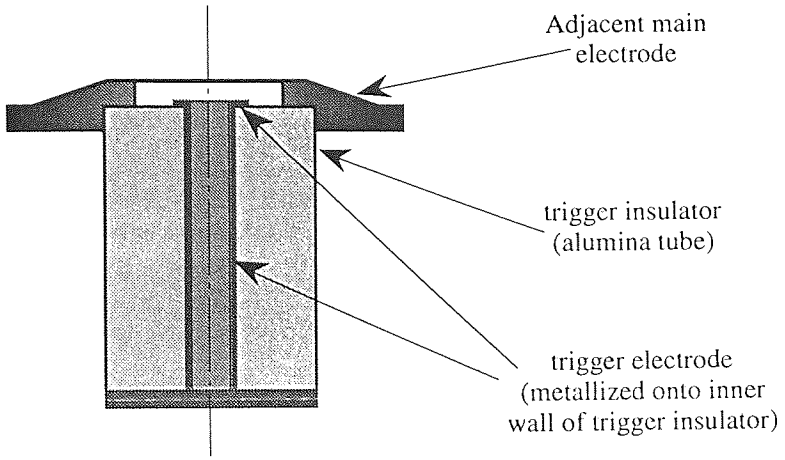

Fig. 1.7 Schematic representation of experimental metallized alumina module

1.3.3 Experimental studies of surface-flashover Metallized alumina modules, of the type shown in Fig 1.7, were operated under ultra-high vacuum (UHV) in a dedicated analytical system. This vacuum system was designed to replicate the normal operating environment of the trigger regime within the evacuated envelope of the TVG device. Diagnostic observations were then made of the electrical and optical phenomena associated with the application of electric field-stress to the alumina insulator of the TVG trigger assembly. The experimental alumina modules and analytical systems are described in Chapter 3. Findings from these experimental studies are then presented in Chapter 4.

1.3.3.1 DC prebreakdown experiments Section 4.1 presents an analytical study of the DC *pre*breakdown behaviour of the trigger-insulator [36], describing the *steady-state* electro-optical processes associated with an insulator-bridged vacuum gap. A *transparent anode* technique [36,37] facilitated the cathode luminescent imaging of prebreakdown electron-emission from the trigger-insulator structure, together with simultaneous optical and electrical analysis. To complement these measurements, optical spectroscopy was used to quantify the nature of the photon-emission observed from the alumina dielectric. This spectroscopic investigation provided further information concerning the physical nature of the electronic processes occurring within the electrically-stressed dielectric of the alumina trigger module [38,39].

1.3.3.2 Pulsed-field breakdown experiments The prebreakdown DC investigations, described above, formed the basis of a pulsed-field study of the trigger insulator, recorded in Section 4.2. This pulsed-field analysis reflected the *dynamic* application of the metal-insulator-metal (M-I-M) regime as a *pulsed*

ignition source in TVG switches. High-speed videographic techniques were used to record images of pulsed-field surface-flashover events within a milli-second timescale [40]. These high-speed images revealed the spatial origin and the physical nature of pulsed optical emissions detected from the trigger-structure.

Further observations of pulsed-field surface-flashover events were undertaken using an ultra-high-speed fast-framing system. Ultra high-speed imaging revealed the initiation of surface-discharge optical phenomena over a sub-microsecond timescale, i.e. the timescale encountered in the closure period of TVG switches under operational conditions [32,33].

1.3.3.3 Surface analysis Surface-analytical techniques, including scanning-electron microscopy (SEM) and energy-dispersive X-ray analysis (EDXA), were used for the detailed study and species-mapping of the surface micro-topography of the experimental alumina modules (see Section 4.3). Careful mapping of the spatial location of observed DC and pulsed-field surface-flashover events was undertaken using computer-based image-enhancement techniques. This spatial mapping enabled the microscopic investigation of the M-I-M regime in the spatial vicinity of the observed flashover events.

Additionally, X-ray photoelectron spectroscopy (XPS) was employed to determine the material constituents of the trigger insulator ceramic. XPS was also used in studies of the nature and state of emitted material which was evolved from the metallized alumina module during pulsed-field surface-flashover events.

1.3.4 Analysis of experimental findings Section 5.1 discusses the findings of DC prebreakdown studies of the alumina dielectric in vacuum in terms of the possible role of defect-centres within the alumina insulator in promoting the observed electrical and optical phenomena [24,41]. The nature of this optical-emission is discussed in terms of charge-transport processes associated with the alumina dielectric [29]. Particular emphasis is placed upon the physical mechanisms of charge-injection into the solid-insulator regime, and how this injected charge can subsequently initiate optical luminosity in the dielectric [42-45]. Section 5.2 expands this DC description of the trigger insulator by considering the apparent field-extraction of electrons from localised regions of luminosity on the dielectric surface.

Following the DC analysis of the trigger region, observations of the pulsed-field breakdown of the alumina dielectric lead to a discussion in Section 5.3 of the

electronic processes associated with the surface-flashover event [46]. Further comment is then made upon the nature of the material species ejected from pulsed-field surface-flashovers in the planar M-I-M regime [47-49]. The initiation of charge-transport in the dielectric is discussed, with particular attention to the possible role of defects within the metallized insulator [50,51]. In Section 5.4, these physical descriptions of DC and pulsed-field electro-optical phenomena are applied to the surface-flashover of a trigger insulator within a TVG switch. An operational description of the TVG surface-flashover trigger structure is proposed (Fig 1.7), along with some discussion of the interaction between the trigger surface-flashover and the electrically-stressed main gap of the TVG.

2. TRIGGERED VACUUM BREAKDOWN

As outlined in Chapter 1, the initiated breakdown of a sealed triggered vacuum gap (TVG) may be induced by the surface-flashover of a solid trigger insulator. This chapter reviews the operational behaviour of a TVG, and discusses various physical phenomena which may influence the insulating performance of the interelectrode vacuum gap. Furthermore, this description of the *vacuum* characteristics of such a device is accompanied by a review of solid dielectrics that often form the envelope and trigger-insulator structures of a TVG switch. Particular attention is paid to the electronic properties of these solid insulator materials, and their behaviour when exposed to electric-field stress under vacuum.

In reviewing the field of triggered vacuum breakdown, this chapter begins in Section 2.1 with a definition of the vacuum state, and provides an outline of the electrical insulation behaviour of an evacuated electrode gap. The prebreakdown electrical behaviour of the vacuum gap is reviewed in Section 2.2. Physical models of charge-conduction through solid insulator materials are presented in Section 2.3, whilst the physical phenomena observed in sealed, insulator-bridged vacuum gaps are introduced in Section 2.4. This is followed in Section 2.5 by a discussion of the surface-flashover and electrical breakdown of solid insulators in vacuum, referenced to the physical models briefly introduced in Section 1.2.

The electronic behaviour of various solid insulator materials in vacuum is reviewed in Section 2.6, along with some of the engineering methods which have been used to modify their insulation performance. The chapter concludes with a review of triggered vacuum gap switches in Section 2.7, and a description of the TVG switching parameters which prompted the experimental study of the solid trigger insulator presented in Chapters 3 and 4 of this thesis.

2.1 Vacuum insulation

The term *vacuum*, at its most general level, describes a volume of gas at a pressure below that of the surrounding atmosphere: the maximum value of this *vacuum pressure* has been specified as 2.5×10^{19} molecules cm^{-3} [52]. Under high vacuum (HV) conditions (i.e. low pressures), the corresponding molecular mean-free-path, λ, exceeds 10mm, and becomes of comparable magnitude to the physical dimensions of the evacuated regime. This relationship between λ and vacuum pressure is illustrated graphically in Fig. 2.1.1.

Fig. 2.1.1 Related measurements defining vacuum (from Roth [52])

Evacuated volumes therefore offer a very low probability of collisions between moving particles and the residual gas molecules within the volume. This feature has led to the widespread use of vacuum insulation in electronic tubes [53], particle accelerators [54] and analytical instruments such as electron microscopes [55].

At gas pressures ranging from a few atmospheres down to medium vacuum conditions of $\approx 10^{-3}$ Torr, the breakdown electric field-strength of the uniform-field electrode-gap has been described experimentally by Paschen curves [56-58]. Paschen curves typically plot the variation of breakdown voltage, V_B, with the *product* of the system pressure, p, and electrode separation, d, i.e. a Paschen plot of V_B versus (p x d) [56]. At high and ultra-high vacuum (UHV) pressures, V_B has been found to diverge from this Paschen law behaviour: in the UHV region, the system pressure is said to be beyond the so-called 'Paschen limit'.

Furthermore, the electrical behaviour of a gas-insulated system has also been found to diverge from that predicted by Paschen curves when the dimensions of the system (d) become small, and the electric fields become high ($E \approx 10$ kVmm^{-1}) and non-uniform [56]. Thus, the *generic* electrical behaviour of a gas-insulated system

may be illustrated by the simplified plot of V_B versus p shown in Fig 2.1.2. In practice, a *series* of such plots, recorded for differing gap spacings (d), would define a more comprehensive Paschen curve description of such a system [56-58].

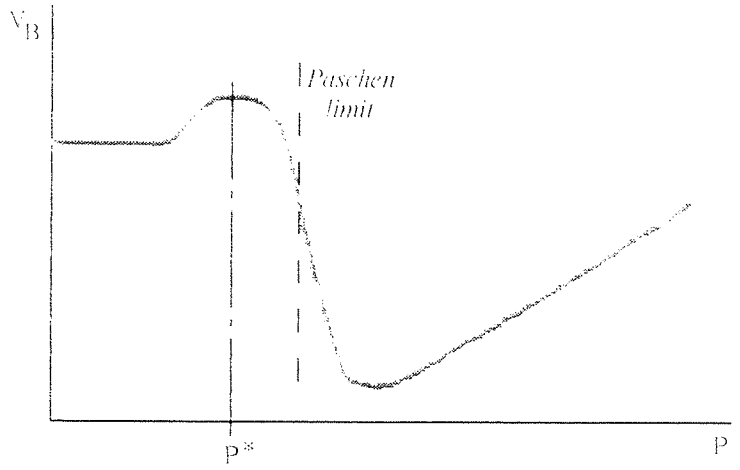

Fig. 2.1.2 Variation of static DC breakdown voltage (V_B) with pressure (P) for a fixed electrode spacing

2.1.1 'Ideal' vacuum-insulated regimes Beyond the low-pressure Paschen limit, the magnitude of E_B reaches a maximum at pressures approaching 10^{-5} Torr [59]. The characteristic pressure, P^*, i.e. at which V_B is maximised, varies according to the electrode material and gap separation. This *pressure effect* [59] region corresponds to an increased molecular mean-free-path ($\lambda_{(1)N} > 10^{-2}$ cm), which now exceeds the physical dimensions of many practical systems [52].

Thus, the modern development of UHV generation and measurement systems [60] has led to the viable production of vacuum-insulated high-voltage gaps. These gaps may be operated with high magnitudes of electric field ($E_B > 10^7$ V m^{-1}) [59], as typified by the use of high-field vacuum insulation in sealed electron tubes.

An absence of any physical *insulating medium* in the plane vacuum gap between two high-voltage electrodes has largely restricted the study of the insulation performance of vacuum gaps to processes associated with the electrodes themselves [61]. Although such a view may be valid for such 'ideal' HV vacuum gaps [62], other physical factors have been found to influence the broader consideration of 'practical' vacuum-insulated regimes. In the particular case of an electron tube, solid dielectric structures often support the HV electrodes, with a sealed dielectric envelope around the evacuated regime. This typical arrangement of a sealed vacuum tube is illustrated in Fig 2.1.3.

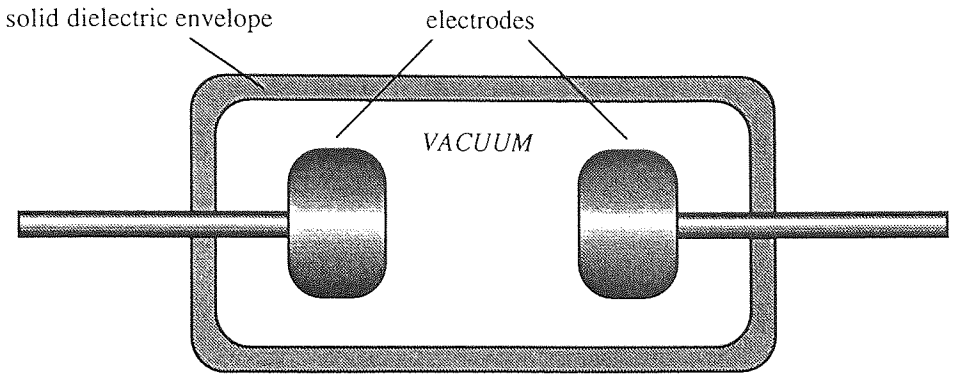

Fig. 2.1.3 Schematic arrangement of a sealed electronic vacuum tube

2.1.2 'Non-ideal' solid-insulator bridged vacuum gaps Breakdown phenomena within evacuated envelopes are generally observed as a 'flashover' along the surface of the solid-dielectric. Furthermore, such events tend to occur at electric-field magnitudes that are considerably lower than those observed for a comparable plane two-electrode vacuum gap [63]. Consequently, the presence of a solid-dielectric member bridging the vacuum space between the electrodes perturbs the 'ideal' geometry of vacuum-insulated electrodes. Figure 2.1.4 illustrates the *generic* structure of a bridged vacuum gap:

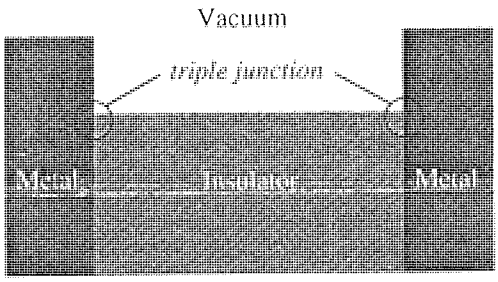

Fig. 2.1.4 Illustrating the bridging of a vacuum gap by a solid insulator

Considering the practical case of sealed, vacuum-insulated electronic tubes (such as triggered vacuum gap (TVG) [32] or vacuum interrupter [64] switches), the solid dielectric material frequently provides an insulating tube envelope. For such applications, glass materials have been widely used to form the envelopes of evacuated electron-tubes. Ceramic materials such as alumina (Al_2O_3) have recently found wider application in electron tube structures, owing to their superior mechanical strength, and the relative ease of forming reliable ceramic-to-metal seals (compared with glass-to-metal seals) at electrode-envelope interfaces [35].

In studies of the possible influence of a solid-dielectric upon the insulating performance of a bridged vacuum gap, Sudarshan and Cross [65] found the DC performance of the vacuum gap to be limited by electronic processes associated with the solid insulator. In particular, electron-emission from the cathode has been found to be enhanced at the cathode/solid-insulator/vacuum interface, or *triple junction* [64].

Similarly, Graneau and Schneider [66] found the insulation-performance of a vacuum-insulated co-axial cryocable to be constrained by surface-discharges across radial glass spacers between the inner- and outer-cable conductors. Thus, Fig 2.1.5 illustrates how this bridging-insulator behaves as an electrical 'weak link' in the vacuum-insulation of two electrodes. These observations clearly indicate that the bridging of a vacuum-insulated electrode gap by a solid dielectric does not represent a *benign* regime. Indeed, it has been generally concluded that the introduction of a solid-insulator has been found to markedly degrade the insulation characteristics of the bridged vacuum gap [63,65,66].

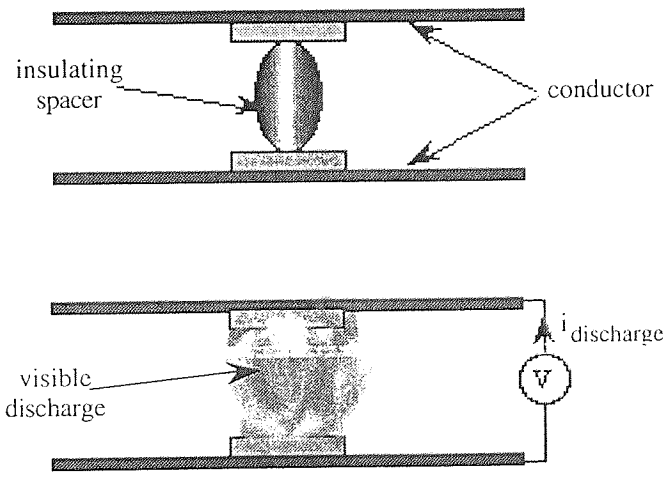

Fig. 2.1.5 Schematic illustration of pulsed-field flashover along a solid insulating spacer within an evacuated electrode-gap [66]

In such 'non-ideal' applications of HV vacuum-insulation in practical engineering designs, the physical phenomena associated with the breakdown of a plane vacuum gap will be reviewed. In this discussion, particular consideration will be given to the *pre*breakdown phenomena which precipitate the electrical breakdown of a vacuum gap. Subsequently, a more detailed consideration will be given to the *in vacuo* behaviour of solid-insulators, since these solid dielectric structures are present in many practical vacuum-insulated HV regimes, as well as forming the trigger insulator of the TVG switch.

2.2 Prebreakdown electronic phenomena in a bridged vacuum gap

Following the description of vacuum insulation given in Section 2.1, this section presents an overview of the physical mechanisms of electron-emission into a plane vacuum-insulated electrode gap. The practical enclosure of a vacuum gap by a solid-dielectric envelope will be considered in Section 2.3 with a review of electron-insulator interaction phenomena. Section 2.4 will then go on to describe electronic charge-transport processes within the solid dielectric, forming a precursor to subsequent discussion of the physical models of insulator surface-flashover that are reviewed in Section 2.5.

2.2.1 Prebreakdown electron-emission into a vacuum gap When electric fields in excess of ≈5-10MVm^{-1} are applied across a vacuum-insulated electrode gap, electrons are "cold"-emitted from the negatively-biased cathode electrode [67]. As the voltage across the vacuum gap is raised, the prebreakdown electron current from a virgin electrode is observed to "switch on" at fields of ≈5-15MVm^{-1}, as shown by region **1** of the prebreakdown I-V plot in Fig 2.2.1. The measured current continues to increase in proportion to the applied field, although discrete discontinuities, or 'steps', are often observed in the I-V characteristics (region **2**) [68].

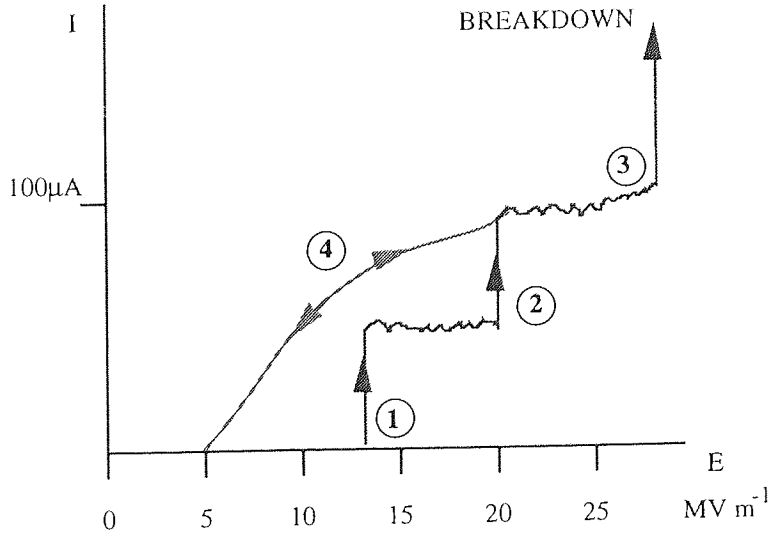

Fig. 2.2.1 Illustrating the typical electrical behaviour of a plane vacuum-insulated electrode gap (after Latham & Xu [68])

A high electric-field threshold is ultimately reached, typically >15-20MVm^{-1}, where the spontaneous electrical breakdown of the gap takes place (region **3**). High-voltage breakdown of the vacuum gap is characterised by the initiation of a high-

current arc between the electrodes [63], and the collapse of the applied voltage. Over the medium to high vacuum region, ambient vacuum pressure has been found to have little effect upon the breakdown threshold of the gap, although the breakdown field value is generally decreased at higher pressures [68].

Following a breakdown event, the subsequent cycling of the gap field reveals a hysteresis in the I-V characteristics, with higher values of prebreakdown current recorded at lower values of gap field. This electrical hysteresis phenomenon is illustrated in region **4** of Fig 2.2.1 [68]. The low-field prebreakdown electron-current increases exponentially with the applied voltage, and follows the Fowler-Nordheim (F-N) equation [58,69]:

$$\ln\left(I/V^2\right) = -\left(dB_2\phi^{3/2}/\beta\right)(1/V) + \ln\left(A_e B_1 \beta^2/d\phi\right) \qquad \{2.1\}$$

The reversible low-field prebreakdown I-V characteristic illustrated in Fig 2.2.1 yields a near-linear Fowler-Nordheim plot, as illustrated in Fig 2.2.2.

Aston University

Illustration has been removed for copyright restrictions

Fig. 2.2.2 Illustrating the influence of electrode separation upon the Fowler-Nordheim plots of the vacuum gap current-voltage characteristics (from Latham [58])

Significant electron-emission is generally predicted to occur at fields in excess of $\approx 5 \times 10^9$ Vm^{-1}, where the F-N plot becomes non-linear [70]. This order of field-strength is approximately two orders of magnitude greater than breakdown field-values observed experimentally (see Fig 2.2.1). Thus, the physical mechanisms that may be responsible for the *enhancement* of the electric field, and the subsequent initiation of vacuum breakdown, are reviewed in the following sections.

2.2.2 'Metallic' model of field electron-emission (FEE) Electron current flow is generally not observed to be uniform over the cathode surface, but is instead localised at discrete "spots" on the cathode surface of emitting area A_e [67,70]. Furthermore, the measured currents often correspond to field-values one hundred times greater than the macroscopic field predicted by the F-N equation shown above. These field values are calculated by simply dividing the applied voltage, V, by the interelectrode gap separation (d); i.e. the macroscopic field magnitude, E_m, may be expressed as

$$E_m = \frac{V}{d} \qquad [\mathrm{V\,m^{-1}}] \qquad \{2.2\}$$

According to the F-N picture of electron field-emission, a local enhancement of the electric-field to a microscopic value, E_l, is proposed to occur at favourable electron-emission sites on the cathode. Thus, a geometrical field-enhancement factor, β, was introduced, to account for this local enhancement of the electric field [70], and defined by the relation

$$E_l = \beta E_m = \beta \frac{V}{d} \qquad [\mathrm{V\,m^{-1}}] \qquad \{2.3\}$$

With reference to Fig 2.2.2 and eqn 2.1, the gradient of the F-N plot is inversely proportional to the magnitude of field enhancement (β) associated with the measured current-voltage characteristics [71]. However, a knowledge of the electrode surface work-function, ϕ, is required to estimate the local field-enhancement factor, β, from the Fowler-Nordheim plot of main-gap voltage and current (see eqn 2.1). Furthermore, a projection of the F-N plot back to its intercept with the vertical axis yields an estimate of the surface-area, A_e, of the electron-emission centre(s). Such an estimate relies upon the knowledge of constants B_1, B_2 and β, as described in eqn. 2.1.

A long-standing interpretation of the geometric field-enhancement factor, β, has been the possible role of sharp metallic microprotrusions, or 'whiskers', on the cathode surface [70,72,73]. This model has been widely studied using clean, high-purity metal electrodes, which permit clear mapping of the electrode surface micro-topography. Simulated studies of the "cold" emission of electrons from metallic whiskers has also been undertaken using point-plane electrode gaps [70]. Thus, these analytical studies have evolved experimental β values relating to the physical

dimensions of the 'whisker' microtip; i.e. the whisker height, h, and its radius, r. Figure 2.2.3 illustrates such a whisker microprotrusion on the surface of an electrode.

Fig. 2.2.3 Illustrating the geometric enhancement of a macroscopic electric field, E_m, to a higher microscopic field value, E_l, at a microprotrusion on an electrode surface (from Latham [74])

From a practical viewpoint, careful mechanical polishing of the electrode would be expected to remove any whiskers, and thereby eliminate enhanced electron-emitter structures from the electrode surface. Consequently, this polishing process should maximise the voltage-breakdown threshold of the vacuum-insulated gap. However, experimental studies have shown that polished metal electrodes continue to exhibit enhanced FEE [68]. This key finding has therefore prompted further investigations of the prebreakdown electron-emission mechanism.

2.2.3 FEE due to non-metallic cathode inclusions Measurements of enhanced FEE currents from polished electrodes have suggested alternative physical models of enhanced electron-emission from the cathode surface. Following this hypothesis, spatially correlated electron-emission-mapping and electron-microscopy studies of cathode surfaces have revealed FEE to occur from particulate structures on the cathode electrode [75]. As with metallic FEE, the current-voltage characteristics of the electron-emission from these inclusion-sites follow a straight-line F-N plot, as shown in Fig 2.2.2 [75,76]. However, further surface-analysis has revealed these inclusions to consist of insulating oxides of the electrode metal, or 'foreign' deposits of impurity species [61,77]. The following sub-sections review the main physical models that have been used to describe enhanced electron-emission from localised, *inhomogeneous* metal-insulator regions on a cathode.

2.2.3.1 Hot electron emission: I - Filamentary model of FEE Experiments with plane metal electrodes in vacuum have shown that a high external electric-field can lead to the formation of an electroformed conducting channel, or 'filament', in an insulating microparticle on the cathode surface [78]. Under the influence of the electric field, electrons are assumed to tunnel from the Fermi level of the metal electrode into the conduction-band of the insulator. These cold electrons can then accumulate within trap centres in the dielectric, forming a semi-conducting 'channel' of trapped charge. Figure 2.2.4 presents a schematic diagram of the metal-insulator (M-I) regime of the inclusion at the electrode surface. It is interesting to note that the conducting filament presents a 'micropoint' regime at the electrode surface, similar in form to the metallic whisker previously described in Section 2.2.2.

Fig. 2.2.4 Illustrating a conducting channel within the M-I-V regime of an insulating inclusion at the electrode surface, and enhancement of the microscopic electric field (from Latham [61])

As the channel probes the main-gap field, the trapped electrons are heated by the enhanced field that penetrates the insulator, and are transported through the channel under the influence of the penetrating field [68]. When these 'thermalised' electrons reach the microparticle-vacuum interface, they may encounter even higher values of electric field, and be heated to temperatures in excess of 1000°C [68]. Thus, the electrons may be "quasi-thermionically" emitted over the potential barrier at the electrode surface into the vacuum gap.

Artificial M-I-V regimes have been formed by the deposition of carbon particles on the electrode surface [79]. The energy-spectra of prebreakdown electrons emitted from these structures reveal electron-energies 0.2-0.4eV below the Fermi level of

the metal electrode, consistent with quasi-thermionic electron-emission from a conducting filament [68]. An energy-band representation of the M-I-V regime at the electrode surface is shown in Fig 2.2.5.

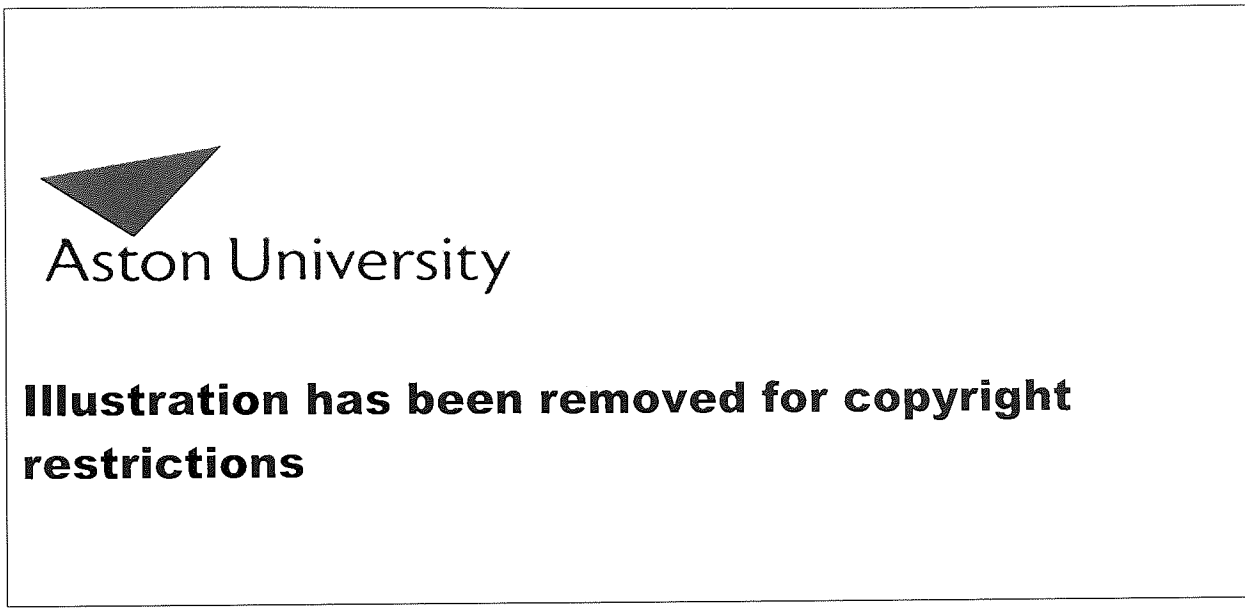

Fig. 2.2.5 Band diagram representation of electron-emission from a conducting channel formed in a M-I-V microregime (from Latham [61])

2.2.3.2 Hot electron emission: II- Antenna Effect An extension of the M-I-V model has involved a consideration of a metallic particle (or 'flake') situated on an oxide layer at the electrode surface. According to this extended model, the microscopic metallic flake forms a M-I-M-V regime on the surface of the oxidised electrode, as illustrated in Fig 2.2.6.

Fig. 2.2.6 Illustrating the "antenna effect" associated with the M-I-M-V regime of a conducting microparticle embedded into the oxidised surface-layer of a metal electrode (from Archer [79])

Thus, the flake is proposed to behave as an 'antenna' by probing the interelectrode gap field, thereby generating an electric field-enhancement ($\beta \approx {}^{h}/_{d}$) across its contact interface with the oxide layer [79]. Electron emission is believed to occur from a conducting channel formed in the M-I electrode / electrode-oxide interface region, according to the M-I-V emission model described in Section 2.2.3.1. It may be assumed that not all of the electrons will escape from the channel, since some will lose energy through collisions and be scattered within the flake [79]. In this scenario, only the electrons that are scattered from the M-I-M channel into vacuum will escape. This hypothesis is supported by *diffraction*-type electron-emission images generated by *coherently* scattered electrons from the cathode [68]. Such cathodoluminescent images have been obtained from 'natural' and artificial graphite M-I-M sites on plane metal cathodes [68].

2.3 Vacuum gaps bridged by a solid-insulator

As outlined in Section 2.1.2, many practical vacuum-insulated systems rely upon solid dielectric insulators to provide physical support of electrode structures, or to serve as insulating envelopes in sealed vacuum-insulated regimes (see Fig 1.1). Where a solid insulator bridges the vacuum-gap between a pair of metal electrodes, the electric-field threshold for voltage-breakdown of the interelectrode gap may be dramatically reduced [62]. To reflect the practical importance of this phenomenon, this section reviews the physical phenomena observed in a "bridged" vacuum gap.

2.3.1 Electronic charging of solid insulators This is a particularly important *external* manifestation of electronic processes that occur within solid insulators, and has accordingly been widely reported [62,80]. Using an electron-beam deflection technique, de Tourreil and co-workers [81] observed *positive* charging at the surface of a cylindrical insulator, with the application of parallel electrical fields in vacuum. More recently, electrostatic probe techniques, such as that developed by Chalmers *et al* [82,83], have enabled detailed plotting of the surface-charge distribution along the insulator. The four main electrode-insulator geometries that have been studied with this technique are illustrated in Fig 2.3.1.

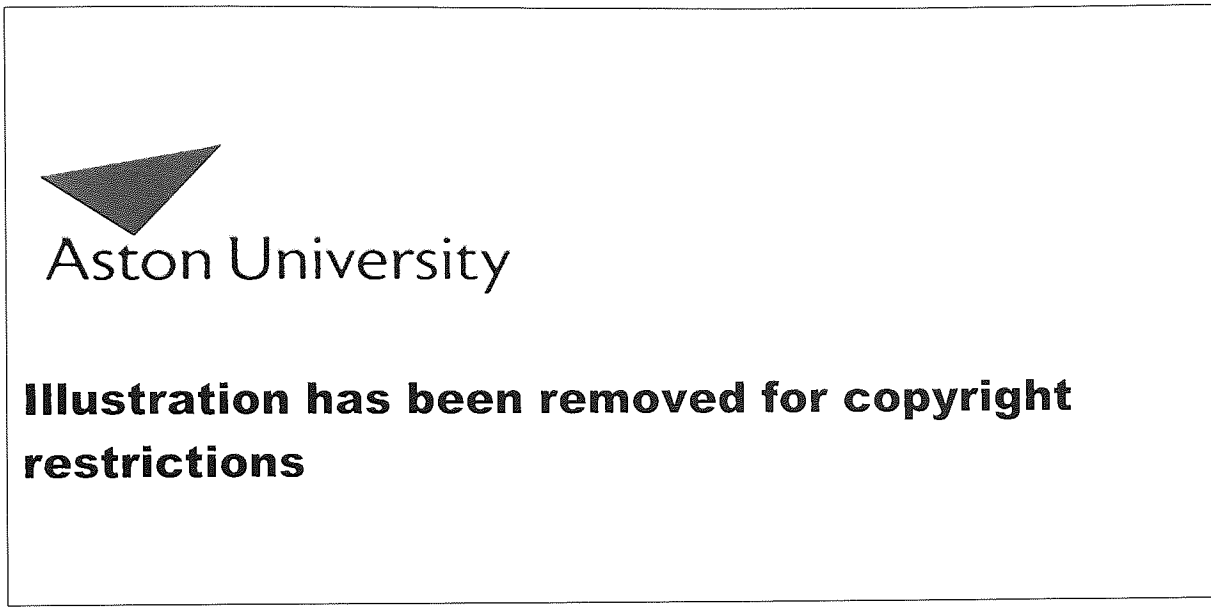

Fig. 2.3.1 Electrode-insulator geometries (from Chalmers *et al* [82,83])

In the recessed-cathode arrangement of Fig 2.3.1(a), the degree of surface-charging and the ultimate voltage-breakdown strength of the insulator were improved with respect to the plane geometry of Fig 2.3.1(b) [83]. Charging in these arrangements appeared to be uniform over the insulator surface, and the measured charge increased in direct proportion to the applied DC voltage. The recessed-cathode geometry gave rise to positive-charging of the insulator, whilst in the plane {Fig 2.3.1(b)} and cathode-insert {Fig 2.3.1(d)} geometries the insulator was charged negatively at low field-values, before becoming positively charged at higher values of applied electric field.

The cathode-insert configuration shown in Fig 2.3.1(d) was found to offer the highest inception and hold-off (withstand) voltages, with the surface-charge distribution appearing in discrete 'filaments' along the insulator in the vicinity of the anode [82,83]. Similar 'filamentary' charge-distributions, of higher magnitude, were observed with the anode-insert of Fig 2.3.1(c), with a concentration of surface- charge near the cathode electrode [82].

The charging of an insulator surface, under the influence of an injected beam of electrons, has been widely explained by the phenomenon of secondary electron emission (SEE) [17,84-88]. For a given insulator material, the SEE yield (δ) may be expressed in terms of the kinetic energy and angle-of-incidence of the incident electrons, i.e. as depicted in Fig 2.3.2.

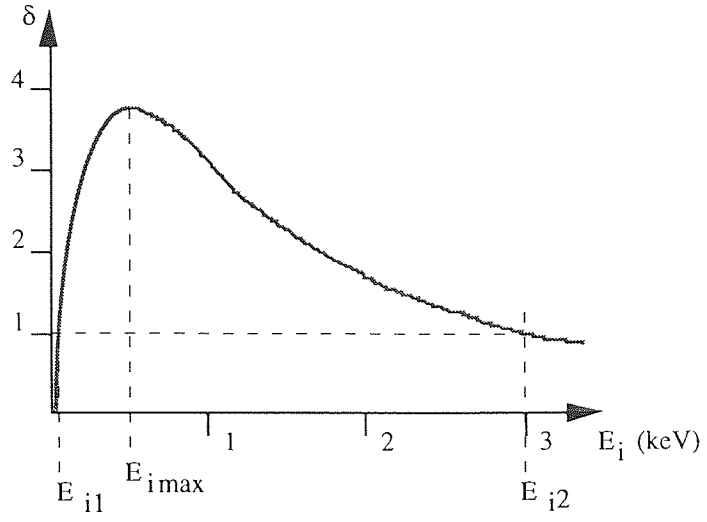

Fig. 2.3.2 Variation of secondary electron emission yield, δ, with incident electron-energy, E_i, for alumina ceramic (after de Tourreil & Srivastava [17])

At electron energies between E_{i1} and E_{i2}, it can be seen from Fig 2.3.2 that the number of secondary electrons emitted from the insulator exceeds the primary fluence of electrons. Thus, the insulator surface becomes positively charged [17]. Conversely, at low electron-energies below E_{i1}, the secondary-electron fluence is less than that of the incident primary electrons, and the insulator-surface becomes negatively charged [83]. As the electron-energy approaches E_{i2}, the positive charge on the insulator-surface is sufficient to attract many of the secondary-electrons back to the insulator, and so the dielectric surface becomes negatively charged [17].

An inclination of the insulator-surface at a critical angle, θ_c, to the electric field results in a SEE yield of unity; i.e. $\delta = 1$ [89]. Under this critical-angle condition, the charge-distribution at the insulator surface is in equilibrium, and there is no net charging of the dielectric. θ_c is independent of the applied field-strength and, as shown in Fig 2.3.2, is a function of the insulator SEE properties [89].

2.3.2 Optical luminosity from solid insulators Electronic charging of the insulator surface is often associated with optical luminosity in the insulator material [23,24,80]. Kofoid [23] observed bright-blue luminosity, accompanied by a diffuse pink glow, from porcelain insulators in the vicinity of the cathode. Other workers have reported luminosity in ceramic materials [90], both near the cathode triple-junction [20,36,39,51,91], and also in the vicinity of the anode triple-junction [36,39,51,80]. Similarly, Milton [92] observed blue luminosity from the cathode-junction region, using a range of both ceramic and plastic insulator materials.

From optical studies of alumina (Al_2O_3) ceramic RF windows, Saito and co-workers [44,45,93] recorded the optical emission spectrum shown in Fig 2.3.3 for electrically-stressed alumina. Similar spectra were also recorded from alumina dielectrics by Sudarshan *et al* [20,21,91], and also by Jardin and co-workers [43] in studies of the electron-beam excitation of an alumina ceramic.

Aston University

Illustration has been removed for copyright restrictions

Fig. 2.3.3 Optical emission spectrum from an alumina r.f. window (from Saito [93])

Referring to Fig 2.3.3, all such spectra are found to exhibit two key features; namely, a blue/UV emission-band around 300nm, and a deep-red spectral line at 695nm. No atomic lines are visible in the optical spectrum [20], and the observed spectral peaks appear to correspond to radiative emissions from defect sites within the dielectric material [20,45,91,93]. The broad emission band around 300nm is generally attributed to radiative electron-recombination at anion (O^-) vacancy defects, or *F*-centres [41,94], in the alumina ceramic [20,25,91,95,96]. Radiative electron-recombination at *substitutional* impurities of chromium (Cr) is believed to lead to the deep-red (695nm) emission recorded from the alumina [44,93,95,96].

Later in this chapter, in Section 2.4, consideration will also be given to how electron trapping at these defect centres could influence the charge-transport process within the insulator. Section 2.5 then discusses the possible role of this charge in the surface-flashover and electrical breakdown of the solid insulator.

2.3.3 Triple junction phenomena In addition to the optical events observed in the bulk of solid dielectrics, further phenomena have been observed in the *triple-junction* regions, i.e. where the high-voltage electrodes are bonded to the insulator

(see Fig 2.1.3). Using a cathode-luminescent screen, Kofoid [23] observed electron-emission from the cathode triple-junction that was accompanied by intense optical emission from the cathode region of the insulator [23,24,97]. With the continued application of electric field-stress, this cathode luminosity is often seen to extend across the insulator towards the anode [51,97].

It has been widely reported that there is an enhancement of the local electric-field at triple-junctions [62]. Thus, numerical analyses [98-100] have shown that there is a *geometric* enhancement of the electric-field stress at the metal-insulator-vacuum junction, that is associated with a solid insulator of permittivity ($\varepsilon_o\varepsilon_r$), and the free-space permittivity (ε_o) of the vacuum environment. It has also been shown that a higher degree of electric-field intensification is introduced by the presence of voids at the metal-insulator (M-I) interface. These combined effects can therefore lead to a 'bunching' of the electric-field equipotentials at the triple junction and an acute enhancement of the local electric-field [12,101,102], as shown in Fig 2.3.4 (b).

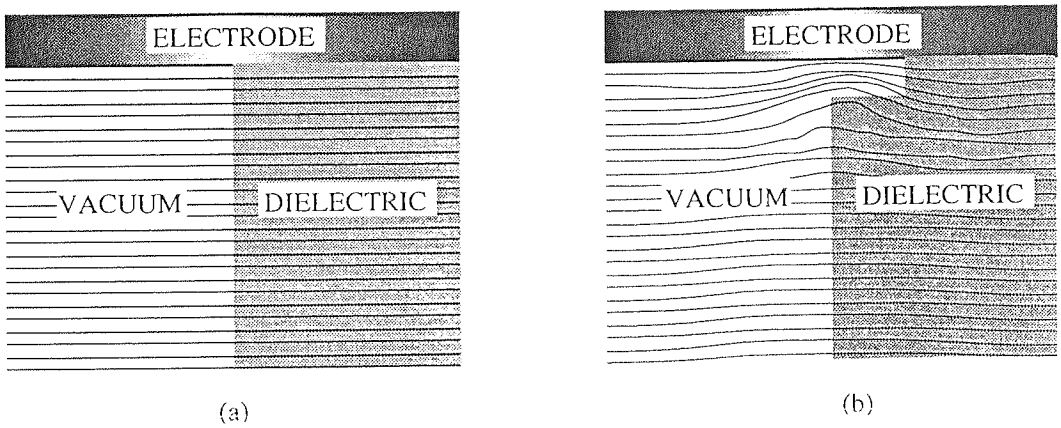

Fig. 2.3.4 Equipotential plots through (a) ideal electrode-insulator-vacuum triple junction, and (b) with small void at the electrode-dielectric interface (after Miller [102])

In modelling the electronic-charging and subsequent flashover of a solid dielectric, Latham and co-workers [51] have highlighted the possible role of non-intimate electrode-contact at the cathode triple-junction in enhancing the injection of electrons into the bulk insulator. This initiation of mobile charge injection can then lead to the filling of trapping-centres in the insulator, such as those described in alumina ceramic in Section 2.3.2 [96].

The growth of this internal distribution of trapped charge along the insulator is consistent with experimental observations of the 'growth' of luminosity along the insulator [51,97]. Furthermore, the continued growth of the trapped charge across the dielectric is proposed to further enhance the local electric-field at the cathode.

This enhanced field may then augment the injection of electrons, leading to the electrical breakdown of the insulator.

The electronic behaviour of the solid-dielectric and void regimes will be further discussed in Sections 2.5 and 2.6 respectively. Section 2.6 also presents some practical techniques which have been used to minimise the influence of such voids on the electrical breakdown performance of the solid insulator [12,102].

2.3.4 Modifications in stressed dielectrics after flashover Following the application of electric-field stress and the surface-flashover of a solid insulator (i.e. as described in Sections 2.3.2 and 2.3.3), physical modifications can occur in the dielectric material. In particular, electrical breakdown of the insulator can result in (i) localised melting and the formation of 'tracks', or "treeing" [31], on the insulator-surface [27,45,93], (ii) a discoloration of the dielectric material [51,97], and (iii) puncture, or "punch-through", in the bulk volume of the dielectric [30,97].

The physical nature of the insulator-breakdown process, that is externally manifested as a surface-flashover event, will be reviewed in Section 2.5, with consideration being given to its role in the ejection of dielectric material, and the generation of surface tracks on the insulator.

2.3.4.1 Surface melting and treeing on solid insulators Damage 'trees' are often observed on solid dielectric surfaces following electrical breakdown events [30,45]: for example, the electron-micrograph presented in Fig 2.3.5 illustrates post-breakdown treeing on a sapphire (Al_2O_3) insulator. These trees, or 'tracks', on the insulator surface have been recorded in the spatial vicinity of optical luminosity in the dielectric, observed during the application of electric-field stress to the insulator [103]. Together with the charge-trapping processes believed to be associated with this luminosity [43,45], the associated charge-conduction processes in the insulator are thought to cause local melting of the dielectric material [27,103]. As illustrated in Fig 2.3.6, this melting of the insulator is manifested in the visible tracks on the insulator surface. The physical processes of charge-conduction in solid dielectrics that are thought to lead to these tracking features will be discussed further in Section 2.4.

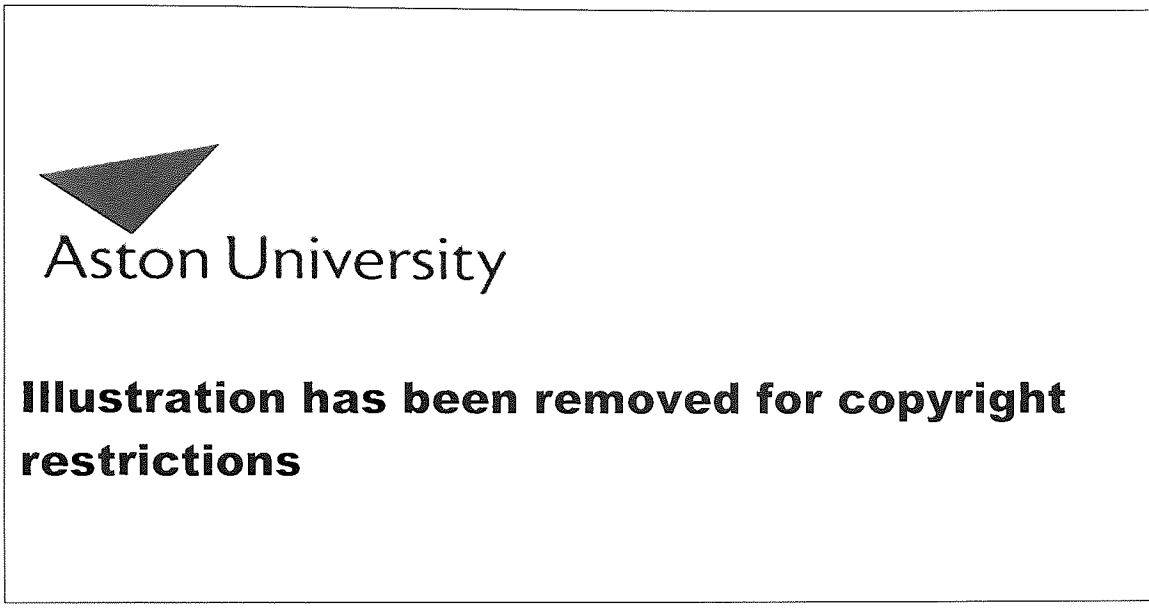

Fig. 2.3.5 Post-discharge 'treeing' on a sapphire insulator (from Saito *et al* [45,103])

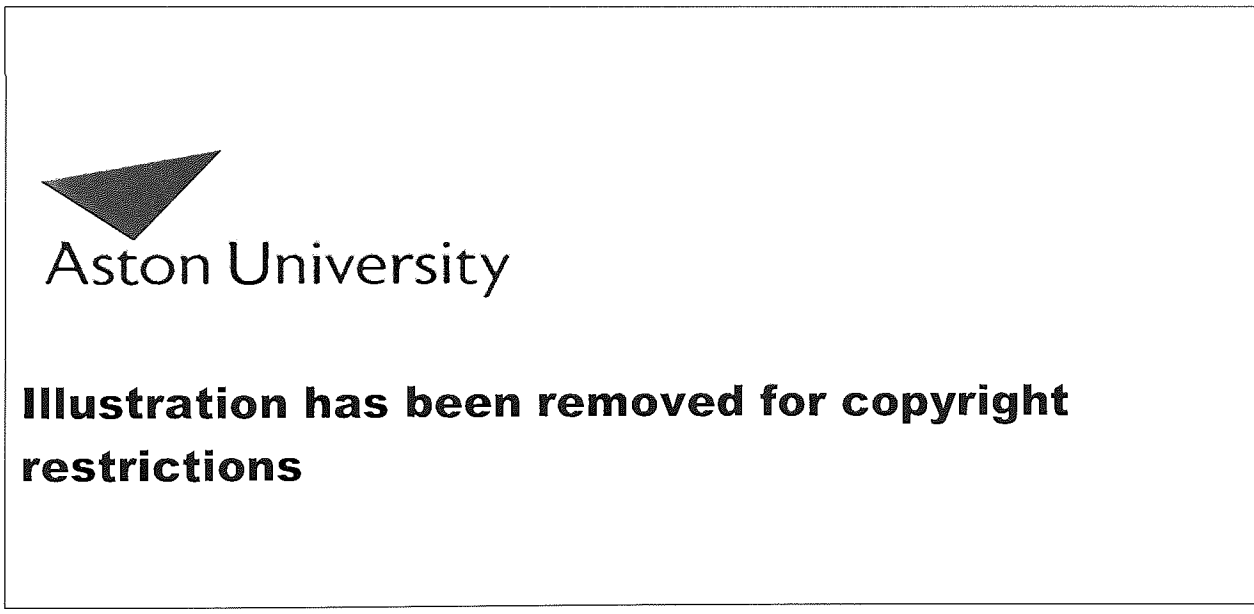

Fig. 2.3.6 Surface melting arising from the pulsed-field surface-flashover of an alumina ceramic (from Saito *et al* [95])

2.3.4.2 Insulator punch-through The ejection of insulator-material has been demonstrated to be a consequence of electrical breakdown of the solid dielectric [30,97]. Thus, Fig 2.3.7 illustrates a region of cavitation in a polycrystalline ceramic which was believed to have resulted from the ejection of ceramic grains due to the explosive propagation of *sub-surface* dielectric currents [30]. It is interesting

to note the absence of such cavities in regions where treeing is visible on the insulator surface. This finding may indicate the flow of *surface* currents in the tree region, leading to the local melting of the insulator surface [30].

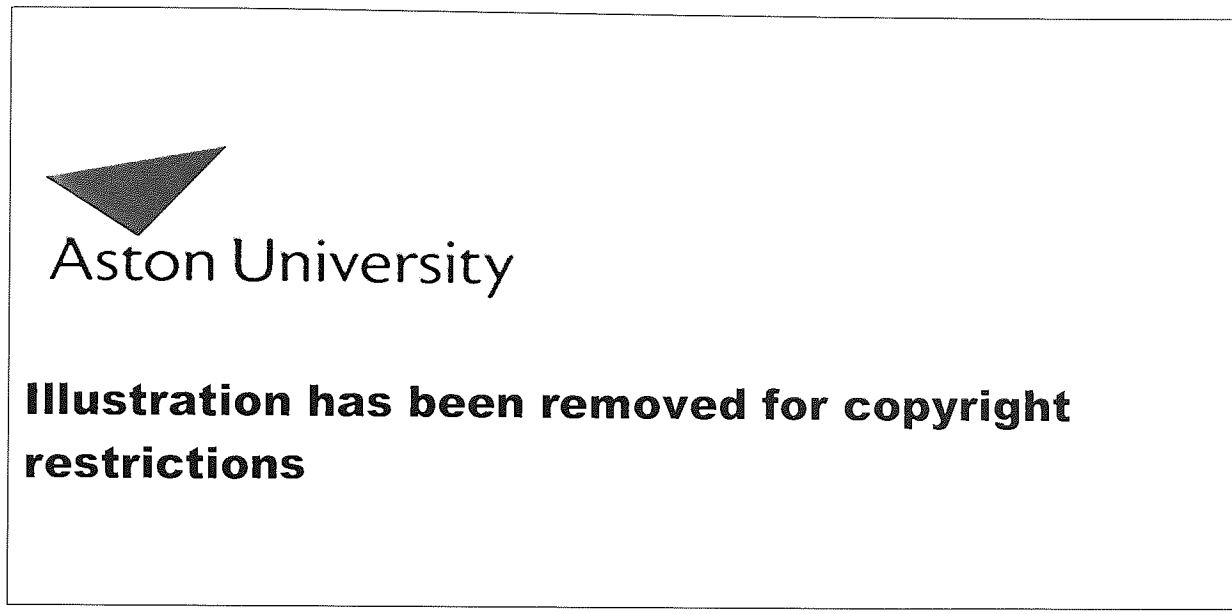

Fig. 2.3.7 Surface treeing and grain-ejection following the pulsed-field surface-flashover of a polycrystalline ceramic (from Le Gressus & Blaise [30])

2.3.4.3 Discoloration of stressed insulators Following surface-flashover events, solid insulators have been found to be discoloured by the deposition of material on the dielectric surface. This deposited material is often formed by arc-erosion products derived from the electrodes that are attached to the insulator (see Figs 2.1.3 and 2.3.1), and may consist of metallic [173] and/or oxidised electrode material [97]. Melting and sublimation of the insulator surface, together with the ejection of insulator material, may also help to modify the appearance of the insulator.

2.4 Charge injection and transport in solid dielectrics

In considering the factors affecting the stability of the macroscopic region of a solid-insulator bridged vacuum gap, it is firstly necessary to consider charge transport processes associated with a solid dielectric, since they are believed to ultimately lead to the electrical breakdown of the vacuum insulated electrode regime [65,66]. Electrical breakdown of the solid dielectric often occurs through a localised surface plasma, or *surface flashover*, rather than the plasma arc observed

in plane vacuum gaps. The physical mechanisms that may lead to the surface-flashover of a solid dielectric will be reviewed in Section 2.5. In this section, attention will be given to the physical processes by which electronic charge may be transported *through* the insulator, giving rise to the prebreakdown phenomena described in Section 2.3.

2.4.1 Conduction through metallic surface layers Electronic conduction may be assumed not to occur *within* the insulator bulk, but instead to rely upon conductive structures on the insulator surface. Such structures may be in the form of a metallic conducting film, which can result from the segregation of a phase of conductive material out of the insulator bulk, or from the deposition of eroded material from the electrodes (see Section 2.3.4.3). Electron-transport may then be proposed as a *surface* process, with electrons tunnelling between metallic 'islands' on the insulator surface [104]. This metallic film regime is illustrated in Fig 2.4.1.

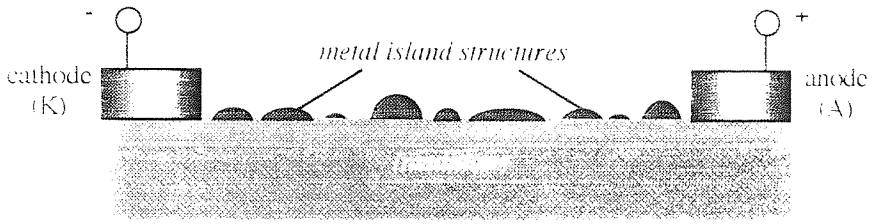

Fig. 2.4.1 Schematic illustration of a planar insulator coated with a thin film of conducting island structures (after Eckertova [104])

In the case of intrinsically pure insulators, and in the apparent absence of any conducting surface-layer, consideration must be given to electronic processes within the dielectric. These 'bulk' conduction processes are evidenced by electro-optical observations of the stressed insulator, where luminosity is observed from radiative electron-recombination at discrete centres within the dielectric material [25] (see Section 2.3.2). Such observations point to a significant transport of electronic charge within the bulk of the insulator. In this review, the transport of electronic charge in both single-crystal and polycrystalline dielectric materials will be considered.

2.4.2 Charge transport in single-crystal dielectrics: I - Band Conduction As illustrated in Fig 2.4.2, a classical physical description of a solid dielectric is that of a wide band-gap semiconductor [105]. According to this energy-band picture, impurities and defects in the dielectric structure represent

electronic donor (anion) and acceptor (cation) energy-levels within band-gap of the insulator. For example, in studies of the conductivity of single-crystal alumina with increasing temperature, Will *et al* [105] observed two discrete activation-energies at 0.4eV and 4.8eV within the 9.6eV [106] band-gap of the alumina material. From spectrographic analysis of these activation thresholds, a donor species of silicon (Si) was identified in the alumina, together with calcium (Ca) and iron (Fe) acceptor species: the concentrations of these substitutional impurity species were a few ppm.

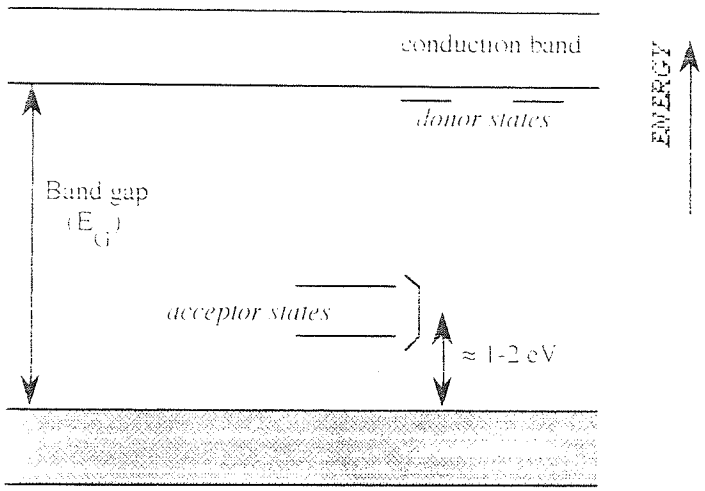

Fig. 2.4.2 Illustrating the energy-band representation of an insulator

A limitation of the band-model interpretation for an insulator is the high-temperature analysis of the dielectric conductivity characteristics [105-108], and the possible perturbation of the physical structure of the insulator. In the particular case of oxide semiconductors, analytical problems are further compounded by the difficulty in determining the precise chemical and physical nature of these insulator materials. Furthermore, a modified physical description is required for chrage-transport in dielectrics which have high populations of lattice-defect sites. In such materials, highly mobile charge-carriers are capable of 'hopping' between defect-sites, and do not enter the conduction-band of the insulator [108].

2.4.3 Charge transport in single-crystal dielectrics: II- Polaron 'Hopping' Following the injection of an electron into the conduction band of an ionic crystal, it can be energetically favourable for the electron to move to a localised site in the crystal lattice [109]. Negative ion vacancies, or *F* centres [94] (see Section 2.3.2), can often present a favourable defect-centre at which the electron may be trapped. As the result of the Coulomb interaction of the trapped electron with negative and positive lattice ions, this *self trapping* process [110]

electron with negative and positive lattice ions, this *self trapping* process [110] results in a local deformation of the crystal lattice. Figure 2.4.3 illustrates the combined entity of the self-trapped electron, and the associated induced polarisation of the crystal lattice. This trapped-electron/lattice-polarisation structure is termed a *polaron*.[109,111].

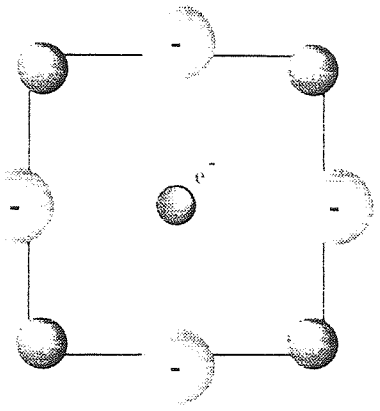

Fig. 2.4.3 Illustrating the self-trapped negative charge of a polaron lattice-site

Distortion of the ionic atoms in the crystal-lattice causes a lowering of the energy of the 'added' electron, and thereby creates a potential well around the localised electron. Figure 2.4.4 presents a schematic model of the polaron, and shows the Coulombic potential-energy well (U(r)) surrounding the trapped electron (which moves within the region of radius r_1).

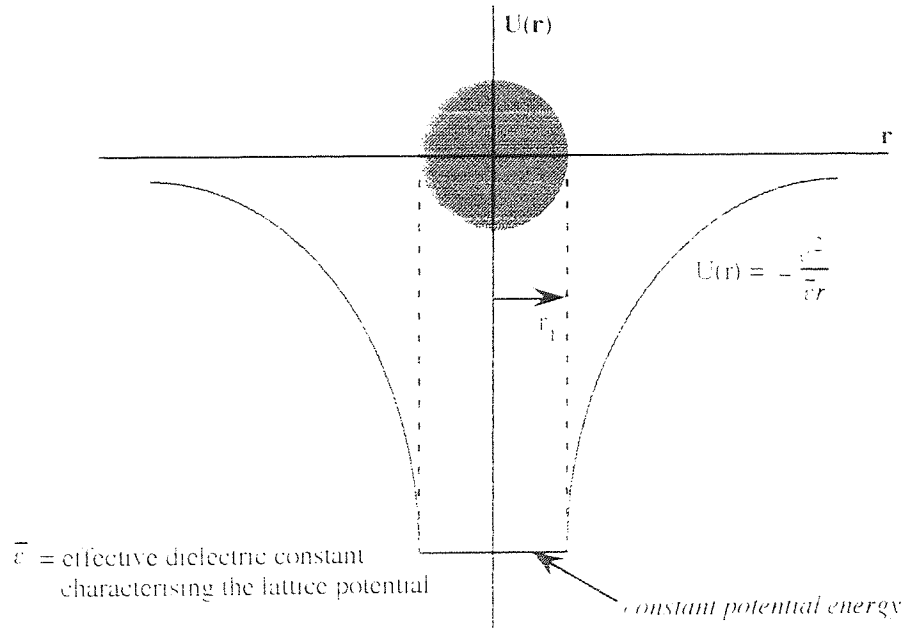

Fig. 2.4.4 Illustrating the potential-well associated with the lattice-distortion around a polaron electron-centre

Since the conduction electron is associated with a *region* of induced polarisation, and is not attached to any particular ion or atom, its mobility within this local region of the crystal lattice is very high [109]. Detrapping of the polaron electron may be thermally activated [108], with a carrier mobility μ described by equation 2.4:

$$\mu \propto e^{-\left(\frac{\bar{\varepsilon}}{kT}\right)} \qquad [m^2\ V^{-1}\ s^{-1}] \qquad \{2.4\}$$

Electrons are therefore able to 'hop' between lattice-vacancy sites, as a result of thermal (phonon) excitation, or due to local distortion of the electrical field in the dielectric [29]. This electron-transport process represents the so-called "polaron hopping", or "electron hopping" conduction mechanism.

2.4.4 Charge transport in polycrystalline dielectrics: I - Ionic Conduction In many polycrystalline dielectric materials, the segregation of impurity materials along grain-boundary defects impedes a precise description of the physical and chemical structure of the insulator. This is because the excess ions (interstitials) at grain-boundaries, and impurity-dopants within the dielectric material (substitutional impurities) give rise to significant populations of free ions in these polycrystalline materials. The presence of these ionic defects has been observed to increase the conductivity of a polycrystalline dielectric, compared to that of the single-crystal form of the same dielectric material [112].

The ionic nature of the crystal causes the mobile ion to see a high electrostatic 'potential well' on either side of each lattice point. High ionic mobility is associated with small ion size and low (electronic) charge. By contrast, the transport of highly-charged ions will induce a high degree of polarisation in oppositely-charged ions within the crystal lattice, and will exhibit a low value of ionic mobility; large-size ions will be impeded by the interaction of their outer-shell electrons with those of ions in the lattice.

The presence of lattice vacancies enhances the ion-conduction process, since neighbouring ions are readily able to move and occupy this vacancy, with the vacancy then appearing to propagate through the lattice in the opposite direction to the ion flow. Thus, this ionic conduction model presents the 'hopping' of ionic vacancies through the crystal lattice, as a result of ion-hopping into the vacancy sites. Figure 2.4.5 presents a one-dimensional schematic diagram of a vacancy bounded on either side by a lattice-ion site. In the field-free regime of Fig 2.4.5(a),

the vacancy has an equal probability of moving in either left or right directions, since the electrostatic potential barrier-height is equal on both sides of the vacancy.

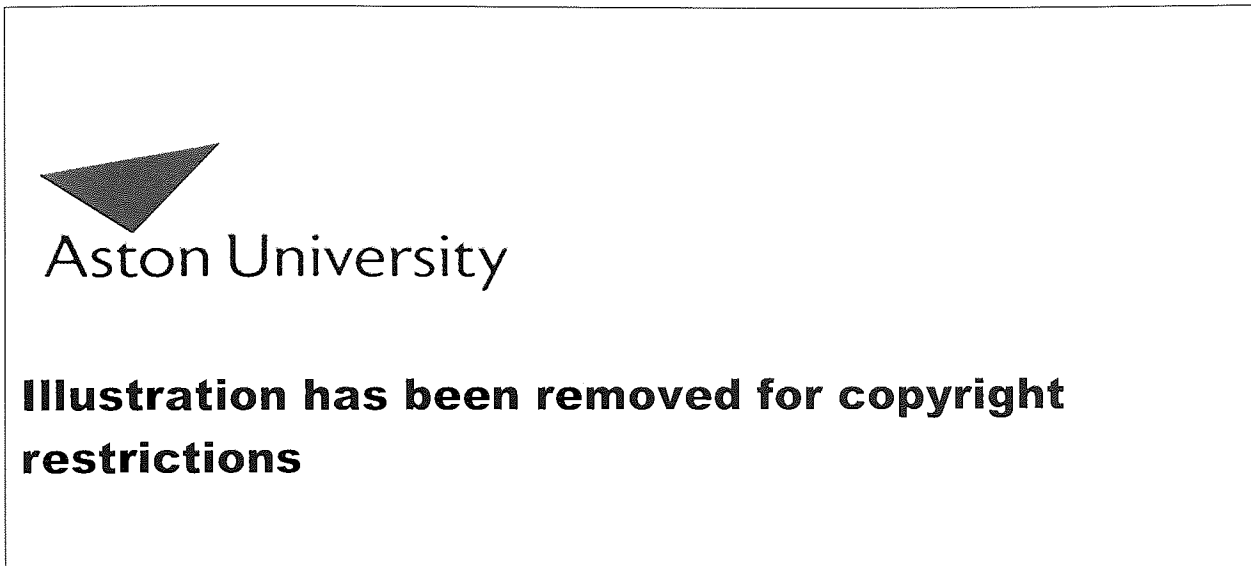

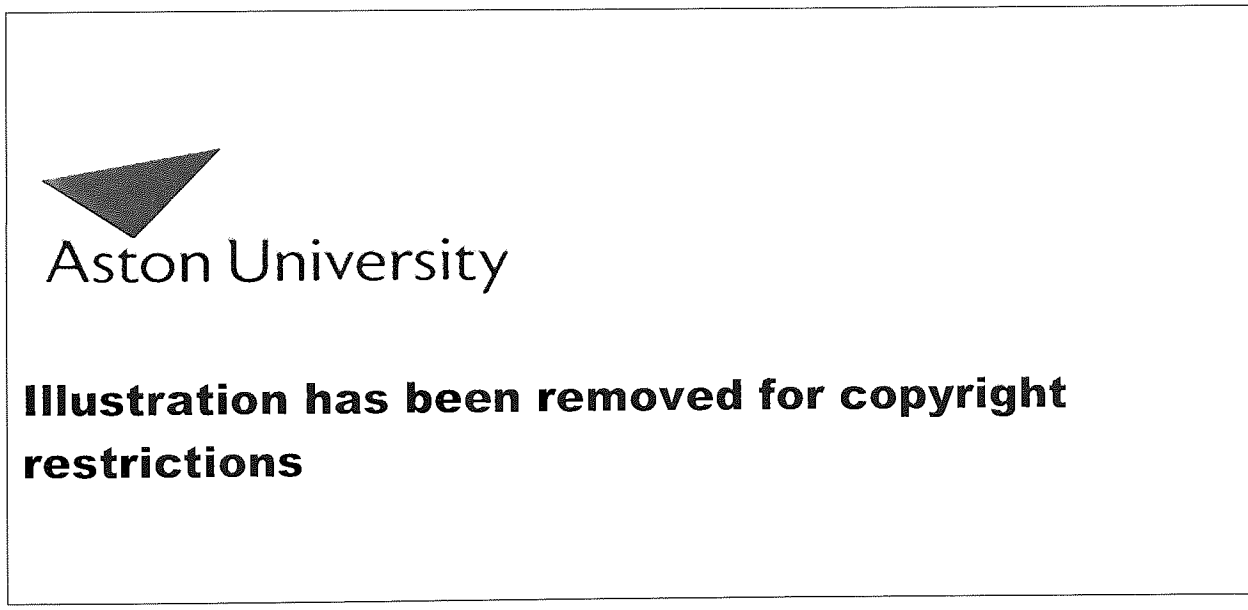

Fig. 2.4.5 (a) Potential-energy barriers to ionic transport, and (b) lowering of the barrier-height with the application of an electric field, **E**. (from Moulson & Herbert [108])

According to this model, ion motion may occur randomly through the crystal lattice [108], with the temperature-dependent ionic conductivity expressed by [113,114]

$$\sigma = \sigma_0 e^{\left(\frac{-E_i}{kT}\right)} \qquad [m^2\ V^{-1}\ s^{-1}] \qquad (2.5)$$

With the application of an electric field **E**, as shown in Fig 2.4.5(b), the potential barrier height E_j is reduced by an amount ΔE_j in the direction of the applied field, where

$$\Delta E_j = e\mathbf{E}\frac{a}{2} \qquad \text{[eV]} \qquad \{2.6\}$$

The measured current-density, **j**, in the direction of the applied field **E**, may then be expressed as

$$\mathbf{j} \propto \mathbf{E}e^{\left(\frac{-E_j}{kT}\right)} \qquad \text{[A m}^{-2}\text{]} \qquad \{2.7\}$$

Ionic conduction provides a reasonable description of charge-transport through materials which have high densities of structural and material defects. In particular, this model provides a good prediction of the electronic behaviour of glass materials, where several distinct phases may be present within the dielectric material [108].

2.4.5 Charge transport in polycrystalline dielectrics: II - Exciton Hopping The dielectric conductivity models considered so far have highlighted the possible roles of point defects within the insulator material. A further consideration is that of a structurally perfect crystalline dielectric, with a population of lattice ions which are in *excited* electronic states. Such an excited-ion 'defect' is termed a *Frenkel exciton* [109]. Given the strong coupling between the outer-shell electrons of the ions, and the capability of *any* lattice-ion to be excited, the excitation energy associated with the exciton may be easily transferred between ions in the lattice.

Thus, the Frenkel exciton may propagate through the crystal lattice without any movement of the ions themselves, in common with the motion of a polaron described in Section 2.4.4. Consequently, the Frenkel exciton mobility is very high, and the excitation energy associated with the exciton may be modelled as 'hopping' between lattice-ion sites [115]. The validity of this conduction model is based upon the excitation of a single ionic level within the dielectric, and the well-defined localisation of the excited ion: this situation is often associated with solid rare gases [109].

2.4.6 Charge transport in mixed-phase materials Many practical insulators are multiphase materials, containing crystalline phases surrounded by

glasses and porosity voids [108]. Consideration must therefore be given to the *macroscopic* behaviour of these constituents, in determining the electronic conduction properties of the material. In a polycrystalline dielectric such as alumina (Al_2O_3), the presence of a conductive glass phase can reduce the resistivity of the major insulating alumina phase.

In the case of a porous dielectric, the macroscopic permittivity ε_m of a dielectric of permittivity ε_2, containing a volume fraction V_f of randomly-located (and random-sized) spheroids of dielectric material (ε_1), was described by Maxwell [108] as

$$\varepsilon_m = \varepsilon_2 \left\{ 1 + \frac{3V_f(\varepsilon_1 - \varepsilon_2)}{\varepsilon_1 + 2\varepsilon_2 - V_f(\varepsilon_1 - \varepsilon_2)} \right\} \qquad [\mathrm{F\ m^{-1}}] \qquad \{2.8\}$$

Figure 2.4.6 illustrates these electronic parameters and the structure of a mixed phase dielectric material.

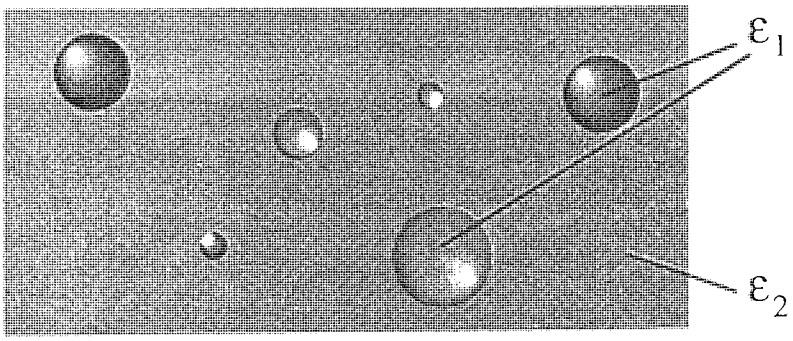

Fig. 2.4.6 A schematic diagram of the physical structure of a multiphase dielectric material

For $\varepsilon_2 \gg \varepsilon_1$ and $V_f \leq 0.1$, equation 2.8 may be simplified to

$$\varepsilon_m = \varepsilon_2 \left(\frac{1 - 3V_f}{2} \right) \qquad [\mathrm{F\ m^{-1}}] \qquad \{2.9\}$$

Alternatively, similar values for the permittivity of a mixed dielectric may also be calculated from the "logarithmic mixing rule" [116], as shown in equation 2.10

$$\log\ \varepsilon_m = \sum_i V_i \log \varepsilon_i \qquad \{2.10\}$$

where V_i are the volume fractions of the phases present in the multiphase dielectric.

The empirical relation given in equation 2.10 [116], together with the simplified Maxwell expression of equation 2.9 [108], have been found to provide permittivity values in good agreement with experimental measurements of mixed dielectrics.

2.5 Surface-flashover of solid-insulators in vacuum

Following the overview presented in Section 1.2, this section presents a detailed description of three contemporary models of surface-flashover, augmented in each case by reviews of experimental observations of the associated surface-flashover phenomena. The coverage of this experimental evidence is extended from the description of DC emission phenomena given in Section 2.3, to include pulsed-field surface-flashover phenomena observed on solid dielectrics in vacuum.

2.5.1 Electron-stimulated desorption (ESD) As described in Sections 2.3.2 and 2.3.3, experimental investigations of solid-insulators in vacuum have often found bright luminosity at the dielectric surface to be associated with the electrical breakdown of the insulator [23,63,90]. A further feature of the electro-optical luminosity observed on the stressed dielectric was its frequent proximity to the cathode electrode [23,24,92] (see Section 2.3.3).

In addition to these optical observations, the breakdown-voltage of a dielectric specimen was seen to increase when baked and allowed to outgas in vacuum [117]. Electrical breakdown events are also frequently accompanied by dramatic increases in the recorded background pressure in the analytical vacuum system [92,118]. These observations therefore strongly suggest that absorbed gas within the dielectric plays an important role in the high-voltage breakdown of the insulator.

Following the surface-flashover of a solid insulator, the insulator surface generally remains positively charged [81]. This charging phenomenon has been widely attributed to the emission of secondary-electrons from the surface-layers of the dielectric, as a consequence of the SEE yield (δ) being greater than unity, i.e. as explained in Section 2.3.1. Anderson [16] proposed the secondary electron avalanche (SEA) [15,101] as a physical model of the surface-flashover process, with primary electrons field-emitted from the cathode: for $\delta>1$, these primary electrons generate a positive surface-charge [119], as shown in Fig 2.5.1.

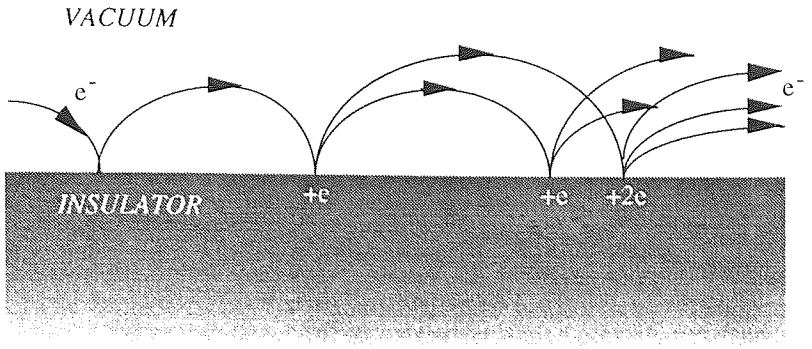

Fig. 2.5.1 Illustrating the positive charging of an insulator surface due to the secondary-emission cascade of "hopping" electrons (after Anderson [16])

As the insulator surface becomes increasingly charged, so the local electric-field at the cathode is enhanced, increasing the field-emission of primary electrons. This increasing cathode field then leads to the emission of increasingly energetic electrons, and so increases the SEE yield at each subsequent electron impact [16,120]. Thus, a multiplication of the electron-current may occur along the insulator surface, giving rise to a cascade of avalanching electrons which follow "hopping" trajectories [16] as shown in Fig 2.5.1. The impact of the cascading electrons is proposed to liberate a "wake" of energetic material from the insulator surface: surface-flashover may then occur within the ionised plasma of this liberated material [16].

Anderson and Brainard [18] extended this electron-avalanche model to consider the desorption of adsorbed gas from the solid-insulator by the impacting electrons. According to these authors, surface-flashover is assumed to involve (electronic) collision-ionisation of a gaseous layer above the insulator surface, generated by the electron-stimulated desorption (ESD) of adsorbed gas from the dielectric surface-layers [18,121], i.e. as illustrated in Fig 2.5.2 (a graphical representation of this ESD process was presented in Fig 1.3 of Section 1.2.1).

As with the earlier model of Anderson [16], the insulator surface becomes positively charged, the local electric-field at the cathode is enhanced, leading to enhanced field-emission of primary electrons. Consequently the rate of gas-desorption is increased due to the higher fluence of primary-electron impacts, with a further increase due to ESD associated with the increased yield of secondary-electrons. This regenerative process continues, with further desorbed-gas atoms ionised as a result of collisions with hopping electrons, until flashover occurs through a conductive channel formed by these ions [18,120].

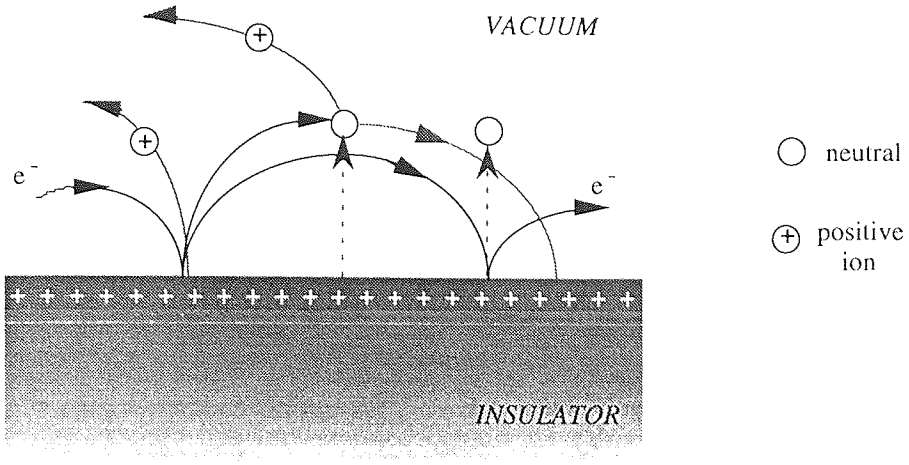

Fig. 2.5.2 Illustrating the evolution of ions and neutrals from the insulator surface due to the impact of prebreakdown "hopping" electrons (after Anderson and Brainard [18] and Latham [120])

Experimental studies of solid-insulator surface-flashover in vacuum have revealed the flashover plasma to propagate at velocities comparable with those observed during gaseous breakdown [19]. In addition, time-resolved measurements of the electron-emission along the insulator surface [122] have been found to agree with those of the electron-trajectories predicted by the ESD surface-flashover model [15,16,18,123,124].

2.5.2 Electron collision-ionisation In addition to observations of electron-emission and gas-desorption from a solid-dielectric in vacuum, an important experimental approach in probing the nature of the surface-flashover phenomenon has been the study of the optical luminosity observed on the insulator surface [125-127]. In particular, *spectroscopic* optical studies have provided quantitative experimental evidence of the physical nature of this luminosity [25,38,39,42,91].

As discussed in Section 2.3.2, the recorded luminosity spectra do not appear to reveal distinct spectral lines of ionised gases, such as might be expected from the electron-impact ionisation of a layer of desorbed gas [18]. Instead, several workers [25,39] have observed luminous events which appear to correspond to solid-state photon-emission processes within the *bulk* of the insulator material. As shown in Fig 2.5.3, Sudarshan and co-workers [20,21,25,91] reported a continuum of optical radiation from alumina ceramics under DC, AC and pulsed [42] electrical excitations.

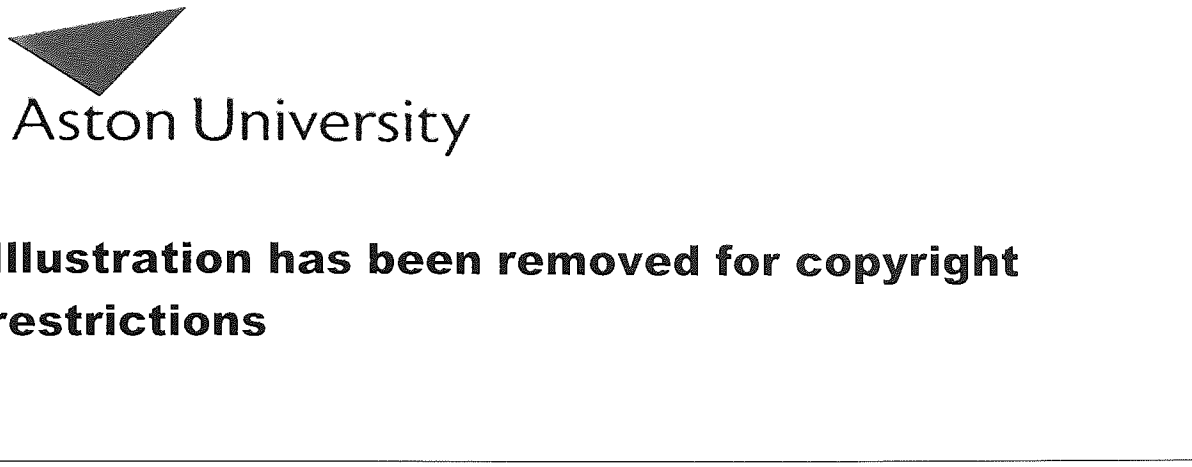

Fig. 2.5.3 Optical emission spectrum from lucalox alumina (99.9% Al_2O_3) (from Jaitly & Sudarshan [25])

Saito *et al* [44,45] recorded similar spectra from the r.f. excitation of single-crystal alumina (sapphire), with a higher wavelength-resolution (Fig 2.3.3). The spectral nature of the detected luminescence was indicative of *solid-state* electron-recombination at defect [41,128-133] and impurity [134,135] trapping centres *within* the solid insulator (see Section 2.3.2). This observation suggests significant charge-transport *through* the dielectric during electrical-breakdown, rather than electron-motion over the insulator surface. Thus, given the apparent electro-luminescent signature [43] of the optical emission from a surface-flashover event, Jaitly and Sudarshan [20,21] proposed that sub-surface charge-transport and trapping phenomena were responsible for the surface-flashover of a solid insulator.

According to this model, only low electric fields are required to detrap electrons from trapping centres that are associated with structural defect-centres within the insulator surface [25,50], and are thought to be responsible for the luminescence observed in the dielectric surface [20,21]. It follows that this field-induced emptying of the traps leaves a net positive charge on the insulator surface. The low conductivity associated with the insulator bulk is proposed to restrict the flow of the detrapped electrons, leading to the formation of a small negative space-charge in the cathode region of the insulator. Figure 2.5.4(b) illustrates these electronic charging processes in the bulk and at the surface of the solid dielectric.

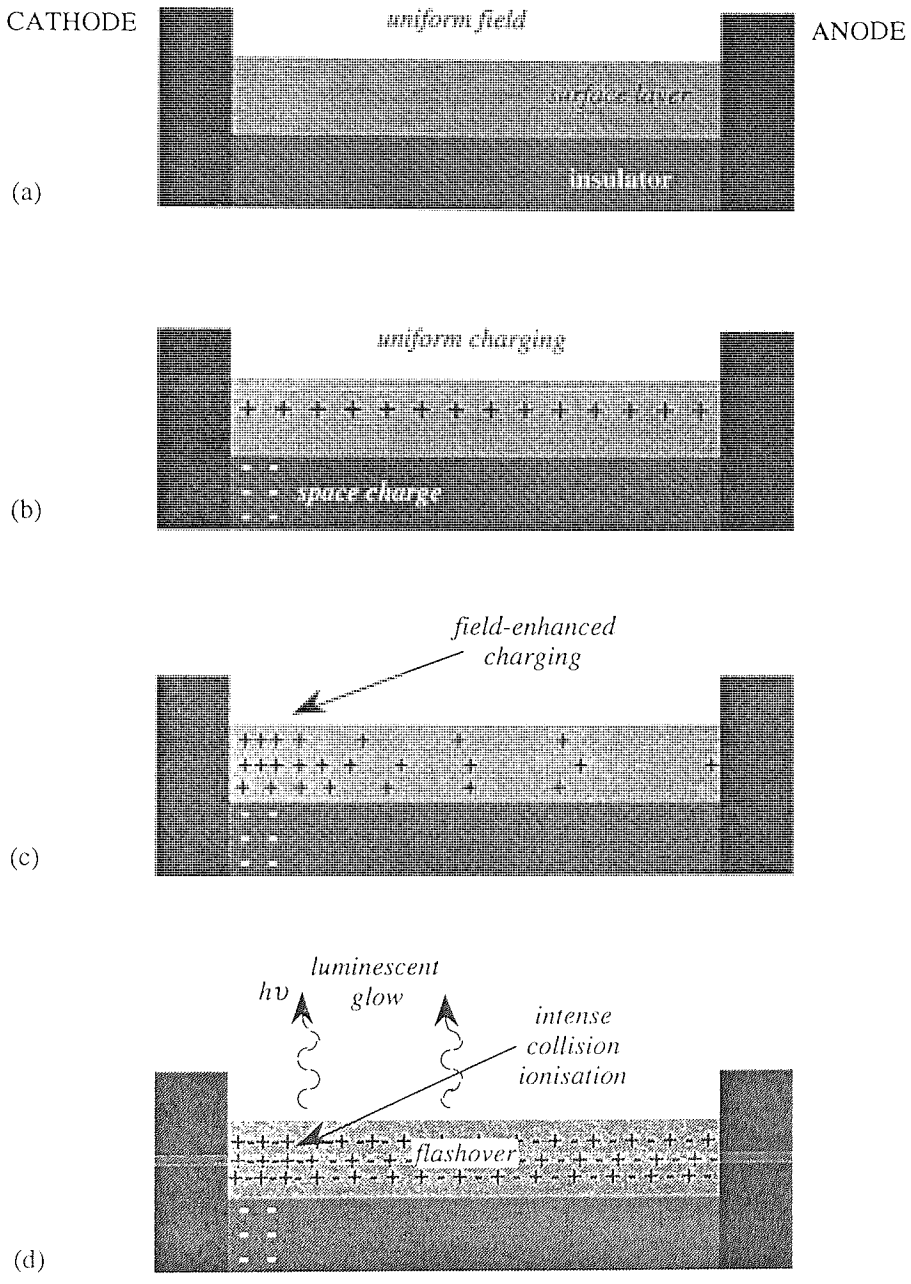

Fig. 2.5.4 Illustrating the sequence of prebreakdown events leading to the surface-flashover of a solid insulator in vacuum (after Jaitly & Sudarshan [20])

As the applied voltage is further increased, more electrons are emptied from surface trapping-centres, and this results in an increased positive charging of the surface. At even higher electric field-strengths, a larger population of electrons will tunnel from the cathode into the insulator, and are transported through the insulator surface in the direction of the applied electrical field by a defect hopping mechanism (see Sections 2.4.3 and 2.4.5). These hopping electrons will in turn be able to ionise lattice-sites within the dielectric [136], release further free electrons, and further increase the positive charging of the insulator surface.

This charging process is also enhanced as a consequence of the increased efficiency of the collision-ionisation mechanism that occurs with increasing field. The preferential accumulation of positive charge in the vicinity of the cathode is attributed to the low mobility of these holes in relation to that of the hopping electrons, and leads to an enhancement of the electric-field at the cathode. Thus, conditions are established for the field-enhanced emission of electrons from the cathode into the surface-layers of the dielectric, i.e. as shown in Fig 2.5.4(c).

At a critical field threshold, this electron-emission/lattice-ionisation process will become regenerative, and lead to the rapid formation of a self-sustaining, highly-conductive plasma of electrons and positive-ions within the surface layer of the insulator. Surface-flashover of the insulator can then occur through this "flashover channel" in the dielectric surface-layer, as depicted by Fig 2.5.4(d).

An important prediction of this picture of insulator-charging is that exoelectrons will be emitted into the vacuum from within the dielectric, owing to the proximity of the positive space-charge region in the insulator surface-layers [91,137]. More generally, this exoelectron emission mechanism, illustrated in Fig 2.5.5, may also occur as a result of the electron-bombardment of any insulator that has a SEE yield $\delta>1$, and lead to the positive charging of the insulator surface [137].

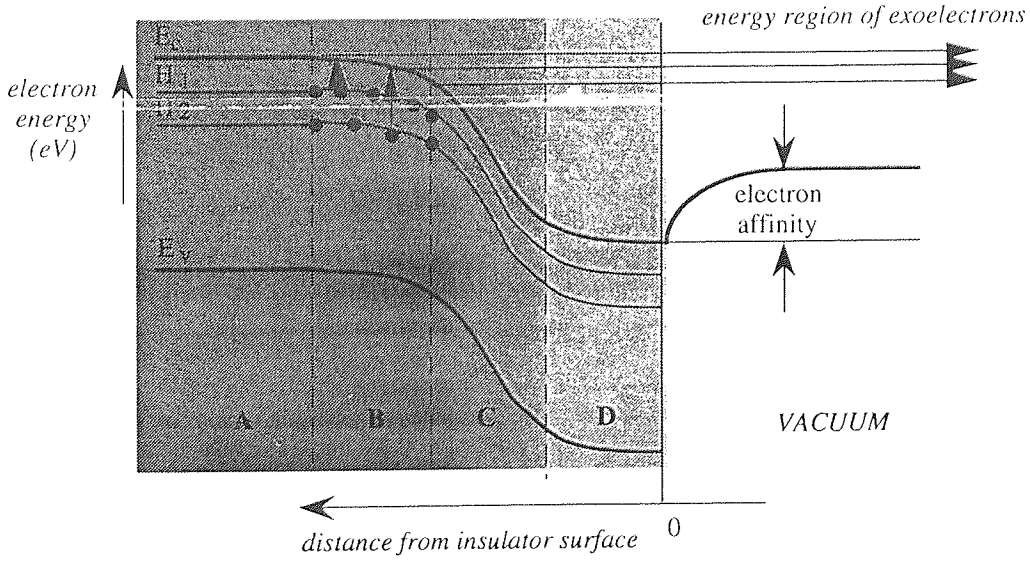

Fig. 2.5.5 Illustrating an exoelectron emission model; region **A**: bulk insulator, **B**: negative space-charge region, **C**: (neutral) boundary layer, **D**: positively-charged surface-layer (after Bommakanti & Sudarshan [137])

2.5.3 Explosive relaxation of trapped polarisation energy On the basis of the apparent *non-ohmic* behaviour of the dielectric surface-layers, as proposed by the electron collision-ionisation model [20,21], several workers [29,138] have analysed the divergence between the measured electronic behaviour of insulator materials in vacuum, and the behaviour predicted by classical theory. Insulators exhibit a very large, finite resistance R', defined by

$$R' = \rho \frac{h}{A} \qquad [\Omega] \qquad \{2.11\}$$

where ρ is the (high) dielectric resistivity, h is the thickness of the dielectric sample, and A its surface-area, as illustrated in Fig 2.5.6(a). Classically, the dielectric will charge and discharge through its own internal resistance, R', with a time-constant τ, given by [29,139]

$$\tau = R'C = \frac{h}{A}\rho\frac{\varepsilon_o \varepsilon_r A}{h} = \varepsilon_o \varepsilon_r \rho \qquad [s] \qquad \{2.12\}$$

Thus, eqn 2.12 suggests that the charge-transport properties of the dielectric are a function only of its electrical permittivity, ε_r, and its bulk resistivity, ρ. For high-resistivity insulators such as alumina (Al_2O_3), where ρ may exceed 10^{18} Ωcm [26], the corresponding time-constant, τ, may be in the region of several days. Such slow discharge periods are clearly not compatible with the timescales involved in the explosive surface-flashover events associated with the electrical breakdown of a solid dielectric in vacuum [140,141].

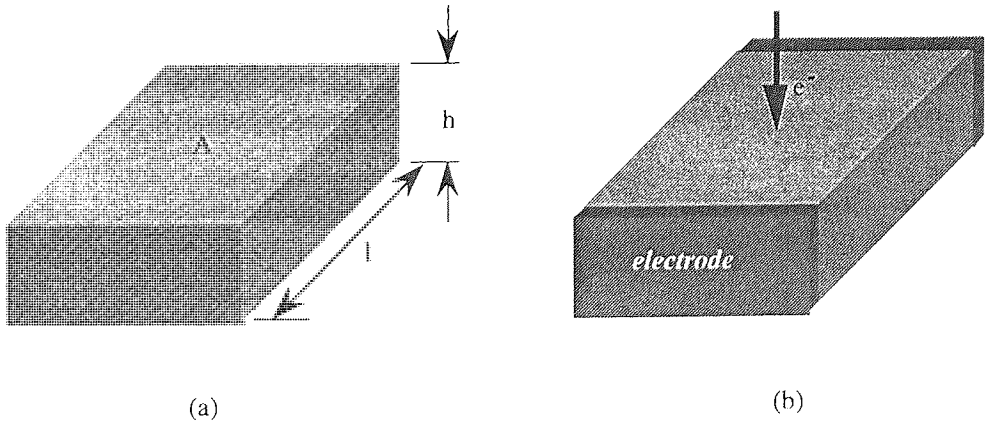

(a) (b)

Fig. 2.5.6 Schematic illustration showing (a) a slab of dielectric material with (b) attached electrodes, and normal incidence of a diagnostic electron-beam

ASTON UNIVERSITY LIBRARY AND INFORMATION SERVICES

In attempting to explain this anomaly, it should first be noted that experimental evidence of electronic transition-radiation from within the insulator during a surface-flashover event [25,39] suggests charge-transport along the dielectric surface involving highly-mobile charge carriers [26]. This prediction was supported by studies of high-purity alumina, in which Will *et al* [105] found the electron-mobility, μ_e, to be $\approx 200 cm^2\ V^{-1}\ s^{-1}$, yielding an electron transit-time $T \approx 3\mu s$ through a 1mm dielectric thickness (l) [26]. Such observations further highlight the possible role of highly-mobile electrons in the electrical breakdown of the solid dielectric in vacuum.

To explore the behaviour of injected-electrons in a solid dielectric, LeGressus and co-workers [27-31] employed the electron-beam of a scanning electron microscope (SEM) as an analytical electron source. As illustrated in Figs 1.5 and 2.5.6(b), insulator samples could be charged in the SEM with a controlled fluence of electrons. Having exposed a dielectric sample to the irradiating electron-beam, a "mirror" electron-image of the SEM chamber could be rapidly obtained using the low-voltage (1keV) beam arrangement shown in Fig 2.5.7. Such a rapid acquisition of an electron mirror-image indicated fast charging of the insulator [27,142].

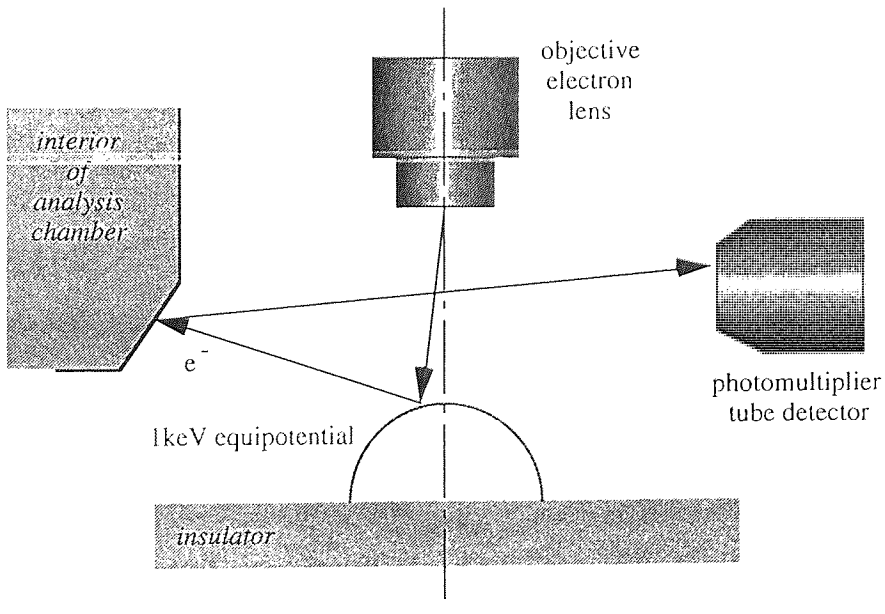

Fig. 2.5.7 Illustrating the electron "mirror" effect obtained by probing a charged dielectric sample with a low-voltage electron beam

Furthermore, secondary-electron spectra recorded from the charged dielectric exhibited well-defined spectral peaks [85,142], suggesting the trapping of incident

electrons at distinct defect centres within the dielectric [142]. On the basis of these findings, the three different types of electron trapping centre illustrated in Fig 2.5.8 were proposed, depending upon the nature of the dielectric material. It was also noted that perturbations of the charged dielectric, such as an increase in temperature (≈100°C) or the application of a voltage pulse between planar electrodes {Fig 2.5.6(b)}, were observed to cause a migration of the trapped surface charge, and a collapse of the electron mirror image [26]. Such a *macroscopic* response of the dielectric to a perturbing stimulus suggests a high density of trapping throughout the bulk of the insulator [28].

To explain these findings, it was proposed that electrons are self-trapped at structural defect sites, according to the polaron model described in Section 2.4.3, and is illustrated schematically for single-crystal and fresh-annealed polycrystalline dielectrics in Figs 2.5.8(a) and 2.5.8(b). As discussed in Section 2.4.3, electrons may be trapped at lattice-sites that display a local perturbation in the electrostatic potential of the crystal structure, thereby creating a localised electrostatic potential-well. Equally, the segregation of impurities along grain boundaries, as shown in Fig 2.5.8(c), can form a further region of defects which constitute local perturbations of the solid dielectric.

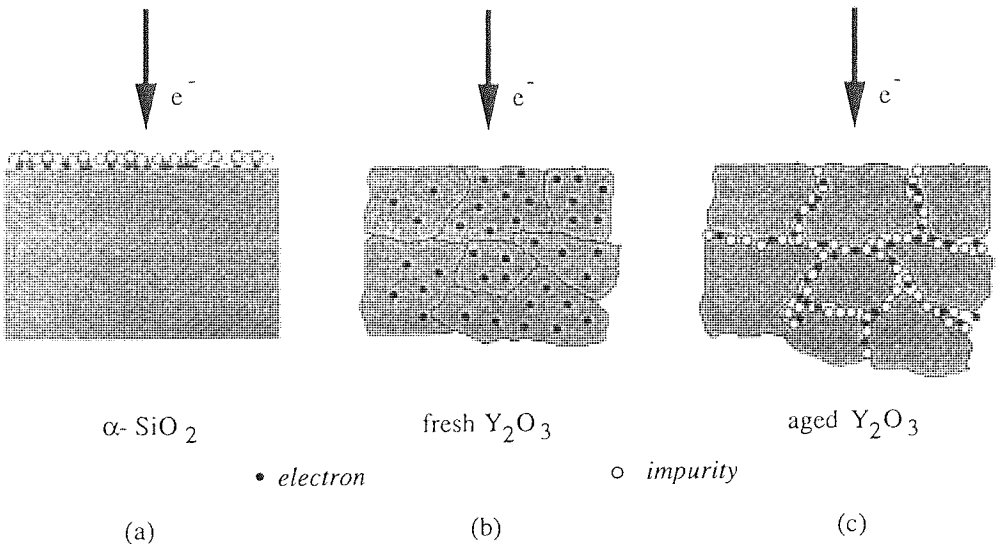

Fig. 2.5.8 Trapping of electrons (a) at the interface of the insulator surface and a contamination layer, (b) in the bulk of the grains of a freshly-annealed dielectric, and (c) in the grain-boundaries of an aged insulator (after Blaise & LeGressus [31])

It can therefore be concluded that the space charge of the electrons trapped within the insulator will give rise to a *polarisation energy* in the dielectric medium. In fact, the polarisation energy, U_p, at each trapped-charge site may exceed 5eV [26], reaching 70eV in the case of Yttria (Y_2O_3) ceramic [28]. According to the highly-mobile picture of the polaron (see Section 2.4.3), a self-trapped electron may be easily detrapped and transported through the crystal lattice under the influence of an electric field or by thermal excitation [143]. Indeed, this perturbation of the charged dielectric can lead to a macroscopic detrapping of trapped electrons, and the destabilisation of the space-charge within the dielectric.

The release of lattice polarisation energy associated with the detrapping of electrons leads to a heating of the phonon-bath of the insulator material, and the generation of a thermal shock wave. Given the large magnitude of U_p at each trap centre, the insulator may be locally ionised, leading to the 'explosive' release of further free electrons, and the generation of ionised dielectric material that can promote the flashover process. As illustrated in Fig 2.5.9 [26,144], the explosive propagation of the thermal shock wave of the excited phonon bath is proposed to desorb material from the relaxing dielectric.

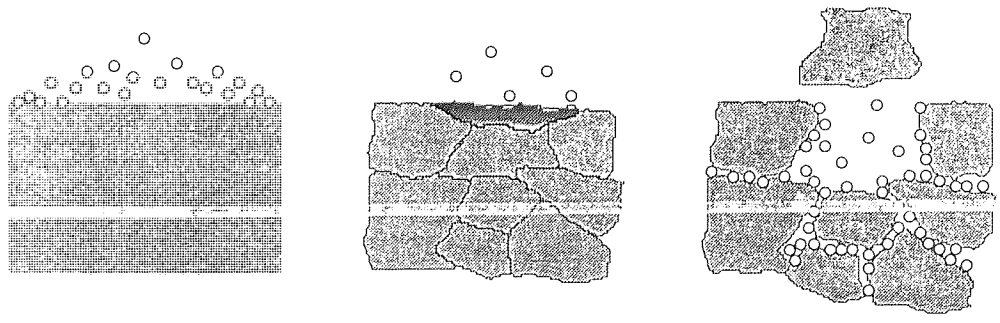

Fig. 2.5.9 Illustrating the surface-flashover process resulting from the destabilisation of trapped charge, and leading to (a) surface decontamination, (b) melting of the dielectric grains, and (c) the ejection of grains from the insulator (after Blaise [26])

2.6 Solid insulator structure and modification

This section will review the various techniques that have been developed to enhance the *in vacuo* voltage hold-off behaviour of solid dielectrics [12]. The structures and properties of a range of solid insulator materials are reviewed in Sections 2.6.1 to 2.6.4. Some of the *structural* techniques that have been used to optimise the arrangement of the dielectric and the electrodes, and so enhance the electrical performance of the insulator, are described in Section 2.6.5. Similarly, Section 2.6.6 describes some of the *material composition* techniques that have been used to enhance the electrical characteristics of solid insulators.

In the case of the trigger insulators used for the TVG switches investigated in this study (see Section 1.3.1), there is often a "systemic" requirement to minimise the trigger breakdown voltage required to 'fire' the vacuum switch. Thus, Sections 2.6.7 and 2.6.8 describe some particular techniques that have been used to reduce and control the voltage-breakdown threshold of these trigger insulators (for further details of TVG switch requirements, the reader is referred to Section 2.7.1).

2.6.1 Solid insulator materials As outlined in Section 2.1.2, various types of glass have historically found widespread use as insulating structural materials. More recently, ceramic materials have been found to offer a similar electrical-insulation performance, but with increased mechanical strength. Furthermore, metallized ceramics facilitate straight forward brazing techniques in the joining of the ceramic insulator to metal electrodes [35]. Thus, the scope of these *electroceramics* includes all non-metallic polycrystalline materials that have been synthesised by a 'firing' or sintering process [145]. The following sub-sections review some of the more widely used electroceramic materials.

2.6.2 Aluminium oxide (alumina) Alumina (Al_2O_3) ceramic is widely used in electrically-insulating components, due mainly to its good dielectric properties and high mechanical strength. Alumina is rarely found as a pure ore in its mineral state *corundum*, but is widely derived from its hydrated-oxide form, bauxite ($Al_2O_3.2H_2O$), which is extracted at low cost as an intermediate product of the refining of aluminium metal [146]. Alumina is a plentiful material in this bauxite form, since bauxite deposits account for approximately 25% of the earth's crust [146].

Within bauxite, alumina is often associated with other metal oxides, such as Fe_2O_3, TiO_2, SiO_2 and Cr_2O_3. In extracting the alumina, the bauxite is mixed with soda

(NaOH) in the Bayer process [145,146], to produce aluminium hydroxide $\{Al(OH)_3\}$. However, sodium compounds may remain as impurities following the precipitation of the aluminium hydroxide from the soda-bauxite slurry mixture, typically at concentrations of $\approx 0.1\%$ Na_2O [145]. Further impurity materials from the bauxite ore, such as TiO_2 and Cr_2O_3, may also persist in the refined alumina [147].

Dehydration of the bauxite oxides at temperatures below 1000°C leads to the formation of an amorphous aluminium oxide product, known as gamma alumina (γ-Al_2O_3). At temperatures above 1000°C, the calcined γ-alumina is converted to the crystalline alpha form (α-Al_2O_3) [148]. Alumina ceramics are then formed by the sintering of granular crystallites at temperatures of 1750°C into a desired shape and form: however, this sintering temperature may be reduced to below 1350°C by the addition of silicate materials as sintering additives [145]. Figure 2.6.1 illustrates the close hexagonal packing (CHP) structure of the α-alumina lattice.

Highly-calcined α-alumina has a specific mass density of 3.97 [146], whilst its electrical properties have been found to vary according to the grade and alumina-content of the sintered ceramic, as shown in Table 2.1.

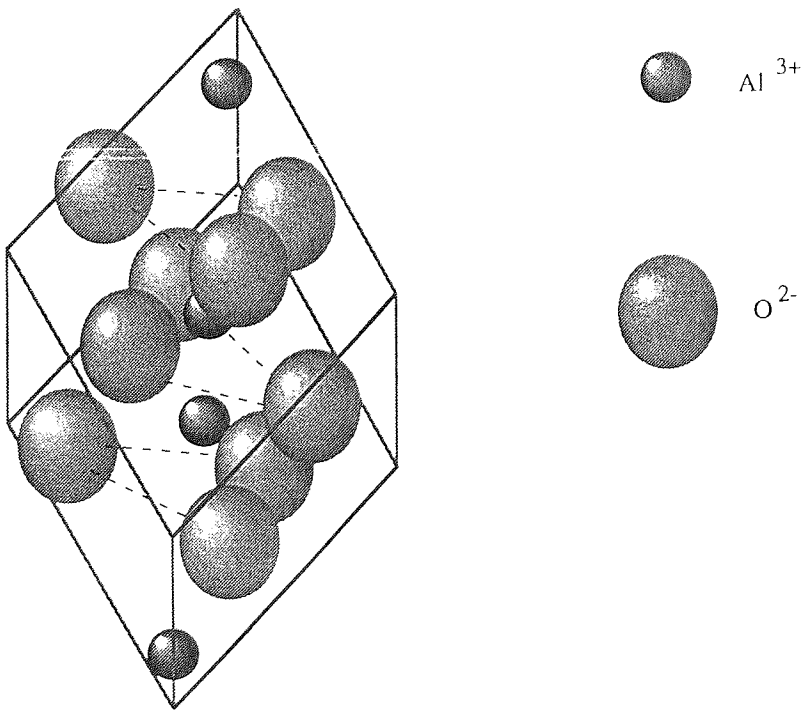

Fig. 2.6.1 Unit cell of α-alumina lattice structure (after Ryshkewitch [146])

Alumina content (%)	85	90	96	99.5	99.9
ε_r at 1MHz	8.2	8.8	9.0-9.3	9.7	9.8-10.1
tan δ at 1MHz ($x10^{-4}$)	9	4	1 - 3	3	0.4 - 2
Resistivity at 300°C (Ωm)	$4.6x10^8$	$1.4x10^9$	$3.1x10^9$	$2.0x10^9$	$1.0x10^{13}$

Table 2.1 Electronic properties of various grades of alumina (after Moulson and Herbert [34])

It follows, therefore, that owing to their influence upon the electroceramic properties, the presence of sintering additives must be carefully monitored in the fabrication of the alumina ceramic. The addition of a glassy phase [149], typically of silica (SiO_2), is used to bind the alumina crystallites into a mechanically-strengthened glass-ceramic matrix [150]. However, this glassy phase may introduce additional modifications to the *electronic* properties of the multiphase ceramic material, as described in Section 2.4.6.

2.6.3 Ferroelectric ceramic materials: I - Barium Titanate In addition to insulating electroceramics such as alumina, ceramic materials are also used in *non-insulating* structures within vacuum-insulated regimes. In particular, ferroelectric ceramics have formed substrate materials in electron-emitting devices such as diode cathodes [151]. Similarly, ferroelectrics such as barium titanate ($BaTiO_3$) have been used as trigger insulators in TVG switches (see Section 1.3.2), and this "TVG ignition" role is described later in Section 2.7.4.1.

In common with all ferroelectrics, barium titanate exhibits a very high electrical permittivity, ε_r, that reaches a maximum value at the Curie point temperature, T_c, as described by the Curie-Weiss law

$$\varepsilon_r = \frac{A}{T - \theta_c} \qquad [\mathrm{F\ m^{-1}}] \qquad \{2.11\}$$

Here, A is a constant for a given ferroelectric material and $\theta_c \approx T_c$ where, for barium titanate, the Curie point is at $T_c \approx 130$°C [108]. To illustrate this pattern of

behaviour, Fig 2.6.2 plots the dielectric behaviour of $BaTiO_3$ with temperature, together with the further influence of the ceramic grain-size upon these temperature-permittivity characteristics.

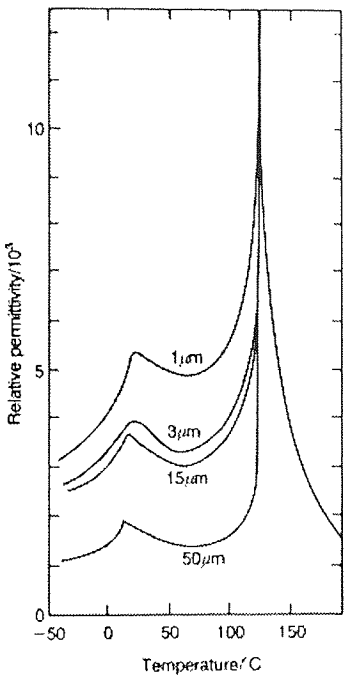

Fig. 2.6.2 The variation of the permittivity of $BaTiO_3$ ceramic with temperature and grain-size (after Moulson and Herbert [108])

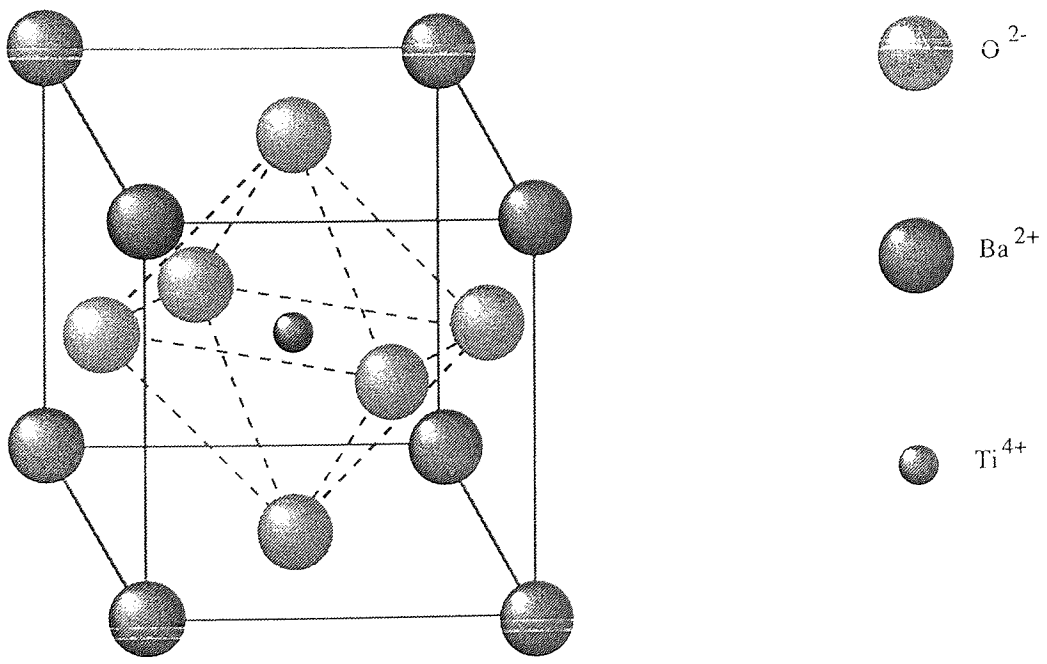

Fig. 2.6.3 Unit cell of barium titanate ($BaTiO_3$) ceramic [108]

Above the Curie point (≈ 130°C), the crystal structure of barium titanate is identical to that of perovskite ($CaTiO_3$), having the structure illustrated in Fig 2.6.3 [108]. Below T_c, this structure is distorted into a tetragonal (quadrilateral) phase, but becomes orthorhombic at temperatures below 0°C.

Owing to the strong temperature-dependence of its high-permittivity behaviour, the practical implementation of barium titanate is problematic, since many applications demand consistent electrical behaviour of the ceramic over a wide range of operating temperatures.

2.6.4 Ferroelectric ceramic materials: II - PZT and PLZT Recently, lead zirconate titanate, $Pb(Ti,Zr)O_3$ or "PZT", has emerged as a widely used ferroelectric material, not least because of its high Curie temperature ($220°C \leq T_c \leq 315°C$) and high electrical permittivity ($\varepsilon_r \approx 1200 - 2800$) [152]. PZT has a perovskite crystal structure (see Fig 2.5.3), and comprises a solid-solution of lead titanate (T_c=495°C) and lead zirconate (T_c=234°C). In fact, a complete range of $Pb(Zr_xTi_{1-x})O_3$ solid-solutions may be formed as a result of the high non-stoichiometry associated with the equivalent size and charge of the Ti^{4+} and Zr^{4+} cations. As illustrated in Fig 2.6.4, the relative permittivity of the PZT solid-solution system shows a maximum peak at a 1:1 ($PbZrO_3$:$PbTiO_3$) compositional ratio.

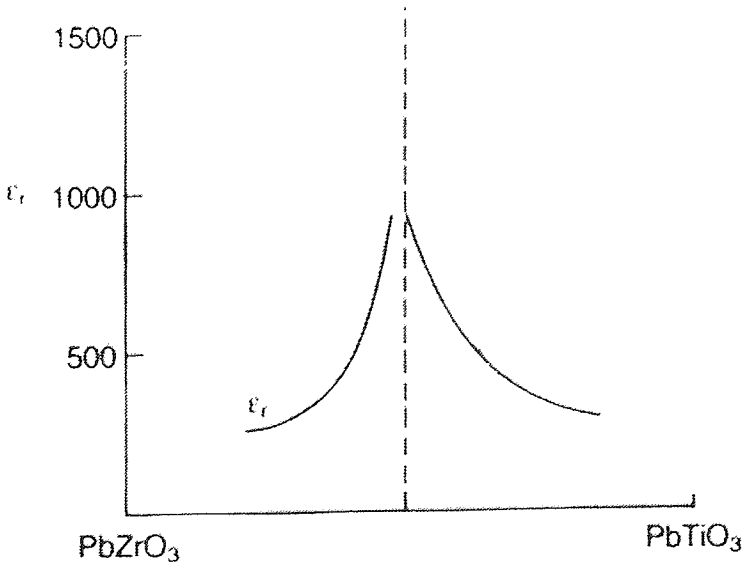

Fig. 2.6.4 Variation of relative permittivity, ε_r, across the compositional range of the $Pb(Zr_xTi_{1-x})O_3$ system (after Moulson and Herbert [152])

Doping of PZT with lanthanum (La) produces a dielectric material known as PLZT, which possesses a high relative permittivity ($\varepsilon_r \approx 2000$) that only becomes significantly affected by applied electric-fields exceeding $2MVm^{-1}$; also, it is largely unaffected by temperature over the range -30°C to +90°C. The crystal structure of the PLZT is a perovskite, comprising the solid-solution system $Pb_{1-3y/2}La_y(Zr_zTi_{1-z})O_3$ [153], where Fig 2.6.5 illustrates the dielectric behaviour of a PLZT composition of $Pb_{0.85}La_{0.1}Ti_{0.2}Zr_{0.8}O_3$.

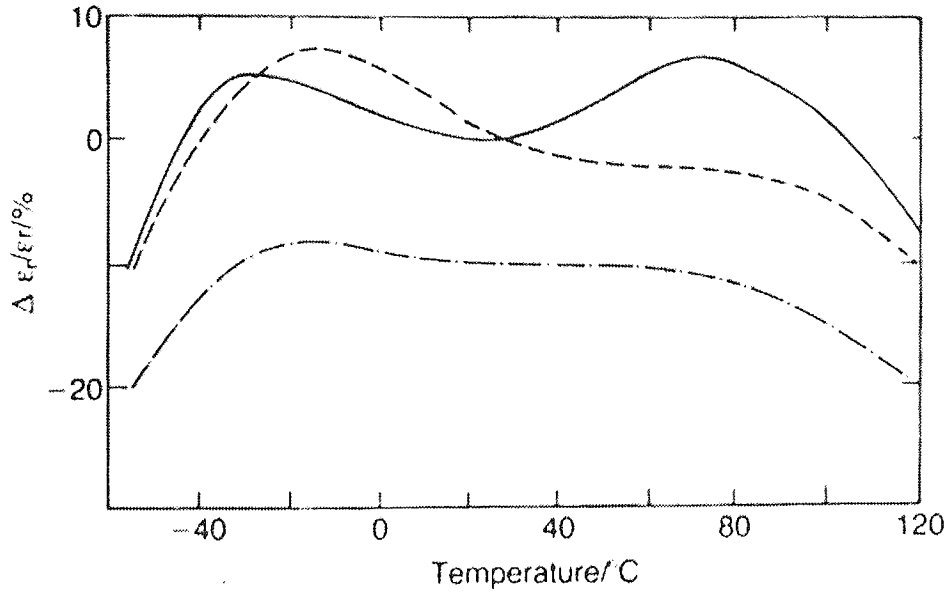

Fig. 2.6.5 Variation of relative permittivity, ε_r, with temperature and electric field, for the $PbZrO_3$:$PbTiO_3$:La_2O_3 (PLZT) system [152]

In common with cathode structures incorporating $BaTiO_3$, PZT [154,155] and PLZT [156,157] ceramics have been widely demonstrated to be highly emissive electron-sources. Indeed, as a result of the superior electrical characteristics shown in Figs 2.6.4 and 2.6.5, PZT-based materials have superseded barium titanate in many applications. As an additional bonus, highly adhesive electrode contacts may be applied to the P(L)ZT ceramics by a simple sputter-deposition of silver (Ag), nickel-chrome (Ni-Cr) or gold (Au) metal [152,158],

2.6.5 Optimised insulator structures It is widely accepted that the electrical-breakdown of a solid-insulator in vacuum is preceded by the accumulation of electronic charge in the surface of the dielectric material [12,17,81]. During the *pre*breakdown phase prior to the surface-flashover of the insulator, the injection of primary electrons into the insulator regime is believed to occur at the cathode triple-junction [12,24,63]. Thus, the structural arrangement and electrical performance of

solid-insulators in vacuum are influenced by these prebreakdown electron-injection processes. Particular emphasis is therefore placed upon the cathode-insulator interface [23,24,82,159].

In maximising the high-voltage withstand capability of the solid dielectric, it is common practice to "shield" the cathode-insulator triple junction, and thereby minimise the extent of the primary electron-injection into the surface-layers of the dielectric [160]. In analytical studies of various electrode-insulator geometries, Wetzer and co-workers [160-163] found that the highest voltage hold-off performance was to be found with insulators that present a minimum exposed surface-area to the cathode electrode, i.e. as illustrated in Fig 2.6.6. This figure also shows how the geometry of the insulator may be used to shield the cathode interface, thereby reducing the fluence of primary electrons from the cathode impacting onto the insulator, and minimising the degree of electronic charging on the dielectric surface (see Section 2.2.1). Alternatively, shield electrodes may be attached to the insulator-electrode structure, masking the line-of-sight trajectory from the cathode triple-junction to the insulator surface.

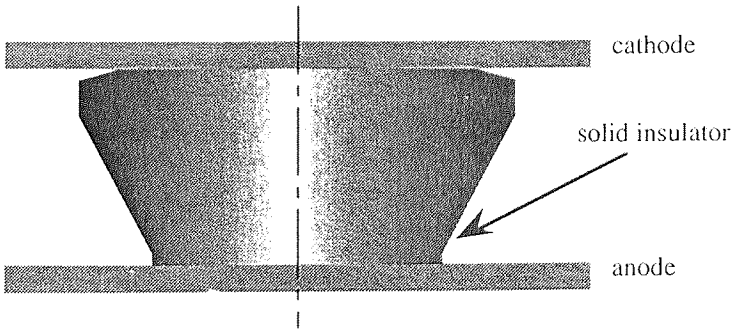

Fig. 2.6.6 Optimised geometry of a high-voltage insulating spacer (after Wetzer *et al* [163])

A further issue concerning the overall insulator performance is the structural integrity of the cathode-insulator junction. As illustrated in Fig 2.6.7, Kofoid [23,24] and Latham *et al* [51] have noted the high electric fields that can exist across voids in this junction region. In eliminating a non-intimate butt-contact, Gleichauf [117] found that a *fused* cathode-insulator joint resulted in a marked improvement in insulator performance.

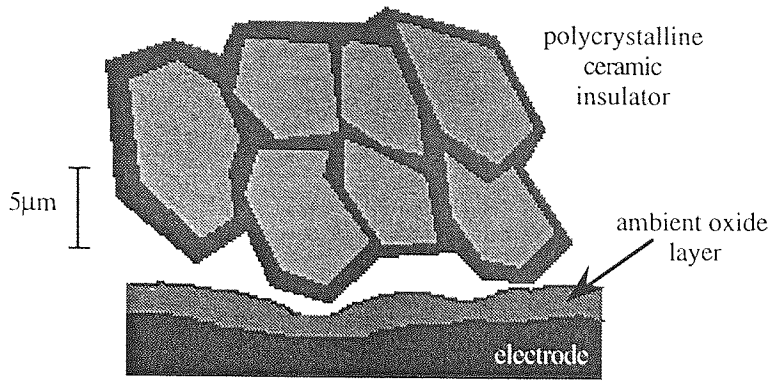

Fig. 2.6.7 Illustrating a non-intimate metal-ceramic M-I interface (after Latham *et al* [51])

2.6.6 Dielectric material-engineering and modification Together with the structural design of an insulating component, various processing techniques have been used to modify the physical and chemical structure of the dielectric, in order to optimise its electrical characteristics. For example, with reference to Sections 2.3.3 and 2.6.5, Miller [12] illustrates how the sensitivity of the cathode triple-junction can be favourably influenced by a *graded* dielectric at the cathode-insulator interface, where the insulator permittivity, ε_r, is increased in the junction region. This locally high value of ε_r causes a shift of the electric-field equipotentials away from the junction region, and thereby reduces the influence of the local field-enhancement across the void [164]. To further clarify this effect, Fig 2.6.8 illustrates the modified field behaviour at the electrode triple-junction of a graded-permittivity dielectric.

Aston University

Illustration has been removed for copyright restrictions

Fig. 2.6.8 Illustrating the reduction of electrical field-stress at an electrode triple-junction by the use of a graded-permittivity solid dielectric (from Miller [12])

At the technological level, Miller describes how a local modification of the dielectric permittivity can be achieved by the use of a *penetrating* metallization on the dielectric surface beneath the electrode [12,35]. In this metallized regime, the molybdenum and manganese metallizing material is assumed to penetrate the surface-layers of the insulator [35], thereby modifying the local value of electrical permittivity in the insulator surface. Quasimetallizing [165] is a similar metallization technique, whereby a metallic coating (e.g. Cr, Mn and Ti) is applied to the *entire* surface of the insulator before it is fired in a high-temperature wet-hydrogen furnace. A quasimetallized ceramic offers a higher value of breakdown voltage, and may subsequently be metallized to allow the attachment of brazed electrodes [165].

The insulating properties of a solid dielectric may also be modified by the application of surface coatings [20,63]. For example, Saito and co-workers [44,45] found that the deposition of titanium nitride (TiN) suppressed the high-voltage surface-flashover of an alumina insulator, and also quenched the luminescence previously observed on an uncoated dielectric. Furthermore, this suppression of the surface-flashover phenomenon has been correlated with a reduction in the secondary electron-emission (SEE) yield of the TiN-coated alumina [96].

The deliberate roughening of a smooth dielectric surface has been found to increase the surface-flashover voltage-threshold [12,63], particularly if the insulator is roughened in the cathode interface region [117]. Conversely, the fine polishing of an insulator is found to lower the flashover voltage [166]. There is also evidence that the furnace processing of a ceramic insulator can influence its flashover characteristics: thus, Jaitly *et al* [167] found that the wet-hydrogen firing of several types of alumina significantly reduced their hold-off voltage capability. However, subsequent firing of these ceramics in dry hydrogen restored their insulating properties, and in some cases exceeded the original unfired characteristics.

2.6.7 Optimisation of trigger insulator flashover properties As noted in the introductory description of a triggered vacuum gap (TVG) switch presented in Sections 1.1 and 1.3.1, the 'jitter' observed in the TVG switching characteristics may be minimised by the careful design of the external trigger-voltage circuit [168]. Indeed, the TVG performance may be further improved by the use of additional inductive components in the trigger circuitry for optimising the shape of the trigger-voltage waveform, and thus improving the consistency of the TVG switch operation [11].

By modifying the behaviour of the ceramic trigger-insulator used in the TVG tube itself, it should then, in principle, be possible to design an optimum switching performance into the valve, and thereby achieve a low-jitter TVG switch without the use of additional pulse-forming networks in the trigger circuit [11]. This section deals with material modifications and physical structures that have been found to improve trigger-breakdown performance, whilst the selection of insulator materials and the exploitation of their intrinsic properties will be reviewed in Section 2.7.4.1.

2.6.8 Optimised TVG structures Investigations aimed at seeking ways to stabilise the flashover process across the insulator surface have included the deposition of carbon [169] and chrome [170] thin-films onto the trigger insulator, in order to provide a homogeneous layer across which surface-flashover can take place. These coating processes also result in a lowering of the insulator surface-resistivity, yielding a low breakdown-value of the trigger-voltage. A limitation of this approach is that the energetic plasma processes present during the triggered breakdown of the TVG switch [13] can rapidly lead to the erosion of these surface films, and a consequent loss of trigger performance [170].

In studying the physical arrangement of the trigger structure, Vozdvizhenskii and Sidorov [171,172] found the delay-time (t_d) of the TVG (see Section 1.3.1) to increase in proportion to the main interelectrode separation (d), and to decrease with increasing trigger-current magnitudes (I_t). These geometrical parameters of the triggered vacuum gap are illustrated in Fig 2.6.9, and are related to t_d by the empirical relation

$$t_d = kd(1 + h/d)I_t^{-\alpha} \quad [s] \qquad \{2.12\}$$

where h is the recess penetration of the trigger insulator. Thus, the TVG firing delay is minimised by a short main-gap length (d), and the proximity of the trigger insulator to the main interelectrode gap, a finding that will be discussed further in Section 2.6.

Aston University

Illustration has been removed for copyright restrictions

Fig. 2.6.9 A schematic illustration of two alternative interelectrode structures that have been used for a triggered vacuum gap (from Vozdvizhenskii and Sidorov [172])

2.7 Triggered vacuum gap switches

As discussed in Chapter 1, the triggered vacuum gap (TVG), or *sprytron* [169], is a high-voltage three-electrode closing switch. Apart from discussing the operation of the TVG device, this section reviews two less-common types of vacuum switch: namely, laser-triggered vacuum gaps (LTVGs), and exploding-wire triggered vacuum gaps (EWTVGs). However, this section opens with a discussion of the *generic* switching parameters of TVG devices, and then goes on to detail a commercial surface-discharge TVG device which formed the basis of the experimental investigation contained in this thesis.

2.7.1 Circuit description of the TVG switch The circuit parameters of TVG switches may be defined from the voltage and current signals observed at the electrode-terminals when the TVG is 'fired'. These parameters are defined with respect to surface-discharge TVGs (i.e. as described in Section 1.1), and may also be applied to the main-gap behaviour of other vacuum closing-switches, such as LTVGs (Section 2.7.2) and EWTVGs (Section 2.7.3).

2.7.1.1 TVG operational modes A triggered vacuum switch may be operated in four 'modes' [9,10], each of which may be described by a particular combination of trigger- and adjacent-electrode polarities. Figure 2.7.1 illustrates the four operational modes of the TVG switch.

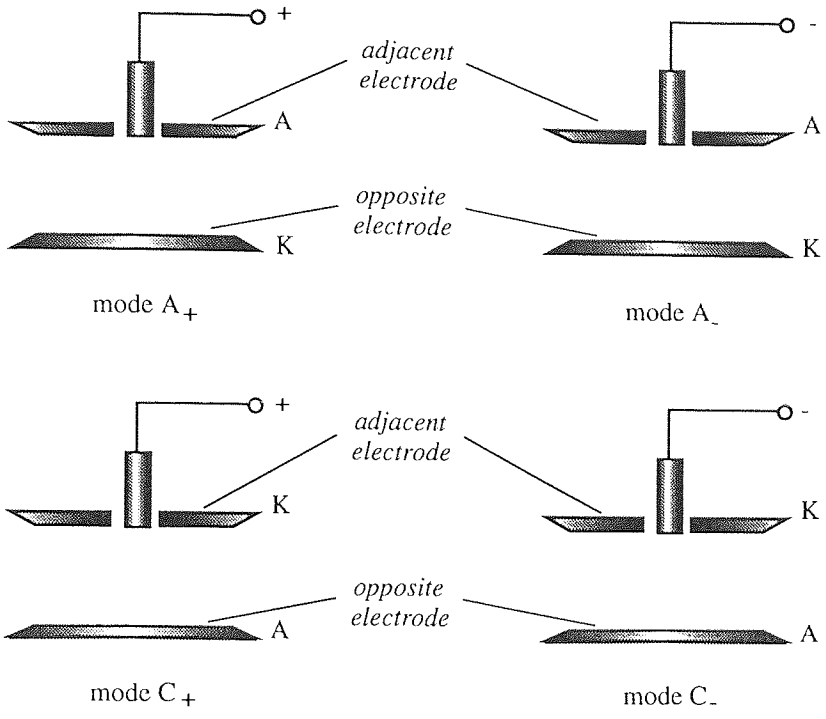

Fig. 2.7.1 Operational modes of a TVG switch

With the adjacent-electrode positively biased as an anode in the main-gap, the TVG may be triggered with a positive trigger pulse in mode A_+; conversely, the main gap may be fired with a *negative* trigger pulse from an adjacent anode in mode A_-. Positive triggering of the gap, with negative biasing of the adjacent-electrode to form a cathode, occurs in mode C_+; operation of the gap using a negative trigger-pulse from the adjacent cathode is described as mode C_-.

An alternative nomenclature describes the TVG mode with respect to the polarity of the *opposite* electrode [14,173]: mode C_+, for example, can therefore describe a positive trigger-pulse applied across the main gap with respect to a negative opposite electrode. For clarity, the modern classification of TVG modes presented in Fig 2.7.1 will be followed throughout this work, although care should be taken when comparing disparate sources of reference.

2.7.1.2 TVG switching performance As a fast, high-power closing switch, the TVG is often used in low-inductance, high peak-current capacitor-discharge circuits, such as the mode C_+ connection shown in Fig 2.7.2. Here, the application of a 'command' logic signal, V_c, to an external trigger-circuit leads to the application of a trigger voltage-pulse, V_t, to the TVG from the trigger-circuit, following a systemic delay-time, T_s.

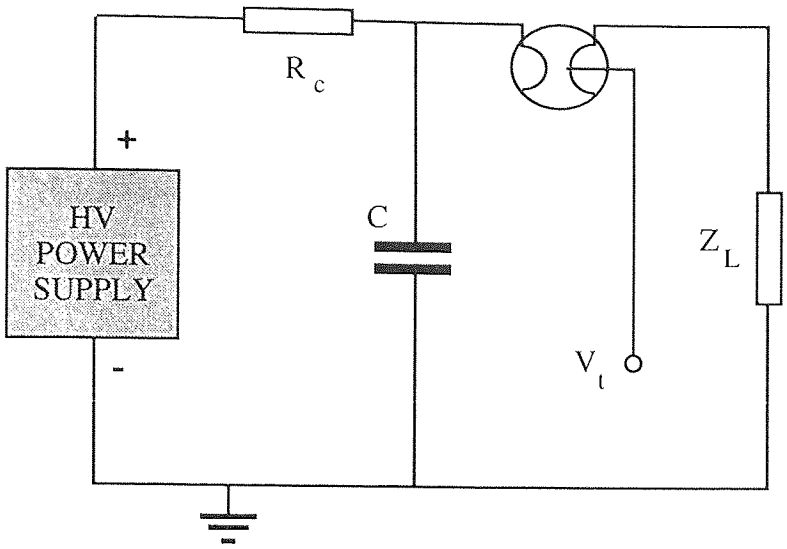

Fig. 2.7.2 Circuit representation of a typical capacitor-discharge application of a TVG switch

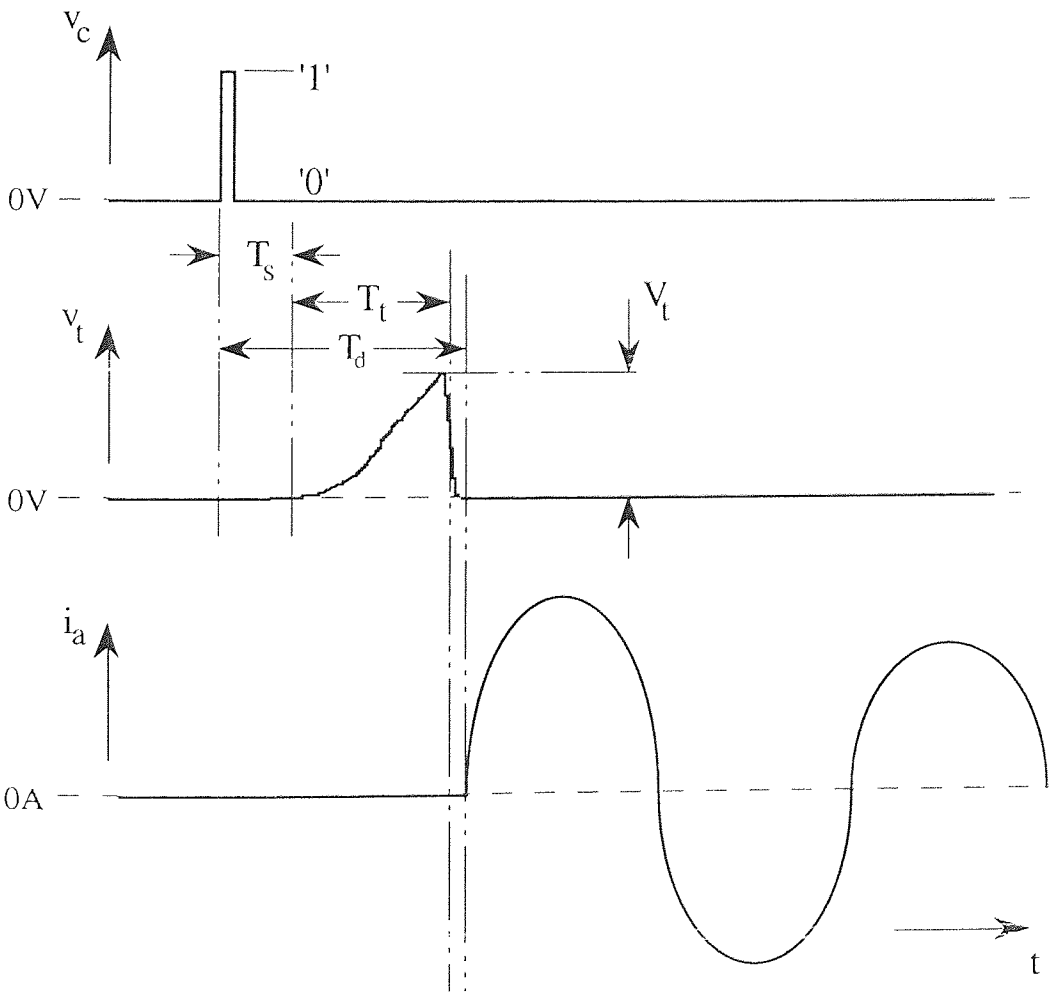

Fig. 2.7.3 Waveform diagram representation of TVG switch closure

The overvoltage breakdown of the trigger insulator ultimately leads to the breakdown of the main electrode gap, and the flow of main-gap current as the capacitor C discharges through the load-impedance Z_L; a sequence of events that is illustrated in the waveform-diagram of Fig 2.7.3.

Performance tests of TVGs have shown there to be little uncertainty, or *jitter*, in the time-delay (T_d - T_t) between the breakdown of the mode C_+ TVG trigger-voltage and the initiation of main-gap current [174]. However, any inconsistency in the voltage-magnitude at which the trigger / adjacent-electrode (M-I-M) structure breaks-down leads to substantial jitter in the measured delay-time, T_t, between the 'command' signal and the breakdown of the applied trigger-voltage, owing to the finite time-rate-of-rise of the trigger-voltage waveform. Consequently, the delay-time T_d, measured between the 'command' signal and the initiation of main-gap current-flow, will also exhibit significant uncertainty.

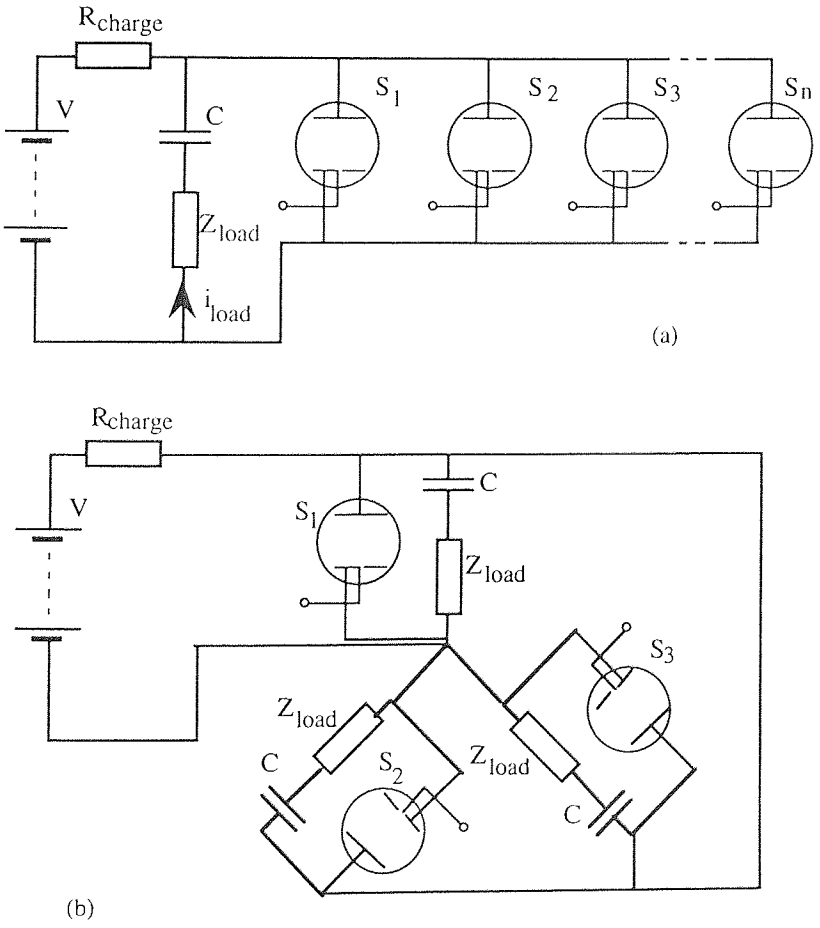

Fig. 2.7.4 (a) Distributed switch and (b) distributed load switching arrays

Jitter in the firing delay-time of a TVG switch becomes increasingly problematic in applications where the TVG is incorporated into an *array* of several switch

elements. Thus, Fig 2.7.4(a) illustrates a distributed switch array, where the synchronised firing of each TVG is required for even commutation of the load current through each of the *n* switch elements. Distributed loads, such as the switched-load array shown in Fig 2.7.4(b), present a similar requirement for synchronised switching of each TVG device. Such circuits are frequently found in detonic applications, where a series of explosive loads demand the precise firing of each switch/load element.

2.7.1.3 Delay characteristics of TVGs Several workers have studied the switch-on delay of the TVG, defined by (T_d - T_t) in Fig 2.7.3. Equally, various techniques have been successfully used to improve the TVG switching performance, minimising this switching delay. This section describes how various circuit parameters may be optimised with respect to this switching delay-time. A further consideration is the optimisation of the trigger breakdown-voltage, V_t, and the consequent enhancement of the trigger delay, T_t. Section 2.7.4 will then extend this analysis, and consider optimum internal-structures and materials within the physical arrangement of the TVG tube itself.

With reference to Figs 2.7.1 and 2.7.3, the switching delay (T_d - T_t) [8] has been found to be minimised with the TVG connected in mode C_+ [173], i.e. with a positive trigger voltage-pulse applied from a negative adjacent electrode, as described by Farrall [7].

Positive triggering has also been found to minimise the likelihood of a misfire [7], although some workers, operating TVGs at low main-gap currents (I_t < 500A), have found the trigger-polarity to have little influence upon the probability of the TVG firing [14]. In addition, Kamakshaiah and Rau [175], together with Arita *et al* [9], have found mode C_+ operation to be *less* reliable than in mode A_+, thereby compromising the benefits of the short delay-times associated with mode C_+ operation [7,173].

Considering the auxiliary 'trigger' connection of the TVG switch, the switching delay (T_d - T_t) is reduced as the electrical-energy available in the trigger voltage-pulse (V_t) is increased [8,175,176]. Accordingly, reduced delays are observed as the trigger current (I_t) [171,173,176,177] and the trigger voltage (V_t) [14] are increased. However, the ultimate magnitudes of these trigger parameters are often restricted by the power-supply limitations of the external circuit, and the switching capability of the trigger pulsed-power supply.

Minimum switching delays have been reported with *negative* trigger bias [10,174], although, as discussed previously [7], this circuit configuration offers an inferior probability of TVG switch closure. Green and Christopolous [173] found the breakdown-magnitude of the trigger voltage pulse to be reduced with negative trigger polarity in mode C_-, compared with an increase in trigger-voltages in mode C_+. For ready comparison, Table 2.2 summarises the respective switching performance of each of the TVG modes.

Mode	Delay time [173,174]	Firing probability [9,175]	magnitude of V_t [173]
A_+	- -	+ +	
A_-	- -	-	
C_+	+ +	+	-
C_-	+	- -	+

Table 2.2 Delay parameters of TVG modes

2.7.2 Laser-triggered vacuum gap (LTVG) switches These devices employ a high-energy photon-beam [178-181], usually derived from a laser, that is focused through a transparent aperture in the LTVG tube onto a small area of one electrode. For clarity, Fig 2.7.5 illustrates the internal structure of a laser-triggered vacuum switch.

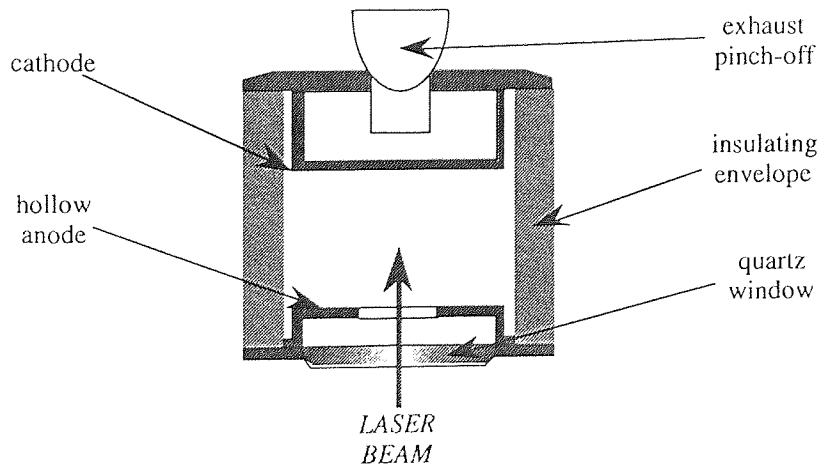

Fig. 2.7.5 Internal cross-section of a laser-triggered TVG switch

Laser-triggered switches have been constructed with the incident laser beam focused onto the main-gap cathode [178-181] or the anode [180]. In general, the

irradiation of positively-charged target electrodes (anodes) has been found to offer slightly superior switching characteristics [182]. In these devices, it is assumed that local heating of the electrode-surface by the incident photons can lead to the evaporation of metal ions and neutrals from the electrode [183], and the formation of a plasma, where target-electrode plasma-velocities of $\approx 10^5$ ms^{-1} have been measured [182]. Indeed, it is the introduction of this evaporated metal plasma into the main inter-electrode gap that is thought to give rise to trigger the vacuum breakdown of the LTVG [13].

In addition to metallic target electrodes [180,181], potassium chloride (KCl) has been used as an additive material in the target electrode, due to its favourable temperature-vapour pressure characteristics, and low ionisation potential [178,179]. Titanium (Ti) has also been used to form a composite KCl/Ti target, the logic being that the Ti appeared to behave as an effective absorber of the laser radiation, and so enhance the heating and vaporisation of the KCl target [178]. Other workers [179], however, have found the energy-density threshold for triggering to be unaffected by the addition of Ti to the KCl target.

As an operational bonus, optical triggering offers a high degree of electromagnetic isolation of the trigger source (such as a fibre-coupled laser diode) from the high-voltage circuit incorporating the LTVG switch. In safety-critical switching systems, this optical triggering arrangement can minimise the likelihood of pre-firing of the TVG. Pre-fires are often caused by the influence of stray electromagnetic radiation upon 'electronic' triggering circuits, leading to the premature application of a high-voltage trigger pulse to the TVG tube.

2.7.3 Exploding-wire TVGs Single-shot triggered vacuum discharges may be initiated by the explosion of a thin metal wire within the evacuated envelope of the TVG. Ron *et al* [184,185] describe such a device, which comprised a *demountable* vacuum gap to allow the replacement of the exploding wire (EW) after each discharge 'shot'. This exploding-wire triggered vacuum gap (EWTVG) is depicted in Fig 2.7.6.

The switching action is initiated by applying a high-voltage ($V_t \approx 20kV$), high-current ($I_t \approx 2kA$) trigger pulse to the wire, where rapid ohmic heating of the wire leads to an explosive vaporisation of the wire material. This event is usually denoted by a voltage spike in the trigger signal, which reflects the momentary open-circuit across the EW [185]. Vaporised EW material is then injected into the main interelectrode gap of the EWTVG, through slots in the inner electrode (Electrode 1 in Fig 2.7.6). The EW vapour propagates with a free-expansion velocity of $\approx 10^3$

ms^{-1} [186], which increases to a measured velocity of $\approx 10^5$ ms^{-1} within the high-voltage interelectrode gap [185]. This injected EW plasma is then believed to bridge the vacuum gap [185], and initiate the electrical breakdown of the EWTVG switch.

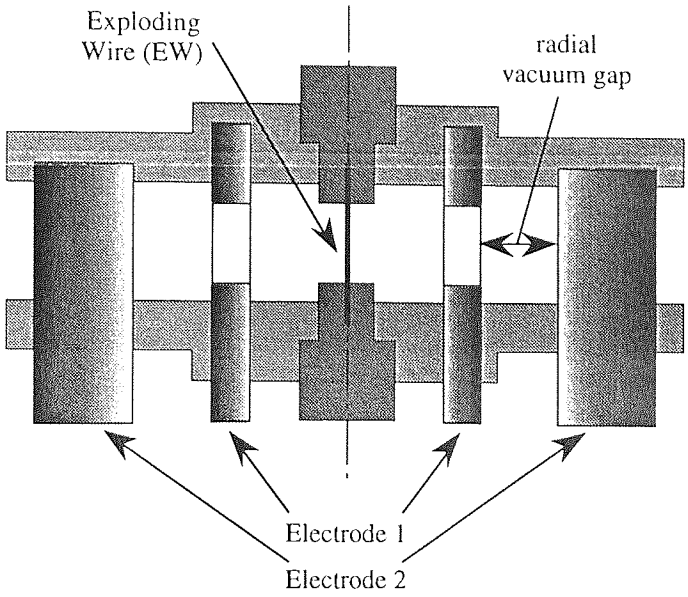

Fig. 2.7.6 Internal structure of an exploding-wire triggered vacuum switch (after Ron *et al* [184,185])

Fast switching of the EWTVG demands a high trigger-energy to be supplied to the wire (EW), in order to directly vaporise the EW, and so avoid the lower-energy *fragmentation* regime [186], where the available amount of metal-vapour from the EW is greatly reduced [184]. This high-energy trigger requirement, together with the single-shot lifetime of the EW, has limited the practical application of the EWTVG as a high-voltage switch.

2.7.4 Surface-discharge TVGs Following the broad description of a surface-discharge TVG presented in Section 1.1, this section first considers the trigger assembly that serves as the ignition source in the TVG switch. Broader consideration is then given to the arrangement of this trigger structure within the envelope of the TVG.

2.7.4.1 Surface discharge trigger structures Lafferty [6] and Farrall [7] were among the first workers to report on the switching capabilities of surface-discharge initiated TVGs. As illustrated in Fig 2.7.7, these early tubes employed a metallized-ceramic trigger assembly, that was axially mounted within one of the main electrodes of the vacuum gap [4,6,7]. When the TVG is 'fired', a high-voltage pulse is applied to the trigger lead, causing current to flow along the lead to

the molybdenum cap. This trigger current then flowed through the upper molybdenum sleeve to a groove, which was cut into the outer-circumference of the metallized alumina cylinder. A short arc discharge was then observed across this groove [7], with the trigger current returning through the lower sleeve.

Fig. 2.7.7 Cross-sectional view of a trigger assembly (from Lafferty [6] and Farrall [7])

A coating of titanium hydride was applied around the region of the groove, providing a source of Ti and H vapour at the onset of the arc discharge across the ceramic gap [4]. The release of these vapour species, and their subsequent ionisation, was believed to sustain the trigger discharge. Trigger currents of 10A were found to cause the breakdown of a 30kV main-gap voltage in under 100ns, with a shot-to-shot jitter of 30ns [4,6]; the corresponding trigger energies were below 10mJ [4], with trigger voltages (V_t) of approximately 1kV [7].

A simplified trigger arrangement was devised by Gupta and Rau [187], which removed the complexity of an additional trigger coating. This arrangement, shown in Fig 2.7.8(a), was found to operate successfully with a mica trigger insulator, in preference to Teflon (PTFE) or epoxy resin. Typically, mica trigger insulators were found to break down at V_t values in the range 1200-1800V ($I_t \approx 8A$), with a lifetime approaching 150 shots. The trigger lifetime was found to be limited by the eventual bridging of the mica gap, due to the deposition of electrode material in the trigger region.

Rau and co-workers [8,188] devised an improved trigger design, illustrated in Fig 2.7.8(b), which was less susceptible to bridging of the trigger insulator: this design has also found further use with other investigators [173].

Aston University

Illustration has been removed for copyright restrictions

Fig. 2.7.8 Simple triggered vacuum gap assemblies (from Rau *et al* [187,188])

Studies of this modified mode C trigger regime {Fig 2.7.8(b)}, using a variety of trigger insulator materials, showed that high-permittivity (high ε_r) materials (such as silicon carbide (SiC, ε_r=285) and barium titanate ($BaTiO_3$, ε_r=1850)) offered the lowest values of trigger breakdown voltage (V_t) [188]. By way of illustration, Fig 2.7.9 plots the variation of the trigger breakdown-voltage, V_t, with respect to the shot lifetime, for a series of TVGs which employed different trigger insulator materials.

Aston University

Illustration has been removed for copyright restrictions

Fig. 2.7.9 Operational consistency of trigger assemblies using various insulator materials (from Vidyardhi and Rau [177])

key: A. fused quartz (ε_r=3.78), B. Supramica (ε_r=32), C. lead titanate (ε_r=192), D. barium titanate (ε_r=1850), E. silicon carbide (ε_r=285)

This lowering of the trigger voltage was matched by a requirement for increased trigger current (I_t), i.e. in order to minimise the jitter recorded in the main-gap switching delay-time [8]. Interestingly, some workers have found the trigger ceramic to be 'conditioned' following a series of triggered main-gap discharges [5,177], which results in a marked decrease in trigger breakdown-voltage. Trigger conditioning, by this "erosion" process [5], has been attributed to a partial metallization of the trigger-ceramic surface, due to the deposition of electrode-material which has been eroded by the main-gap arc.

Specific studies of barium titanate trigger-insulators [173,177], using the trigger arrangement shown in Fig 2.7.8(b), have shown long operational lifetimes, typically exceeding 2000 shots [173]. After this operational lifetime, Green and Christopolous [173] had measured no change in the trigger breakdown voltage, and observed light deposits of copper electrode-material on the surface of the $BaTiO_3$ trigger ceramic.

2.7.4.2 Surface-discharge triggered vacuum switches Many laboratory-based TVG switches are assembled as demountable, continuously-pumped devices [173,175-177,187-189]: an arrangement that facilitates the simple dismantling of the TVG, and inspection of the electrode and insulator components. In many switching applications, such as those presented in Section 2.7.1.2, sealed TVGs represent a stand-alone switching device, and require no ancillary pumping apparatus.

For high-power/high-duty applications, TVG switches have been operated at 30kV with 1kA of main-gap current, a switch-on delay-time of 100ns and 40ns jitter [5]. Furthermore, the RVU-3 switch, described by Vozdvizhenskii and Sidorov [5] and illustrated in Fig 2.7.10, was operated at a pulse repetition frequency of 500Hz. In fact, more than $2x10^5$ cycles were commutated under this condition, with each cycle consisting of a 10kA current-pulse of 30μs duration. Further tests at 1kHz (1μs, 500A pulses) have also been reported, over a 10^6 shot life, using a smaller-size triggered vacuum switch [190]. Thus, the capabilities of high-power TVG switches may be considered as being equivalent to more 'conventional' pulsed-power switching tubes, such as gas-filled spark gaps and thyratrons.

Aston University

Illustration has been removed for copyright restrictions

Fig. 2.7.10 A cross-section of a sealed triggered vacuum switch (from Vozdvizhenskii and Sidorov [5])

key: 1. ceramic cylinder, 4./5. main electrodes, 6./7./8. copper shields, 9. trigger electrode, 10./11. dielectric spacers, 12. metal insert

Where short operational lifetimes are required, especially in single-shot detonic applications {see Fig 2.7.4(b)}, small-size TVG switches can provide high power-densities within a small tube envelope. For example, Fig 2.7.11 illustrates a miniature triggered vacuum switch that employs a sintered carbon film on the surface of the trigger ceramic [169] to achieve a low trigger-voltage breakdown threshold. Indeed, trigger voltages as low as 50V were reported for the film-trigger TVG shown in Fig 2.7.11, with a corresponding trigger resistance in the range 30Ω-10KΩ [169]. Low trigger-voltage, surface-discharge TVGs may therefore be most attractive as a pulsed-power switch element, since they require relatively simple, low-voltage triggering circuitry. More generally, surface-discharge triggered vacuum switches offer a robust switching technique, with straight-forward trigger circuits able to control single [2,3] and multiple-arrays of TVG devices [191].

Fig. 2.7.11 Sectional diagram of (a) sealed miniature triggered vacuum switch, with (b) sintered carbon trigger film (from Bayliss *et al* [169])

2.7.5 Technological basis for investigation - a commercial TVG A miniature commercial TVG was selected to be the subject of this work, since it offered a simple internal structure; furthermore, its small dimensions allowed the application of high inter-electrode electric-fields, available within the laboratory. This device is illustrated in Fig 2.7.12, and consists of two copper main-electrodes that are supported by an alumina ceramic envelope. A third *trigger* electrode is formed by a ring of metallization on the end-face of a cylindrical alumina trigger-insulator, with this alumina tube set into the centre of the adjacent main electrode. As shown in the schematic of Fig. 2.7.13, the internal construction of this commercial tube is similar to the miniature TVG presented in Fig 2.7.11.

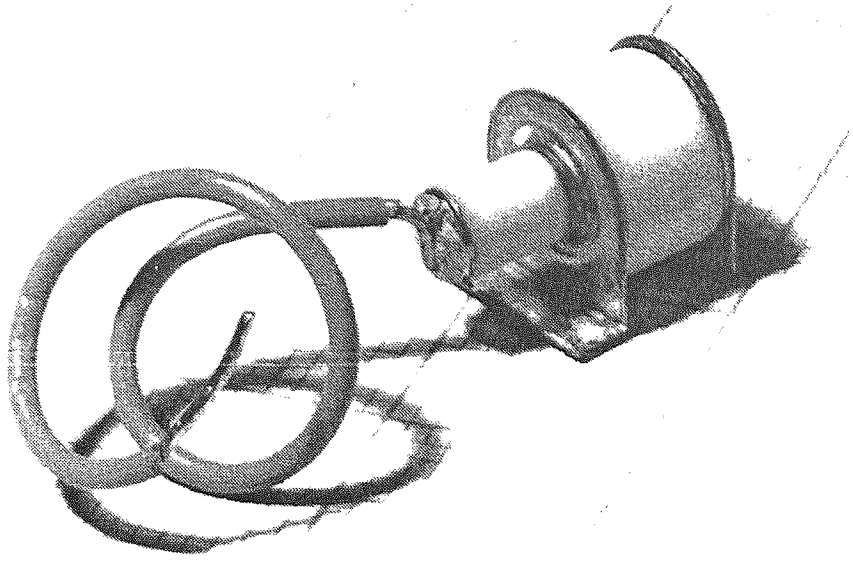

(a)

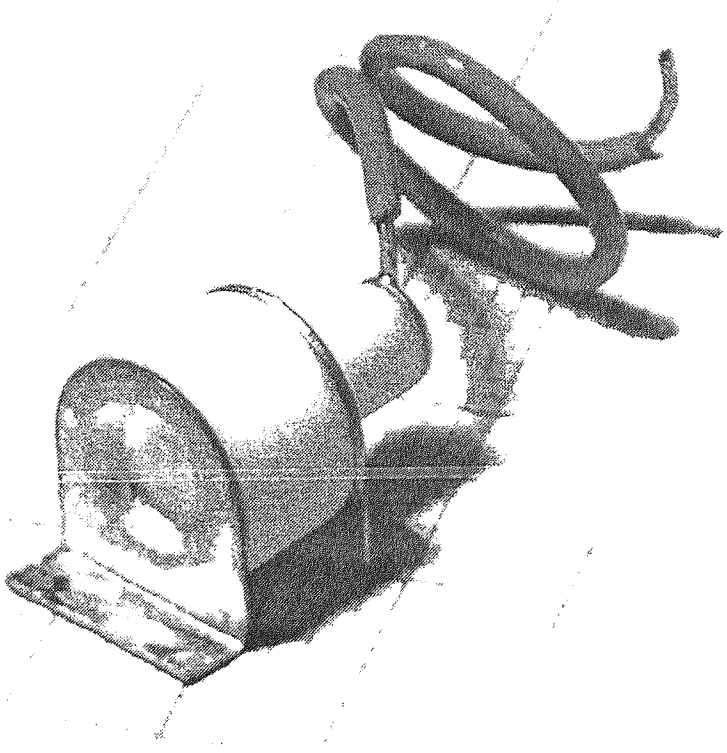

(b)

Fig. 2.7.12 The commercial TVG switch used for the present study, viewed from (a) the trigger / adjacent electrode assembly, and (b) the opposite main electrode

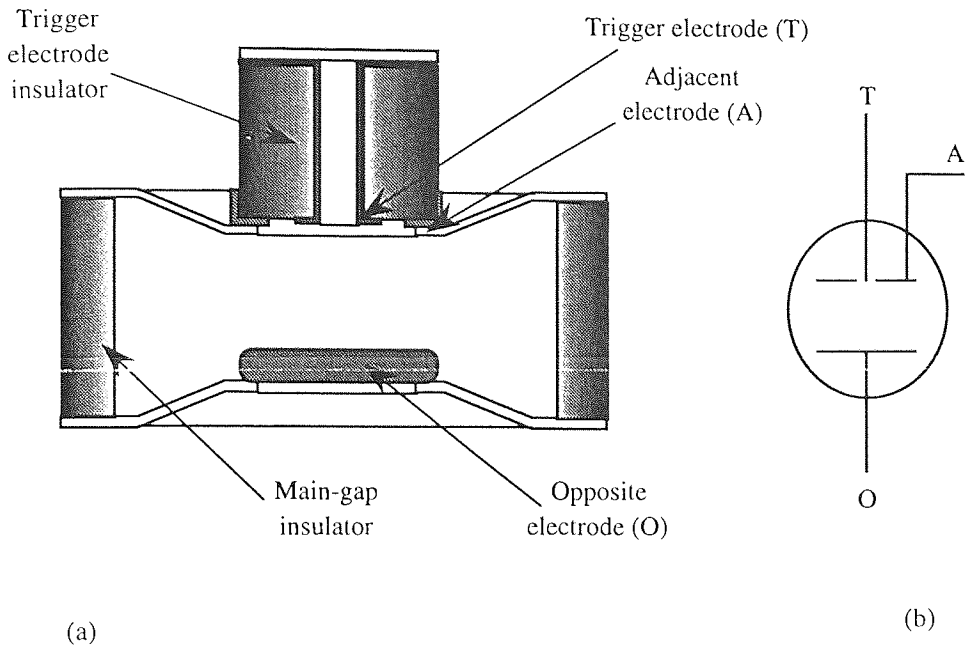

Fig. 2.7.13 (a) Sectioned illustration of commercial triggered vacuum switch, with (b) circuit representation of three-electrode TVG

As will be described in greater detail in Chapter 3, various test specimens were prepared, which replicated the internal structures of the triggered vacuum tube shown in Figs 2.7.12 and 2.7.13. Chapter 3 also presents designs of the experimental systems used to observe and characterise the vacuum behaviour of these test trigger structures.

3. EXPERIMENTAL SYSTEMS

A series of electronic and optical analytical techniques were used to diagnose the *in vacuo* characteristics of alumina ceramic, which formed the trigger insulator used in the commercial triggered vacuum switch shown in Section 2.7.5. Furthermore, several surface-analysis techniques were employed in an investigation of the material structure of the alumina ceramic trigger modules, and looked into the influence of this structure upon the electro-optical characteristics of the alumina module.

3.1 Experimental trigger specimen modules

To permit the observation and characterisation of the operational mode of a surface-discharge TVG trigger structure, experimental modules were assembled from the metallized trigger ceramic of the commercial TVG switch (Section 2.7.5). Several module designs were used, each lending itself to the study of particular aspects of triggered vacuum switch operation.

3.1.1 Metallized alumina modules Figure 3.1.1 illustrates the assembled form of the experimental specimens used in much of this work, whilst Fig 3.1.2 presents a sectioned engineering drawing of these metallized alumina modules.

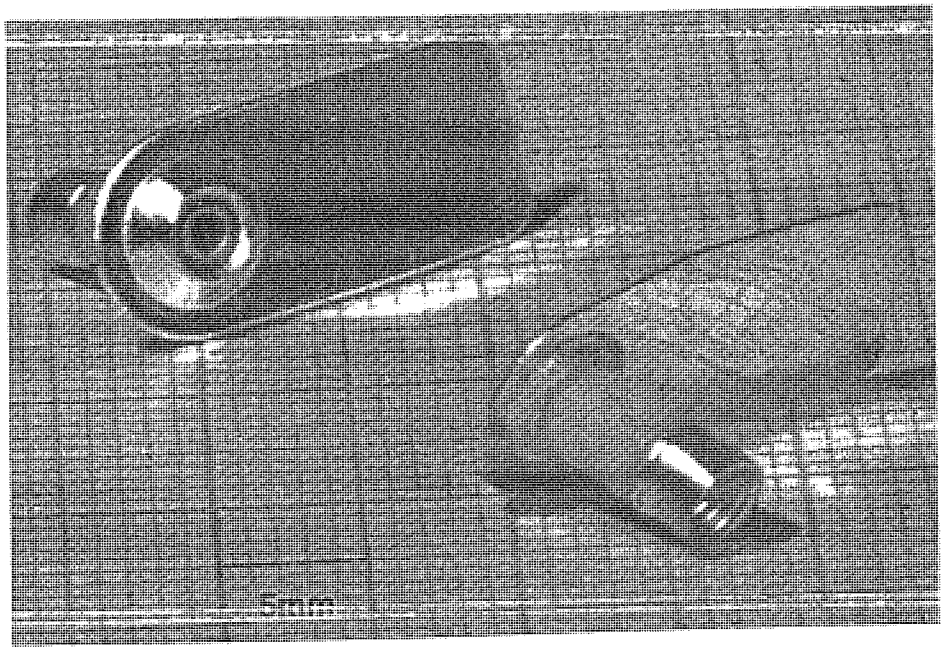

Fig. 3.1.1 Experimental alumina modules, showing threaded trigger connection and adjacent copper electrode tag

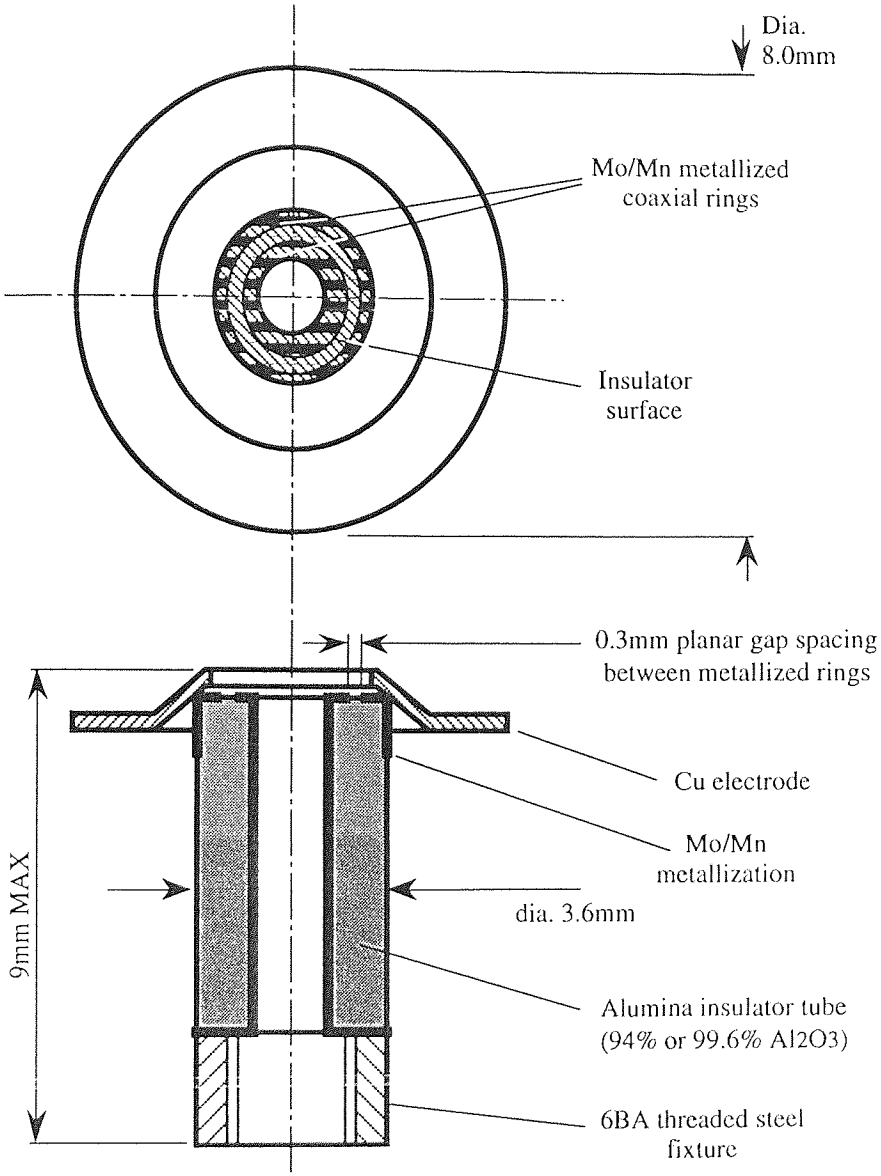

Fig. 3.1.2 End-elevation and sectioned axial views of the metallised alumina module

Two concentric rings of Mo/Mn metallisation were applied to one end-face of the alumina ceramic, forming a pair of co-axial planar electrodes, with the outer ring of metallizing brazed into an adjacent-electrode copper tag. This experimental M-I-M ceramic-electrode structure thus replicated the adjacent-trigger electrode assembly of the TVG switch illustrated in Figs 2.7.12 and 2.7.13. A threaded-fastener was brazed onto the extended metallisation of the inner electrode-ring, replacing the trigger-lead connection of the commercial TVG tube (Fig 2.7.12); this fastener allowed a rigid, UHV-compatible fixture of the specimen module into the analytical vacuum system described in Section 3.2.

3.1.2 Confined electrode regime The internal electrode structure of a sealed TVG switch is ultimately confined by the solid dielectric envelope which supports the main electrodes (see Section 2.7). In order to assess the influence of this body-envelope upon the behaviour of a "confined" experimental trigger structure, electrode modules were prepared with an alumina cylinder brazed onto the outer (adjacent) copper electrode. Figure 3.1.3 shows the form of these 'confined' trigger specimens, and displays the coaxial mounting of the alumina cylinder about the centre-axis of the metallized alumina ceramic.

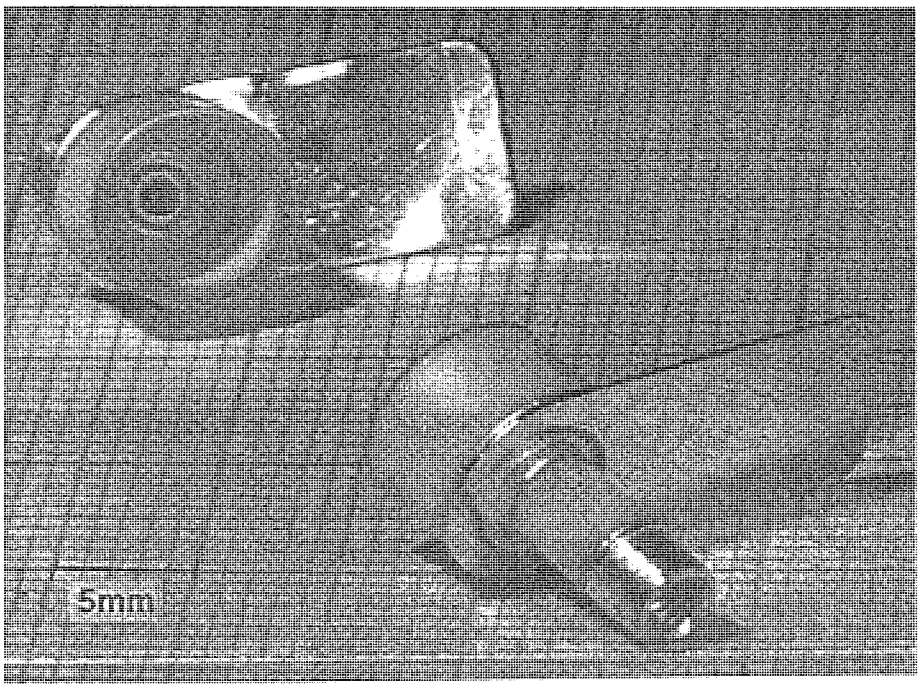

Fig. 3.1.3 Outline form of 'confined' electrode modules

3.1.3 'Bulk' dielectric alumina specimens Further experimental modules were prepared using alumina cylinders, metallized along their internal-diameter, with this metallisation brazed to a threaded fastener as shown in Fig 3.1.4. Electrode-rings were not metallized onto the end-face of the ceramic; instead, a single metallized band was applied midway along the outside-diameter of the alumina. Thus, the 'bulk' specimen module allowed the study of the *intrinsic* behaviour of the alumina ceramic dielectric, by the experimental application of radial electric-fields through the *bulk* thickness of the alumina tube.

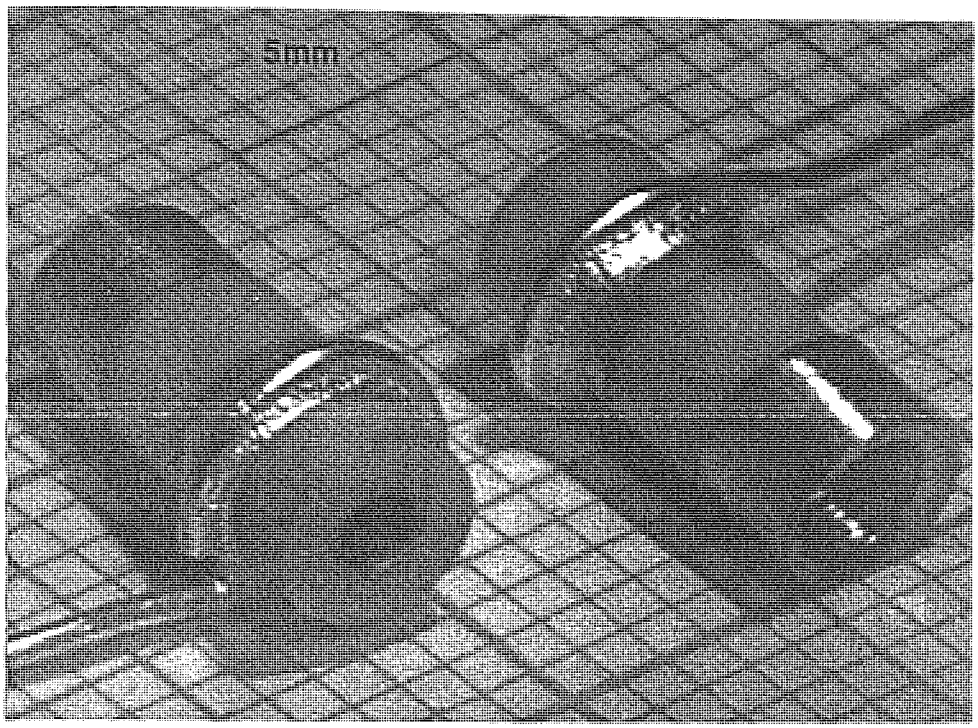

(a)

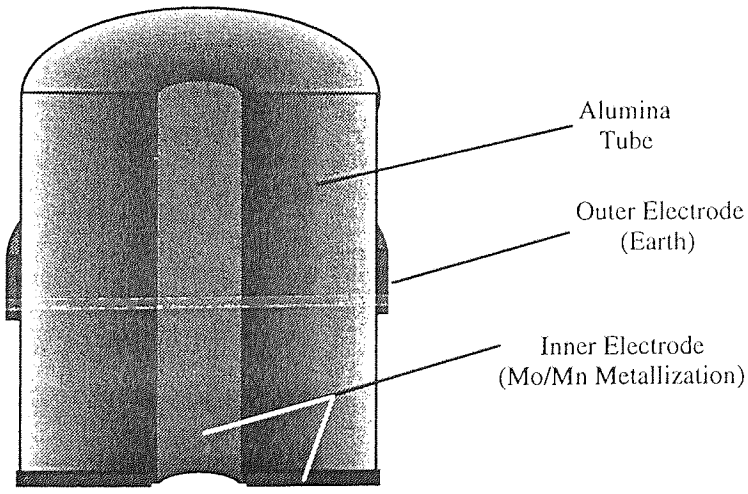

(b)

Fig. 3.1.4 (a) Outline form and (b) schematic sectioned drawing of metallized 'bulk' alumina tube modules

3.1.4 Encapsulated alumina modules Figure 3.1.5(a) depicts a demountable alumina-module assembly, consisting of a metallized alumina specimen mounted within a glass-bulb envelope. The trigger- and adjacent-electrode terminations were spot-welded to tungsten (W) leads, using an intermediate thickness of nickel (Ni)

foil as an electrochemical passivation material between the copper terminations and the tungsten leads, as illustrated in Fig. 3.1.5(b).

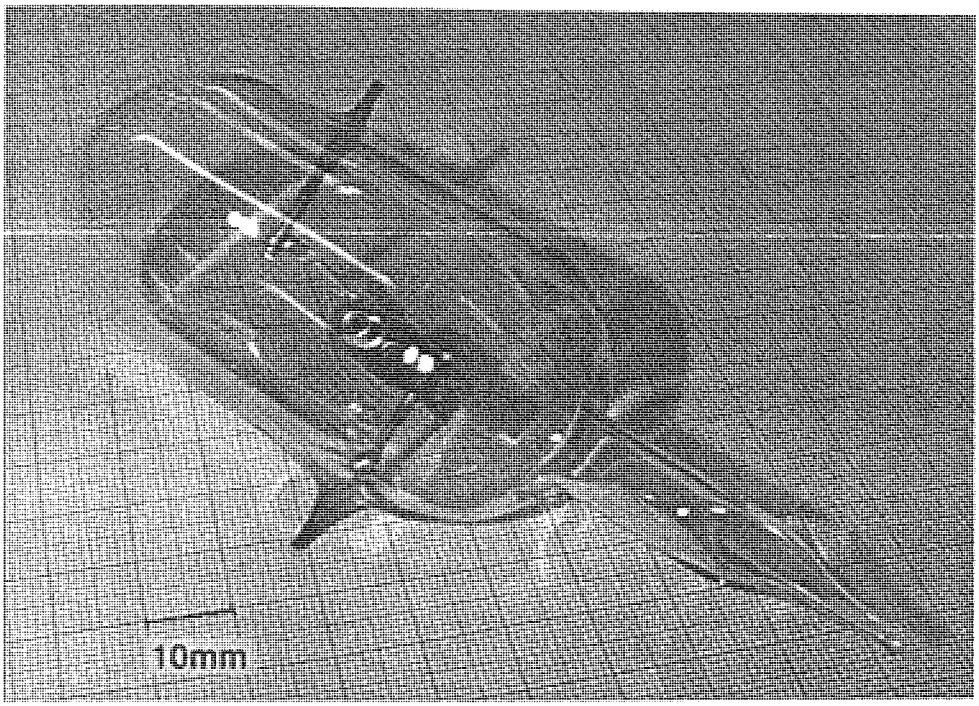

(a)

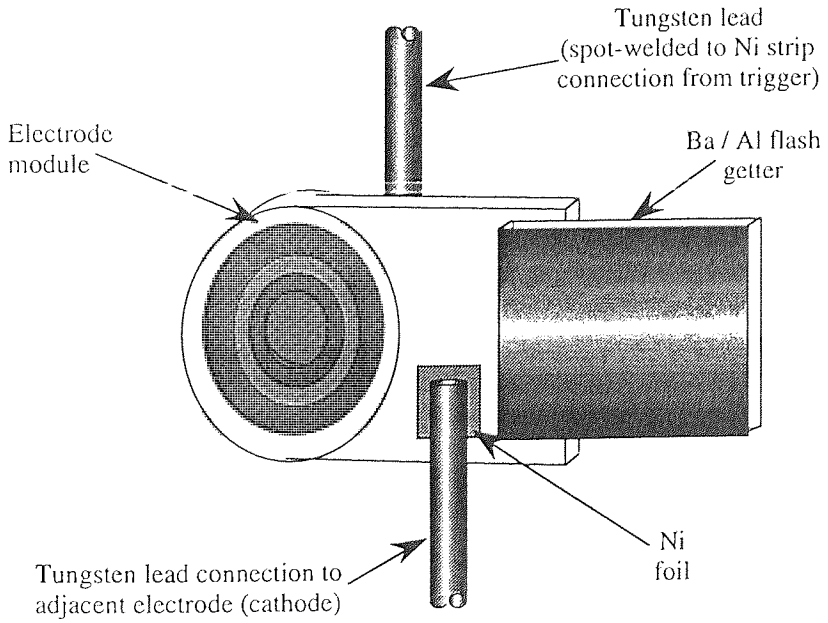

(b)

Fig. 3.1.5 (a) Demountable glass-bulbed alumina module, and (b) detail of encapsulated trigger specimen fixture

Fused glass-bead seals [35] secured the leads and the trigger specimen into the glass bulb. A strip of Ba/Al flash getter material (SAES-Milano type 'Stabil') was spot-welded to the copper-tag (adjacent electrode) of the specimen module. The getter was activated following the evacuation and sealing of the glass envelope, to maintain the vacuum-integrity of the sealed bulb module.

This sealed, evacuated trigger regime was therefore particularly suited to experimental observations requiring a short working-distance between a remote diagnostic detector and the alumina module. However, this specimen arrangement lacked any facility for *in vacuo* diagnostic techniques, which demanded more flexible analytical systems such as those described in Section 3.2.

3.2 Analytical systems

A suite of dedicated laboratory facilities were used to investigate the electro-optical characteristics of the alumina ceramic modules described in Section 3.1. An ultra-high vacuum (UHV) system was necessary, in order to replicate the UHV environment of the alumina when it is used as a trigger insulator within a TVG switch (see Sections 1.1 and 2.7). Further analytical instrumentation was combined with this vacuum system, in order to characterise the *in vacuo* behaviour of the alumina modules.

3.2.1 Experimental system The studies of surface-flashover phenomena described in this work were performed using the dedicated ultra-high vacuum (UHV) system illustrated in Fig 3.2.1. This UHV system comprised a cylindrical stainless-steel chamber (20cm diameter, 20cm length, 7 litre internal volume), evacuated by a turbomolecular pump and rotary-vane backing pump. A 250W radiant heater enabled the baking of electrode specimen modules to 400°C, and assisted the evacuation of water-vapour from the internal chamber surfaces.

An auxiliary vacuum system was also used, based upon a similar test chamber with a liquid nitrogen-trapped oil diffusion pump: this secondary scheme has been described elsewhere [36]. Further details of the experimental vacuum system design may be found in Appendix A.

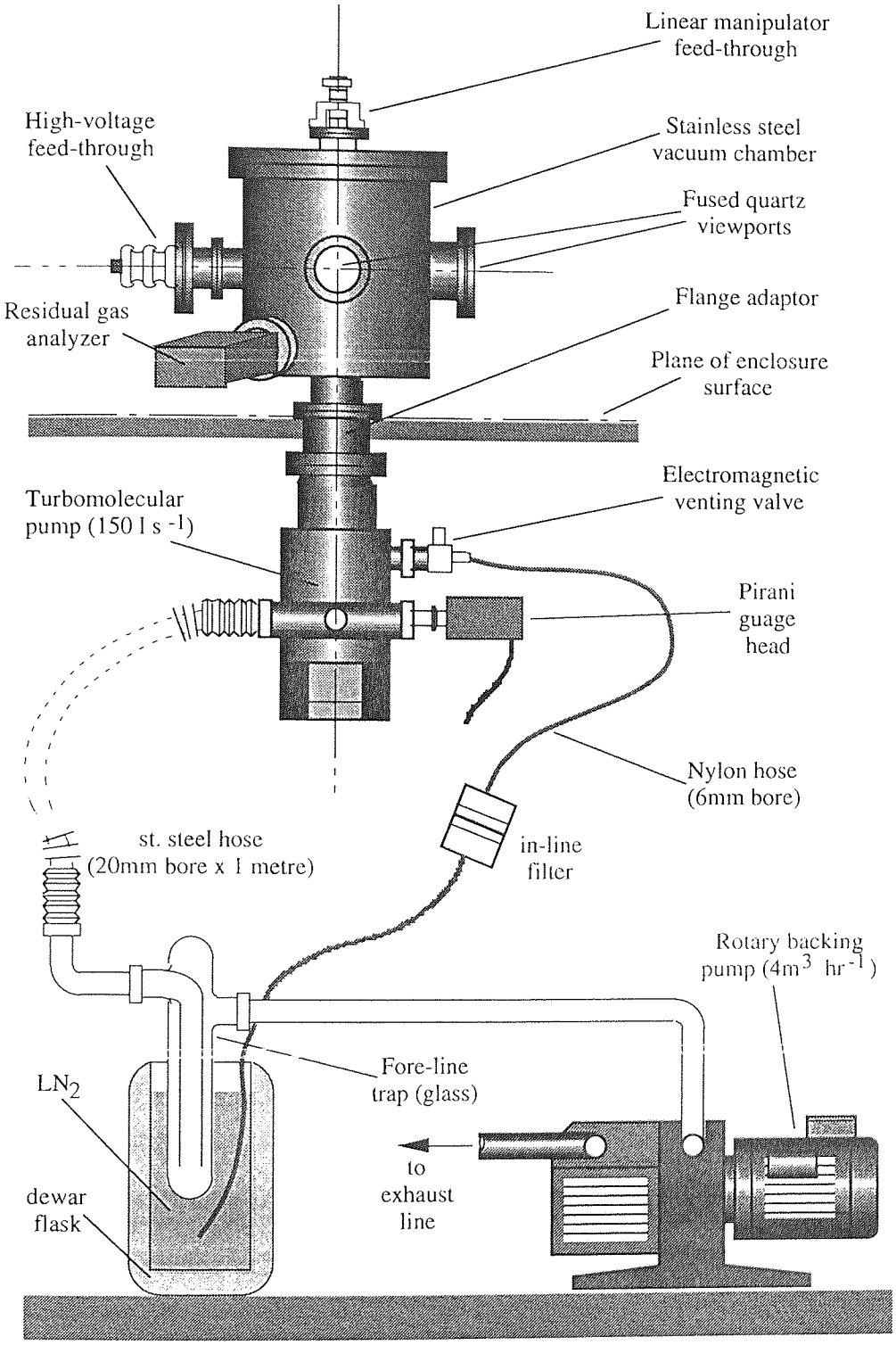

Fig. 3.2.1 General arrangement of analytical UHV system

3.2.2 Transparent Anode electrocathodoluminescence imaging A three-electrode experimental regime was realised by the addition of a plane electrode in front of the alumina module. This third electrode was transparent, thereby enabling the simultaneous observation of optical events on the end-face of the alumina module. Furthermore, with the application of a positive transverse DC

voltage to the transparent anode, the impact of any electrons emitted from the planar metallized-alumina structure would result in the generation of visible light (transition radiation) on the anode. Figure 3.2.2 shows the arrangement of an alumina specimen module behind the transparent anode, with a *transverse* gap of 1mm between the specimen end-face and the transparent anode.

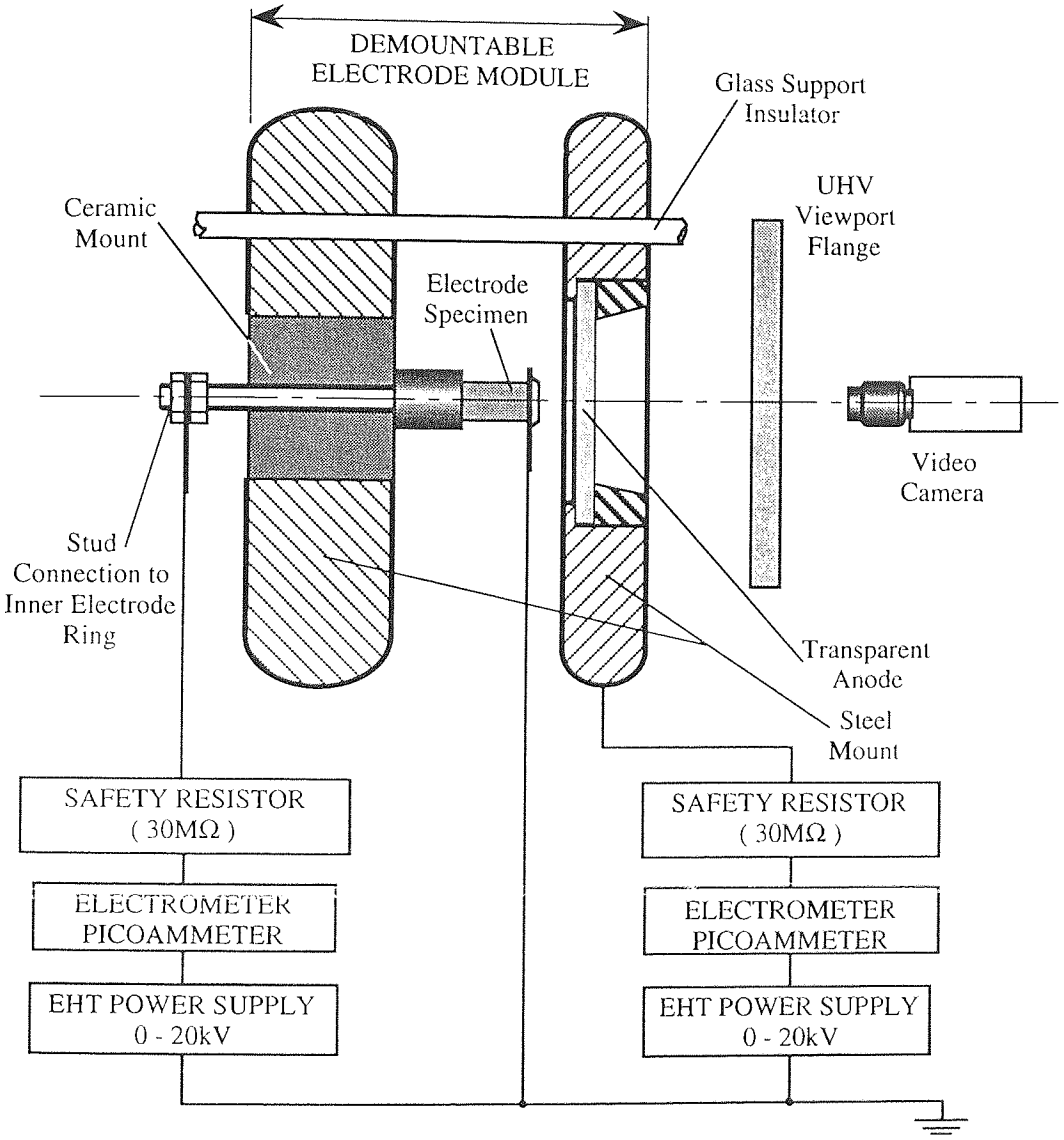

Fig. 3.2.2 Schematic of electrode module and Transparent Anode

3.2.2.1 Transparent Anode specimen fixture The *transparent anode* consists of a glass substrate disc, which is coated with a thin layer (few μm thickness) of tin oxide [37]. High-voltage DC connections were made to the inner electrode-ring of the electrode module, and to the transparent anode, by ceramic feed-throughs rated at 20kV. External safety resistors (30MΩ) limited the circuit currents to *pre*breakdown values of less than 500μA, whilst solid-state electrometers, connected to the HV power supplies, measured the electrode currents. Figure 3.2.3

presents orthogonal views showing the fixture of an alumina module behind the transparent anode, as illustrated schematically by Fig 3.2.2.

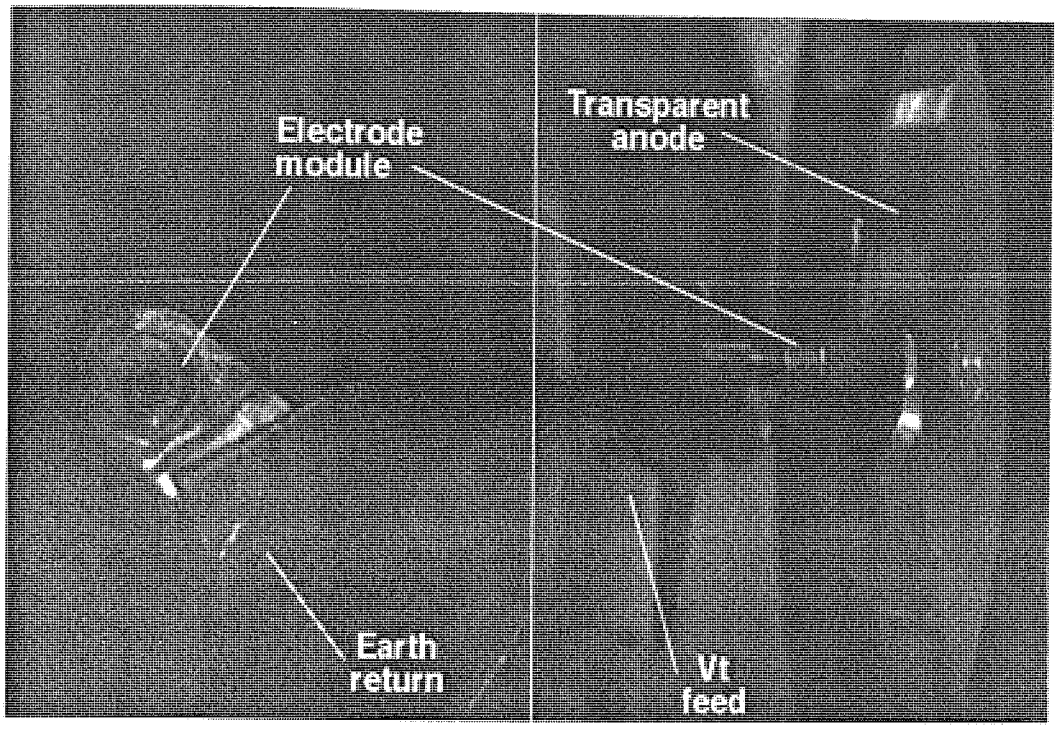

(a) (b)

Fig. 3.2.3 Arrangement of alumina module behind Transparent Anode, showing (a) front- and (b) side-views of module fixture

3.2.2.2 Electrode module fixture and connection Figure 3.2.4 shows a front-view of an electrode module located within the analytical vacuum system.

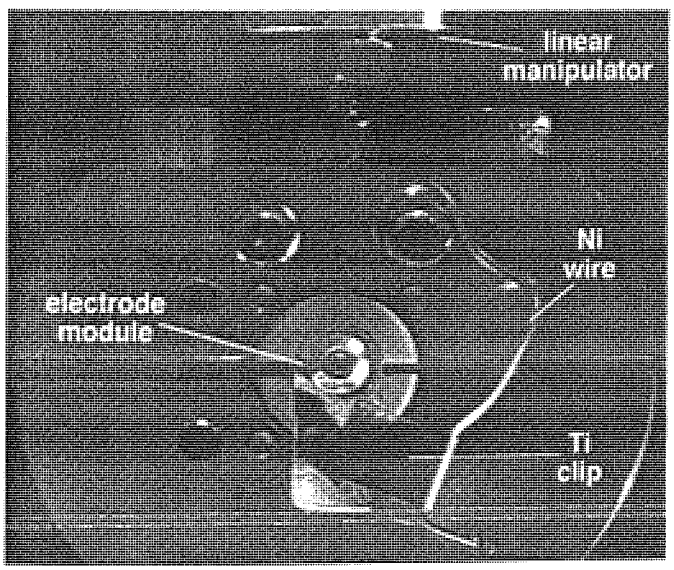

Fig. 3.2.4 Front view of electrode module clamped within stainless steel fixture

The electrode specimen module was fastened to a threaded copper rod (Cu: oxygen-free, high-conductivity {OFHC}); this OFHC copper support-rod was located within two semi-cylindrical shells of alumina ceramic, with the ceramic / copper assembly clamped in a stainless-steel fixture. To allow *in situ* vertical movement of the module, as determined by external diagnostic instruments, the alumina-module assembly was attached to a linear manipulator.

A high-voltage connection to the electrode module was made through an insulated feed-through in the chamber wall (Fig 3.2.1); the outer electrode-ring (and copper tag) were terminated to earth by a nickel wire and a titanium-foil clip.

3.2.3 Pulsed power supplies For studies of the *pulsed*-field behaviour of alumina insulators, two pulsed power supply units (PSUs) were constructed. These respective PSUs offered (i) high-voltage (+7kV), slow time rate-of-rise, and (ii) extra-high voltage (+30kV), fast time rate-of-rise pulsed-voltage sources. Output voltage characteristics of the HV and EHV PSUs are presented in Sections 3.2.3.1 and 3.2.3.2 respectively, whilst the PSU circuit designs are detailed in Appendix B.

3.2.3.1 High-voltage 0-7kV power supply This supply was based upon an existing trigger PSU used in the firing of TVG5 switches [192], and therefore provided experimental high-voltage pulses identical to those used in practical TVG firing circuits. Positive voltage pulses were derived from the first half-cycle of a damped-sinusoidal voltage waveform, having a maximum amplitude of +7kV, and a time rate-of-rise, $dV / dt \approx +5kV\ \mu s^{-1}$ (see Fig 3.2.5(a)).

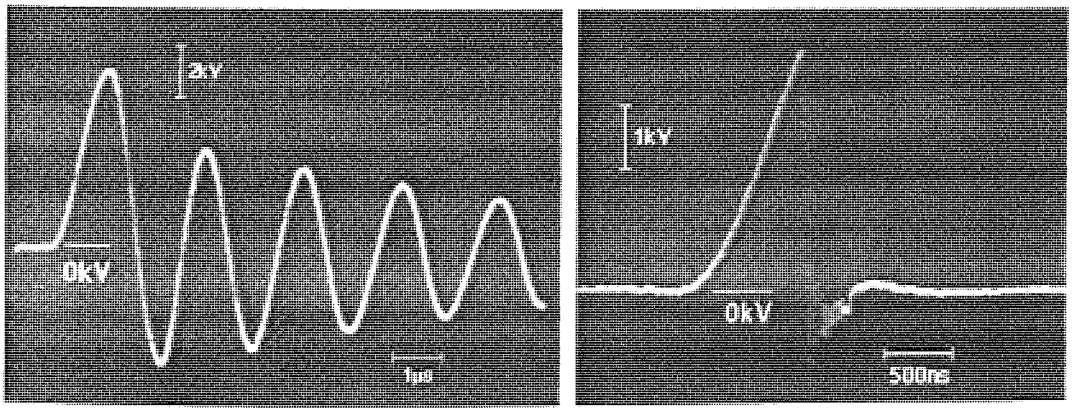

(a) (b)

Fig. 3.2.5 Oscillograms of (a) open-circuit 6kV high-voltage (HV) pulse from pulsed PSU, and (b) breakdown pulse measured across alumina module

When applied to the metal-insulator-metal (M-I-M) structure of the metallized electrode-rings on the alumina module, the breakdown value of the HV pulse, V_t, was found to be of the order of +4kV: a typical pulsed-breakdown voltage waveform is shown in Fig 3.2.5(b).

3.2.3.2 Extra high-voltage 30kV power supply A further pulsed PSU produced extra-high voltage (EHV) pulses of the form illustrated in Fig 3.2.6(a), with a maximum pulse voltage-amplitude of +30kV, and a leading-edge time-rate-of-rise, $dV / dt \approx +750kV\ \mu s^{-1}$. When this EHV signal was applied to the inner electrode-ring of the metallized alumina module, the breakdown value of the EHV pulse, V_t, was found to be of the order of +20kV: Fig 3.2.6(b) depicts a typical breakdown voltage waveform.

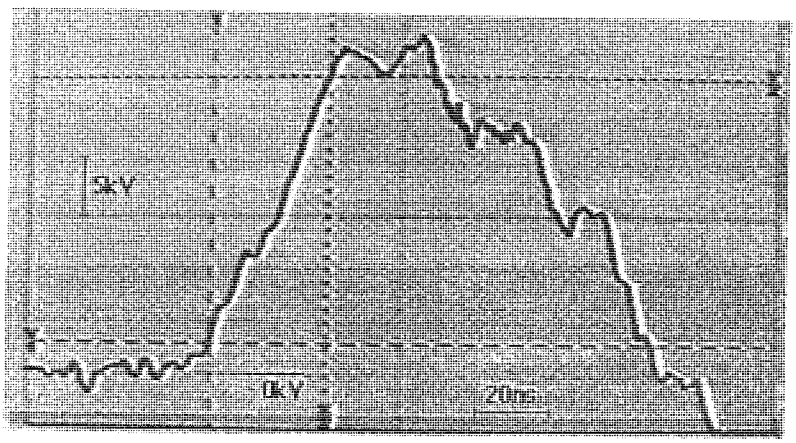

(a)

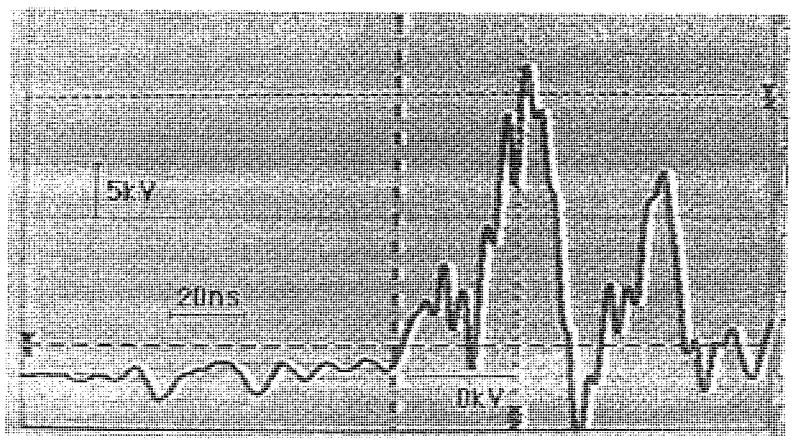

(b)

Fig. 3.2.6 Oscillograms of (a) open-circuit 30kV extra high-voltage (EHV) pulse from pulsed PSU, and (b) breakdown pulse measured across electrode module

3.2.4 Remote diagnostics Together with the *in vacuo* facilities outlined in Sections 3.2.1 and 3.2.2, which were used to monitor the electronic behaviour of alumina modules, the following *external* diagnostic systems were established, to enable the recording and analysis of optical events on alumina modules.

3.2.4.1 Video recording and image processing A quartz viewport in the vacuum chamber wall facilitated the viewing of the end-face of the specimen (this viewport is labelled as **1** in Fig 3.2.7), whilst a second viewport (**2**) allowed observation of the alumina specimen orthogonal to its main centre-axis.

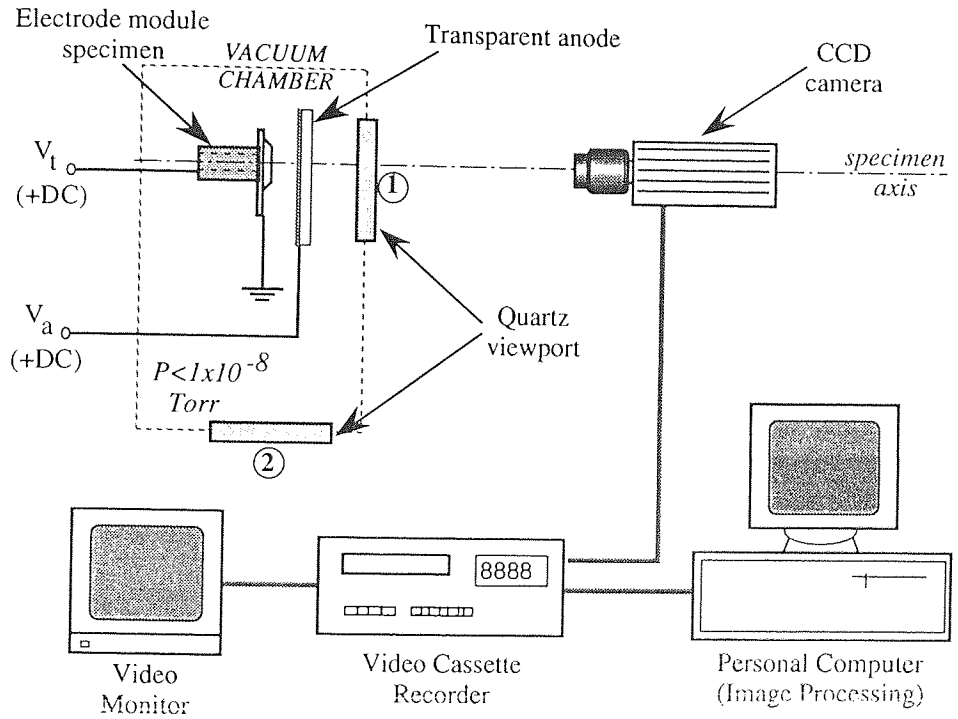

Fig. 3.2.7 System schematic of electrode module and the Transparent Anode

These front- and side-elevation views of the alumina module are shown in Fig 3.2.8. Auxiliary background-illumination was used to highlight the physical features of the specimen: however, this was routinely removed for the duration of experiments. The electrode module was viewed through the vacuum-chamber viewports (**1** and **2**), and through the transparent anode (through viewport **1**), using colour (Canon type EX-1) and high-resolution monochrome (EEV type 710, 768 pixels x 576 lines resolution) CCD cameras. In this system, the monochrome CCD camera was used in conjunction with a 100mm photographic macro lens and 50mm of lens extension, to provide magnified imaging of the end-face of the metallized-alumina electrode module. Events observed on the end-face of the module and/or on the transparent anode were recorded using VHS video recording techniques.

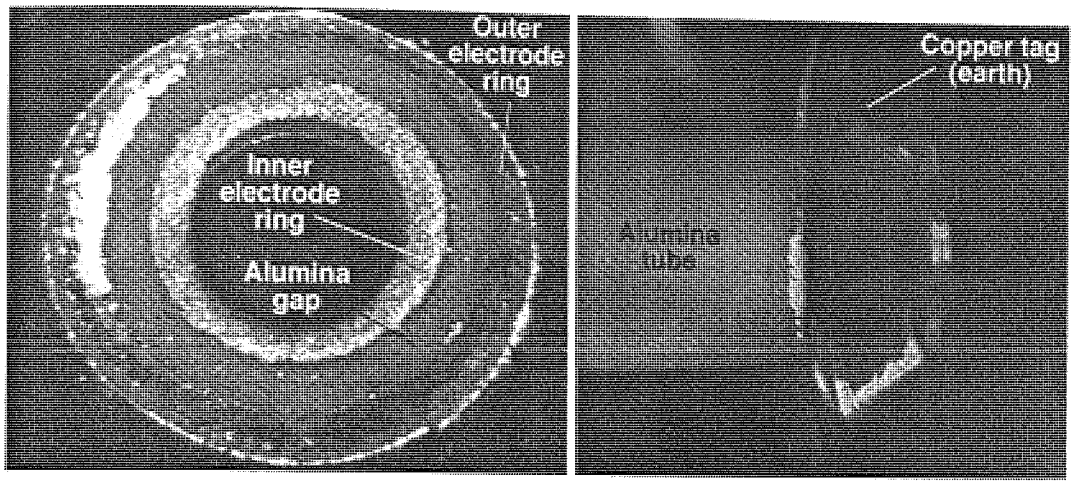

(a) (b)

Fig. 3.2.8 (a) Front (port **1**) and (b) side (port **2**) views of the metallized alumina module

3.2.4.2 High-speed videography In addition to the 'conventional' CCD imaging and VHS video recording techniques described in Section 3.2.4.1, an intensified high-speed video camera (256 x 256 pixels resolution, 1000 frames per second (fps) recording speed) and image processor (Kodak 'Ektapro' type EM 1012 [193]) facilitated the high-speed imaging of fast optical processes associated with pulsed-field surface-flashover events occurring on the metallized alumina module.

Figure 3.2.9(a) shows how this high-speed imaging facility was incorporated into the experimental system, whilst Fig 3.2.9(b) illustrates the high-speed camera head, along with its image processor and digital frame-store. For these measurements, a minimum framing period of 1ms was used to image the optical events associated with the pulsed breakdown of the specimen (maximum full-frame recording speed 1000 fps), with the image-intensifier of the high-speed camera operated between 70% and 95% of its maximum gain.

For observations of pulsed-field surface-flashover events, the high-speed video camera system was operated in a *'rolling'* recording mode, whereby 1ms frames were continuously read into a 1200-frame digital memory. Thus, the fast-video could be manually post-triggered, to stop the continuous digital image-recording following the application of a voltage-pulse to the alumina module.

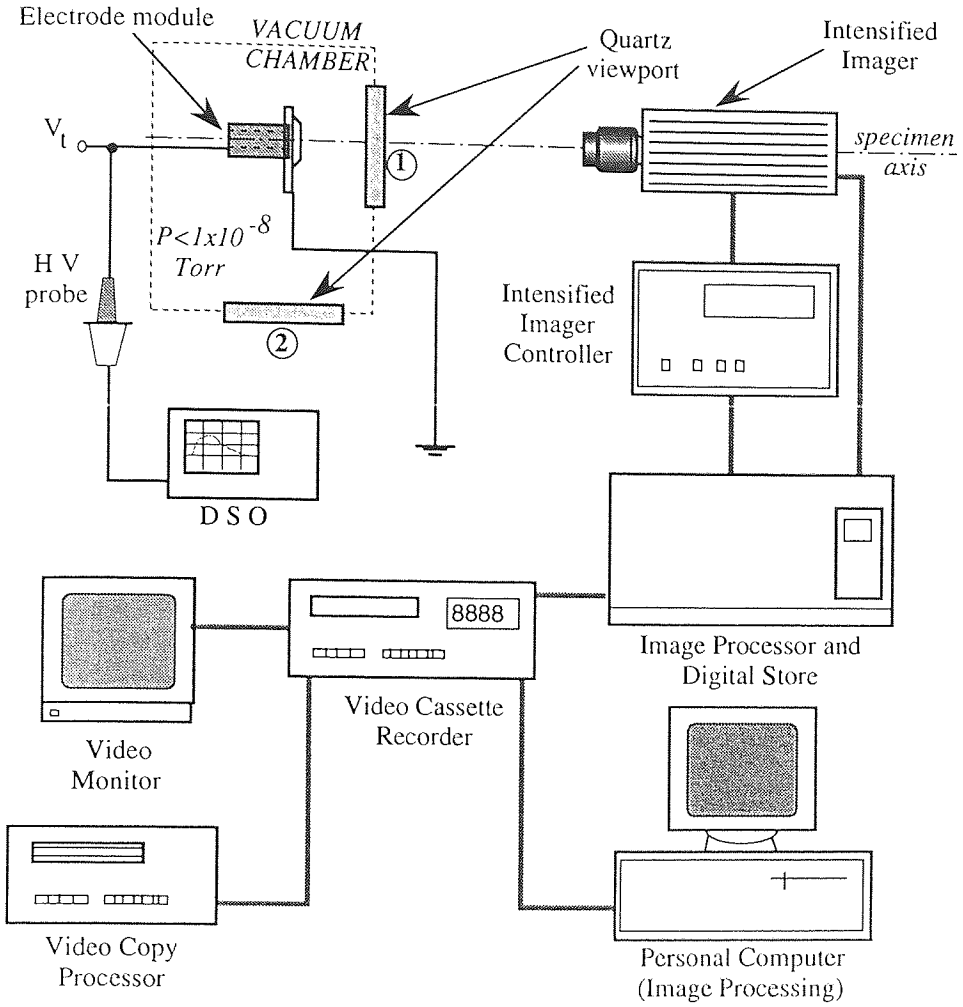

(a)

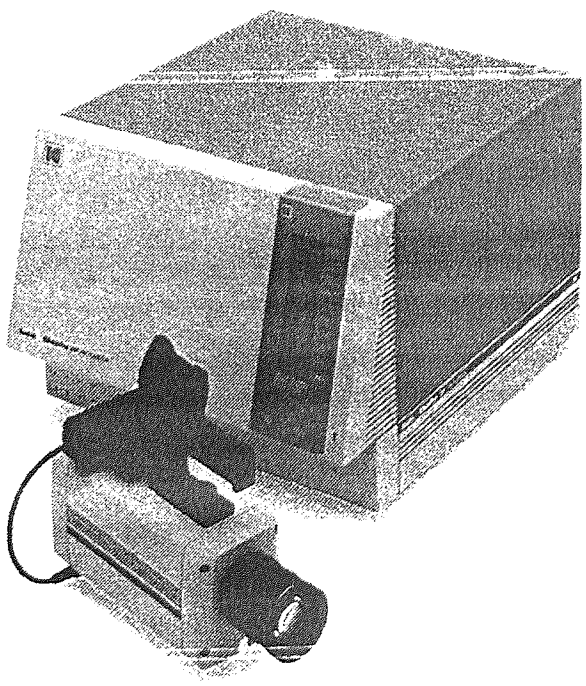

(b)

Fig. 3.2.9 (a) High-speed imaging system, with (b) intensified CCD camera and processor

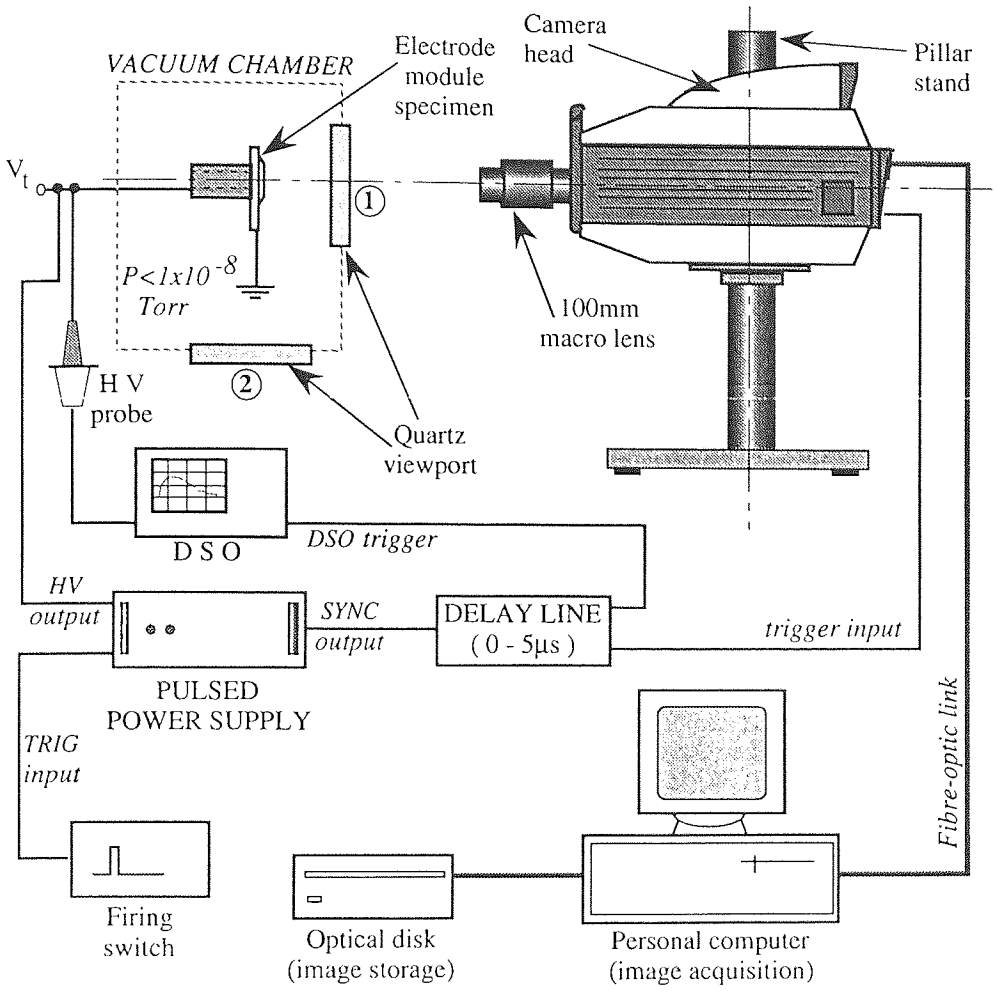

(a)

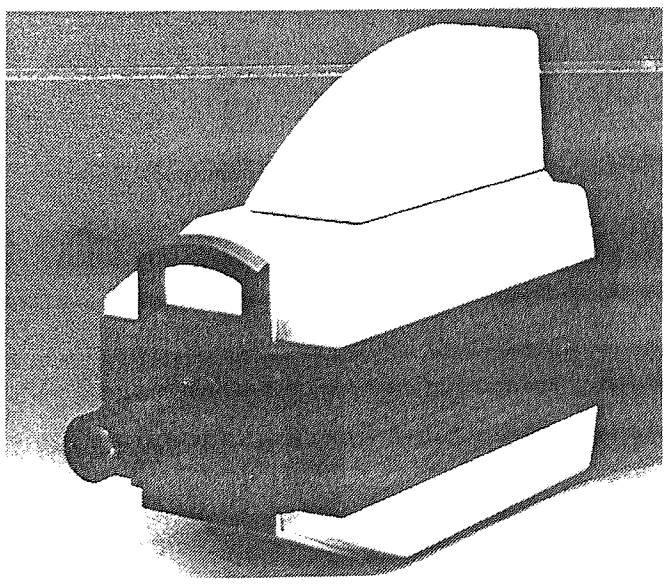

(b)

Fig. 3.2.10 (a) General arrangement of fast-framing experimental system, incorporating (b) ultra high-speed camera head

3.2.4.3 Fast frame imaging Ultra high-speed imaging of the pulsed-field surface-flashover events associated with the metallized alumina modules was undertaken using a fast-framing camera (Hadland Photonics type 'Imacon 468'). This camera offered an ultimate temporal resolution of 10ns at a framing speed of 10^8 frames-per-second [194], although it lacked the high optical-gain capability of the intensified high-speed video system described in Section 3.2.4.2. The performance of this camera, compared to that of the VHS and high-speed video systems, is summarised in Section 3.2.4.4.

The camera head, illustrated in Fig 3.2.10(b), consisted of four independent intensified-CCD channels, with a single photographic macro lens (125mm) used to focus light from the electrode module into all four channels. A 10-metre fibre-optic link connected the fast-framing camera to a personal computer (pc). The pc provided both remote-control of the camera-head operation, and also the downloading of high-resolution frames (586 x 385 pixels) from each of the four CCD sensors.

Referring to the schematic layout of the fast-framing experimental system presented in Fig 3.2.10(a), a manual firing switch was used to initiate the firing-circuit of the pulsed PSU, with a logic (SYNC) output from the PSU used to trigger the camera head. An adjustable delay line was inserted into the trigger-circuit to the camera, to compensate for internal delay within the pulsed PSU in the output of a HV pulse (V_t) to the experimental module .

The applied HV pulse was monitored using a 2 Gsamples s^{-1} digital storage oscilloscope (DSO), (Hewlett-Packard type HP54542A), in conjunction with a 1000:1 high-voltage probe. Triggering of the DSO was synchronised with the operation of the camera head, providing temporal correlation between the recorded frame-images and the measured oscillogram of the HV pulse.

3.2.4.4 Evaluation of imaging techniques The VHS videographic techniques described in Section 3.2.4.1 were found to provide high spatial resolution when coupled with high-magnification photographic optics: feature sizes of less then 50μm could be resolved with this system. This system was limited to a video frame-rate of 25Hz, which gave a time-resolution of 40ms.

The highest temporal resolution was achieved with the ultra-fast framing camera, which was able to detect photon-emission from pulsed-breakdown events in 100ns

frames (see Section 4.2). Beyond this framing speed, the camera was unable to detect optical emission from the experimental regime. However, this Imacon camera did offer adequate spatial resolution, and provided clear images of 100μm features.

The high-speed video system outlined in Section 3.2.4.2 offered only mediocre time- and spatial resolution, although its high optical gain characteristics allowed the imaging of low-intensity luminosity within the experimental alumina modules, which will be described in Section 4.2.1.2. Table 3.1 summarises the performance of the three imaging systems described in Section 3.2.4.

imaging technique	*minimum frame period*	*spatial resolution (pixels)*	*optical gain*
VHS video	40ms	768 x 576	1
Ektapro high-speed video	1ms	256 x 256	100 - 10000
Imacon 468 ultra-fast frame	100ns	576 x 385	10 - 7000

Table 3.1 Performance comparison of optical imaging systems

3.2.4.5 Optical spectrometry To enable a spectral characterisation of the optical phenomena observed on experimental alumina modules, the high-resolution CCD camera described in Section 3.2.4.1 was interchangeable with a lens fixture, which coupled light emitted from the alumina module through a fibre-optic light-guide into a scanning monochromator (Rees Instruments 'Monolight', type 6602 [195]). Figure 3.2.11 (a) shows the experimental system configuration used for optical imaging and high-speed spectroscopy, and Fig 3.2.11 (b) illustrates the monochromator instrument:

The use of quartz optics allowed the detection of short-wavelength photonic emissions, with a wavelength cut-off of approximately 220nm. Thus the CCD camera facilitated the spatial imaging of optical events associated with the metallized-alumina module, whilst the scanning monochromator allowed a quantitative measurement of the spectral data associated with these optical events.

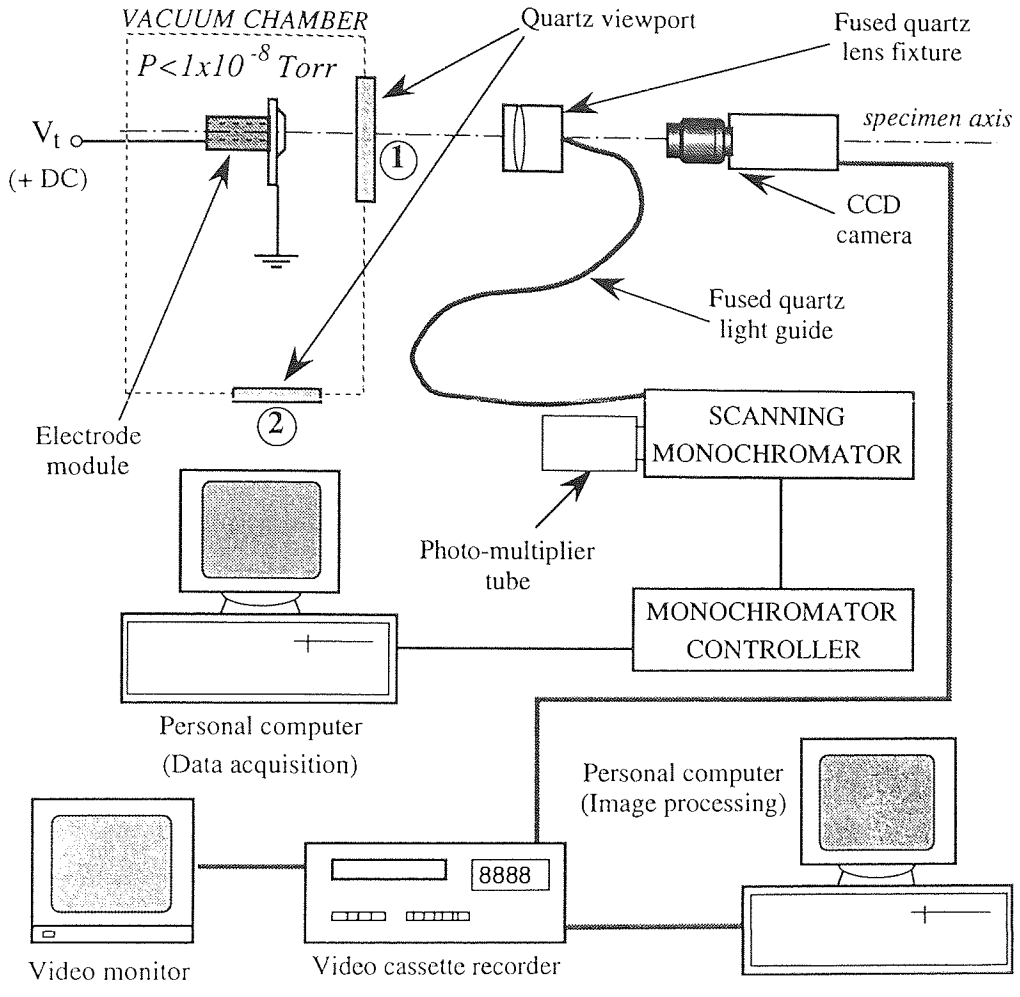

(a)

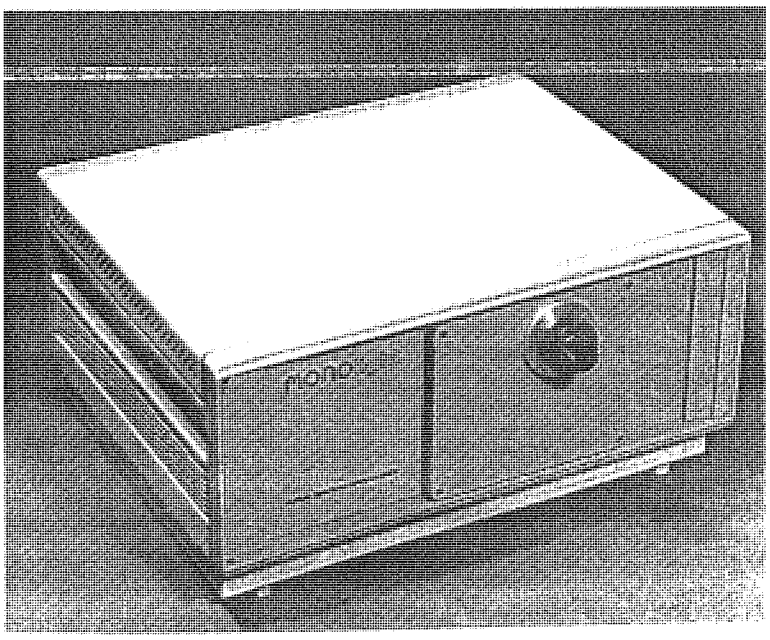

(b)

Fig. 3.2.11 (a) Experimental layout of optical imaging and spectroscopy system, with (b) detail of high-speed scanning monochromator

3.3 Surface analysis techniques

A series of surface analysis techniques were employed to provide (i) high-resolution *spatial* information concerning the surface micro-topography of experimental specimens and structures, and (ii) *quantitative* information describing the nature and state of the materials under investigation.

3.3.1 Scanning electron microscopy (SEM) Electron micrographs provided high-contrast, high-resolution images of metallized alumina modules; such images provided a clear depiction of the M-I-M module structure (Fig 3.3.1(a)), together with detail of microscopic surface features (Fig 3.3.1(b)) [196,197].

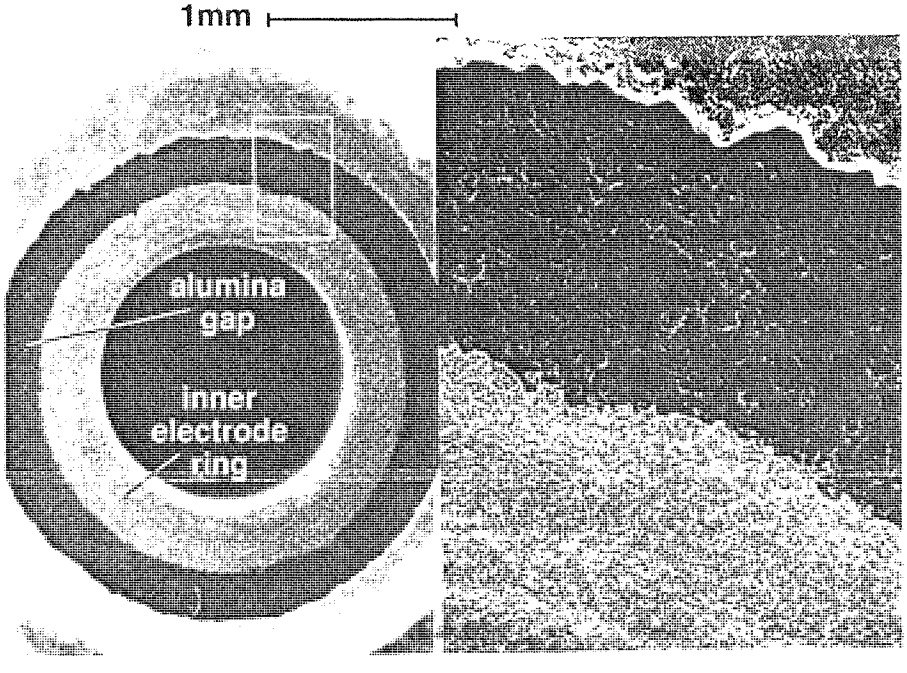

Fig. 3.3.1 Electron micrographs showing (a) front-face of metallized alumina module, and (b) detail of metallized alumina M-I-M structure

The SEM instrument (Leica Cambridge type S360), which is illustrated schematically in Fig 3.3.2, had a specified electron-beam spot-size of 40Å, although a practical resolution-limit was found to be ≈200Å. An energy-dispersive X-ray analysis (EDXA) system (Oxford Instruments type EXL, with LZ5 windowless detector) complemented the SEM, and allowed for diagnosis of the material species within the surface-layers of an investigated sample.

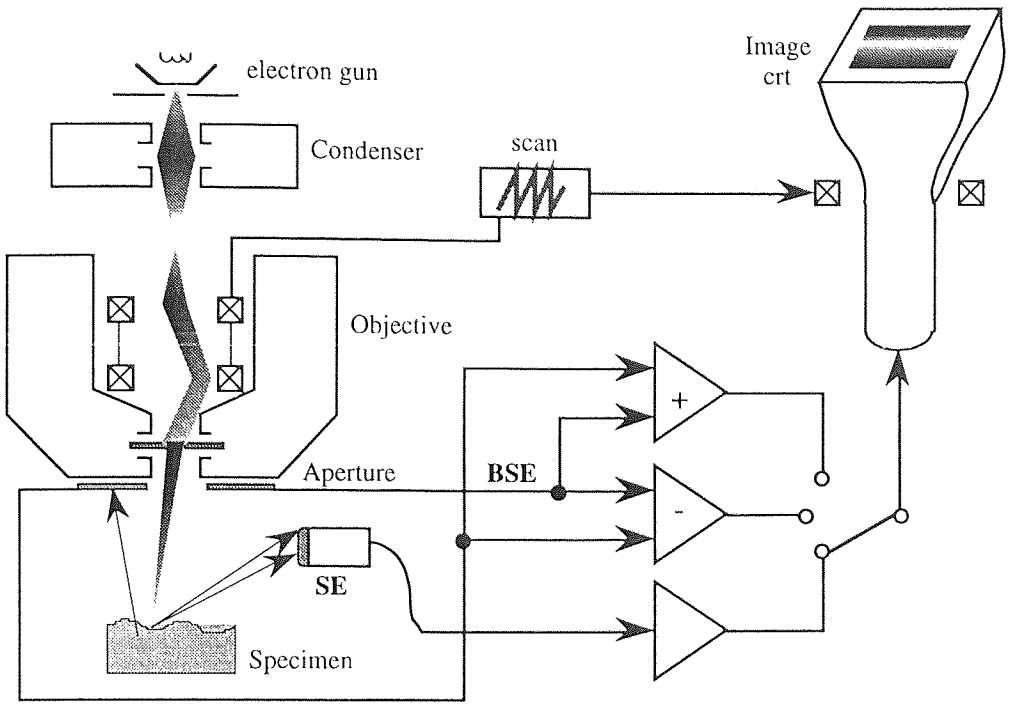

Fig. 3.3.2 General arrangement of a Scanning Electron Microscope (SEM) (after Turner [196])

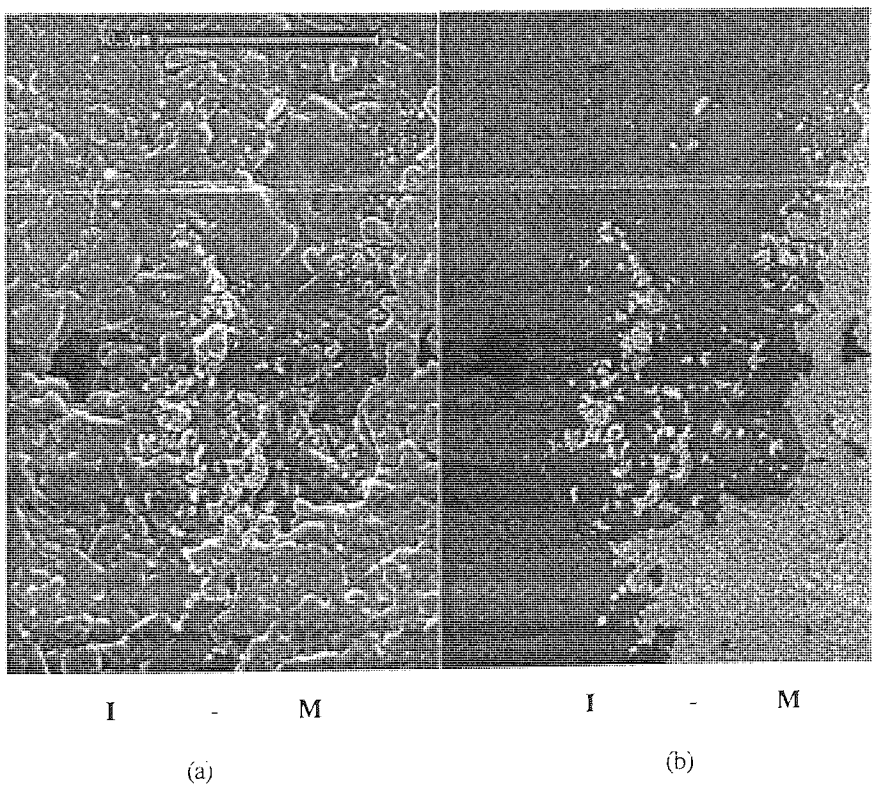

Fig. 3.3.3 (a) Back-scattered electron (BSE) and (b) secondary-electron (SE) images, showing M-I region of metallizing edge on alumina substrate

Acquisition of back-scattered electron (BSE) images, of the forms shown in Figs 3.3.1(a) and (b), required a conductive coating (carbon or gold) to be applied to the alumina module: i.e. to drain electronic charge, which would otherwise accumulate in the ceramic and cause blurring of the electron-image. In consequence, this corruption of the alumina module by the conductive coating meant that BSE imaging was only suitable for the analysis of alumina specimens which required no further high-voltage experimental operation.

Where spatial information was required from an alumina module *prior to* high-voltage analysis, a lower-contrast, lower-resolution secondary-electron (SE) image could be obtained from an *uncoated* alumina specimen. Use of a low-energy ($\approx$ 1keV) electron-beam minimised the effects of charging in the alumina insulator. Comparative BSE and SE images of a metallized region of alumina ceramic are shown in Fig 3.3.3.

3.3.2 Large area X-ray photoelectron spectroscopy (LAXPS) Surface analytical studies were undertaken in an ESCA (Electron Spectroscopy for Chemical Analysis) multi-technique surface-analysis system (Vacuum Generators type 'Escalab' 200D). The general form of the XPS configuration in such an instrument is shown in Fig 3.3.4:

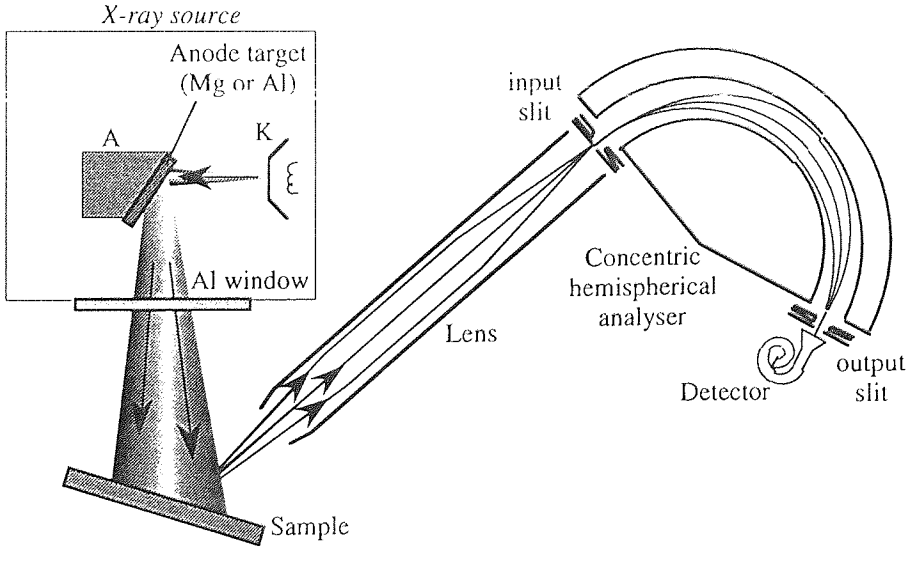

Fig. 3.3.4 General arrangement of an X-ray photoelectron spectrometer (after Smith [198])

X-rays were generated from magnesium and aluminium anode-targets, allowing a differentiation of Auger and photoelectron peaks in the recorded electron-energy

spectra arising from the k_α radiation of each target material [198]. Recorded XPS spectra could then be compared with reference data [199], in order to determine the species and state of the material under analysis. Analyses were made of (i) the material constituents of the alumina ceramics used in the metallized modules described in Section 3.1, and also of (ii) emitted material, or *efflux*, collected from pulsed-field surface-flashover events on the alumina modules, using a niobium metal target.

3.3.2.1 Surface analysis of alumina ceramic The alumina ceramics used in this study (Morgan-Matroc, type 'GM') were of 94% purity, with a mean grain-size of 10μm. A remaining fraction of oxide-glass locked the alumina grains into a ceramic matrix, where this 'glassy phase' consisted of alumina, silica (SiO_2) and CaO, with trace (few ppm) concentrations of metal-oxides including sodium, titanium and chrome. XPS analysis was undertaken to qualify these ceramic constituents, and thereby characterise the alumina material.

3.3.2.2 Analysis of collected efflux material Niobium (Nb) foil targets were used to collect any material emitted out of the alumina module, arising from pulsed-field surface-flashover events. Fig 3.3.5 illustrates the experimental arrangement, showing how this foil is attached to the copper tag of a metallized alumina module.

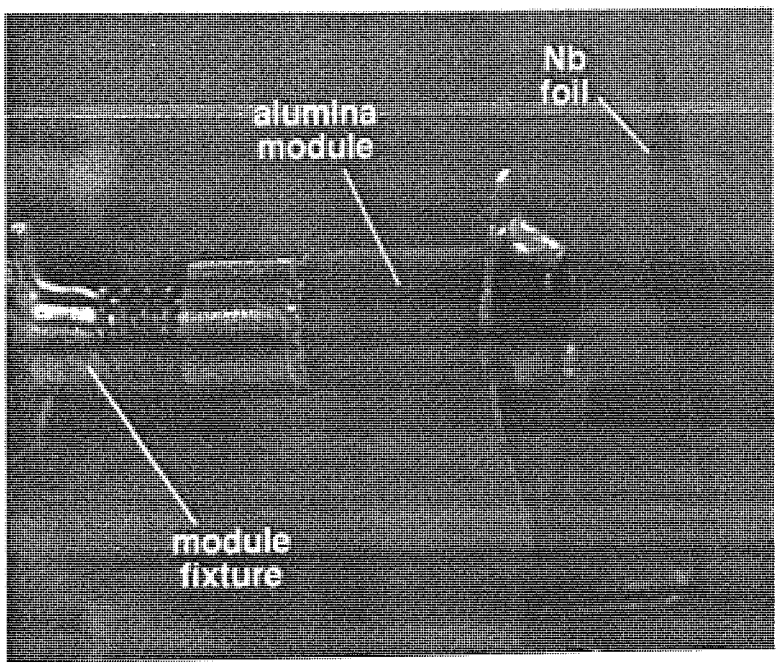

Fig. 3.3.5 Experimental arrangement of alumina module with niobium foil collector

Niobium was selected as a target material since the characteristic electron-energy peaks of its XPS spectra were very distinct from those of the materials in the alumina module [199], i.e. Al , Si and Ca in the alumina ceramic, with Cu and Ag in the brazed copper tag.

3.3.3 Microprobe Rutherford Backscattering Spectrometry (μ-RBS)

To complement the XPS characterisation of the alumina ceramic described in Section 3.3.2.1, further non-destructive material-analysis was undertaken using microprobe Rutherford Backscattering spectrometry (μ-RBS) [200,201]. The μ-RBS technique offered a high spatial resolution of 50μm [201], in contrast to the broad-area coverage of XPS analysis. Such a small spot-size of the analytical ion-beam (1.5MeV He^4 ions) was particularly suited to the analysis of alumina ceramics within the specimen modules described in Section 3.1. Figure 3.3.6 illustrates the backscattering of the diagnostic helium-ion beam from the inter-electrode ceramic region of an alumina module.

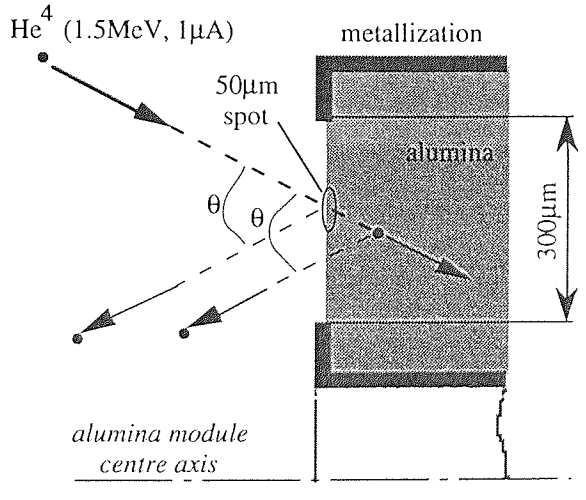

Fig. 3.3.6 Schematic representation showing μ-RBS analysis of metallized alumina module

In this study, the He ion source and RBS detector were aligned with a back-scattering angle, θ, of 165°. With reference to the construction of the alumina modules shown in Fig 3.1.2, analysis of the exposed 300μm region of the alumina-module end-face appeared to be feasible. The arrangement of the module suggested negligible interference of the ion-beam with the surrounding metallization of the planar co-axial electrodes, nor with the adjacent copper tag.

3.4 Surface engineering of trigger ceramics

An ultimate objective of this work was to investigate possible methods by which the consistency of the pulsed-breakdown behaviour of the trigger-insulator dielectric might be improved. Such a well-characterised metal-insulator-metal (M-I-M) structure could then provide a repeatable and reliable source of electrons, suitable for use in cold-cathode vacuum switches such as TVGs.

Observations of prebreakdown photon-emission from alumina (Al_2O_3) dielectrics have suggested *solid-state* charge-transport within the insulator, consistent with electron-recombination at impurity and structural-defect centres in the dielectric [39,44,202]. Thus, enhancement of these conduction processes was sought by the controlled increase of the populations of impurities and defects in the insulator surface. To this end, implantation of metallic ions, into the metallized end-face of alumina modules, was investigated as a possible surface-engineering technique.

Ion implantation of the alumina could provide a two-fold effect: firstly, the provision of a uniform semiconducting layer within the insulator bulk, offering better repeatability in the electrical characteristics of ceramic samples. Secondly, the implantation of this layer *into* the bulk of the insulating dielectric afforded protection of the film from erosion by the main-gap discharge plasma associated with the firing of a TVG switch [170].

Two ion-implantation schemes were evaluated, with the resulting implanted-ceramic modules investigated using the experimental techniques described in Section 3.2. Analyses of the prebreakdown characteristics associated with the implanted modules were performed, together with operational studies of these implanted structures when assembled as trigger-insulators in TVG switches.

3.4.1 Direct implantation of Cr ions into alumina Ion implantation of chromium (Cr) offered a simple one-step process for producing a buried metallic layer of chromium within the surface of the alumina substrate. Chromium was selected as a dopant material owing to the intensity of radiative electron-recombination observed from Cr impurity-centres during vacuum prebreakdown of alumina ceramics, i.e. such as reported by Saito *et al* [44]. Thus, this implantation process sought to enhance the prebreakdown emission-characteristics of the insulator, by the controlled introduction of excess Cr into the alumina.

Metallic-ion doping densities in the region of 10^{16} Cr cm^{-2} were used: an ion fluence that was expected to yield a surface-resistivity of the order of 10^{11} Ω-cm [203]. Figure 3.4.1 shows a schematic illustration of the chromium-implantation of alumina ceramic.

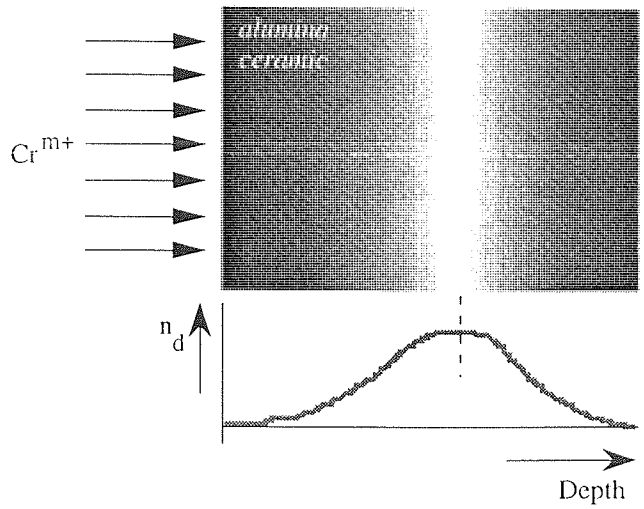

Fig. 3.4.1 Illustrating the implantation of chromium (Cr) ions into alumina ceramic

Unfortunately, the benefits offered by the simplicity of this Cr implantation process were offset by the requirement for a high ion-beam energy, approaching 1MeV, for a 0.5μm mean penetration depth. Furthermore, the energetic implantation of high-mass Cr ions into the alumina was likely to cause significant structural damage to the ceramic. This damage is illustrated by the Monte Carlo [204] distributions of implanted Cr ions shown in Fig 3.4.2, and the corresponding histograms of vacancy-production in the surface-layers of the implanted alumina (Fig 3.4.3).

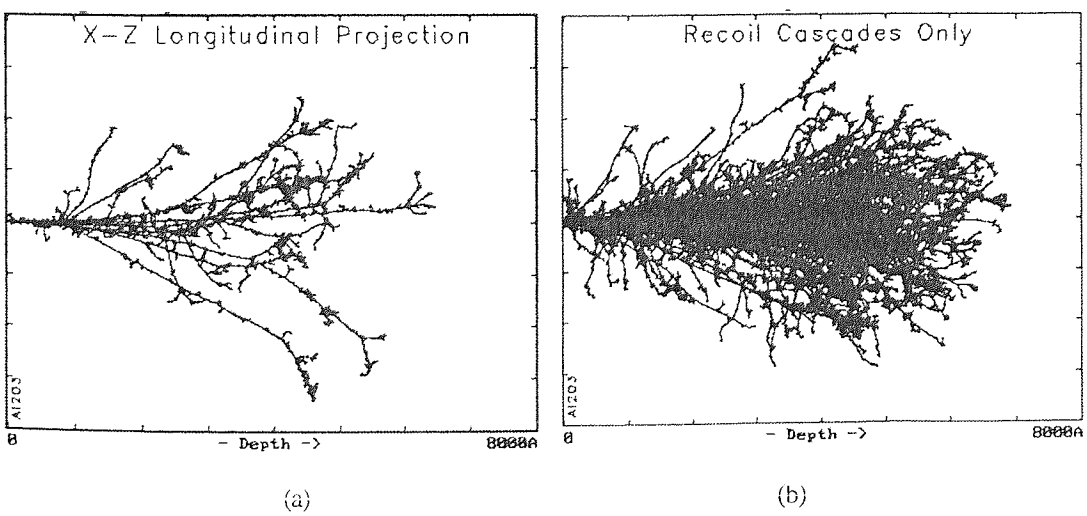

Fig. 3.4.2 Computed plots of longitudinal penetration of 1MeV Cr ions into Al_2O_3 substrate, modelled for (a) 10 and (b) 100 implanted Cr ions

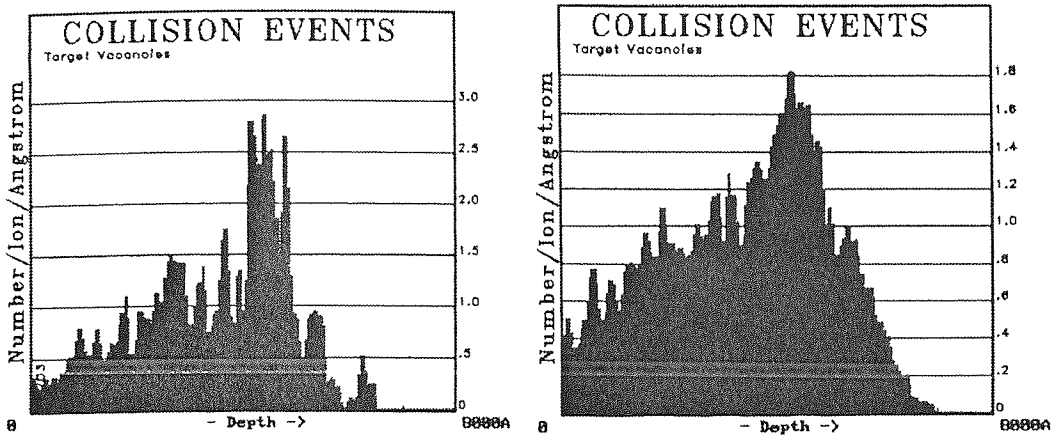

Fig. 3.4.3 Depth profiles of vacancy-production arising from implantation of 1MeV Cr ions into Al_2O_3 substrate, modelled for (a) 10 and (b) 100 implanted Cr ions

Significant micro-structural damage and amorphisation in Cr-implanted alumina has been reported by McHargue [205], for 300keV ion fluences exceeding $6x10^{17}$ Cr cm^{-2}; the above computations predicted a mean vacancy-yield of 6350 vacancies in the alumina per implanted chromium ion.

3.4.2 Implantation of B ions through TiN film A second surface treatment involved the application of a magnetron sputter-coated titanium nitride (TiN) thin-film onto the alumina specimen, followed by the implantation of boron (B) ions into the alumina, through the TiN film: Fig 3.4.4 illustrates this process.

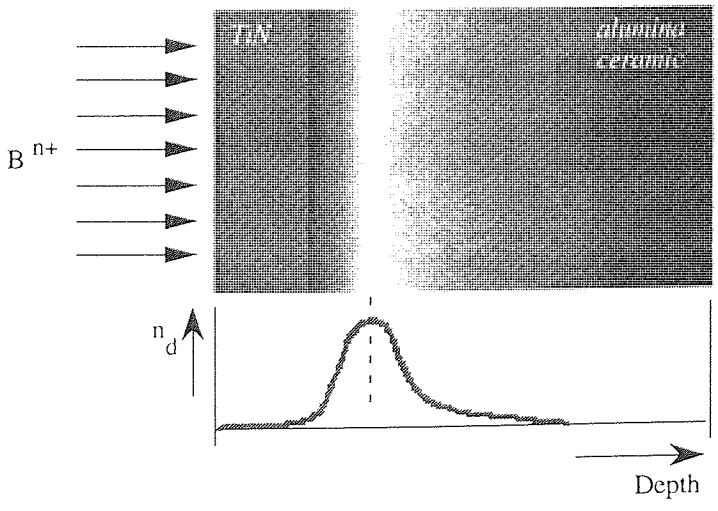

Fig. 3.4.4 Implantation of boron ions into alumina ceramic through a TiN film

The implanted semi-conducting layer of boron was thus protected by the TiN film, and the ion-energy was reduced to approximately 100keV for boron implantation into the alumina through a 2000Å TiN film. In addition, the implantation of light B ions (Z_B = 5 amu), at a low beam-energy, was less destructive to the TiN-coated alumina structure, with a notable decrease in the vacancies produced in the insulator sample. A mean yield of 470 vacancies in the TiN-coated alumina for each implanted boron ion was predicted by the ion-range computations shown in Figs 3.4.5 and 3.4.6.

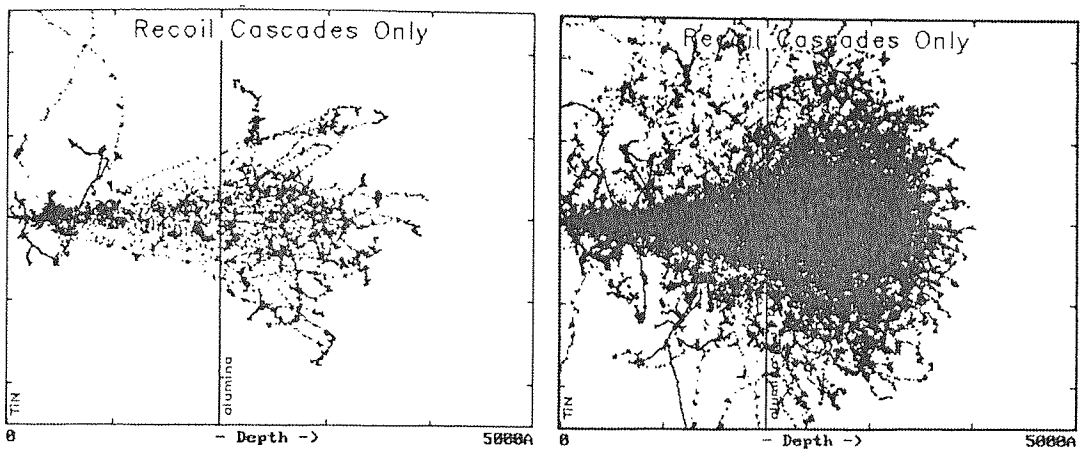

(a) (b)

Fig. 3.4.5 Computed plots of longitudinal penetration of 100keV B ions through 2000Å TiN film into Al_2O_3 substrate, modelled for (a) 50 and (b) 500 implanted B ions

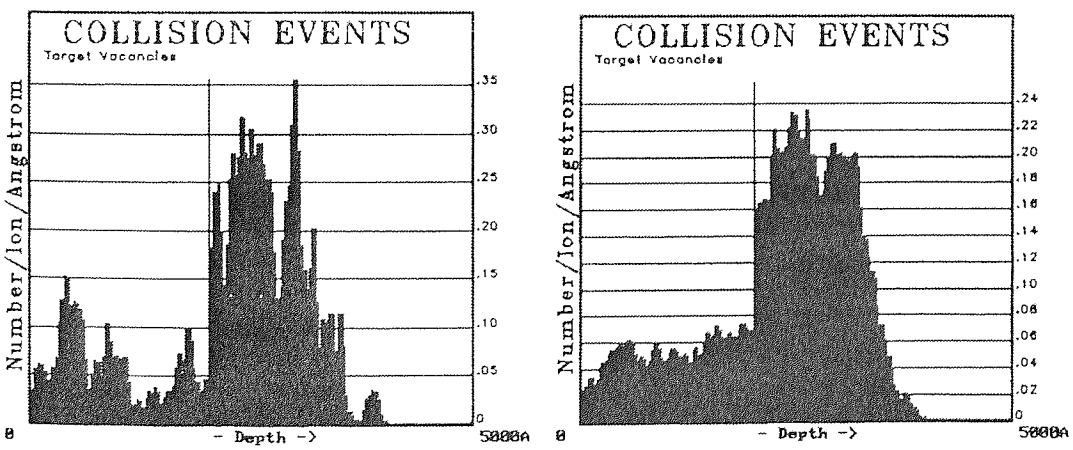

(a) (b)

Fig. 3.4.6 Depth profiles of vacancy-production arising from implantation of 100keV B ions through 2000Å TiN film into Al_2O_3 substrate, for (a) 50 and (b) 500 implanted ions

Analytical studies of both these implanted alumina modules, and the experimental specimens described in Section 3.1, are presented in Chapter 4. This chapter begins with a steady-state DC investigation in Section 4.1, which explores the electronic and optical characteristics of the alumina specimens in an ultra-high vacuum environment. Section 4.2 then goes on to investigate the pulsed-field breakdown and emission phenomena observed from the ceramic modules.

4. EXPERIMENTAL FINDINGS

In analysing the vacuum behaviour of a trigger ceramic, the findings of this experimental study present a steady-state DC characterisation of the prebreakdown electrical and optical phenomena recorded from an alumina insulator in vacuum. Section 4.2 goes on to describe the pulsed-field emission phenomena observed on an alumina dielectric. The material composition and surface-topography of the alumina insulator is analysed in Section 4.3, together with surface-analytical studies of emitted material associated with pulsed-field electrical breakdown of the alumina. This experimental evidence will then be drawn together in Chapter 5, and discussed in relation to the ignition of a triggered vacuum gap by the surface-flashover of a solid-insulator.

4.1 Experimental findings I - DC characterisation

A key objective of this study was to record the DC prebreakdown electrical-characteristics of the alumina trigger specimen, with *concurrent* observation of the optical processes associated with the insulator. To facilitate this, a transparent anode technique was employed to determine the spatial origin of any electron-emission from the alumina module. For clarity of presentation, observations of these two- and three-electrode electro-optical phenomena will be presented separately, although later discussion will draw upon both sets of findings.

4.1.1 DC Prebreakdown electrical characteristics and optical imaging

4.1.1.1 Electro-optical observations of metallized alumina specimens After mounting the specimen module and evacuating the system, a positive DC voltage, V_t, was slowly applied to the inner electrode-ring of the specimen up to a maximum amplitude of +5kV. With the outer electrode-ring grounded, corresponding values of DC prebreakdown current, I_t, were measured using an electrometer picoammeter (see Section 3.2.4.1 for details of the experimental set-up). Optical emission phenomena were observed chiefly (i) on the (metallized) end-face of the electrode modules, and (ii) in a minority of specimens on the cylindrical outer-diameter of the alumina module.

(i) Optical phenomena on end-face of alumina module At an applied voltage of +2.5kV, a ruby-red glow was initiated in the alumina region between the ring-electrodes. Raising V_t beyond 2.5kV caused the intensity of this glow to increase, appearing as a bright annulus, and red/pink in colour to the naked eye: it was thus

termed a "doughnut" discharge. When V_t reached +4kV, several bright-blue 'spots' were simultaneously observed in the alumina gap near to the inner ring-electrode.

The measured electrical I_t-V_t characteristics of the alumina specimen are given in Fig 4.1.1, together with images of the optical events at the end-face of the alumina sample corresponding to applied DC voltages of +2.5kV and +4kV (labelled *image A* and *image B* respectively). Note that the images presented in Figs 4.1.1(b) and (c) only portray photon-emission from optical events associated with the alumina module, with no additional illumination used in the analytical system.

Holding V_t at a steady value of +5kV, the deep-red 'doughnut' emission was observed for a further 30 minutes. During this time the intensity of the doughnut was seen to diminish, and at the end of the 30-minute period the doughnut was no longer visible, although the bright-blue spots persisted. A second I-V characteristic was recorded from the specimen module after this 30-minute period under DC voltage-stress: the form of this 'aged' I-V plot, depicted in Fig 4.1.1 (a), shows a near-linear planar I-V characteristic for the electrode specimen, with an increase in measured DC prebreakdown current following the 30-minute period.

Application of a negative DC voltage to the inner ring electrode, i.e. polarity reversal of the planar field between the inner and outer electrode rings, produced only a slight modification of the shape of the planar I-V characteristic of the electrode module; the planar current magnitude remained largely unaffected by planar voltage polarity.

Image-processing techniques were subsequently used to quantify the spatial intensity distribution of the 'doughnut' and the bright-blue spots. Thus, processing the image shown in Fig 4.1.1(c) (Image B) produced radial line-scans through the doughnut and through a spot, as illustrated in Fig 4.1.2. This spatial light-intensity data showed that the doughnut emission was most intense in the vicinity of the (positive) inner electrode-ring, whereas the bright-blue spot appeared brightest in the region equidistant between the two electrode-rings.

LIBRARY AND INFORMATION SERVICES

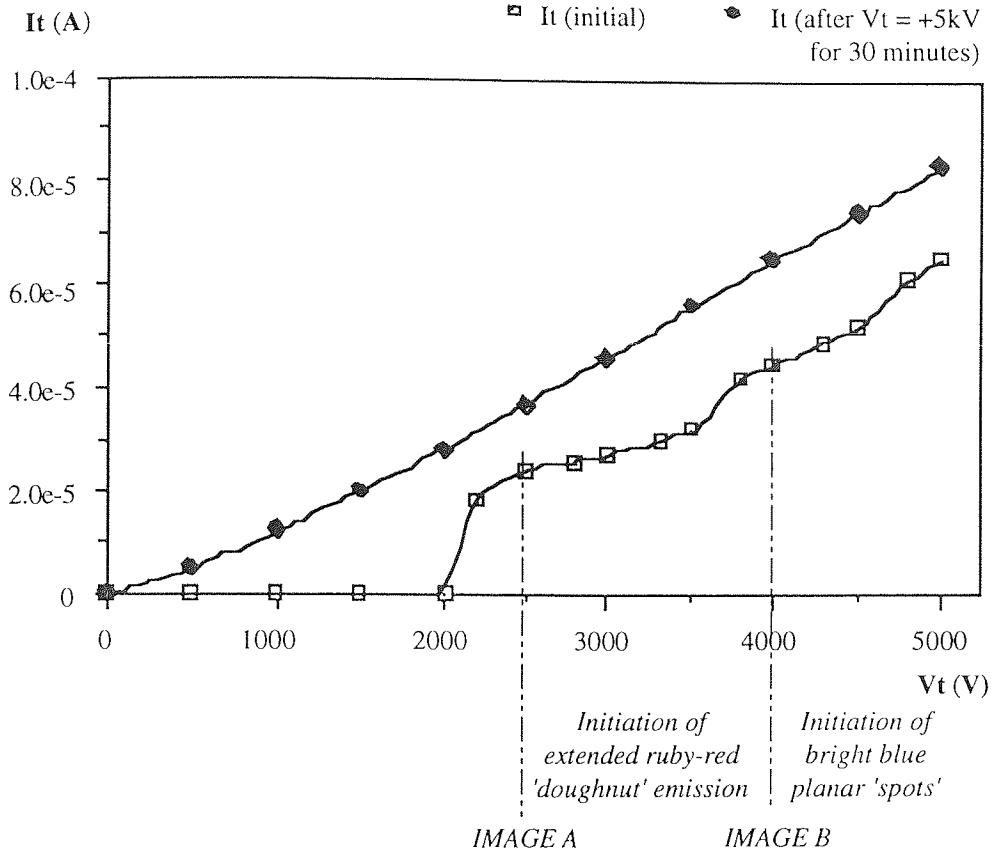

(a)

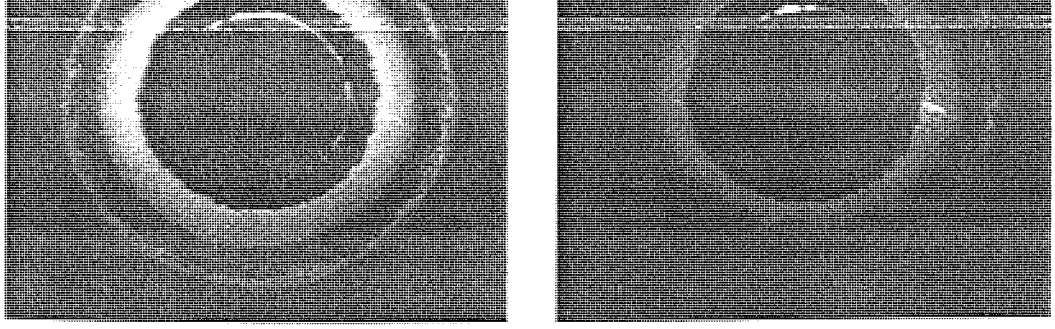

(b) *Image A*

(c) *Image B*

Fig. 4.1.1 (a) I-V characteristics of planar DC prebreakdown, recorded from i) initial measurements, and ii) following 30 minute exposure of the alumina module to +5kV. Corresponding images of (b) 'doughnut' emission (V_t = +2.5kV: *Image A*), and (c) localised bright-blue 'spots' (V_t = +4kV: *Image B*) from the 300μm wide alumina region

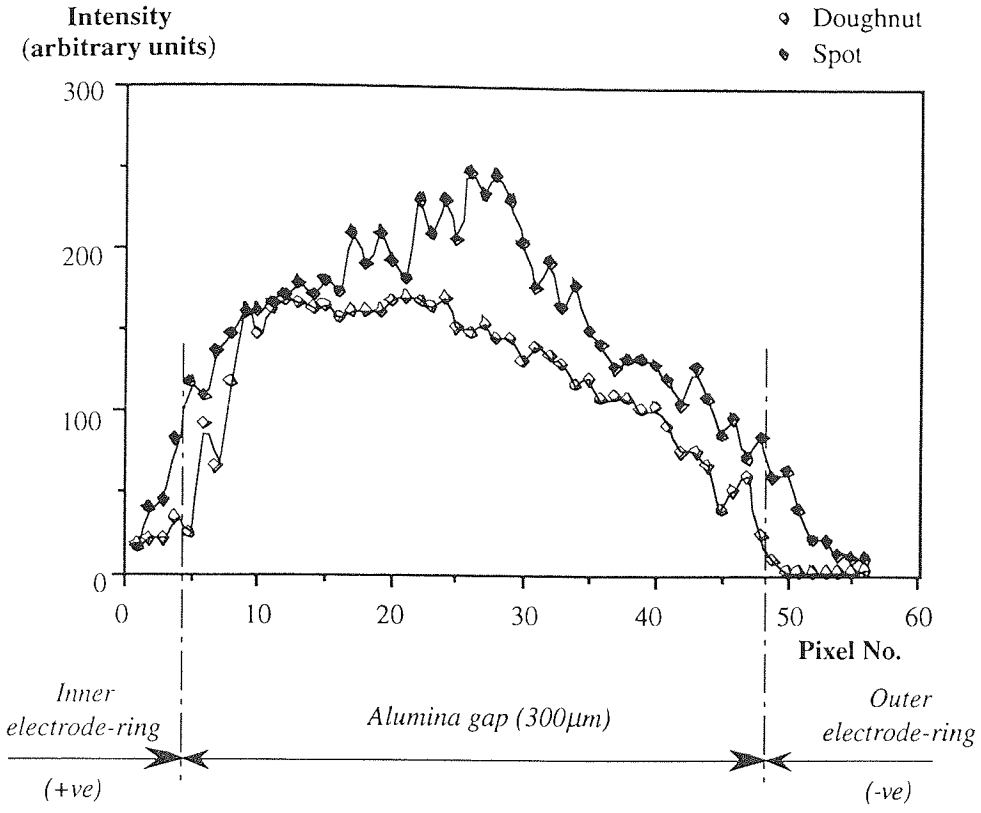

Fig. 4.1.2 Line-scans of pixel-intensity through the doughnut and bright-blue spot regions of Image B {Fig 4.1.1(c)}

(ii) Optical phenomena on outer-diameter of alumina module With applied DC voltages (V_t) of up to +8kV, some alumina modules were found not to emit any visible light from the metallized end-face of the ceramic. The DC prebreakdown currents (I_t) measured through these specimens were substantially smaller than those of typical alumina modules (see Fig 4.1.1(a)): Fig 4.1.3(a) plots the I_t-V_t characteristic of such a "dark" alumina module.

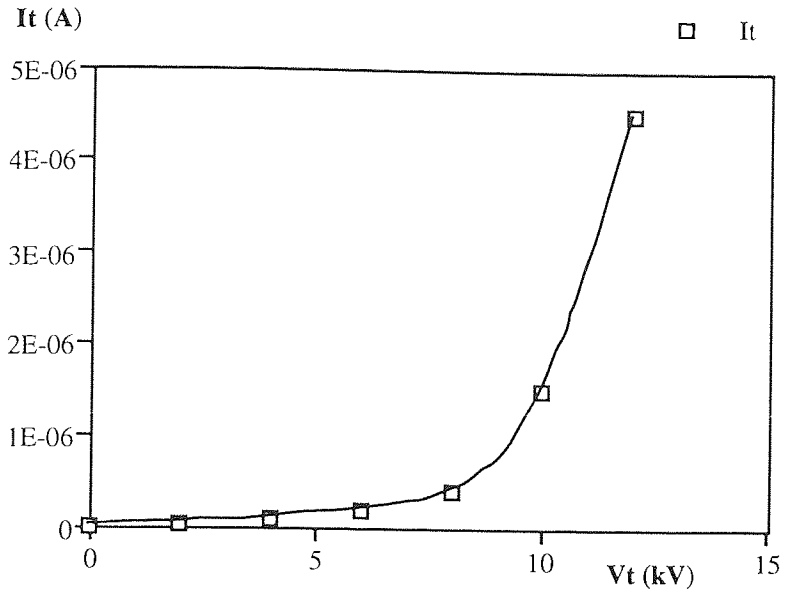

(a)

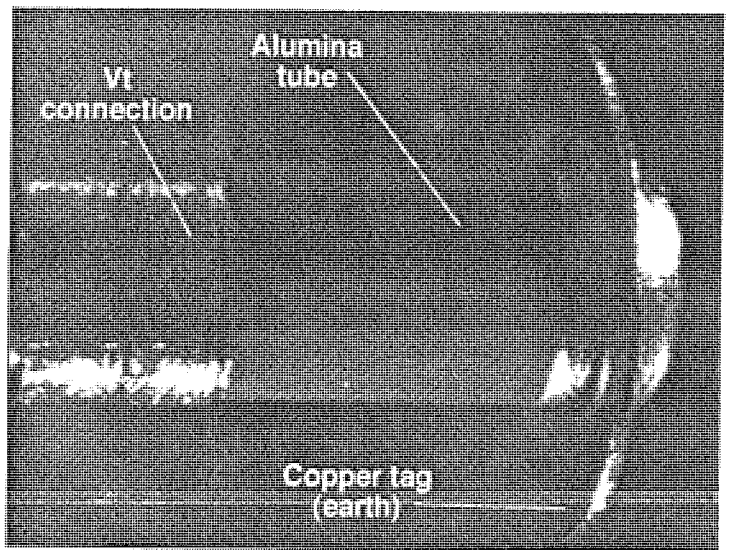

(b)

Fig. 4.1.3 (a) DC prebreakdown I-V characteristic of (b) 'dark' alumina module

As V_t was slowly increased to +10kV, luminosity was observed on the outer-diameter of the alumina module, i.e. viewing the side of the alumina ceramic tube, as shown in Fig 4.1.3(b). This luminosity was seen to consist of two regions: (i) discrete bright-blue 'spots' in the ceramic region close to the copper-tag cathode, and (ii) an extended red/pink glow through the length of the alumina tube, which appeared most intense in the ceramic region near the anode (V_t) connection. Figure 4.1.4(a) shows the typical form of this luminosity observed along the alumina tube, whilst Fig 4.1.4(b) plots the intensity of the luminosity along a line-scan through the luminous regions from the anode to the cathode.

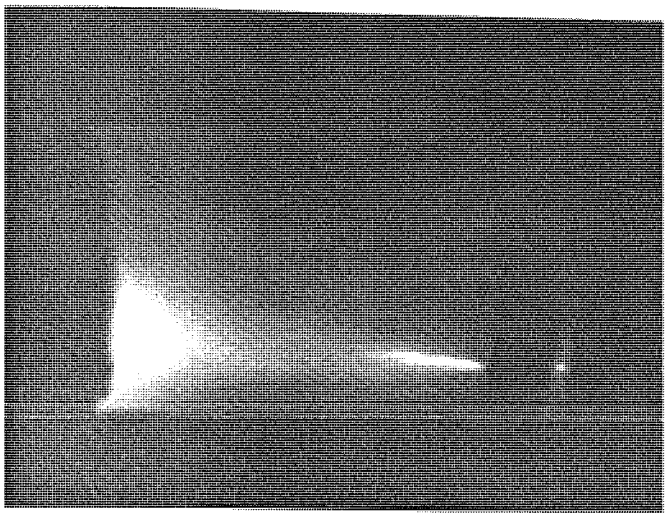

(a)

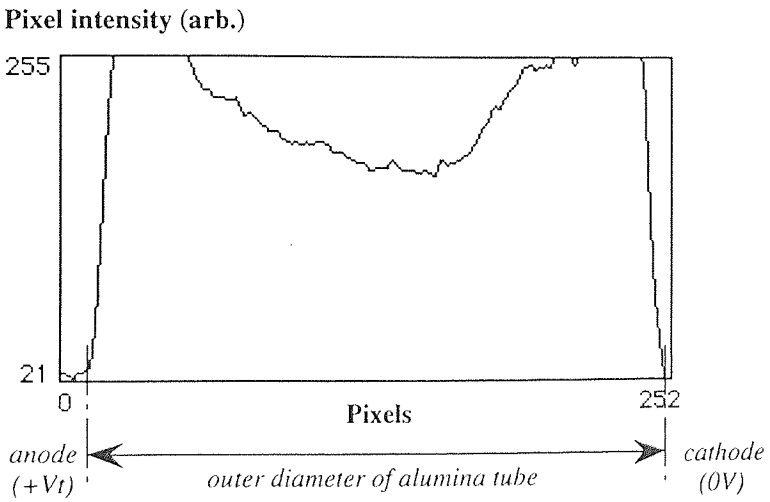

(b)

Fig. 4.1.4 (a) DC prebreakdown optical emission along the alumina cylinder (V_t = +10kV, I_t = 1.5μA), and (b) pixel-intensity line-scan through the cathode and anode luminosity regions

4.1.1.2 Electro-optical observations of 'bulk' dielectric alumina modules 'Bulk' electrode samples were operated under ultra-high vacuum of $2x10^{-8}$ Torr, following a 2-hour baking cycle at 400°C. The experimental system is described in Section 3.2.4.1, with images of optical phenomena on the end-face of the sample (Fig 4.1.5(a)) captured using a high-resolution monochrome CCD camera. Figure 4.1.5 presents images recorded for positive- and negative-polarity of applied DC voltage (V_t) at the inner-wall electrode:

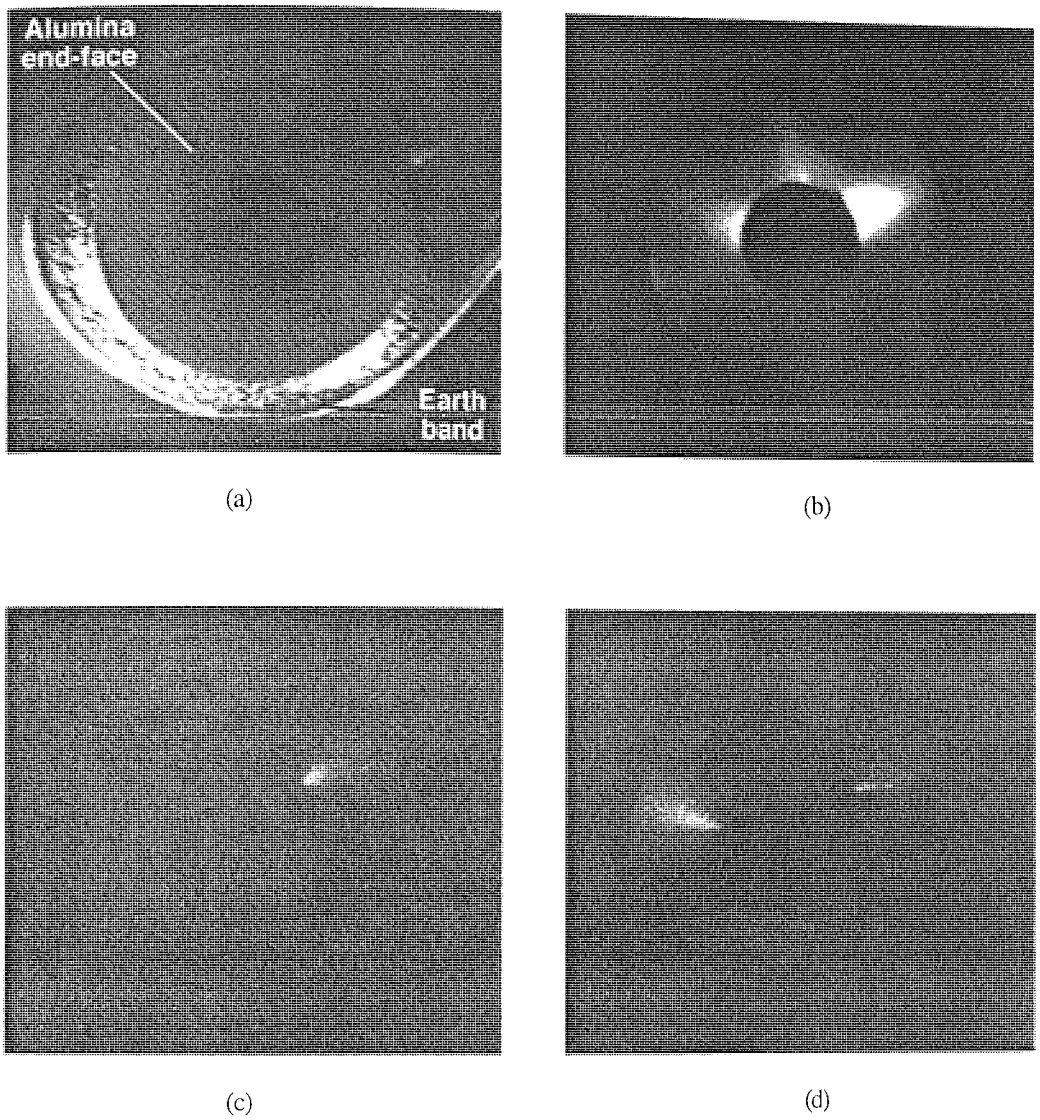

Fig. 4.1.5 Images of (a) specimen outline, and optical events recorded for (b) a positive inner-electrode voltage (V_t) of +4kV (I_t = 1.2μA), and (c), (d) a negative inner-electrode voltage (V_t) of -4.5kV ($I_t = 3.8 \times 10^{-7}$A)

Optical events were first observed at an inner electrode voltage, V_t, of 2.5kV, with stable emissions visible at voltages between 4kV and 5kV. Luminescence was observed within the bulk of the insulator, shown in Figs 4.1.5 (b), (c) and (d), and appeared ruby-red in colour: this luminosity was consistent with the 'doughnut' discharges observed on metallized alumina modules having ring-electrodes, described in Section 4.1.1.1.

With a positive DC voltage ($+V_t$) applied to the centre-conductor of the bulk module, 'fan-tail' shaped regions of luminosity were observed on the alumina ceramic (Fig 4.1.5(b)); the apex of each 'fan-tail' was situated in the ceramic region close to the outer (cathode) electrode. For a negative DC bias ($-V_t$), similar 'fan-tails' of luminescence were observed on the ceramic, with each 'fan-tail'

having its apex close to the inner (negative) electrode. Planar (I_t-V_t) prebreakdown characteristics were recorded concurrently with these optical observations, for positive and negative voltage-polarities, and are shown in Fig 4.1.6.

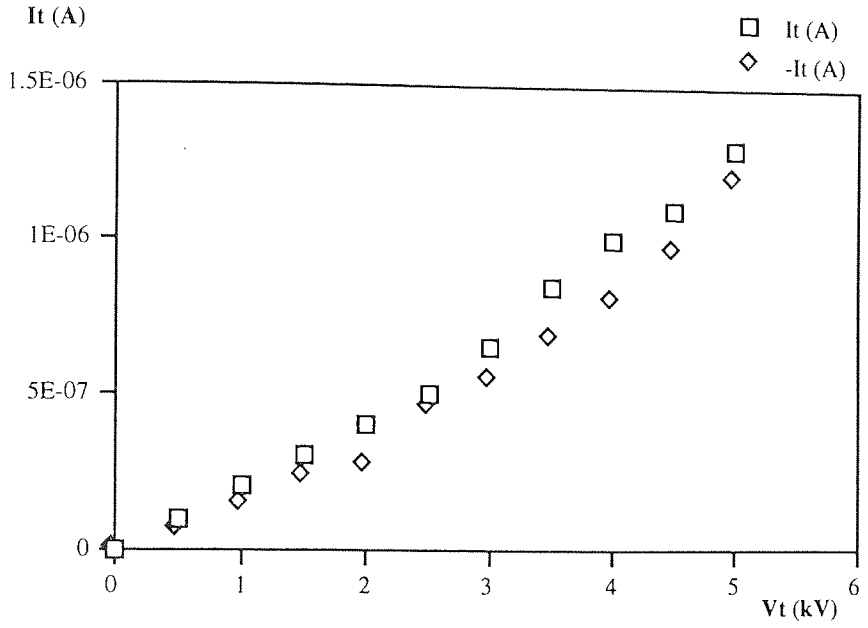

Fig. 4.1.6 'Bulk' specimen planar I-V characteristics (positive and negative voltage-polarities)

4.1.1.3 Electro-optical observations of ion-implanted alumina modules Metallized alumina modules, implanted with chromium ions at discrete dosage rates in the range 10^{16} to 10^{18} Cr cm^{-2}, were subjected to DC electrical fields within the analytical vacuum system described in Section 3.2.4.1. As the applied DC voltage, V_t, approached +3kV, the measured prebreakdown current I_t was observed to rise at an increased rate, as shown in the current-voltage plot of Fig 4.1.7(a). Concurrent with this 'turn-on' of the measured current was the initiation of bright-blue spots within the 300µm-wide alumina gap, as observed previously in plain alumina modules at V_t values exceeding 4kV (see Section 4.1.1.1). A corresponding image of these 'spots' is given in Fig 4.1.7(b).

Evaluation of further implanted alumina modules produced similar electrical and optical characteristics to those shown in Fig 4.1.7. Differing implantation dosages of Cr in the modules, and the application of negative voltage bias (-V_t) were not observed to influence these DC prebreakdown characteristics.

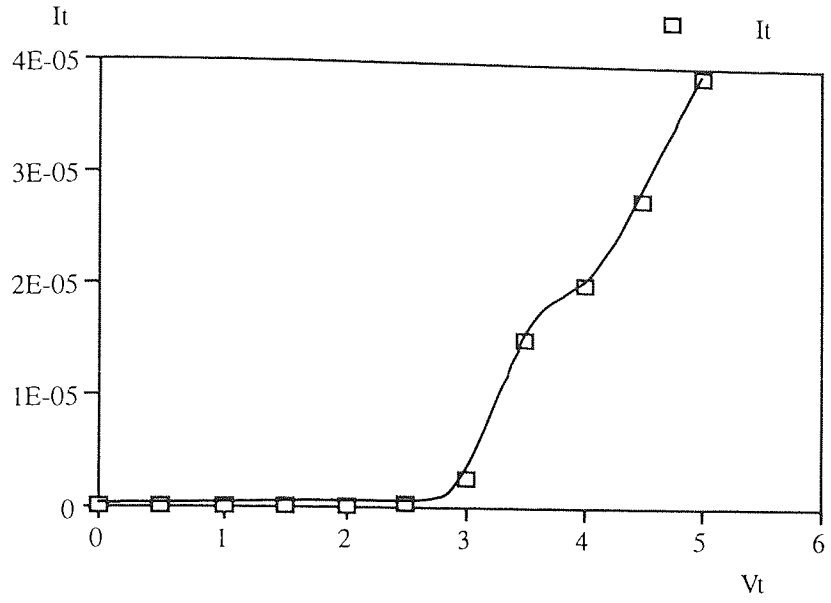

(a)

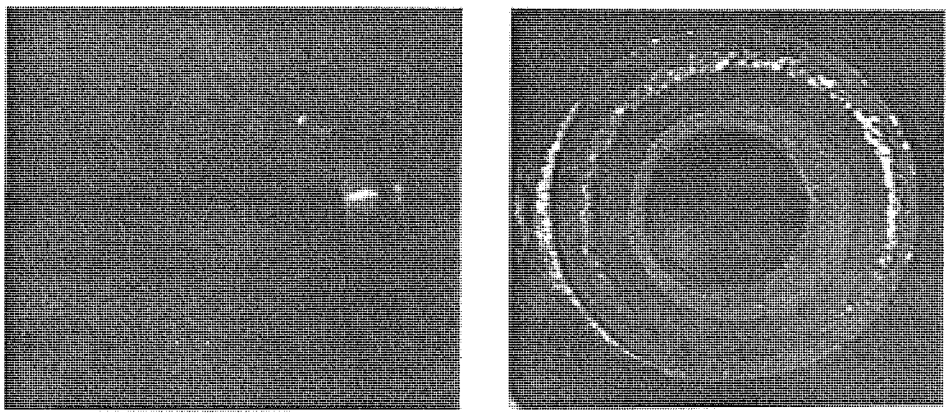

(b) (c)

Fig. 4.1.7 (a) Planar V_t-I_t characteristics, with associated (b) planar spots on (c) metallized end-face of Cr-implanted alumina module

Application of DC electrical fields to boron-implanted, TiN-coated modules caused a large ohmic current flow, with no optical events visible on the front-face or along the side of the modules. With a metallic Ti layer over the front-face of the alumina module, a measured module resistance of a few ohms indicated a gross non-stoichiometry in the TiN film.

4.1.2 Spectral nature of DC prebreakdown photon emission In order to quantify the nature of the luminosity observed in the alumina modules, spectrometric studies of the DC prebreakdown photon-emission phenomena were undertaken.

4.1.2.1 High-speed optical spectrometry The light emitted from the alumina specimen was focused through a lens fixture into a glass fibre-optic light-guide. This was in turn connected to the input of a high-speed scanning monochromator, with 180μm input slits limiting the spectral wavelength-resolution of the instrument to 5nm. Two-hundred spectral scans were made over the wavelength-range 3000Å to 8500Å, each scan having 80ms duration, and the average of these readings recorded. V_t was subsequently increased to +10kV, and a second optical spectrum recorded. The spectral data recorded for V_t values of +8kV and +10kV are presented in Fig 4.1.8. Significantly, similar forms of luminosity spectra have been recorded for alumina by other workers [21,45].

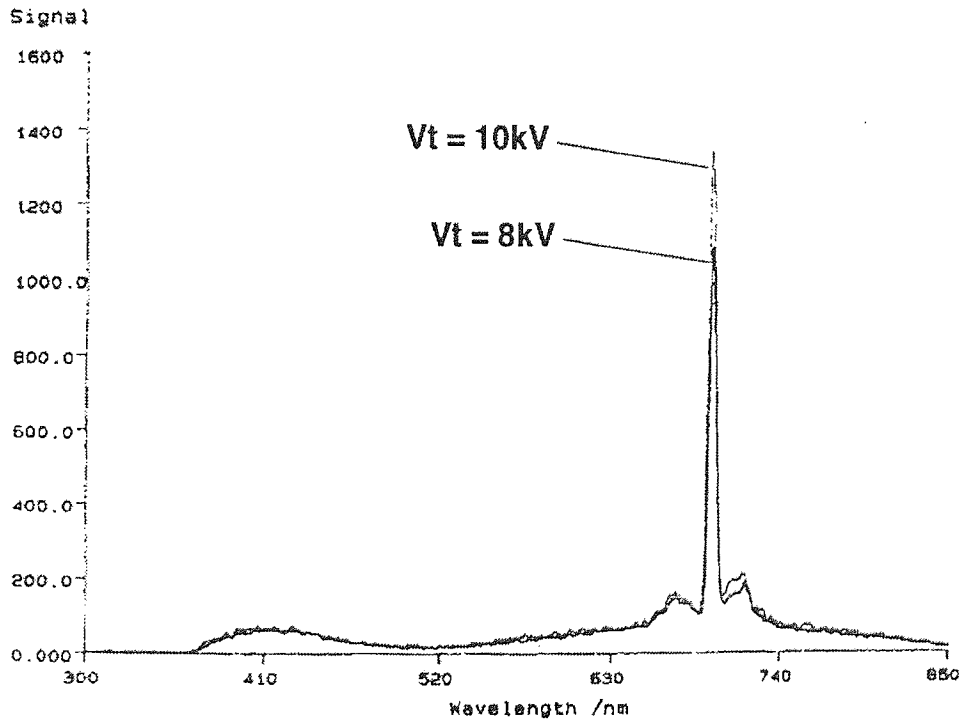

Fig. 4.1.8 Optical spectrum of 'doughnut' and localised 'spot' emission observed on the end-face of the alumina specimen, for applied voltages (V_t) of +8kV and +10kV (200 spectral scans (averaged), 5nm half-power bandwidth)

This spectrum is characterised by (a) a broad band of emission around 410nm, with a short-wavelength cut-off at 380nm arising from the glass materials of the UHV viewport and the fibre-optic light-guide, and (b) a major emission-peak at 694nm, with weak emission-peaks at 672nm and 715nm. Increasing the value of V_t from +8kV to +10kV led to an increase in the intensity of the light emitted from the sample, although the wavelength characteristics of the spectrum remained

unchanged. A noticeable intensification was seen in the deep-red emission-peaks around 694nm.

4.1.2.2 High-resolution optical spectrometry Following a 24-hour rest period, +5kV DC was slowly applied to the inner electrode-ring of the alumina specimen. An I_t-V_t characteristic was recorded, similar to the 'aged' I-V plot depicted in Fig 4.1.1(a), and showing a near-linear form. Increased prebreakdown current magnitudes were recorded, by comparison with those of the initial test outlined in section 4.1.1. As V_t was increased, localised blue 'spots' were once more seen to 'switch-on' in the 300µm alumina gap near to the inner electrode-ring, but the ruby-red 'doughnut' emission was not observed. V_t was subsequently increased slowly from +5kV to +8kV, and the 'doughnut' emission was re-established.

The light emitted from the alumina specimen was then focused through a fused-quartz lens-fixture into a fused-quartz fibre-optic light-guide, which was in turn connected to the input of a high-speed scanning monochromator. In this arrangement, 0.833µm slits at the monochromator input limited the spectral resolution of the instrument to a half-power bandwidth (HPBW) of 0.8nm. Two-hundred spectral scans were made over the wavelength-range 2000Å to 7000Å, each scan having a time-duration of 1s. and the average of these readings recorded: the spectral data recorded for a V_t value of +8kV are presented in Fig 4.1.9.

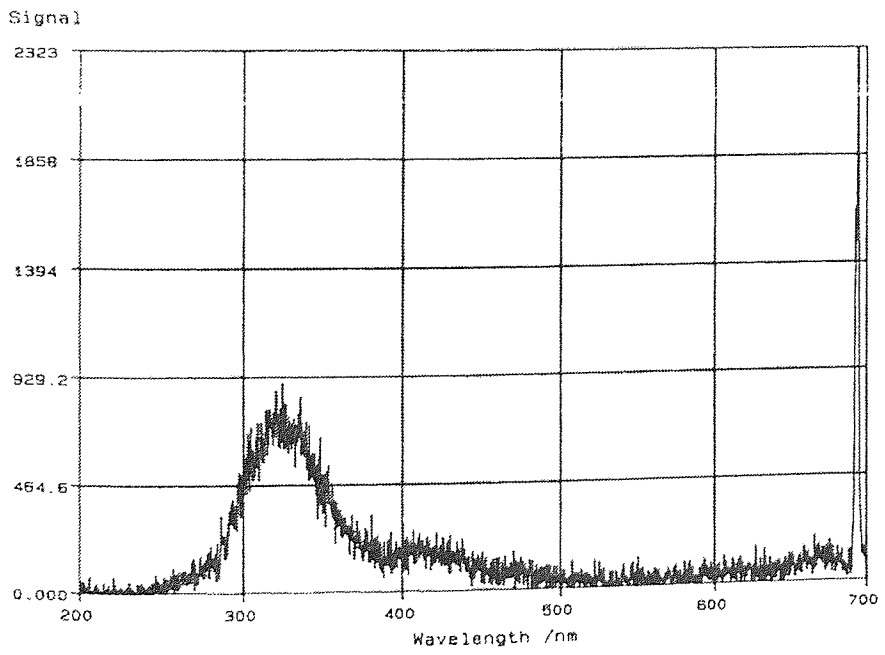

Fig. 4.1.9 Optical spectrum of 'doughnut' and localised 'spot' emission, for applied voltage (V_t) of +8kV (200 spectral scans (averaged), 5nm HPBW)

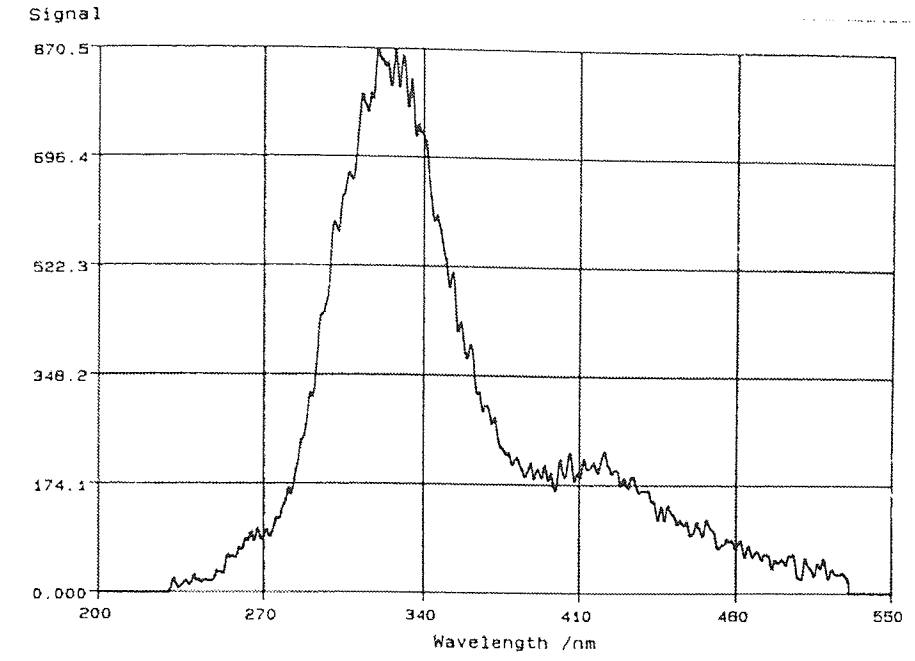

(a)

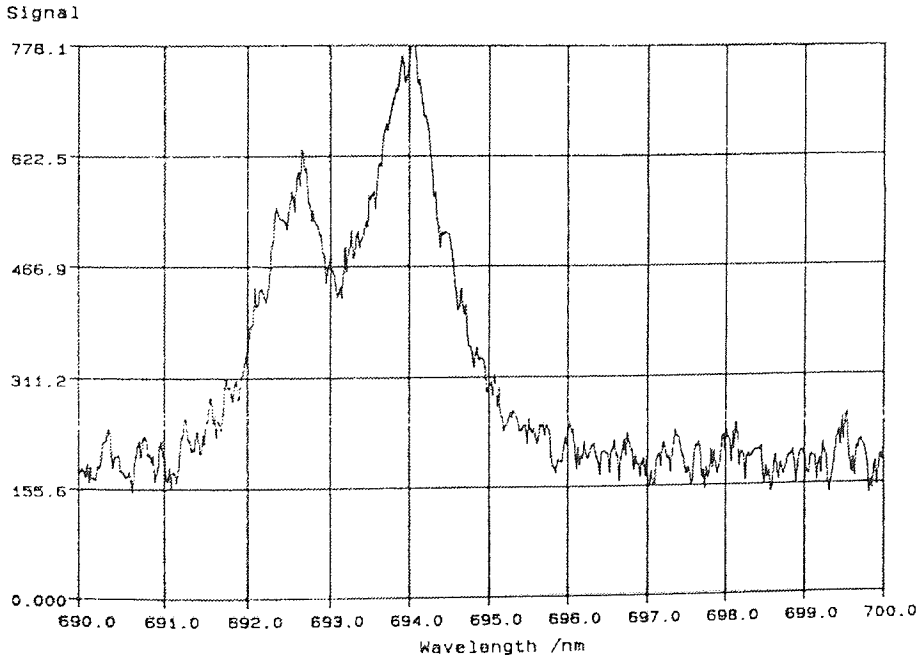

(b)

Fig. 4.1.10 Spectral expansions of (a) UV / blue region, and (b) deep-red emission peak (1300 spectral-scans, 0.3nm HPBW)

Two broad bands of emission were observed around 3250Å and 4100Å, with a short-wavelength cut-off at 2200Å arising from the fused-quartz materials of the UHV viewport and the fibre-optic light-guide. Figure 4.1.10(a) presents an expanded spectral-plot of these two short-wavelength bands, and reveals a strong emission-peak could be seen at 6935Å, with weak emission-peaks at 6700Å and

7150Å. A series of 1300 spectral-scans were then made over the interval 6900Å to 7000Å, with the monochromator input slits narrowed to give a finer wavelength-resolution of 0.3nm HPBW. Figure 4.1.10(b) illustrates a measured doublet of two closely-spaced spectral lines of 6926Å and 6940Å wavelengths, resolved from the previous emission-peak of 6935Å shown in Figs 4.1.8 and 4.1.9.

In order to investigate the effects of a low-pressure gas ambient upon the prebreakdown behaviour of the alumina insulator, argon (Ar) gas was bled into the vacuum system. V_t was slowly applied to the alumina specimen over the voltage range $0 \leq V_t \leq 10$kV and system pressures of 10^{-6}, 10^{-5} and 10^{-4} mBar. Compared with earlier specimen operation under $<10^{-8}$ mBar (ultra-high) vacuum, no change was detected in the observed phenomena, neither in the electrical characteristics nor in the optical signature of the alumina specimen at each of these pressures.

Continued application of a DC voltage (V_t) of +8kV to the inner electrode-ring of the sample, under vacuum, led to an eventual dimming of the doughnut emission after a period of four hours. However, the bright-blue spots persisted for a further two hours before they were no longer visible; the measured I_t-V_t characteristics of the alumina specimen remained unchanged.

4.1.3 DC prebreakdown electron emission

4.1.3.1 Transverse prebreakdown electrical characteristics Following the planar characterisation of the electrode specimen, the transparent anode described in Section 3.2.1 was introduced into the electrode regime, and further measurements and observations were made with this more complex three-electrode arrangement. For the measurement of the transverse I-V characteristic depicted in Fig 4.1.11, (measured across the transverse gap between the transparent anode and the electrode module), the inner ring voltage was held at +3kV DC, with the outer electrode-ring grounded, giving a quiescent planar current of 30 μA. This planar condition was established since no measurable, stable transparent anode current (I_a) was found to flow (for transparent anode voltages less than +10kV) in the absence of an applied potential between the planar ring-electrodes; i.e. no measurable main gap current was found to flow at low transverse fields in the absence of a planar current.

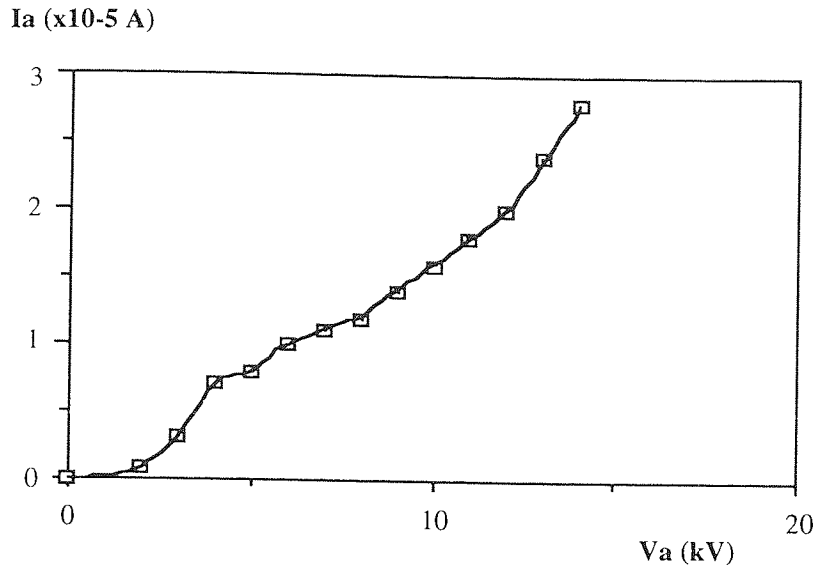

Fig. 4.1.11 Variation of transparent anode current (I_a) with transparent anode voltage (V_a); quiescent inner-ring voltage V_t = +3kV

The transparent anode voltage, V_a, was then fixed at +2.5kV, and the inner ring voltage, V_t, slowly varied from 0V to +5kV (outer electrode-ring grounded), and the corresponding values of main gap current, I_a, were recorded. This measurement was repeated for increasing discrete values of V_a, and a resulting set of transverse I_a-V_a characteristics are shown in Fig 4.1.12(a).

For transparent anode voltages (V_a) below 10kV, no transverse current was measured until the inner electrode-ring voltage (V_t) was in the range of 500V to 1kV DC. With zero potential applied to the inner ring (V_t=0), no main gap current was detected for V_a values typically below 10kV, and no optical events were observed on the transparent anode. However, the transparent anode current of 2.3×10^{-6}A (measured for zero inner-ring voltage) at a transparent anode voltage (V_a) of +10kV, corresponded to the formation of a cathode spot on the outer ring electrode. The estimated main gap field under this condition is 10MVm^{-1}.

Finally, the inner electrode-ring voltage, V_t, was again slowly varied, for discrete transparent anode voltages (V_a) of 0V, +5kV and +10kV. The variation in the planar current, I_t, was recorded, giving the set of planar I-V characteristics shown in Fig 4.1.12(b); this result showed a depletion of I_t as V_a was raised.

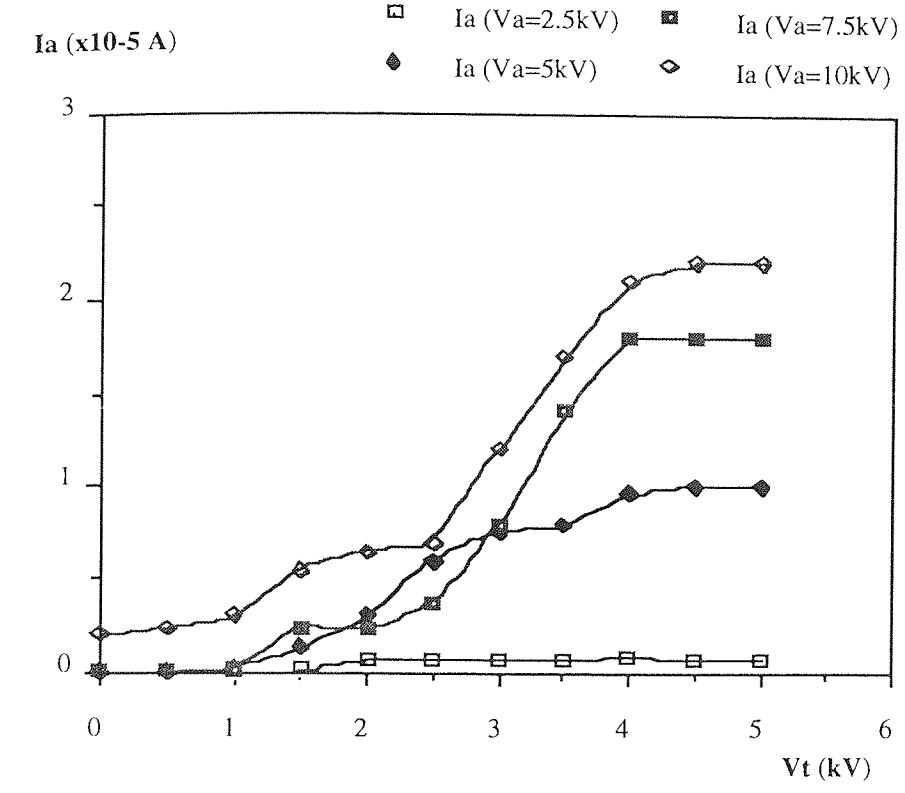

(a)

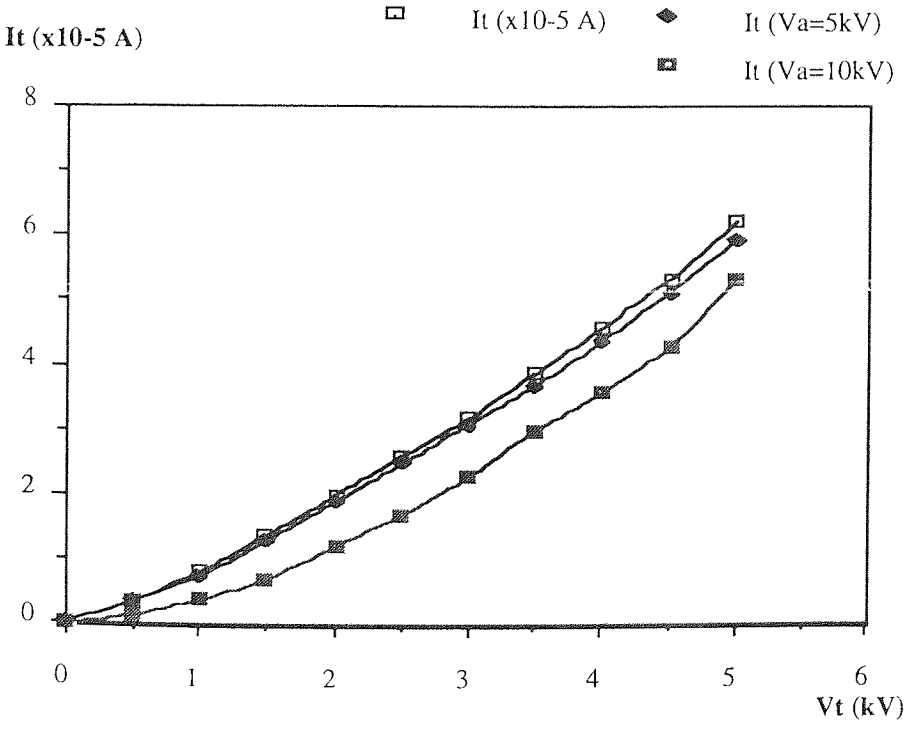

(b)

Fig. 4.1.12 (a) Transverse behaviour of transparent anode current, I_a, with inner ring voltage, V_t, for transparent-anode voltages $\{V_a\}$ of +2.5kV, +5kV, +7.5kV and +10kV, and (b) associated planar I-V characteristics, showing the variation of inner electrode-ring current, I_t, with planar voltage, V_t, for transparent anode voltages $\{V_a\}$ of 0V, +5kV and +10kV

4.1.3.2 Transverse electro-optical phenomena With the transparent anode mounted in the analytical system, and the electrode-module inner-ring DC voltage (V_t) set at +3kV, the image depicted in Fig 4.1.13(a) was observed through viewport **1** (see Fig 3.2.7):

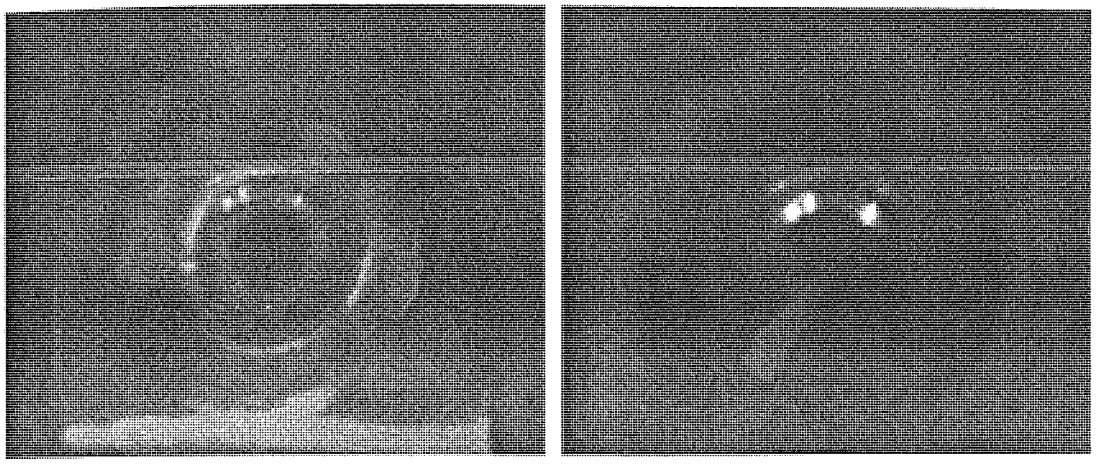

(a) (b)

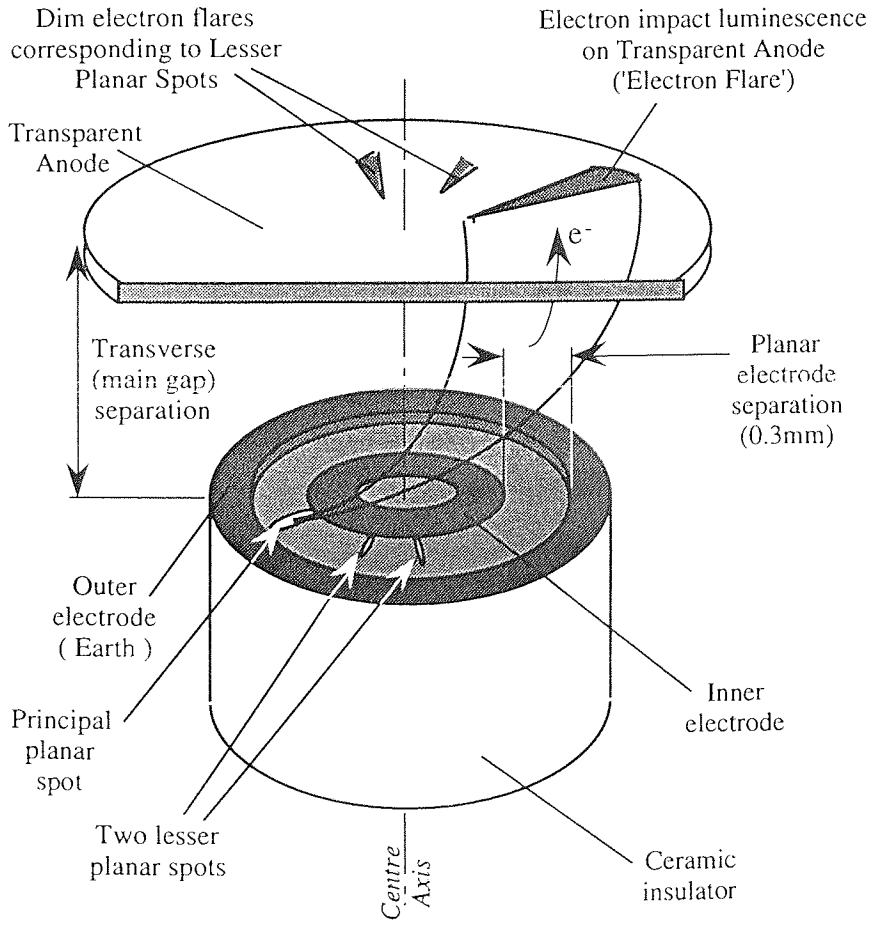

(c)

Fig. 4.1.13 Prebreakdown images for the three-electrode arrangement, with planar voltage only (V_t = +3kV), and (b) with application of transverse voltage (V_t = +3kV, V_a = +7kV); (c) schematic representation of three-electrode prebreakdown image

As described for a previous experimental specimen module in Section 4.1.1, an extended deep-red glow ('doughnut') was seen in the alumina gap of the electrode-module, accompanied by three discrete bright-blue 'spots'. A positive DC voltage, V_a, was then slowly applied to the transparent anode, where a main gap voltage (V_a) of +7kV DC and 10 μA main gap current (I_a) gave the image shown in Fig 4.1.13(b). Again, bright-blue 'spots' were clearly visible within the 300μm alumina gap between the ring-electrodes, but they were now accompanied by luminous 'flares' visible on the transparent anode as a result of impacting electrons.

Referring to Fig 4.1.13(c), the planar spots in the alumina gap appeared to be the 'roots' of this electron emission. With reference to both Figs 4.1.13 (b) and (c), the 'electron flare' images on the transparent anode were observed to be radially opposite the planar spots, and the initiations of these two phenomena were coincident in time. Increasing the main gap voltage beyond 7kV to 10kV caused the electron flare image to intensify, and at the same time these flares appeared to migrate towards the centre-axis of the electrode-insulator structure.

After a period of time, typically 1 to $1^1/_2$ hours, the bright blue spots which were visible in the ceramic gap disappeared. When these spots expired, the transverse current (I_a) collapsed by three orders of magnitude, the electron flare image on the transparent anode disappeared: at this stage the testing was concluded. However, the planar current appeared unaffected by this change in optical events. In addition, it follows that these planar-spot processes are believed to give rise to the transverse I-V characteristics of Section 4.1.1.

4.1.3.3 Desorbed gas analysis Using the residual gas analyser (RGA) of the analytical vacuum system described in Section 3.2.1, a definite change in the gas background was measured when a *planar* potential, V_t, was applied between the ring-electrodes of the alumina module, and optical events were observed within the 300μm alumina gap (see Figs 4.1.1 and 4.1.13). The residual gas background detected during this planar prebreakdown activity of the electrode specimen is shown in Table 4.1.

With the application of only a transverse field, with V_a<10kV, and in the absence of any planar field (both inner and outer ring-electrodes grounded), there was no detected change in the residual gas background.

As a matter of procedure, the RGA and vacuum ion gauge were switched off whilst electrode current measurements or observed phenomena were recorded: this

precaution avoided the recording of any electronic interference from the RGA or ion gauge filaments with the electrode specimen within the vacuum chamber. As a matter of experimental procedure, electrical measurements were therefore not recorded whilst residual gas or vacuum measurements were made, and vice versa.

Mass (amu)	2	14	16	28	32
Amplitude	25	12	5	100	20
Species	H_2	N	O	N_2	O_2

Table 4.1 Residual gas background during planar prebreakdown

4.1.3.4 Electro-optical observations of confined alumina modules 'Confined' alumina modules, of the type described in Section 3.1.2, were analysed under DC electrical fields in the analytical vacuum system shown in Fig 3.2.4. For clarity, Fig 4.1.14 describes the fixture of the confined module behind a transparent anode electrode:

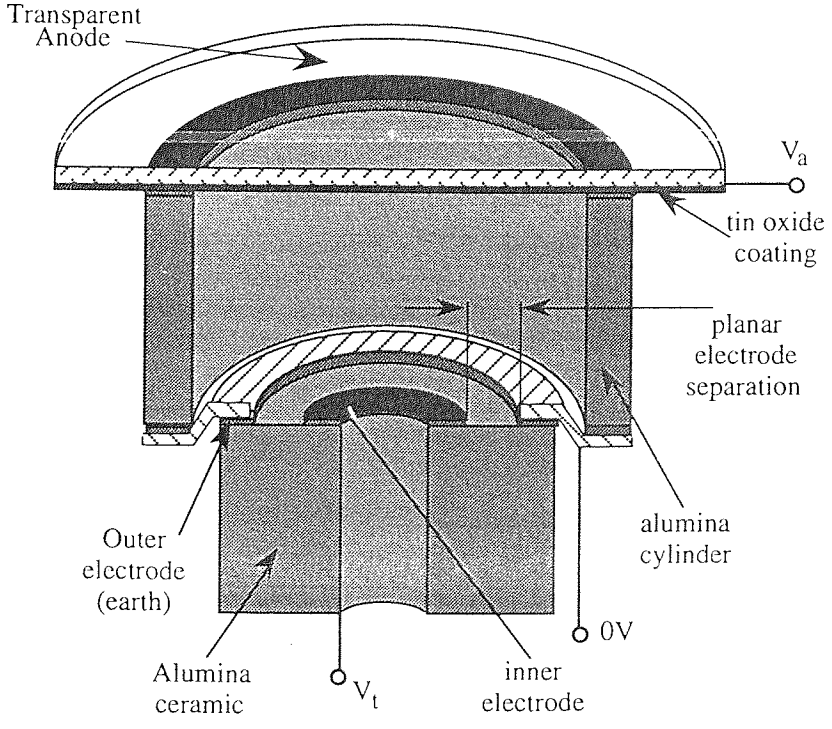

Fig. 4.1.14 Schematic illustration of the confined module structure

The transparent anode was fixed in butt-contact with the opposite end of the ceramic cylinder. A slight anti-parallelism was allowed between the ceramic tube and the glass, so as to leave a small slit at this junction, and allow effective pumping of the internal volume of the confined electrode module.

The slow application of a *transverse* DC voltage, Va, to the transparent anode, gave rise to the measured main-gap currents (Ia) displayed in Fig 4.1.15. This measurement was then repeated at fixed values of *planar* voltage, V_t, applied to the inner-ring electrode of the alumina module. Application of the planar voltage (V_t) across the 300μm alumina region of the module resulted in a measured enhancement of the transverse (main-gap) current, I_a, measured through the transparent anode.

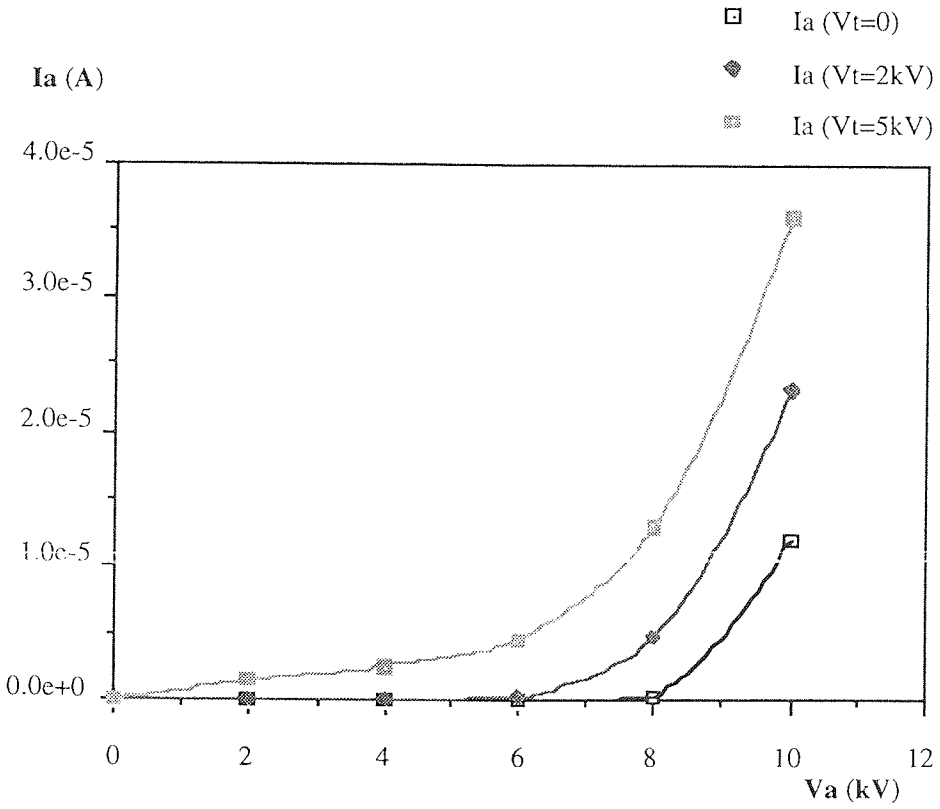

Fig. 4.1.15 Transverse I_a-V_a characteristic of confined main-gap, for a range of fixed planar voltage (V_t) values

Figure 4.1.16 records the DC prebreakdown characteristics associated with the 300μm alumina region of the specimen module. The form of these V_t-I_t characteristics was similar to those recorded for conventional metallized alumina modules in Section 4.1.1.1. The planar DC characteristics appeared to be unaffected by the subsequent application of transverse voltages (V_a) across the ceramic cylinder.

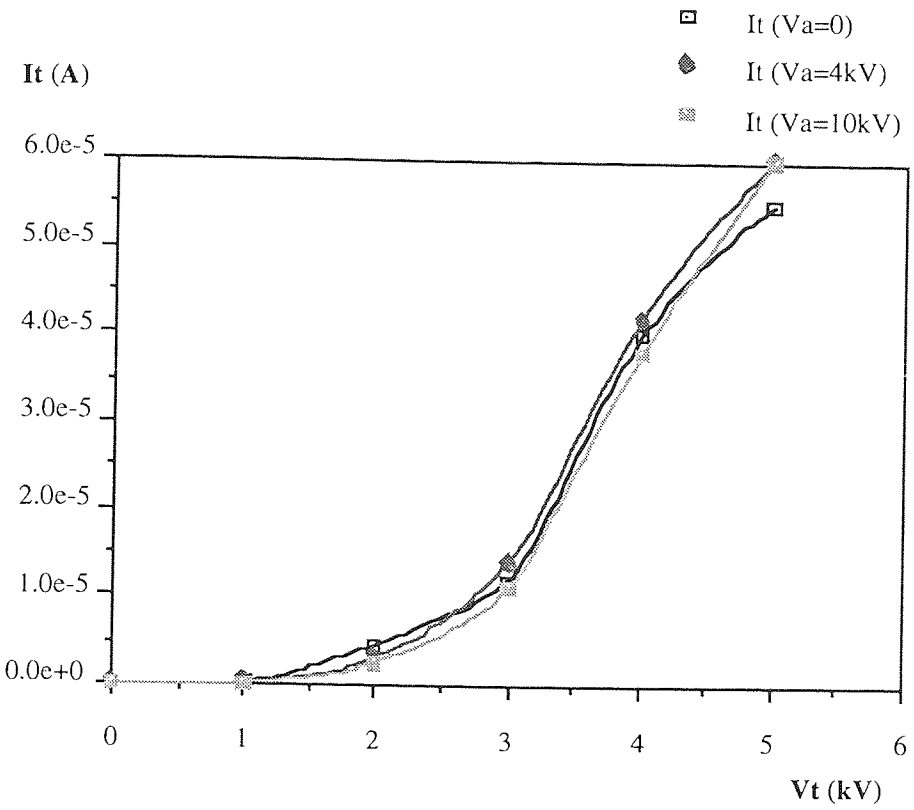

Fig. 4.1.16 Planar I_t-V_t characteristics, for a range of fixed main-gap (transverse) voltages (V_a)

In concert with these electrical measurements, optical events associated with the confined alumina module were recorded using a CCD camera (see Section 3.2.4.1). Figure 4.1.17 gives an annotated end-view of the confined module, looking along the specimen axis (through viewport 1 of Fig. 3.2.7) at the metallized ceramic region of the alumina module.

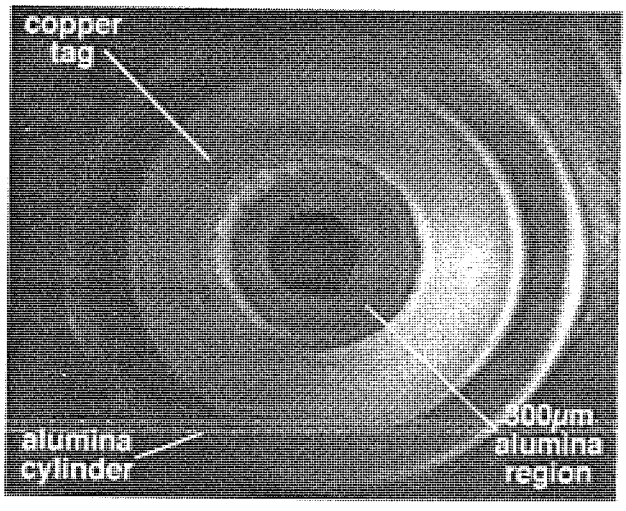

Fig. 4.1.17 Front view of confined alumina module

Applying a transverse DC voltage (V_a) of +8kV to the transparent anode, with a recorded main-gap current (I_a) of 21μA, the image depicted in Fig 4.1.18(a) was observed. A purple-coloured glow was observed within the alumina envelope, accompanied by several luminescent flares on the transparent anode (visible in lower left quadrant of Fig 4.1.18(a)). A bright region of luminosity was also observed at the butting junction of the alumina cylinder with the transparent anode.

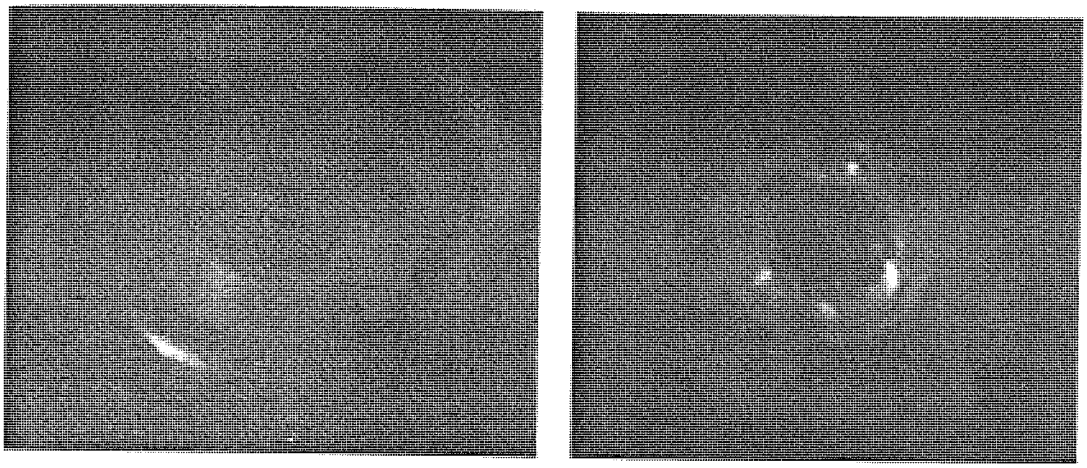

(a) (b)

Fig. 4.1.18 (a) Transverse and (b) planar prebreakdown images recorded from confined alumina modules

Application of a planar voltage (V_t) to the inner ring-electrode caused the ignition of optical processes within the 300μm alumina region on the end-face of the alumina module. Once again, an extended red 'doughnut' glow was observed in the alumina gap, together with several discrete blue 'spots': phenomena that are illustrated in Fig 4.1.18(b). With a small transverse voltage-bias, V_a, applied across the ceramic cylinder, the onset of these planar phenomena caused a purple glow to appear within the confined region inside the ceramic cylinder.

Referring to both Figs 4.1.18(a) and (b), the presence of transparent-anode luminosity *beyond* the outer-diameter of the ceramic envelope suggested electron-emission from sites outside the confined electrode regime. Further electron-emission was indicated from the alumina module itself, by the simultaneous rise in I_t and observed luminosity, coincident with the application of V_t and the initiation of planar events within the 300μm alumina region.

Following the *in vacuo* DC analysis of the confined alumina module, the specimen was removed from the vacuum system, and an area of discoloration was clearly visible on the outer-diameter of the ceramic cylinder envelope. The discoloured region of ceramic is illustrated in Fig 4.1.19(a), with an accompanying schematic diagram given in Fig 4.1.19(b).

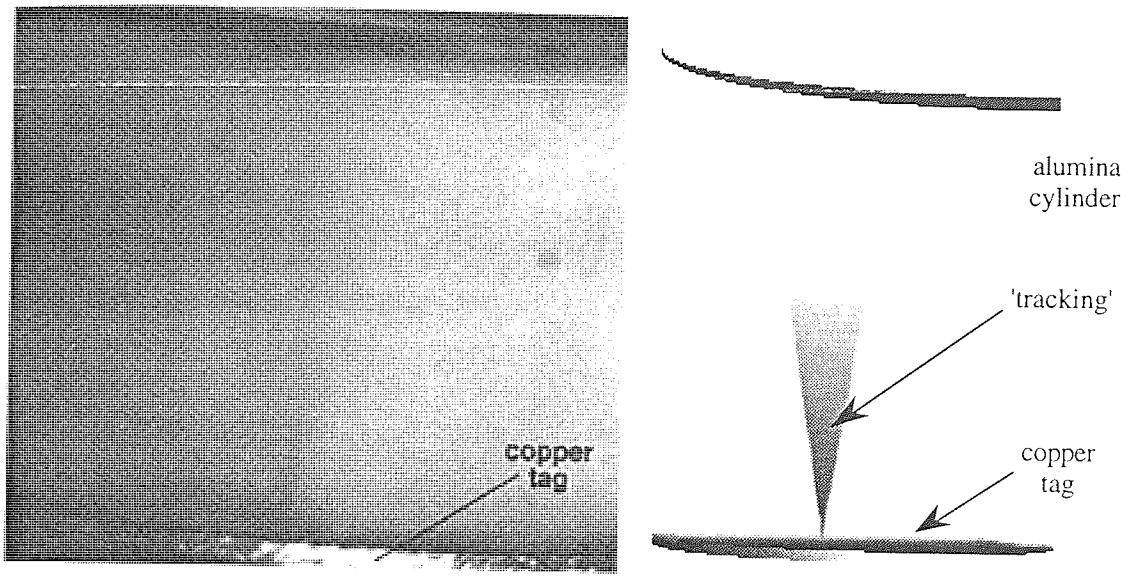

Fig. 4.1.19 (a) Photographic and (b) schematic pictures of tracking along alumina cylinder of confined alumina module

This discoloration on the ceramic cylinder appeared as a dark-coloured 'track', and was in the same spatial location as the bright region of luminosity observed on the transparent anode, described in Fig 4.1.18(a). The track appeared to stem from a discrete site, at the cathode region at the base of the ceramic cylinder, formed by the copper-tag on the alumina module. Similar forms of tracking have been observed by other workers [36,40,42], in the region of surface-flashovers along the solid insulator in vacuum .

4.2 Experimental findings II - pulsed field

On the basis of the steady-state DC analysis presented in Section 4.1, a further series of experiments were undertaken to observe the pulsed field behaviour of the alumina ceramic. High-voltage pulses, of the forms outlined in Section 3.2.3, were applied to the alumina specimens described in Section 3.1. Concurrent with the application of a pulsed electrical field, high-speed images were recorded of all associated surface-flashover events, using the imaging apparatus shown in Section 3.2.4. These high-speed recordings were made both along the centre-axis of the specimen, and also viewing across the metallized alumina end-face, orthogonal to this principal centre-axis.

High-speed video and ultra-fast framing imaging techniques were employed in the optical studies of emission phenomena associated with the pulsed-field surface flashover of alumina ceramics. High-speed videography [40] provided clear images with improved temporal resolution over the conventional VHS video techniques described in Section 3.2.4.1. Ultra-fast framing produced highly time-resolved images of surface-flashover phenomena, but with a reduced dynamic range of detected light-intensity.

4.2.1 Imaging of optical events on module end-face

4.2.1.1 Pulsed-field optical phenomena By viewing the end-face of the alumina tube along the specimen axis through viewport **1** (i.e. as shown in Figs 3.2.8(a) and 3.2.9), and applying a high-voltage pulse (V_t) to the inner electrode-ring, the image depicted in Fig 4.2.1(a) was observed. This image reveals several bright 'jets' radiating outwards in straight lines from the exposed Al_2O_3 dielectric. Furthermore, by tracing back the jet trajectories it appears that they all originate from a luminous centre (or region) situated in the 300μm-width alumina gap.

For clarity, Fig 4.2.1(b) presents a schematic representation of this relationship between the 'jets' and the luminous centre observed in Fig 4.2.1(a). From Fig 4.2.1(a), it will be seen that some jets display some degree of divergence along their length. However, it is not clear whether this divergence arises from the divergent emission of a jet, or from the subsequent divergence of the jet as it propagates in vacuum following its *collimated* emission from the ceramic.

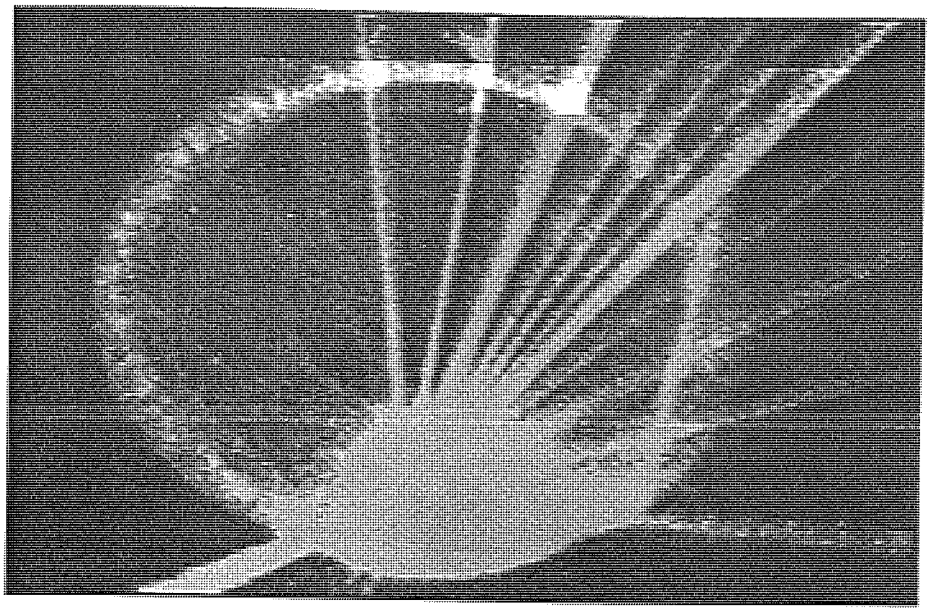

(a)

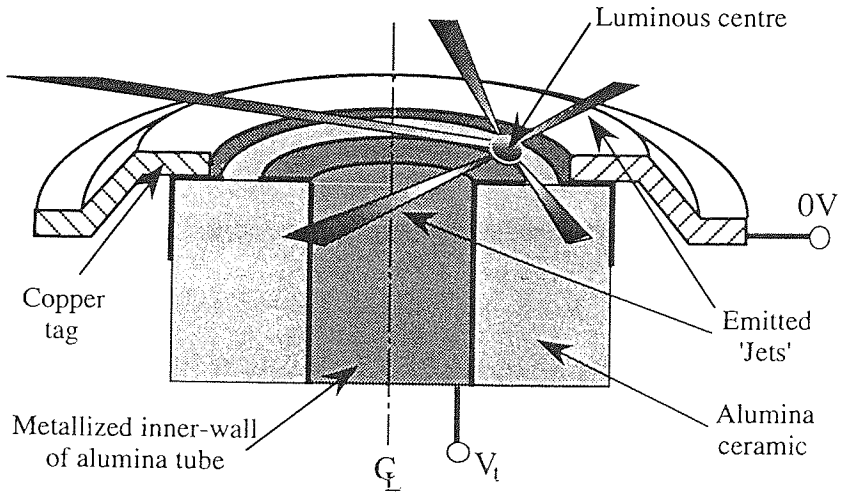

(b)

Fig. 4.2.1 (a) Captured image and (b) schematic illustration of pulsed breakdown event on front-face of alumina module {V_t = +4kV, 1ms framing period}

A careful graphical projection of the jet-trajectories does not indicate a single point of convergence, i.e. a 'point source' of jet emission is not indicated. Instead, the jet trajectories appear to originate from a number of points, suggesting a finite *distribution* of jet sources within a luminous centre in the alumina gap. To further probe the nature of these luminous centres, Fig 4.2.2 plots the variation of the observed intensity from a typical luminous centre, such as that shown in Fig 4.2.1(a). This luminosity was plotted along a radial line-scan from the inner electrode-ring, through the 300μm alumina region, to the outer electrode-ring. The pixel-plot shows that the luminous centre appears to have maximum intensity close

to the inner electrode-ring (anode), with the intensity gradually falling-off towards the outer electrode-ring.

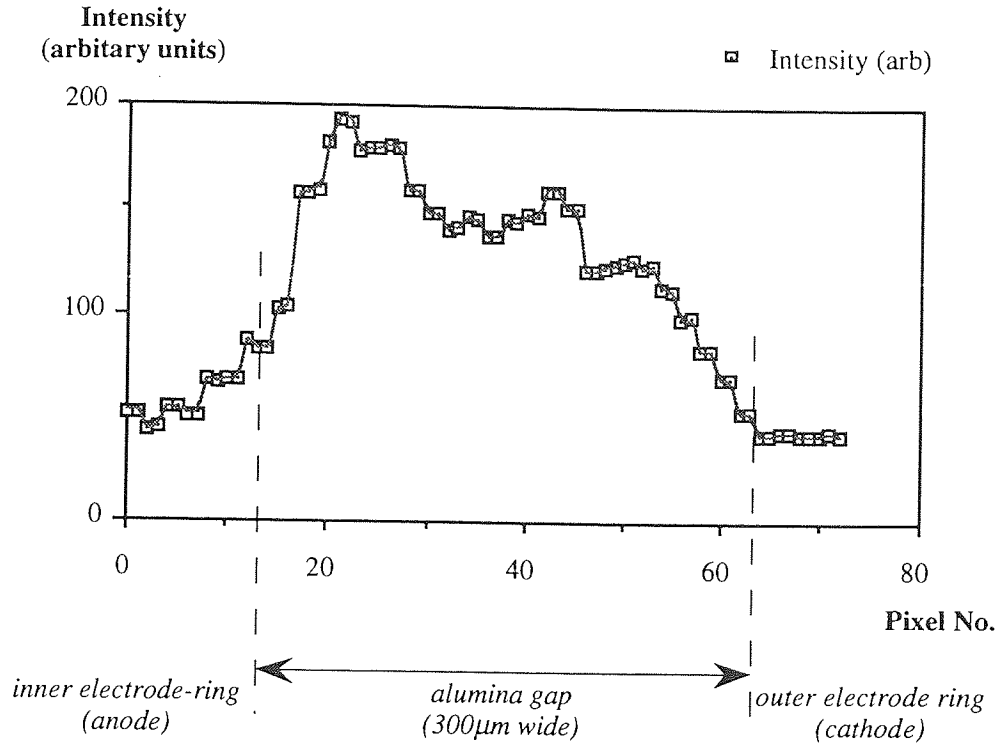

Fig. 4.2.2 Spatial variation of observed optical-intensity along a radial line-scan through a luminous centre observed in the alumina gap between the electrode-rings

Stored images of pulsed flashover events were recorded within a 1200ms camera operation period, with a 1ms aperture for each of the 1200 stored frames (see Section 3.2.4.2). It was therefore possible to view both the initial 1ms frame of photon-emission from the flashover event, together with any remnant emission recorded in subsequent video frames. This temporal analysis is included in Sections 4.2.1.2 and 4.2.1.3:

4.2.1.2 Persistence of luminous centres in the alumina gap Following a flashover event, and the accompanying emission of 'jets' from the alumina gap, further 1ms video frames showed a decaying glow within the 300μm interelectrode gap at the sites of initial luminous centres. Observing this decaying glow using low-pass optical filters, it was possible to establish that the photon-emission was deep-red in colour. Furthermore, from a typical series of post-breakdown images, such as those presented in Fig 4.2.3(a), it can be shown that a luminous-centre decays typically over a 10ms interval.

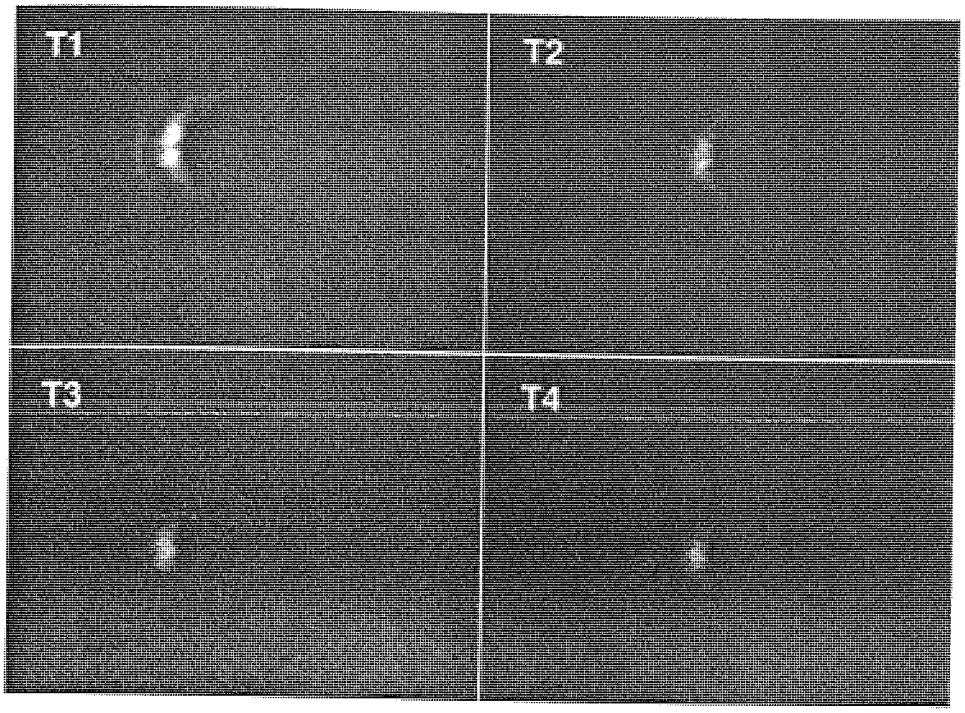

(a)

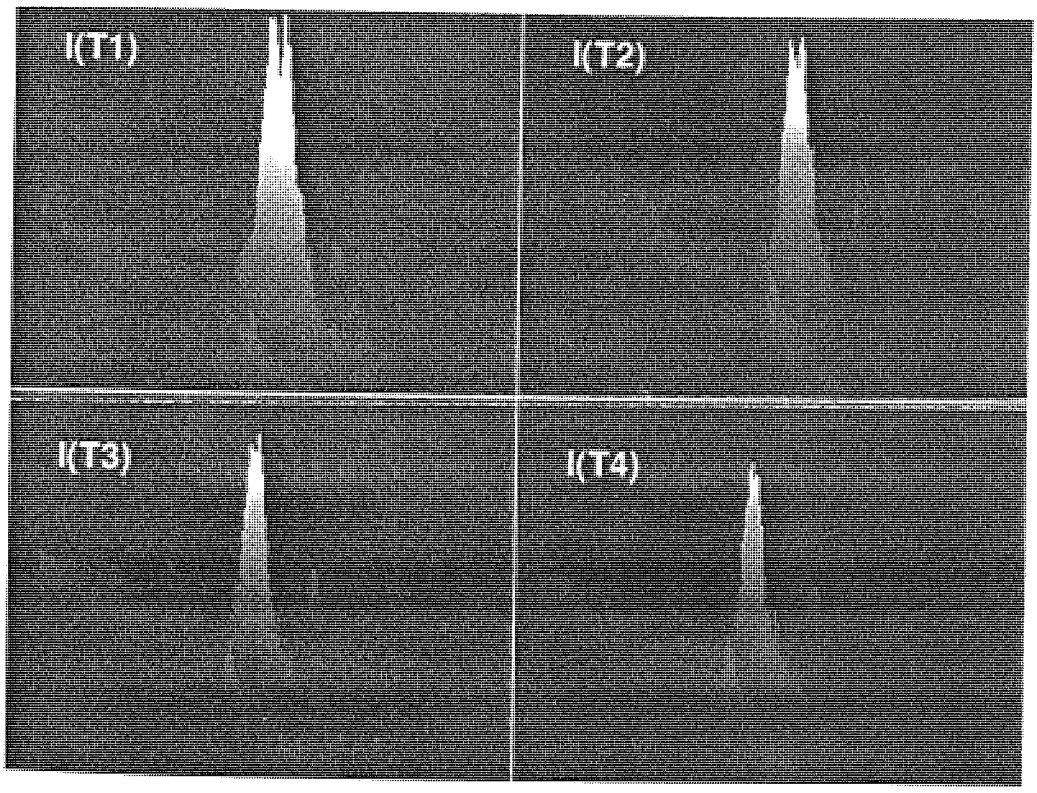

(b)

Fig. 4.2.3 Composite series of four successive 1ms frames, showing (a) recorded images and (b) corresponding intensity profiles of the post-breakdown decay of a luminous centre in the alumina gap

The application of a pixel-intensity sampling technique to each of these recorded images yielded the time-varying plot of the maximum optical intensity within the luminous centre shown in Fig 4.2.4: this analysis indicated that the post-breakdown intensity of the luminous centre exhibited a logarithmic decay, with a time constant of ≈5ms.

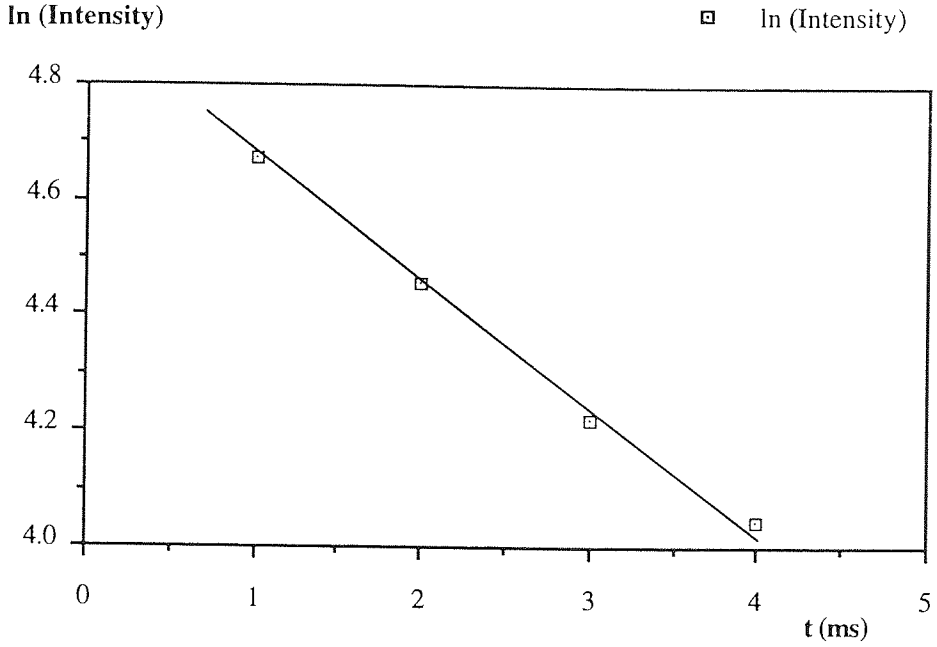

Fig. 4.2.4 Decay of peak measured-intensity of luminous centre with time.

4.2.1.3 Propagation of emitted 'jets' In recordings of flashover events, the 'jet' type of emission shown in Fig 4.2.1 was only observed within a single 1ms frame period, with subsequent frames showing no indication of these jets. Thus, the jets apparently propagate away from the alumina specimen within this 1ms time-frame. It follows, therefore, from the observed length of these jets (viz. ≈10mm), that a *minimum* value for the jet velocity would be $\approx 10 ms^{-1}$.

Similar jet velocities were observed following the application of +20kV EHV pulses to the alumina module, as described in Section 3.2.3.2. Figure 4.2.5(a) presents a pulsed-field breakdown image recorded over a millisecond exposure. A luminous centre is again visible in the alumina gap, but is now accompanied by a bright glow in the metallized inner bore of the alumina cylinder. Further luminosity is also visible along the edge of the outer electrode-ring (cathode), and can be seen to extend along the cathode-edge, either side of the main luminous centre. These optical phenomena are described pictorially in Fig 4.2.5(b).

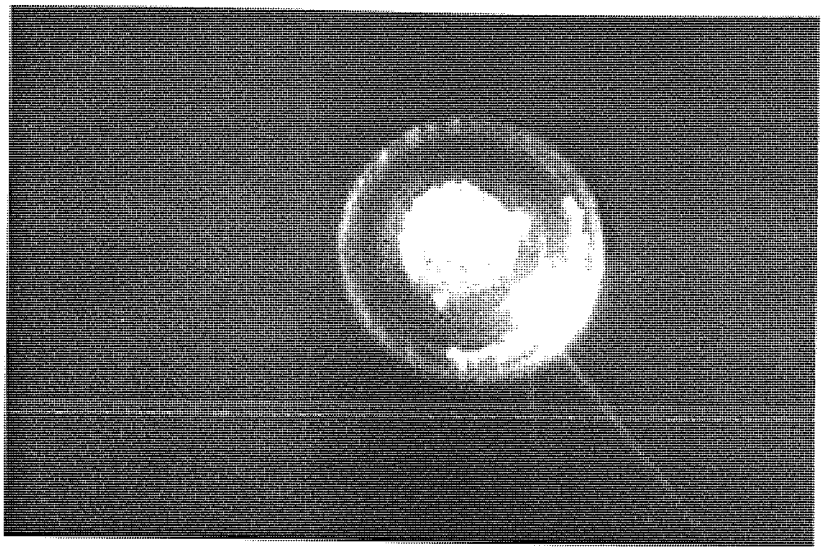

(a)

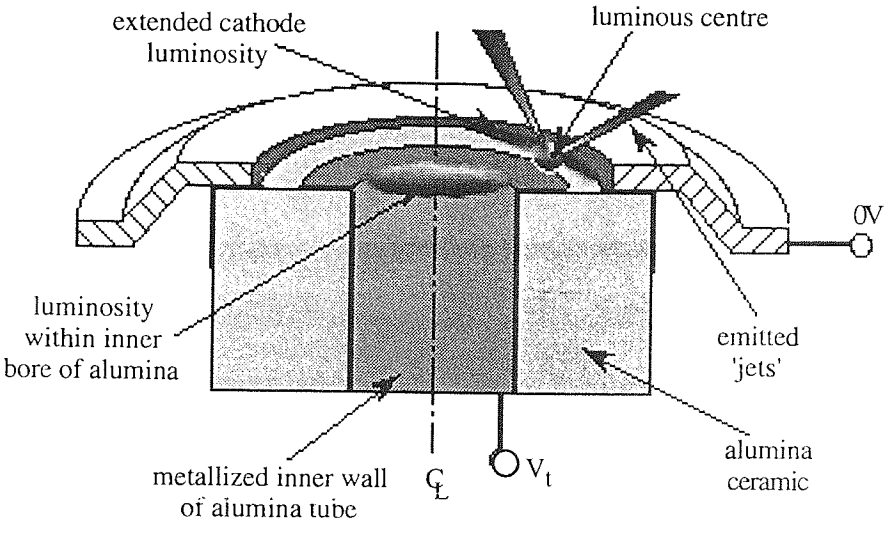

(b)

Fig. 4.2.5 (a) Captured image and (b) schematic sketch of pulsed breakdown event on front-face of alumina module {V_t = +20kV}

The nature of these EHV surface-flashover phenomena is further investigated in the ultra-fast studies of *initiating* optical events described in Section 4.2.2, and in orthogonal observations of the propagating jets shown in Section 4.2.3.

4.2.1.4 Influence of body envelope upon jet propagation Viewing the end-face of a confined alumina module (of the type illustrated in Section 3.1.2), along the specimen axis through viewport 1 (Fig 3.2.9), the outline form of the module is shown in Fig 4.2.6(a).

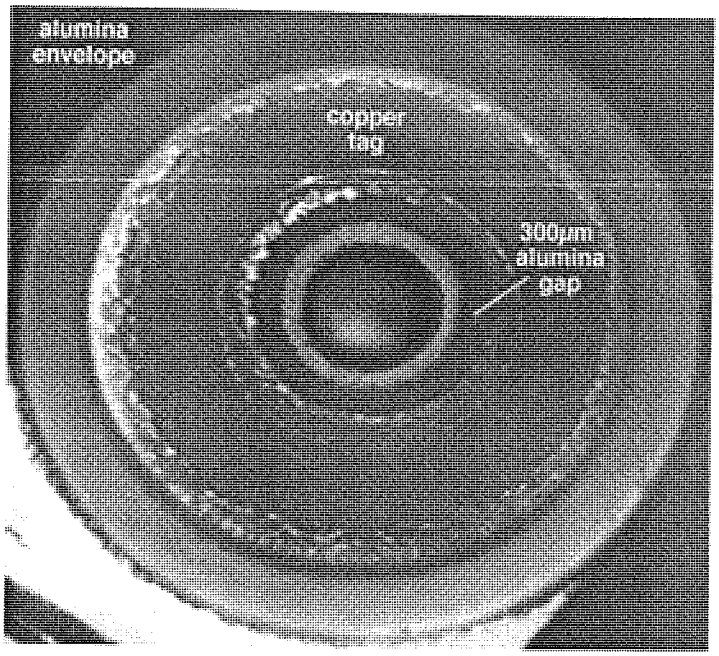

(a)

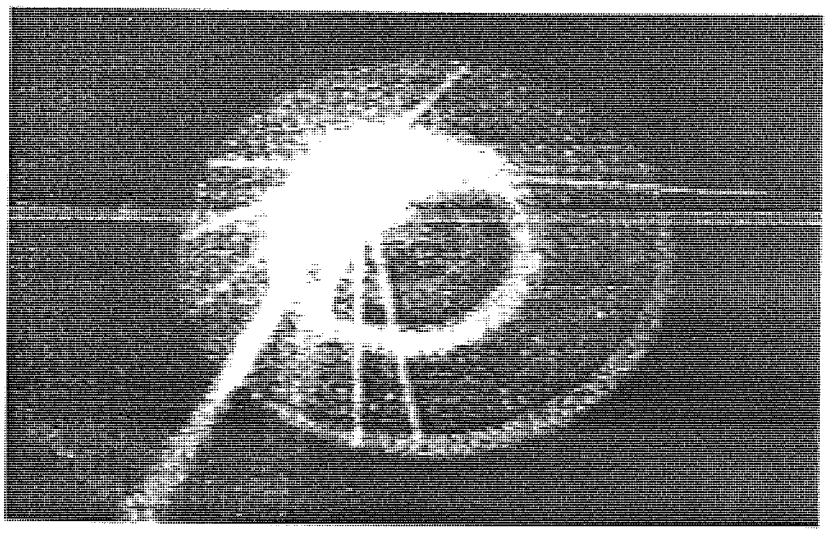

(b)

Fig. 4.2.6 (a) Outline of front end-face of 'confined' alumina module, and (b) millisecond image of pulsed flashover event

Applying a high-voltage 6kV pulse (V_t) to the inner electrode-ring, the image depicted in Fig 4.2.6(b) was observed using the high-speed video apparatus described in Section 3.2.4.2. Several bright jets were seen to radiate outwards in straight lines from the exposed Al_2O_3 dielectric, apparently from a luminous centre

situated in the 300μm-width alumina gap. With reference to Fig 4.2.6(b), only three jets were seen to emerge from the confined volume of the alumina envelope. The remaining jets emitted from the metallized alumina module appear to 'terminate' at the inner wall of the ceramic envelope, and do not exhibit any ballistic reflections from the alumina surface.

Figure 4.2.7 presents a further picture of emitted jets emerging from the open end of the ceramic cylinder. In this side elevation of a confined alumina module, viewed through viewport **2** of Fig 3.2.9, Fig 4.2.7(b) presents a composite image of two emerging jets with the outline of the confined module.

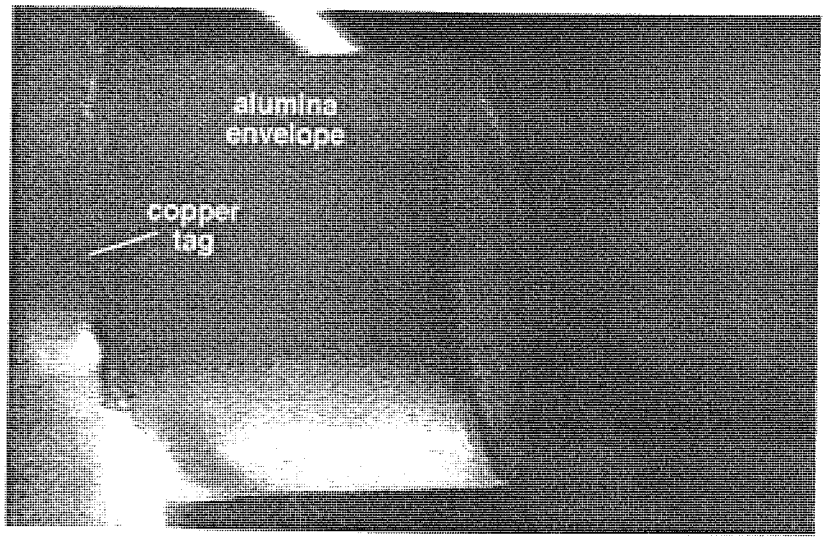

(a)

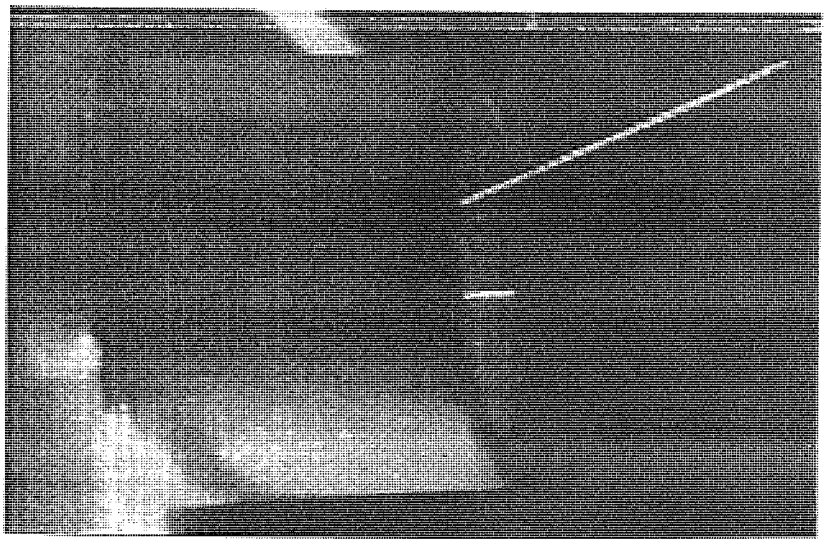

(b)

Fig. 4.2.7 (a) Side view of 'confined' alumina module, with (b) composite millisecond image of pulsed flashover emission

Figure 4.2.8 presents a clearer representation of the behaviour of the jets observed in Figs 4.2.6(b) and 4.2.7(b). An extensive study of jet phenomena is presented in Section 4.2.3, which includes further orthogonal views of pulsed-field breakdown events on standard alumina modules.

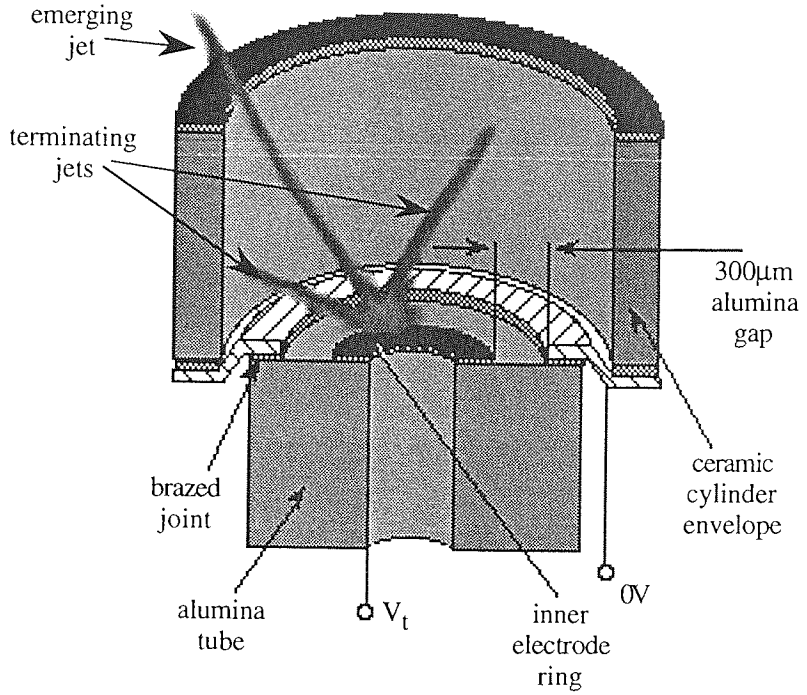

Fig. 4.2.8 Schematic illustration of observed jet behaviour within a confined electrode regime

4.2.1.5 Pulsed field optical emission from 'bulk' dielectric modules Extra-high voltage (EHV) pulses, of +20kV magnitude (see Section 3.2.3), were applied to the inner conductor of 'bulk' dielectric modules; i.e. having the form described in Section 3.1.3. Figure 4.2.9(a) depicts the front view of a specimen module, whilst Fig 4.2.9(b) shows a high-speed videograph of the optical emission from the ceramic during the initial 2ms period following the breakdown of the EHV pulse (V_t).

Intense luminosity can be seen throughout the thickness of the alumina ceramic tube, with the inside bore of the module appearing dark by comparison. Subsequent optical emission from the bulk sample is illustrated in the consecutive 2ms frames of Figs 4.2.9(c) to 4.2.9(f). The intensity of the detected luminosity is seen to diminish, and the spatial extent of the luminous region contracts into four 'lobes' of luminosity around the inner electrode (anode) of the bulk module.

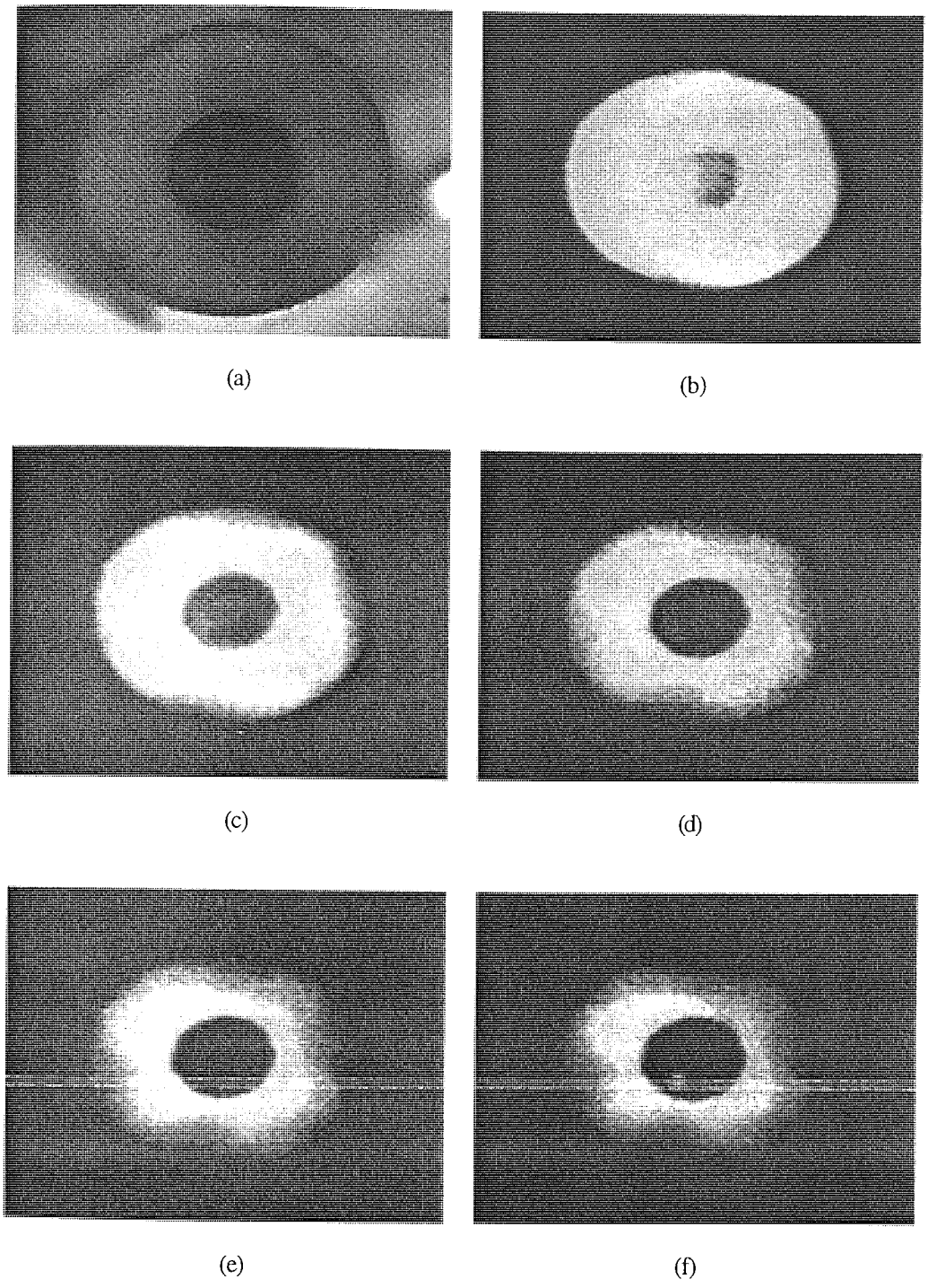

Fig. 4.2.9 (a) Front view of 'bulk' alumina module, with {(b) - (f)} consecutive 2ms frames of EHV pulsed breakdown event

It should also be noted that the application of +6kV HV pulses (see Fig 3.2.5(a)) to the bulk module did not result in breakdown, and no optical emission was detected.

4.2.2 Initiation of pulsed-field surface-flashover events The lower optical gain of the fast-framing camera system, compared to that of the high-speed video apparatus (Section 3.2.4.2), prohibited the fast-frame imaging of HV pulsed-field events. However, the brighter luminosity associated with the EHV pulsed-breakdown events, as shown in Fig 4.2.5, was suited to observation using the ultra-fast framing apparatus described in Section 3.2.4.3.

4.2.2.1 Temporal development of surface-flashover Sub-millisecond imaging of EHV surface flashover events was therefore feasible using the Imacon 468 camera, and Fig 4.2.10 depicts a series of micro-second frames (Frames *A*, *B* and *C*), leading up to a final milli-second frame (Frame *D*), showing the optical phenomena associated with the surface-flashover event. For clarity, the timing-diagram associated with these images is given in Fig 4.2.11.

Considering the initial microsecond frame of Fig 4.2.10(b), a localised area of luminosity is visible on the inner edge of the outer ring-electrode (cathode). A region of less-intense luminosity is visible near the outer edge of the inner electrode-ring (anode), radially opposite to the cathode luminosity across the 300μm alumina gap. Further dim luminosity can be seen within the metallized inner bore in the ceramic tube of the alumina module.

Following a 2μs inter-frame period, Fig 4.2.10(c) depicts a second microsecond-duration frame. The intense luminous zone near the outer electrode-ring appears enlarged with this luminous zone apparently spreading outwards along the electrode-edge, either side of the luminous zone. The corresponding area of luminosity near the outside edge of the inner electrode-ring now appears more intense, together with brighter optical emission from within the metallized inner-bore of the sample.

Moving forward to Fig 4.2.10(d), the luminous areas associated with the inner electrode-ring, on its outer edge and within the inner bore, now appear very bright in intensity. The luminous zone near the edge of the outer electrode-ring has diminished, and has become more 'diffuse' in appearance.

Finally, Fig 4.2.10(e) shows the brightness of the luminous zone near the inner-electrode edge to have intensified, with four jets appearing to emanate from locations situated within this zone. Some luminosity remains within the inner-bore of the module, and at the inside edge of the outer electrode-ring.

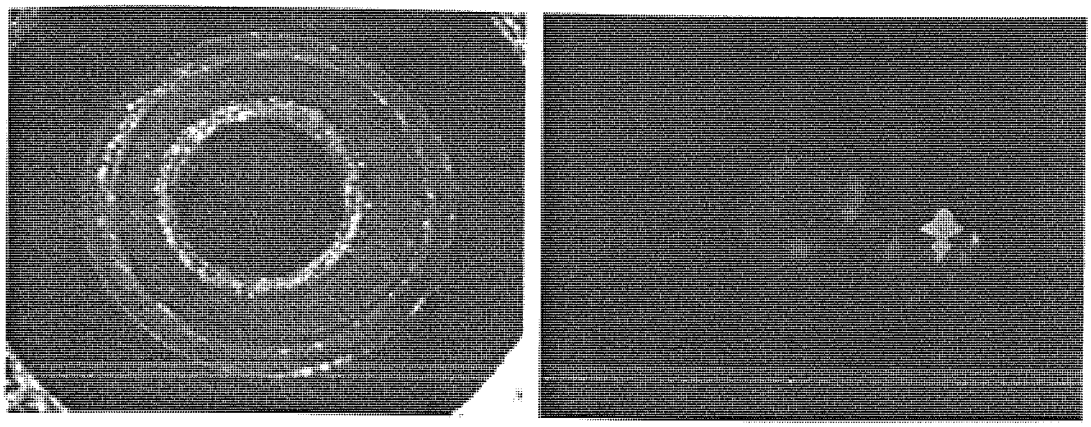

(a) (b) *Frame A*

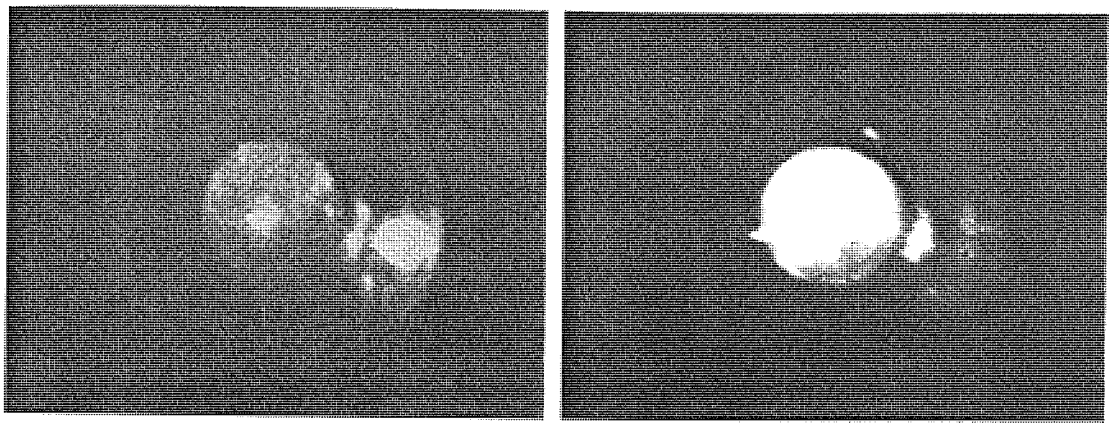

(c) *Frame B* (d) *Frame C*

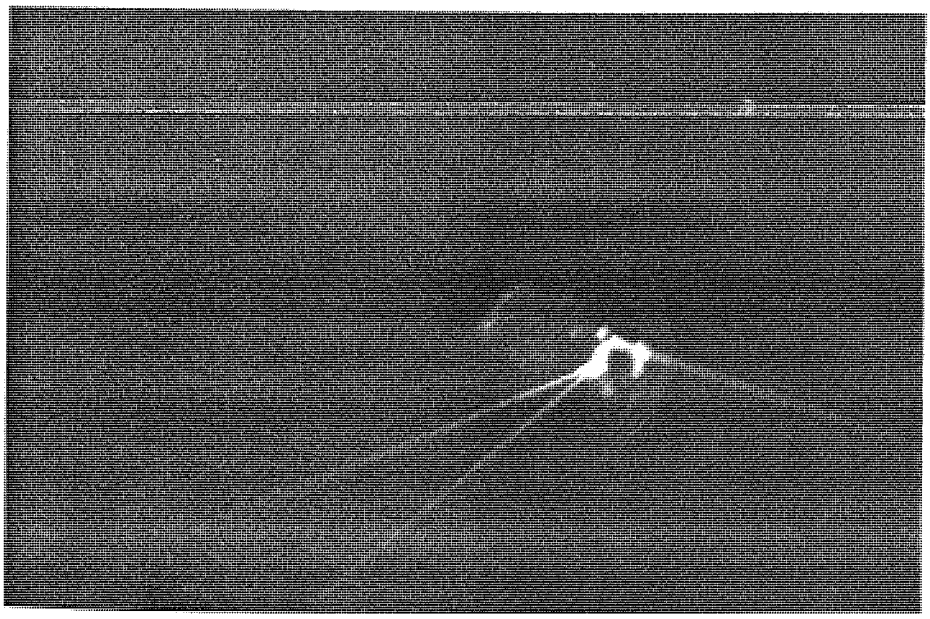

(e) Frame D

Fig. 4.2.10 (a) Front view of alumina module, with {(b) (c) (d)} 1μs frames of surface-flashover event (2μs interval between frames), and (e) final 1ms frame showing 'jet' emission

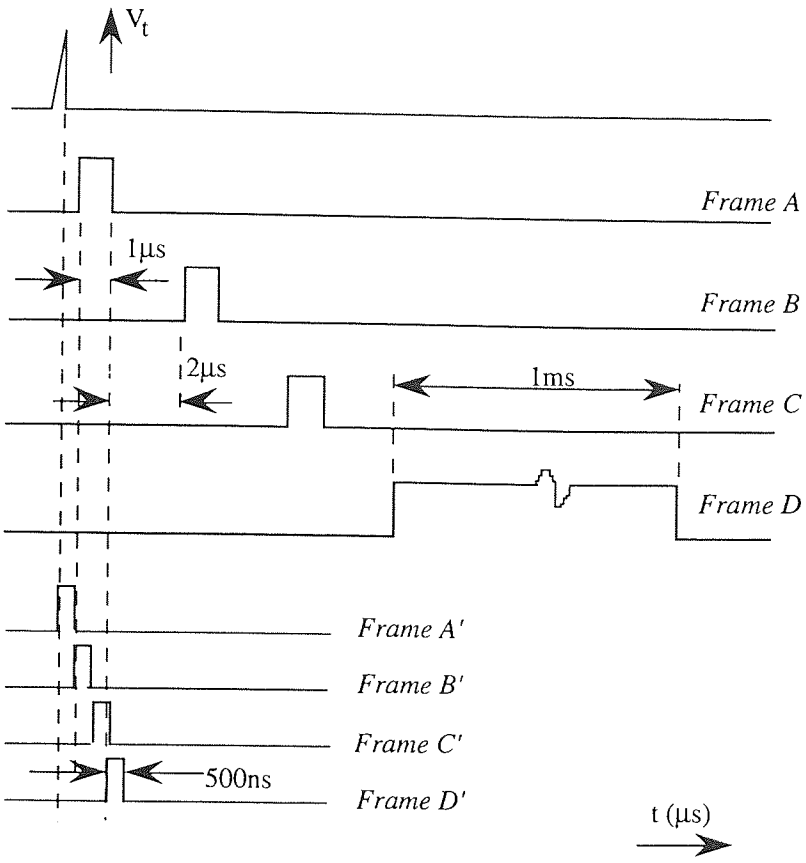

Fig. 4.2.11 Waveform timing diagram, showing the exposure-times of the image channels with respect to the applied EHV pulse, V_t

4.2.2.2 Temporal development of luminous zones In order to examine the initial growth of the luminosity phenomena described in Fig 4.2.10, further images of surface-flashover events were recorded over sub-microsecond frame periods. Thus, Fig 4.2.12 illustrates a sequence of four consecutive frames, each of 500ns duration, which were timed so as to record optical events immediately following the collapse of the applied voltage pulse, V_t. The timing sequence of these four frames is illustrated in the lower set of timing pulses of Fig 4.2.11, which also shows their temporal relationship to the previous series of 1μs frames given in Fig 4.2.10.

With reference to the module outline shown in Fig 4.2.10(a), the initial 500ns frame presented in Fig 4.2.12(a) indicates two small 'spots' to the right of the picture, which appear to be located near the inner edge of the outer ring-electrode. A further small spot of luminosity is visible on the left side of the specimen, on the inside edge of the inner electrode-ring, near to the inner bore of the alumina tube.

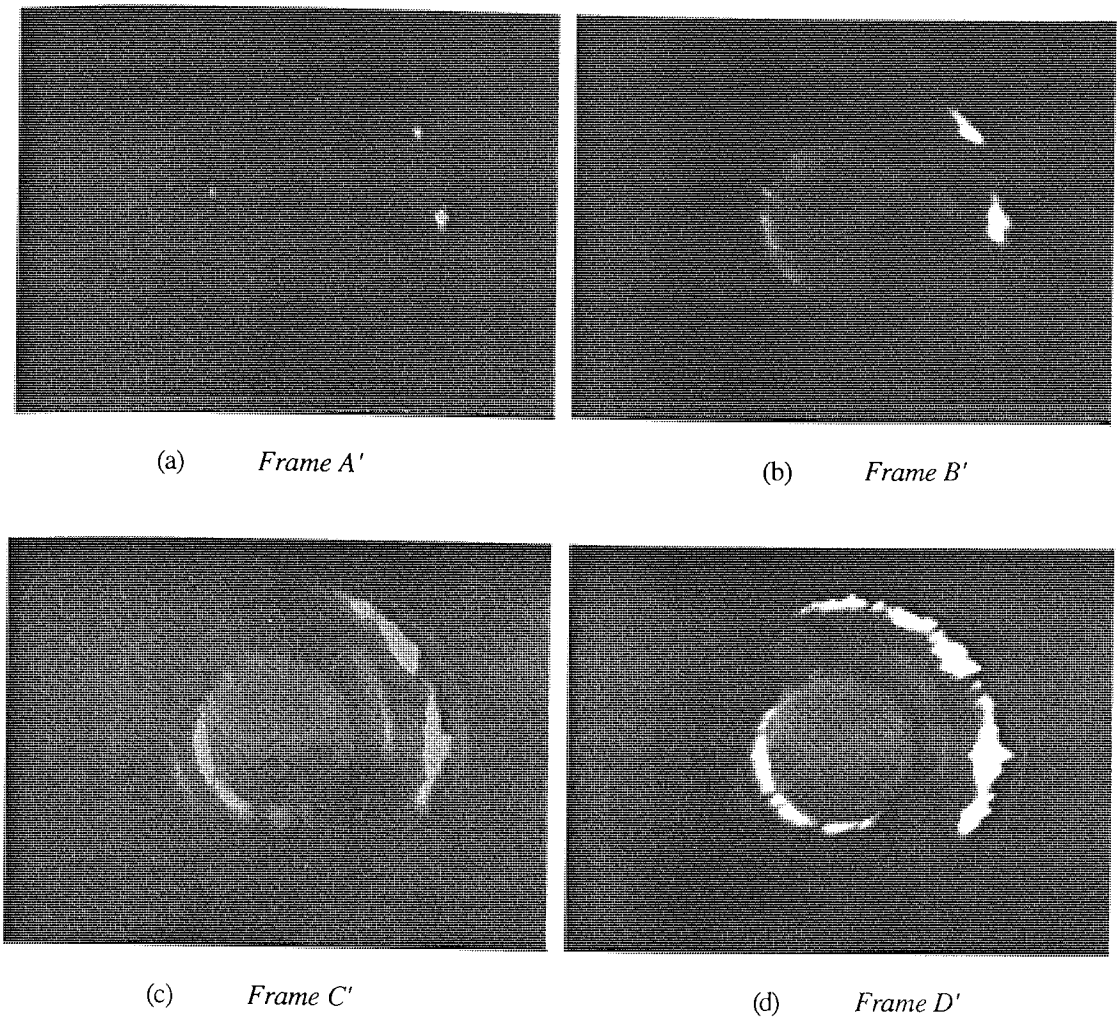

(a) *Frame A'* (b) *Frame B'*

(c) *Frame C'* (d) *Frame D'*

Fig. 4.2.12 Consecutive 500ns frames showing the initiation and development of a pulsed-field surface-discharge on the metallized end-face of the alumina module

The second frame, illustrated in Fig 4.2.12(b), shows the two 'cathodic' spots near the outer electrode-ring to have grown. A further area of dim luminosity is now visible on the inner electrode-ring, near to the lower cathodic spot. The luminous region on the inside edge of the inner electrode-ring has extended considerably, with some extended luminosity now visible within the inner bore of the sample.

In Fig 4.2.12(c), the cathodic luminosity regions have extended considerably. An extended region of luminosity is visible around the inner periphery of the inner electrode-ring, together with a luminous area around its outer periphery, in the vicinity of the cathodic emissions. Fig 4.2.12(d) shows the further development of these optical phenomena, after another 500ns period.

4.2.2.3 Initiation of surface flashover luminosity The framing speed of the Imacon camera was increased to 10^7 fps, yielding a framing period of 100ns. Shuttering of the first frame image was synchronised with the EHV pulse signal, as described in

Section 3.2.4.3. Figure 4.2.13 presents an oscillogram of the EHV pulse, together with the synchronisation signal from the fast-framing camera. The exposure periods of the four camera channels are superimposed upon this waveform diagram, with the start of frame 1 denoted by the switching of the synchronisation signal.

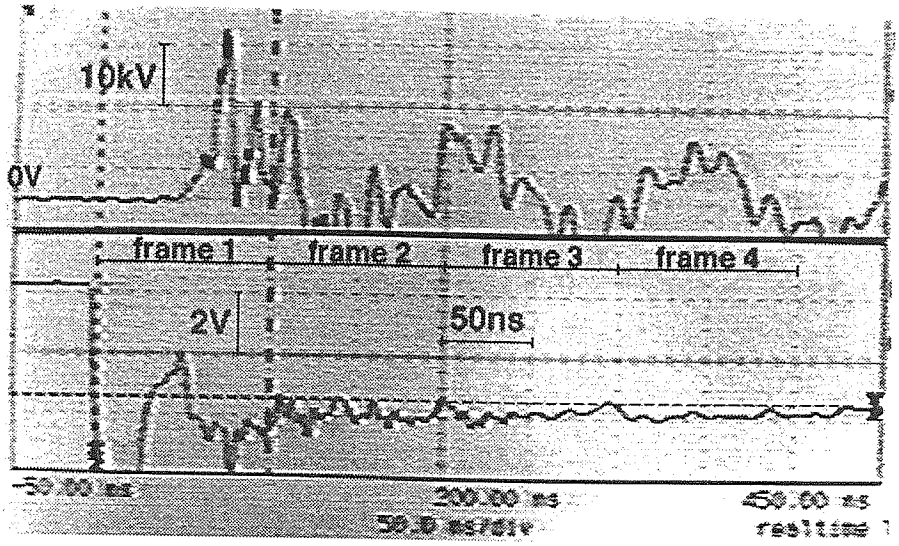

Fig. 4.2.13 Oscillogram of extra high-voltage breakdown pulse (V_t = +25kV, upper trace) and corresponding synchronisation pulse-edge (TTL, lower trace) marking capture of first frame

Referring to Fig 4.2.13, breakdown of the applied EHV voltage-pulse occurs towards the end of the first frame period. Figure 4.2.14(b) displays the corresponding image recorded from frame 1, which shows no visible emission from the alumina module. In frame 2, shown in Fig 4.2.14(c), three distinct luminous spots have formed, near the inside edge of the outer electrode-ring. Accompanying these cathodic spots are further regions of luminosity, located on the inside edge of the inner electrode.

The following 100ns image of Fig 4.2.14(d) (frame 3) shows the appearance of a fourth luminous centre on the outer electrode. The luminosity associated with the inner electrode-ring now appears diffused, and of lesser intensity. By frame 4 (Fig 4.2.14(e)) the four cathodic spots near the outer electrode have brightened, and appear larger. Extended luminosity is now clearly visible within the inner electrode / inside bore of the module, with a broad region of luminosity formed on the inside edge of the inner electrode-ring, radially opposite to the four cathodic spots of the outer electrode.

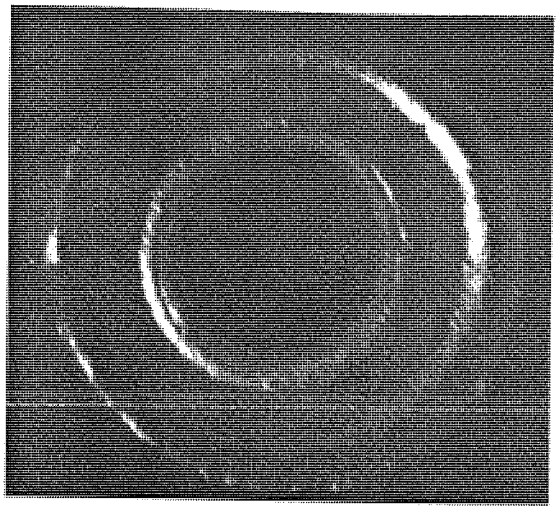

(a)

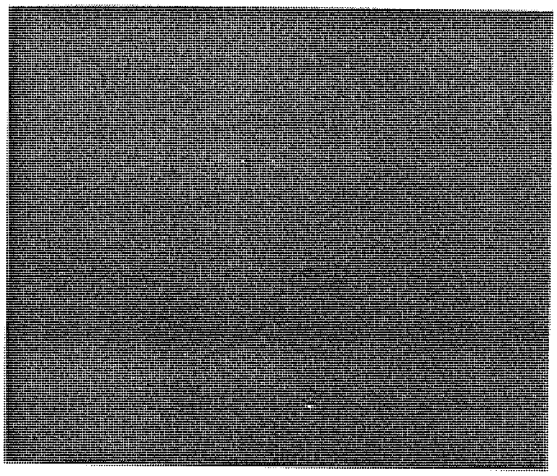

(b) Frame 1

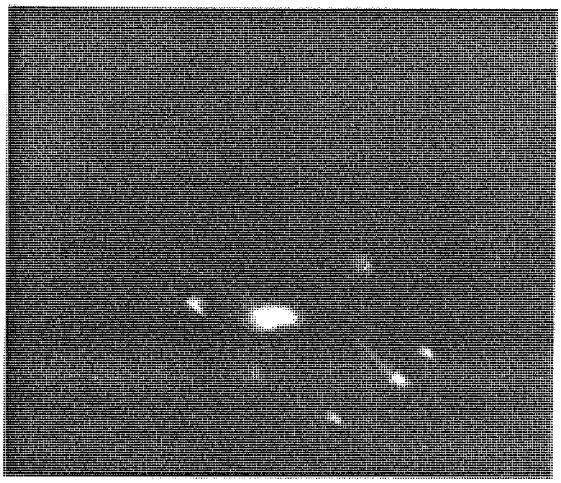

(c) Frame 2

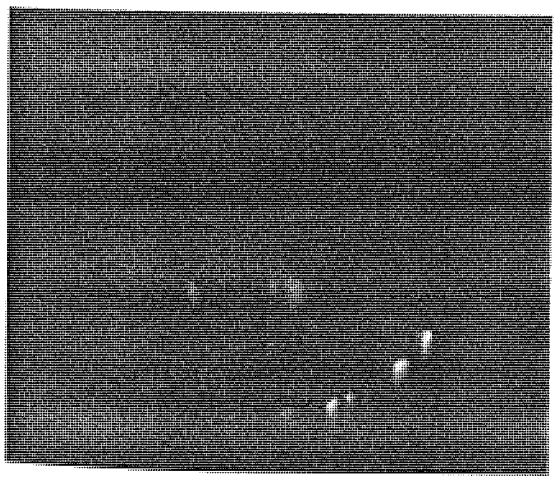

(d) Frame 3

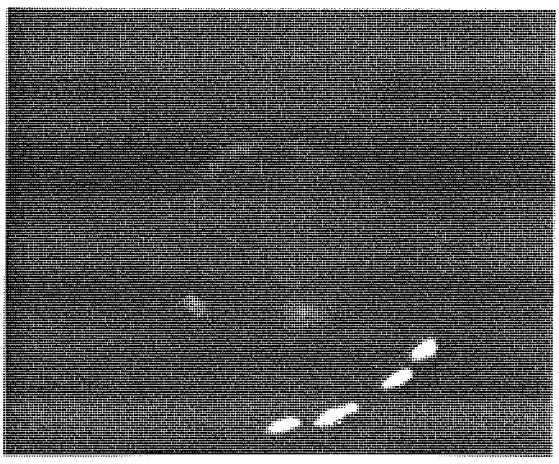

(e) Frame 4

Fig. 4.2.14 (a) Illuminated front-view of alumina module, and sequence of four consecutive 100ns frames {(b) - (e)} showing initiation of pulsed-field breakdown event

4.2.3 Orthogonal recording of surface-flashover events For these measurements, the alumina specimen was viewed in the plane of its metallized end-face through viewport **2**, i.e. orthogonal to the centre-axis of the specimen, as shown in Fig 3.2.8(b).

4.2.3.1 Pulsed field optical phenomena The application of a high-voltage pulse, V_t, to the inner-electrode ring led to the type of events captured in Fig 4.2.15(a).

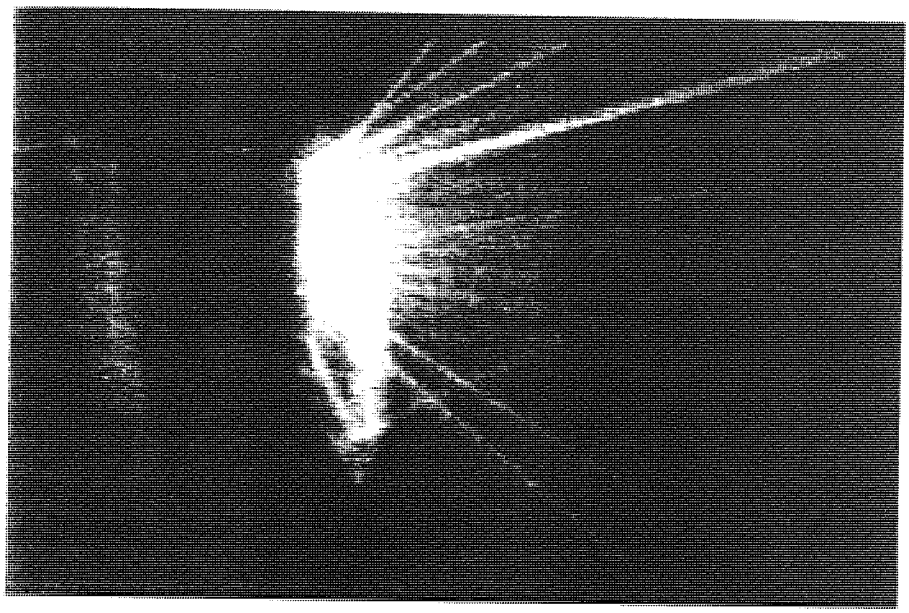

(a)

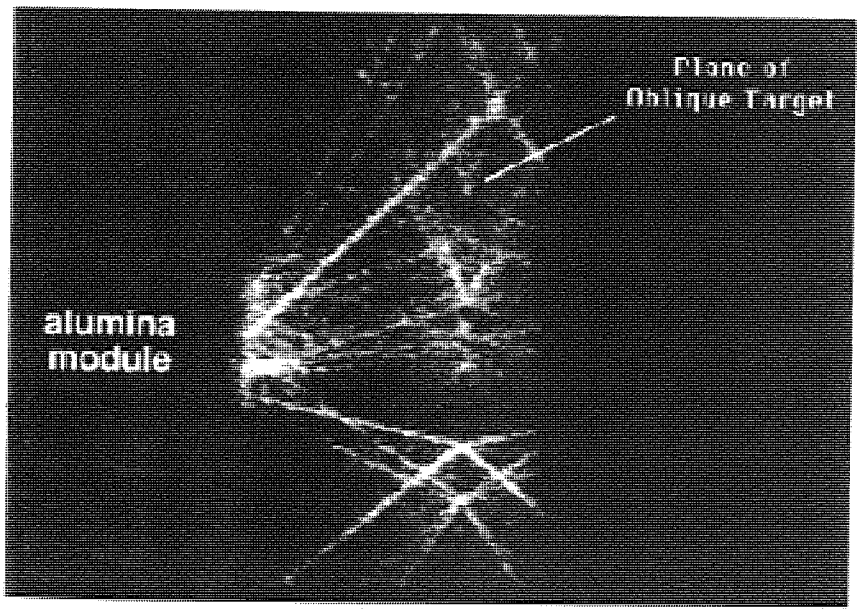

(b)

Fig. 4.2.15 Captured 1ms frames of (a) optical activity associated with a pulsed-breakdown flashover event, viewed orthogonally to the end-face of the alumina specimen, and (b) emitted jets striking a tin oxide-coated glass target ($V_t = 4$ kV)

This high-speed video image shows several bright 'jets', which appear to emerge from a localised emission-centre on the end-face of the alumina tube. These phenomena appear similar in form to those recorded from the front-face of the alumina module in Section 4.2.1. In particular, a jet emerging in a downward direction appears to strike the braze-material securing the copper earth-tag to the metallized alumina module, and exhibit a *ballistic* behaviour as it is deflected into the vacuum-space away from the alumina specimen.

As depicted in the image of Fig. 4.2.15(b), the introduction of a tin-oxide coated glass target in front of the alumina sample gave rise to similar deflections of incident jets as they struck the target. However, by replacing the glass with an alumina-ceramic target material, the emitted jets appeared to terminate at the alumina, with no evidence for the occurrence of any deflection "events". This termination of jets on alumina surfaces was also observed in the body envelopes of 'confined' electrode modules, as shown in Section 4.2.1.4

Some jets were also seen to exhibit a *modulation* of the intensity recorded along their path length. This effect has been quantified in Fig 4.2.16, by performing a line-scan of the detected pixel-intensity along the length of a jet: it will be seen that, apart from confirming a modulation effect, the optical-intensity of the jet falls off with distance away from the alumina sample.

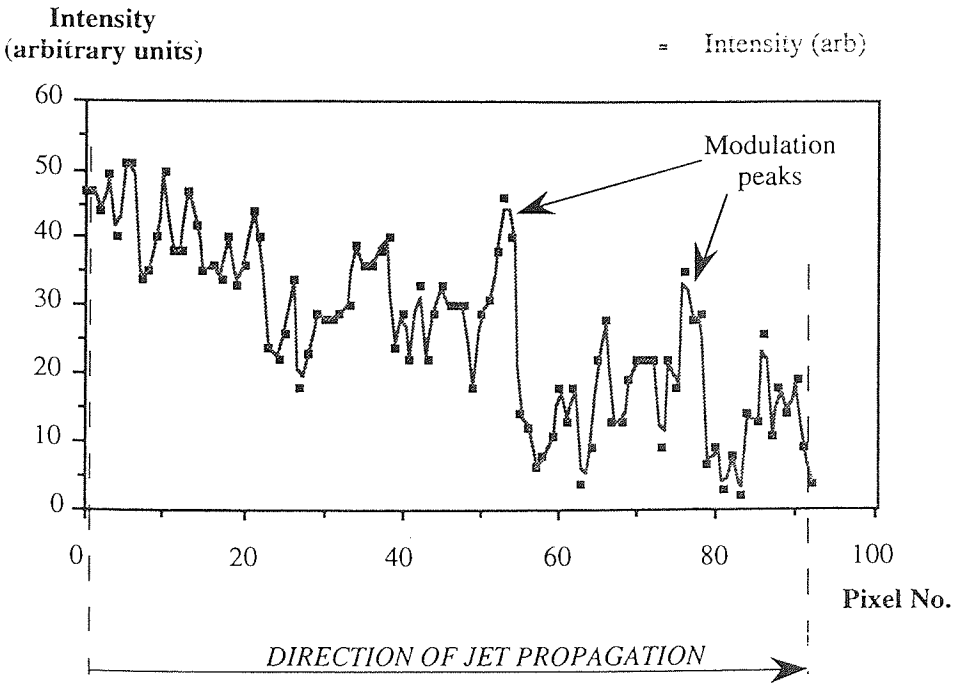

Fig. 4.2.16 Spatial variation of observed optical intensity along an emitted 'jet'

Earth-screening of the experimental system limited the electromagnetic coupling of high-voltage electrical pulses with the high-speed CCD detector array, and thereby minimised any possible contribution of electromagnetic interference to the recorded modulation of the jets in the CCD image [206]. Given the presence of both modulated and non-modulated jets of similar intensities within a single frame (Fig 4.2.15), such electrical noise effects would be expected to influence the entire image. The presence of non-modulated jets suggests that any interference effects appear to be negligible. The 'bright zones' detected within modulated jets must therefore be taken into account in later discussion of the physical nature of these jet phenomena.

4.2.3.2 Pulsed-field optical emission along outer-diameter of alumina module In a minority of DC analyses, no optical events were observed on the end-faces of some alumina modules (see Section 4.1.1.1). Similarly, the end-faces of these modules did not exhibit any *pulsed-field* optical phenomena, and were characterised by a "soft' breakdown-voltage waveform, as illustrated in Fig 4.2.17(b):

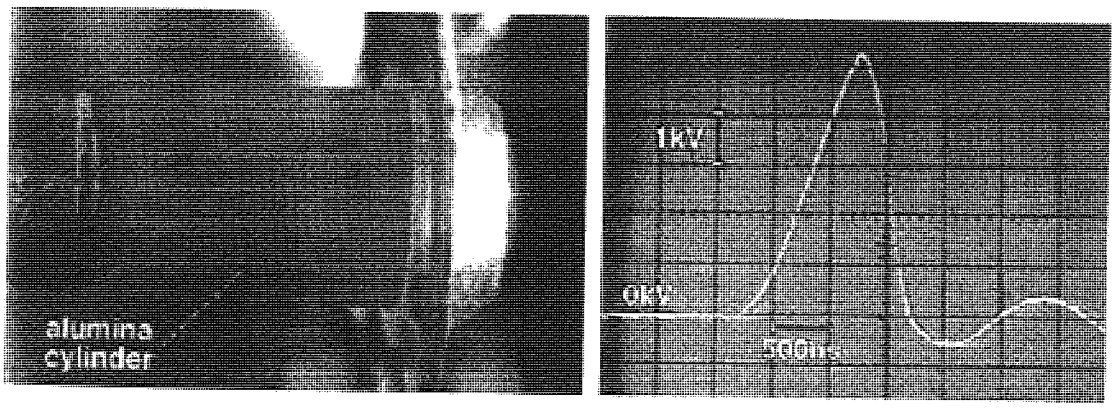

(a) (b)

Fig. 4.2.17 (a) Side view of alumina module, and (b) oscillogram associated with a pulsed flashover along the side of the alumina cylinder

Viewing the side of the alumina module (Fig 4.2.17(a)) through viewport **2** of Fig 3.2.9, optical emissions were observed along the side of the alumina cylinder when a HV pulse was applied to the inner electrode. A series of high-speed video frames are presented in Fig 4.2.18 which record the optical emission from the side of the module over four consecutive frames, each frame of 1ms duration.

A bright region of luminosity was observed near to the high-voltage connection of the threaded fixture at the base of the alumina cylinder. The intensity of this luminescence decayed over the framed period, with a time constant ≈5ms: this rate

of decay was similar to that observed for events on the front-face of the module, as described in Section 4.2.1.2.

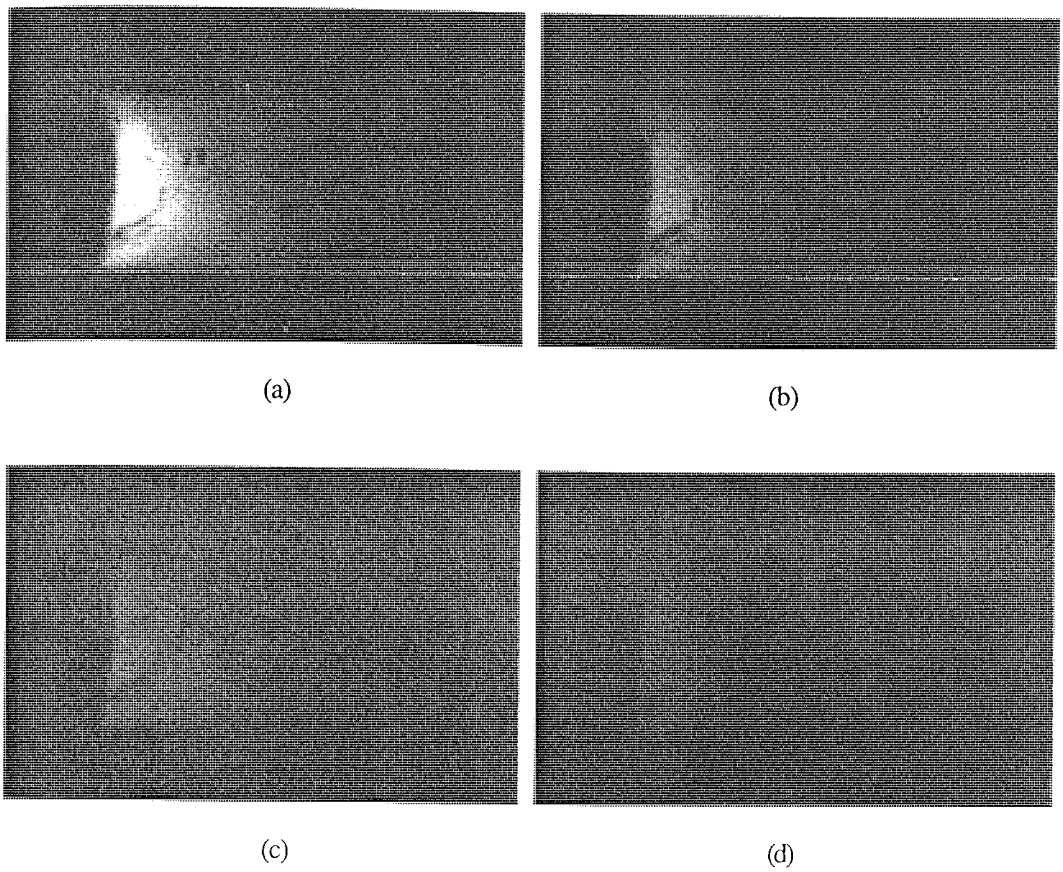

Fig. 4.2.18 Consecutive millisecond frames of photon-emission from a flashover event along the side of the alumina cylinder

Figure 4.2.19 plots the spatial intensity of the recorded luminescence through a line-scan from the anode connection along the ceramic surface.

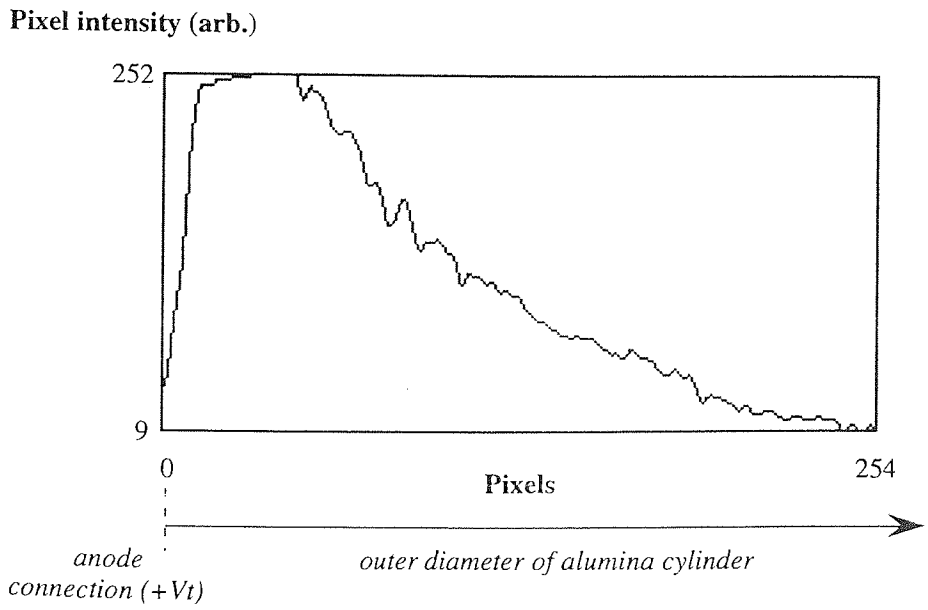

Fig. 4.2.19 Pixel-intensity line-scan of photon-emission from a flashover event

4.2.3.3 Development and propagation-velocity of jet phenomena To improve upon the millisecond time-resolution in the estimated jet velocity outlined in Section 4.2.1.3, further fast-frame images were recorded, orthogonal to the alumina module axis. Figure 4.2.20(a) shows a view of the module through viewport **2** (see Fig 3.2.10), whilst Fig 4.2.20(b) records the optical phenomena associated with an EHV surface-flashover on the front face of the alumina.

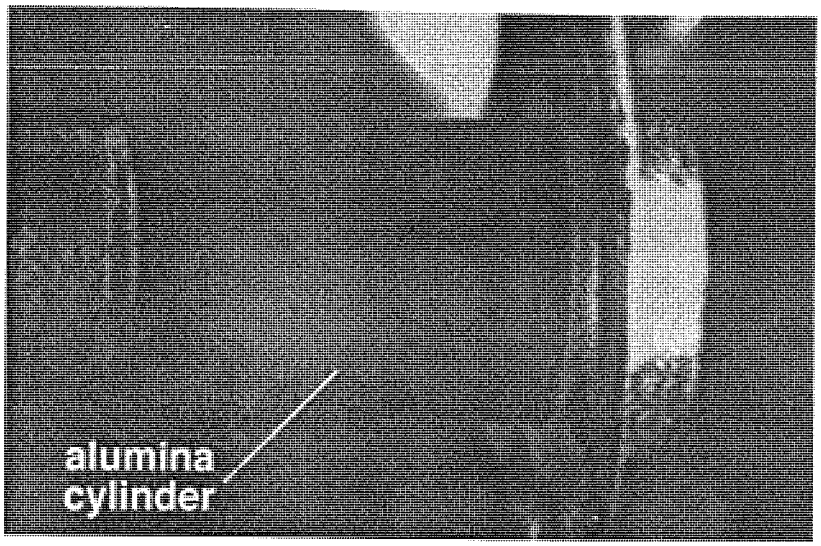

(a)

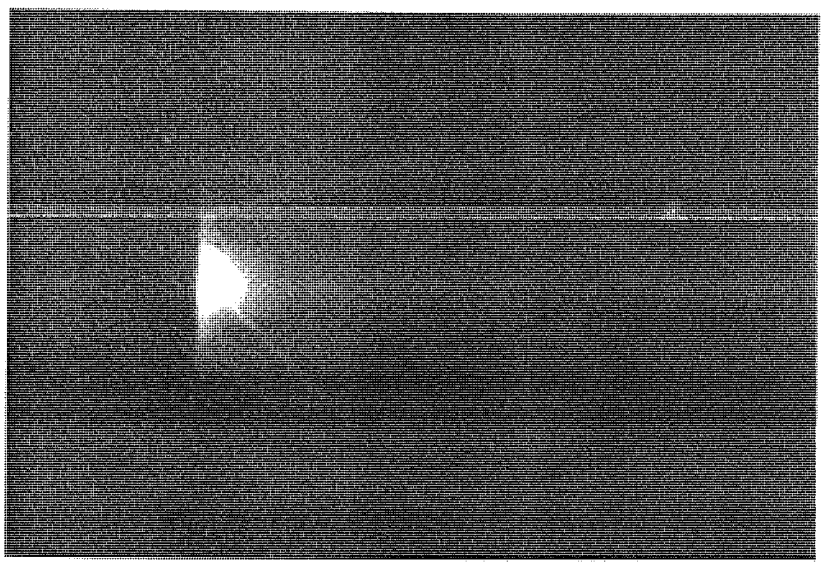

(b)

Fig. 4.2.20 (a) Side view of alumina module, and (b) 1ms frame of flashover event

From the 1ms frame of Fig 4.2.20(b), the recorded jet length of ≈5mm denotes an estimated jet velocity of $\approx 5 ms^{-1}$: this *minimum* estimate of jet velocity is comparable to the $10 ms^{-1}$ figure displayed in Fig 4.2.5(a). Furthermore, a bright region, or "flash", is visible at the 'root' of these jets, obscuring a full view of the

jets themselves. Thus, the faster operation of the Imacon camera could afford a temporal separation of the respective "flash" and jet events.

Figure 4.2.21(a) presents an initial 5μs image showing the side profile of a surface-flashover event, showing the bright 'flash' region on the front face of the alumina module. This frame is followed by a longer 1ms image (Fig 4.2.21(b)), which shows a group of jets propagating away from the site of the luminous centre.

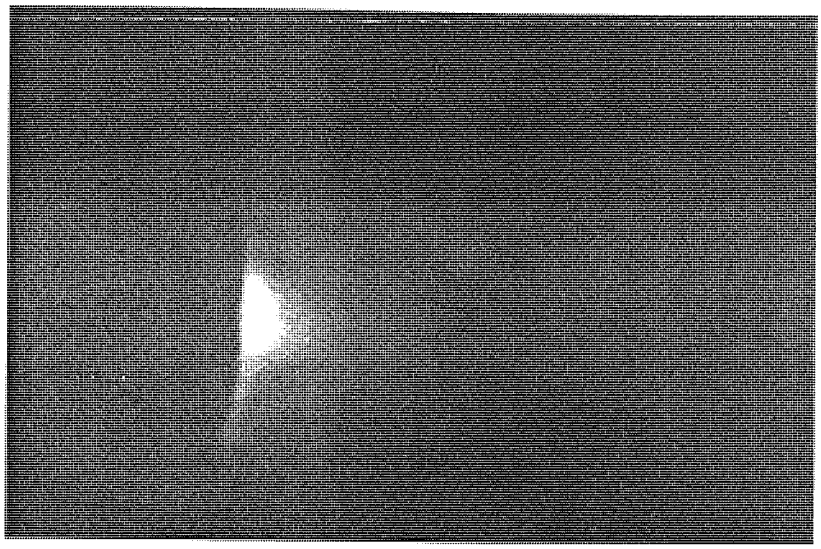

(a)

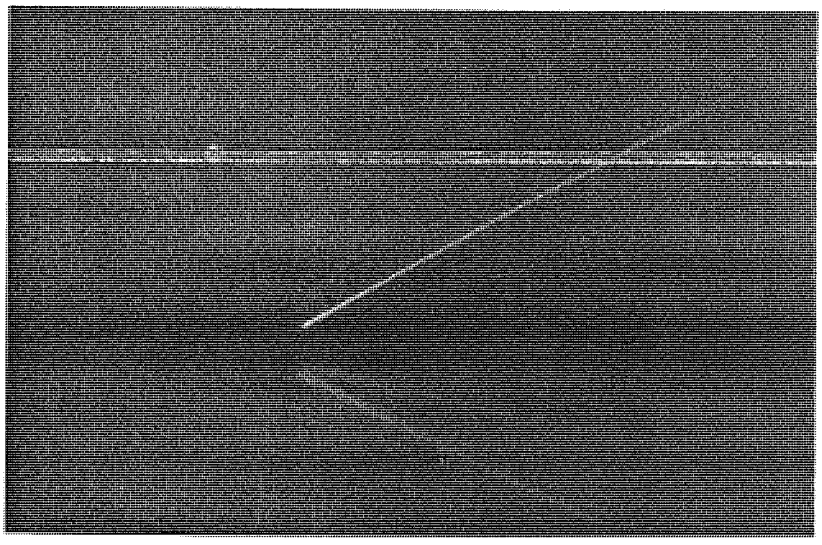

(b)

Fig. 4.2.21 (a) Initial 5μs and (b) subsequent 1ms frames showing side profile of EHV pulsed breakdown event

For an accurate estimate of the jet velocity, Fig 4.2.21(b) does not offer sufficient time-resolution of the captured jet image. Consequently, the camera framing speed

was increased to 20000 fps, which produced the consecutive series of 50μs frames shown in Fig 4.2.22. For clarity, the intensity-levels of these images were inverted, producing sharper outlines in the captured frames of the propagating jets.

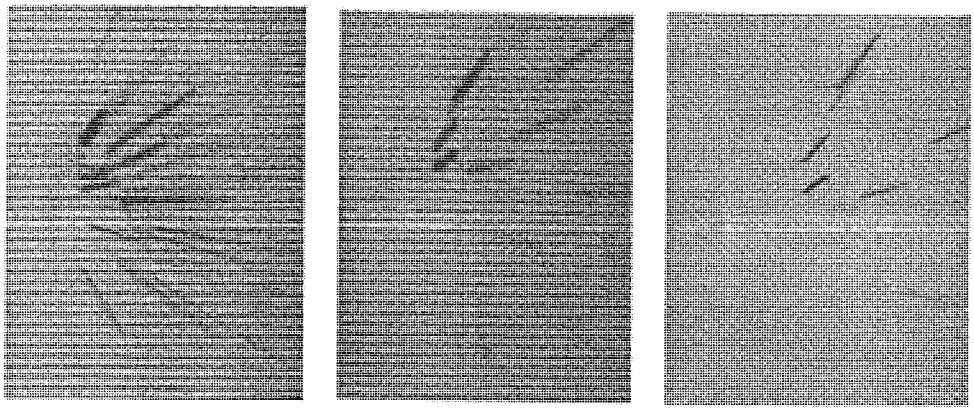

(a) (b) (c)

Fig. 4.2.22 Consecutive 50μs frames of propagating jets (inverted images)

In all three of the frames shown in Fig 4.2.22, the recorded lengths of the jets are in the region of $1mm \leq l_{jet} \leq 5mm$. Given this range of lengths within each 50μs framing period, the jet velocity, v_{jet}, may be estimated to be in the range $20ms^{-1} \leq v_{jet} \leq 100ms^{-1}$.

4.2.4 Spectroscopy of pulsed flashover events The ballistic behaviour exhibited by the jets prompted a spectroscopic study of the possible nature of the observed surface-flashover phenomena. Optical and electronic techniques were employed, to investigate the characteristics of any material species associated with the jets or luminous centres.

4.2.4.1 Spectral nature of optical emissions The direct observation of breakdown-events with a naked, dark-adjusted eye reveals the emitted radiation to be bright-blue in colour. This observation can be confirmed by recording successive breakdown flashover events with a series of low-pass optical filters placed on the optical axis between the experimental module and the intensified high-speed camera. Thus, imaging pulsed-field flashover events through successive filters, starting with a filter having a cut-off wavelength of 467nm, there was a progressive attenuation of the recorded emission, until no emission was recorded from the jets with a 678nm filter in place.

In contrast, optical emission from the localised luminous centres in the alumina gap (as shown in Fig 4.2.1(a)) continued to be detected with each of the above filters; it

was only by inserting a 706nm filter that the photon-emission from the luminous centres was ultimately masked from the high-speed CCD detector. These findings therefore suggest that the emitted jets contain a high spectral content of blue photon-emission, whereas the luminous centres in the 300μm-wide ceramic region of the electrode-samples appear to emit photons that are predominantly in the deep-red (680-700nm) wavelength region.

4.2.4.2 Current measured through auxiliary anode collector A transparent anode [25,26] was introduced into the experimental regime, and located at a parallel spacing of 2mm from the end-face of the metallized alumina tube. The anode was terminated to ground (0V) via a 10Ω current-viewing resistor (CVR). Figure 4.2.23 shows an oscillogram of a negative current-pulse collected through the anode, of approximately 10A amplitude.

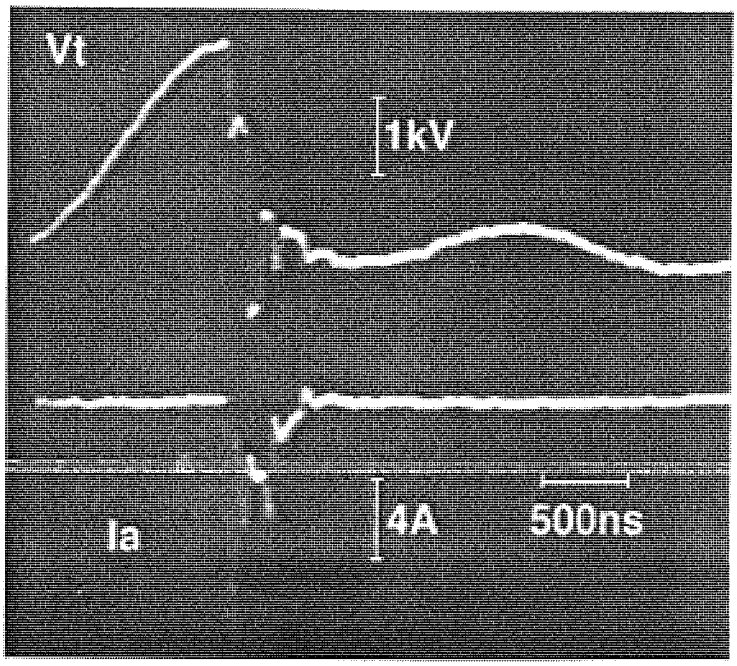

Fig. 4.2.23 Oscillogram of voltage-breakdown waveform (amplitude $V_t \approx +3kV$), together with the current-pulse waveform (I_a) recorded through a transparent anode

This waveform indicated an emission of negative current from the alumina specimen, coincident in time with the collapse of the applied HV pulse (V_t) across the alumina insulator. The current-pulse shown in Fig 4.2.23 corresponds to the observed impacts of jets upon the anode target illustrated in Fig 4.2.15(b). The magnitude of the collected current exceeded an estimated 1A of displacement current, arising from the electrode module - transparent anode parasitic capacitance.

4.2.5 Spatial correlation of DC and pulsed-field emissions Alumina modules were subjected to pulsed fields as described in Section 4.2.1, followed by a study of their DC prebreakdown behaviour. Figure 4.2.24 displays the outline of an alumina specimen, whilst Fig 4.2.25 shows the imaged photon-emission and recorded oscillogram from a pulsed breakdown event.

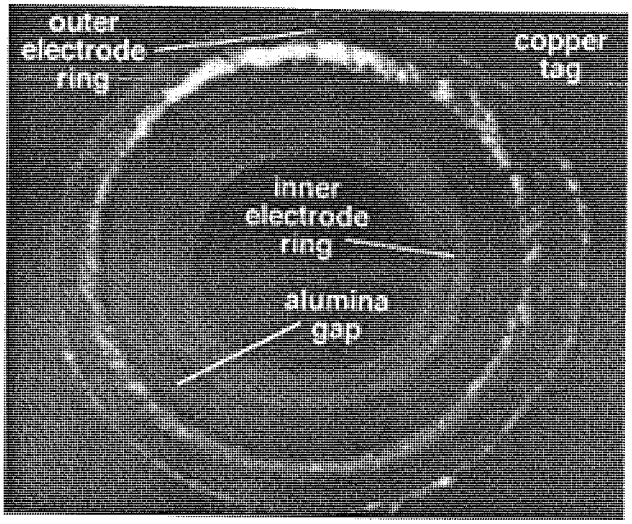

Fig. 4.2.24 Outline view of alumina module front-face

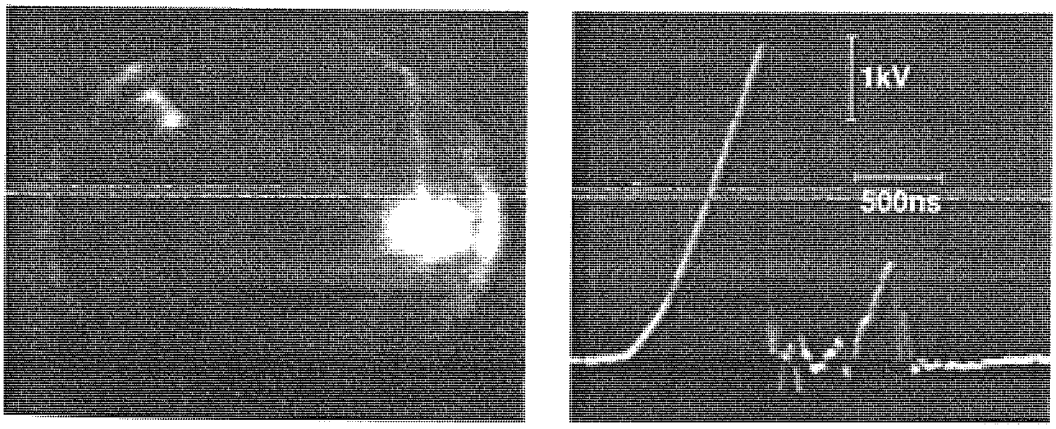

Fig. 4.2.25 (a) Pulsed breakdown event, and (b) corresponding voltage-pulse (V_t) oscillogram

Referring to Fig 4.2.25(a), two surface-flashover luminous centres (Section 4.2.1.1) are visible within the alumina gap, with a major luminous centre to the right of the image appearing to emit several bright jets. Recordings of two luminous centres from a single breakdown event were typified by the form of oscillogram shown in Fig 4.2.25(b), where the first breakdown pulse is followed by a second rising half-cycle of the applied voltage waveform (Fig 3.2.5(a)).

Applying a DC electrical field to the same alumina module, the prebreakdown image depicted in Fig 4.2.26 was observed. This image portrays an extended 'doughnut' emission around the annulus of the alumina gap, with a single bright-blue 'spot' on the right side of the ceramic annulus. An unusual feature of this image was the appearance of a bright red/pink region on the left side of the 300μm alumina annulus. This red/pink region was situated radially opposite to the blue spot, and its appearance coincided with the ignition of this spot.

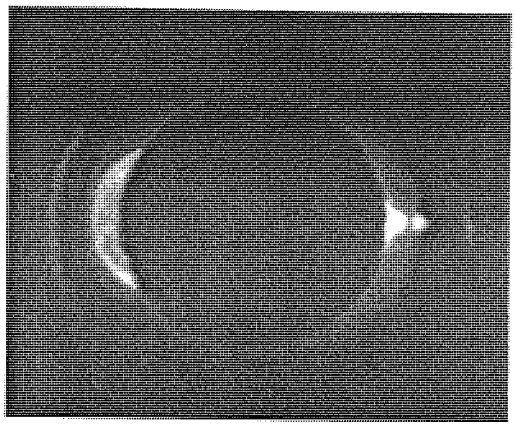

Fig. 4.2.26 Image of DC prebreakdown photon-emission (V_t = 3kV, I_t = 40μA)

Comparison of the pulsed-field and DC images, portrayed in Figs 4.2.25(a) and 4.2.26 respectively, revealed that the (pulsed) luminous emission centre and the bright-blue DC spot appeared to be located within the same spatial region. This spatial correlation was also found with initial DC observations, followed by the application of HV pulses; i.e. in the reverse sequence described for Figs 4.2.25 and 4.2.26.

To pursue this apparent spatial correlation between pulsed and DC electro-optical events, Section 4.3 includes a detailed study of the electro-optical behaviour and surface-microtopography of an alumina module. The scanning electron microscopy (SEM) techniques detailed in Section 3.3.1 allowed a detailed mapping of the physical microstructure of alumina modules. SEM analysis could be undertaken both before and after the *in vacuo* electro-optical analysis of the 'mapped' module within the experimental system.

4.3 Experimental findings III - surface analysis

A series of surface-analytical studies provided a detailed description of the structure and constitution of various experimental specimens. The scope of this analysis was divided into two key areas, namely (i) the characterisation of experimental alumina modules, and (ii) the investigation of target materials which were exposed, in vacuum, to ejected material resulting from the pulsed-field surface-flashover of trigger modules.

4.3.1 Surface topography of alumina module Scanning electron microscopy was employed for a detailed investigation of the surface microfeatures of the metallized alumina modules whose electrical and optical characteristics are detailed in Sections 4.1 and 4.2. Figure 4.3.1 presents an electron micrograph of the 'active' end-face of an alumina module, described in Section 3.1.1, as it would be viewed experimentally along the centre-axis of the specimen.

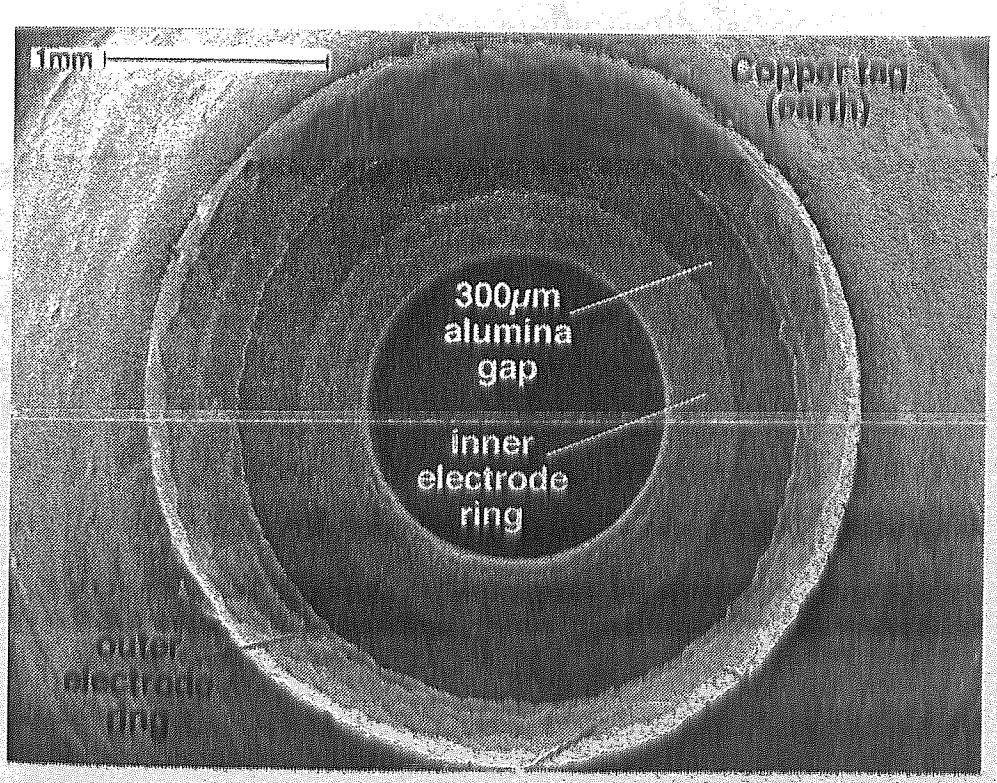

Fig. 4.3.1 Electron micrograph showing front face of metallized alumina module

Figure 4.3.1 clearly shows the arrangement of the co-axial metallized rings on the end-face of the alumina tube, together with the silver-copper braze joint which secures the copper tag of the adjacent electrode to the outer metallized ring. Interestingly, two small cracks can be seen in this braze, and are visible towards the

bottom of Fig 4.3.1. Sections 4.3.2 and 4.3.3 will go on to present magnified views of local surface features on the alumina modules.

4.3.2 Microstructure of metallized ceramic M-I region Key areas of the M-I-M regime in the alumina module are the interfaces between the alumina dielectric and the electrodes. Thus, Figs 4.3.2(a) and (b) present orthogonal micrographs of the M-I interface at the edge of the metallized inner electrode-ring.

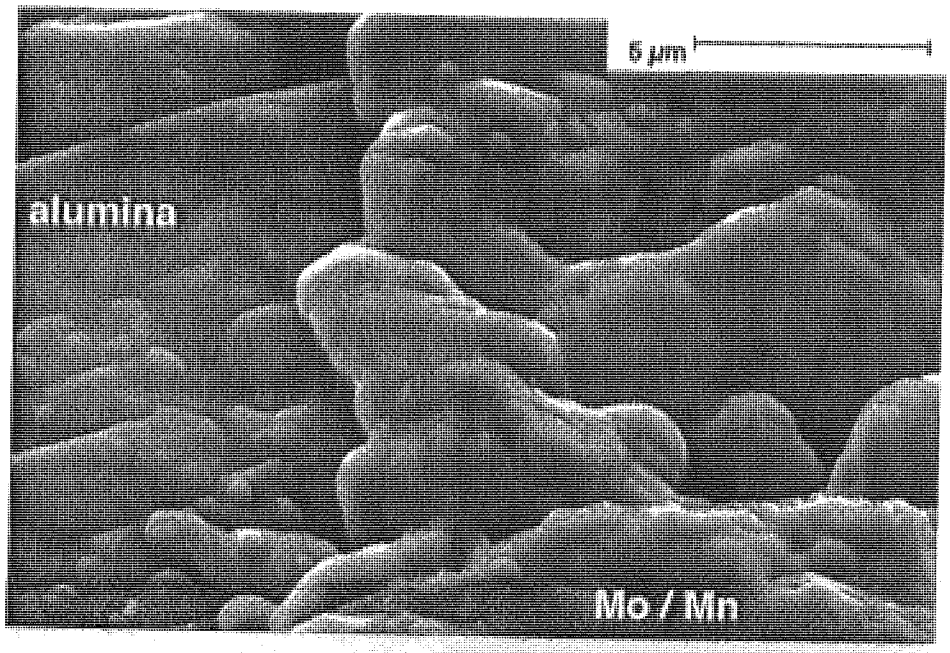

(a)

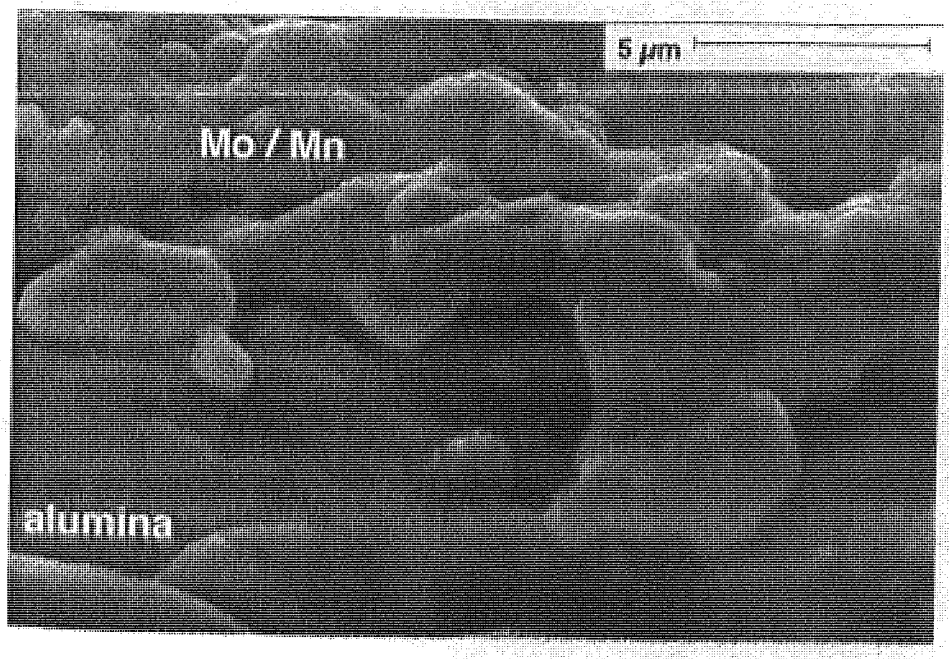

(b)

Fig. 4.3.2 Metallized alumina M-I regions at edges of (a) outer and (b) inner electrode rings

These micrographs indicate that the molybdenum/manganese (Mo/Mn) metallization does not appear to be in *intimate* contact with the alumina ceramic substrate. Instead, Fig 4.3.2(b) shows several areas of metallization which are in point contact with the ceramic, with these contact areas separated by voids between the alumina and the metallization.

Similar voids in the metallizing edge can also be seen around the outer electrode-ring, as illustrated by the micrograph of Fig 4.3.3. Many alumina modules showed the copper-silver (Cu / Ag) braze, which secured the adjacent copper tag to the outer electrode-ring of the alumina tube, to have run out to the extreme edge of the outer-ring metallization.

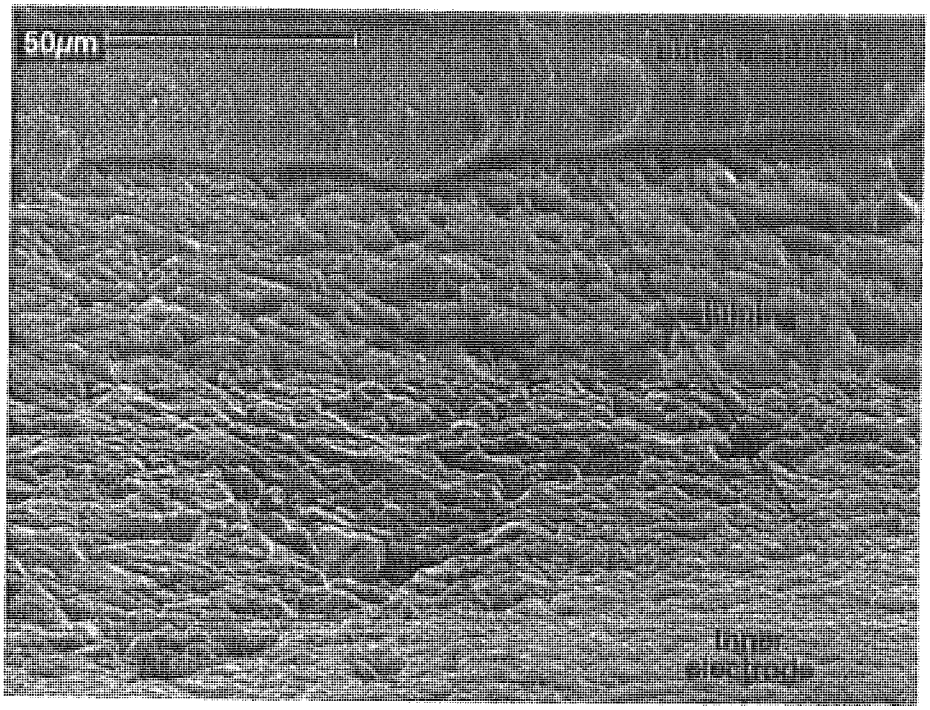

Fig. 4.3.3 Oblique view across the inner electrode-ring and the 300µm alumina region towards the brazed outer electrode-ring

4.3.3 Surface microtopography of alumina ceramic Figure 4.3.4 illustrates the granular structure observed in the alumina ceramic of the electrode module. This micrograph indicated a mean grain size of approximately 10µm, which is in keeping with the specification of the ceramic material outlined in Section 3.3.2.1.

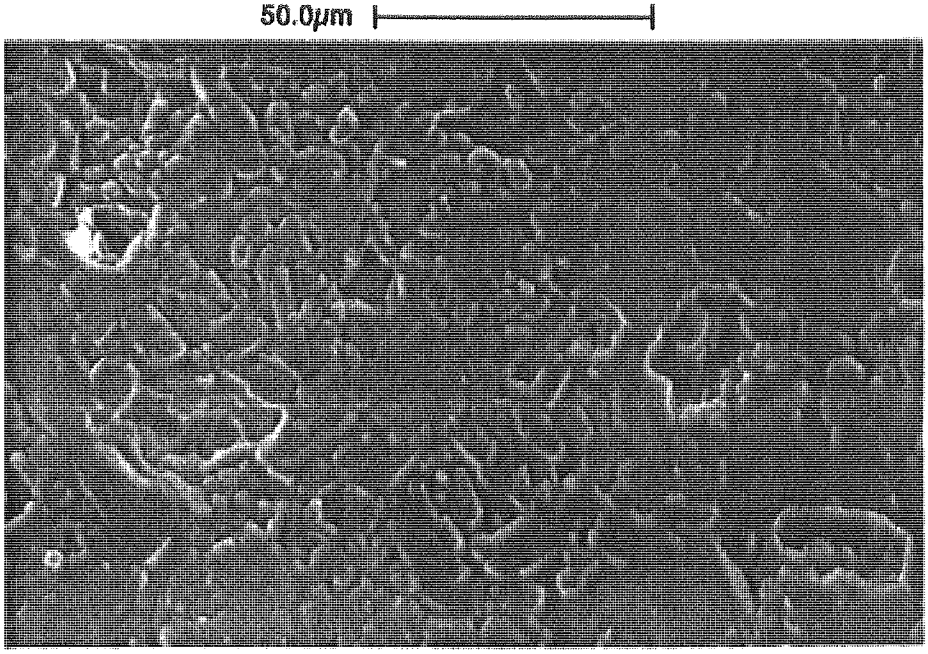

Fig. 4.3.4 Surface detail of alumina region between the electrode rings

However, it is apparent from Fig 4.3.4 that there is widespread *porosity* within the ceramic surface. The lateral dimensions of the pores are between 10μm and 20μm; by comparing the electron-beam working-distance at the surface and at the bottom of each pore, measurements of pore depth were found to be in the region 5μm to 30μm. Further details of these pore structures, and their possible influence upon the electrical and optical properties of the alumina ceramic, are described in the following sections.

4.3.4 Microfeatures at sites of localised optical emission phenomena

Uncoated alumina modules were analysed under the SEM to give secondary-electron (SE) images of the alumina surface *prior to* the introduction of the module into the experimental system (see Section 3.3.1). As illustrated in Fig 4.3.5(a), this analysis produced a topographical map of the metallized ceramic. These 'mapped' ceramic samples were then subjected to DC electrical fields within the experimental system described in Section 3.2.2, whilst concurrent optical events observed on the alumina module were imaged using the analytical system of Section 3.2.4.1.

A typical DC prebreakdown image is presented in Fig 4.3.5(b), showing the localised 'spots' and extended 'doughnut' photon-emissions which were previously described in Section 4.1. Careful analysis of the prebreakdown image in Fig 4.3.5(b) showed that the bright-blue spots, which were observed in the exposed alumina region, appeared to correlate with the locations of pore sites identified in the SE micrograph of the alumina module (Fig 4.3.5(a)).

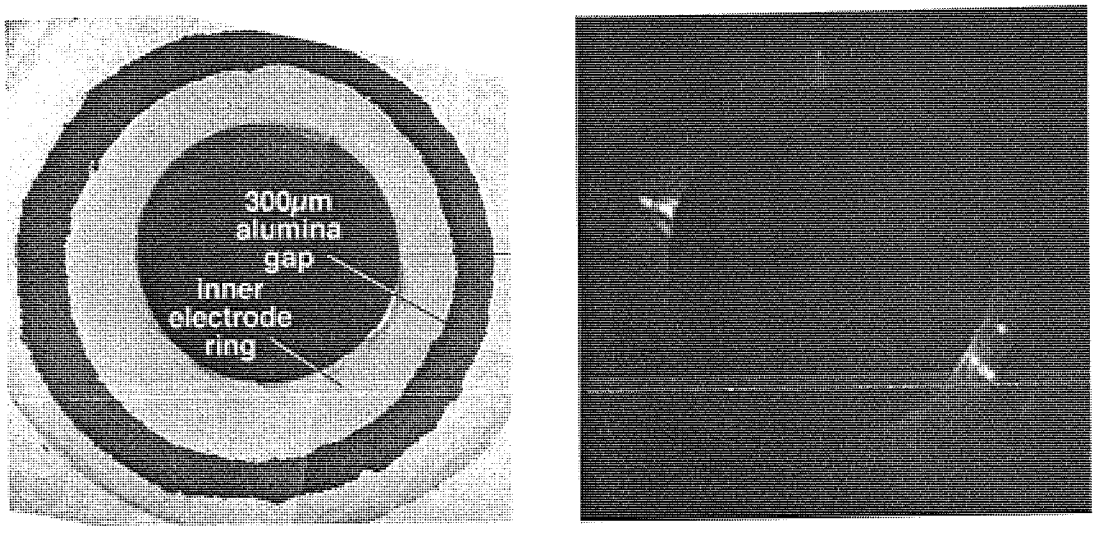

(a) (b)

Fig. 4.3.5 (a) Secondary electron image of alumina module, with (b) image of DC prebreakdown photon emission (V_t = +4kV, I_t = 1.5μA)

Figure 4.3.6 presents magnified images of the ceramic surface-topography and DC prebreakdown image, in order to clarify the apparent spatial relationship between the ceramic pores and the observed DC photon-emission from the alumina specimen.

Figure 4.3.6(b) shows two DC spots which were imaged in the lower right portion of Fig 4.3.5(b). As shown in the secondary electron micrograph of Fig 4.3.6(a), these two bright-blue spots appear to coincide with the spatial locations of two pores in the alumina region of the metallized module.

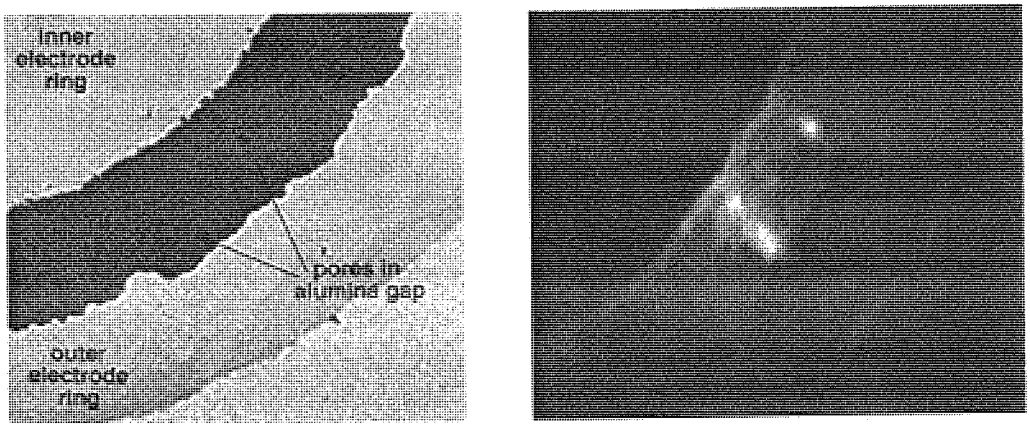

(a) (b)

Fig. 4.3.6 (a) Secondary electron (SE) image of alumina region, with (b) corresponding DC prebreakdown 'spots' at porous sites

The alumina module was then removed from the experimental system and sputter-coated with a gold film in readiness for back-scattered electron (BSE) analysis in the SEM (see Section 3.3.1). Thus, Fig 4.3.7 portrays a detailed BSE image of the alumina region shown in the SE micrograph of Fig 4.3.6.

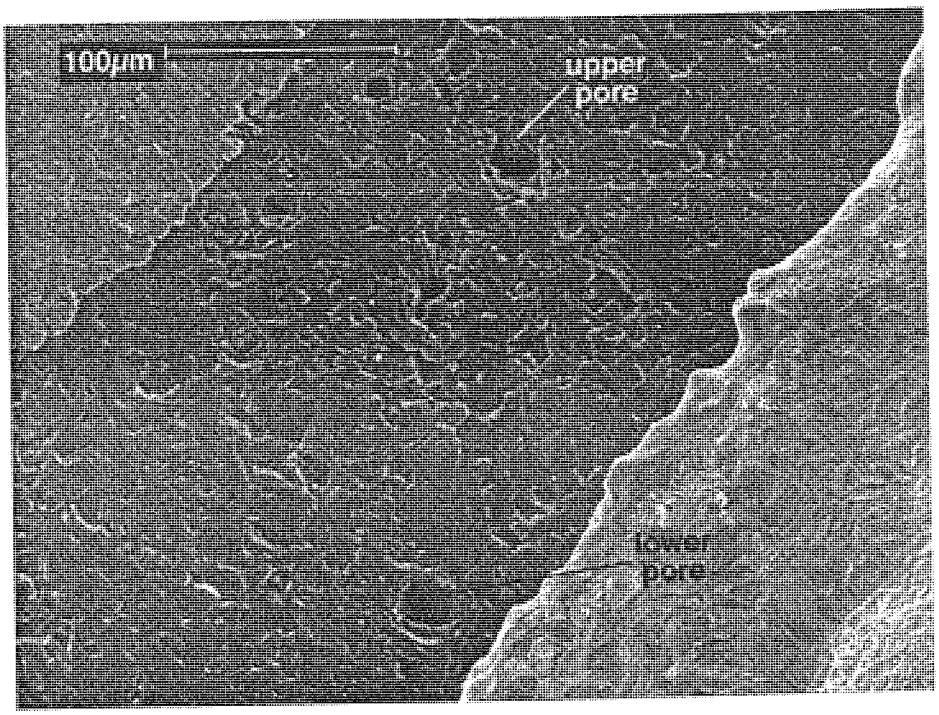

Fig. 4.3.7 Back-scattered electron (BSE) image of porous alumina region

Two pores are clearly seen in the ceramic region between the two ring-electrodes: prebreakdown photon-emission had been previously observed in the vicinity of these pore defects (see Figs 4.3.5(b) and 4.3.6(b)). Electron micrographs of the two pores are shown in Figs 4.3.8(a) and 4.3.8(b): the lateral dimensions of these pore cavities were around 20μm, with the depth of both pores measuring ≈25μm.

(a) (b)

Fig. 4.3.8 Back-scattered electron (BSE) images of (a) upper and (b) lower pores observed in alumina region

Similar observations of high-voltage (HV) pulsed breakdown events, described in Section 4.2.1.1, also revealed a spatial correlation of this porosity in the alumina with the location of luminous optical emission centres in the pulsed-field surface-flashover of the alumina module. This finding was consistent with the observed correlation of pulsed breakdown events with DC prebreakdown spots, reported in Section 4.2.5.

4.3.5 Species profiling of alumina trigger ceramic Analytical investigations were undertaken of the alumina ceramic used in the experimental specimens described in Section 3.1. X-ray photoelectron spectroscopy (XPS) and microprobe Rutherford backscattering spectrometry (μ-RBS) were employed, as complementary surface analysis techniques.

4.3.5.1 XPS signature of alumina material Two types of XPS spectra were recorded from the alumina ceramic: photoelectron spectra were recorded at normal (0°) beam incidence with respect to the alumina sample, and also at a 'glancing angle', ϕ, of 85°; i.e. incidence of the glancing-angle X-ray beam was at 5° to the sample surface. Figure 4.3.9 illustrates these normal and glancing-angle (ϕ) geometries of the diagnostic X-ray beams; the corresponding XPS spectra are depicted in Figs 4.3.10(a) {ϕ=0°} and 4.3.10(b) {ϕ=85°}.

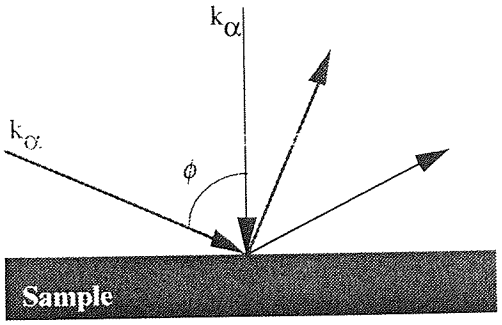

Fig. 4.3.9 Illustrating normal-incidence and glancing-angle X-ray beam geometries

With reference to Fig 4.3.10, both XPS spectra show the aluminium (Al), silicon (Si) and oxygen (O) constituents of the alumina (Al_2O_3) ceramic. A large carbon (C) signal may also be seen, which arose within the UHV system of the ESCA instrument from the deposition of successive monolayers of vacuum-pump oil. The normal-incidence spectrum of Fig 4.3.10(a) displays a small calcium (Ca) peak, indicating the presence of Ca impurity within the *bulk* of the alumina.

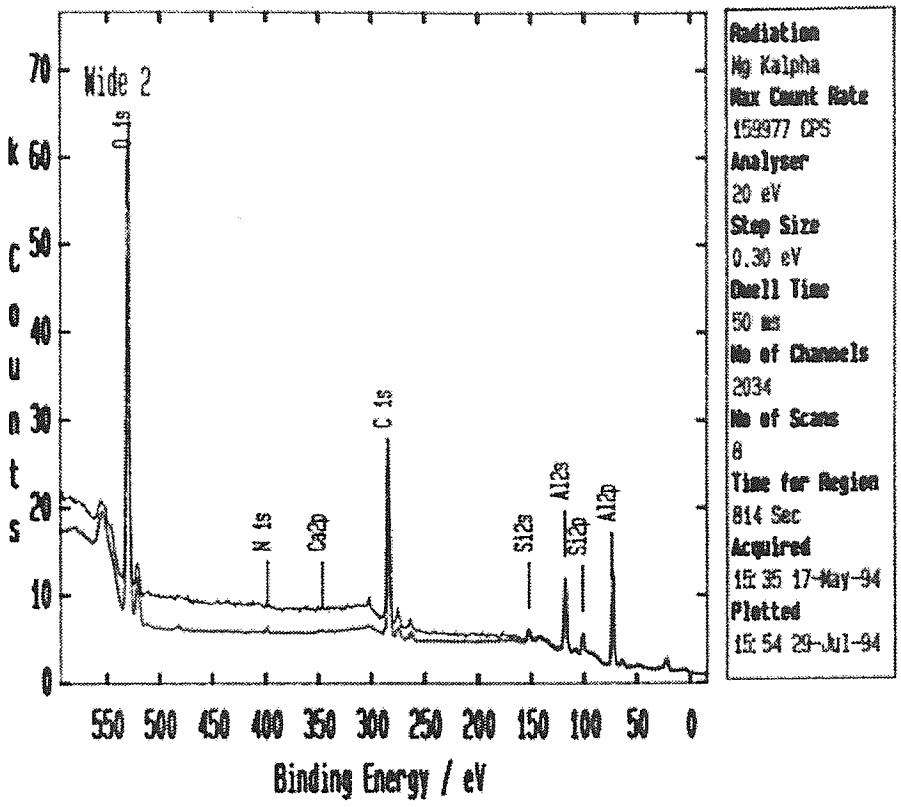

(a)

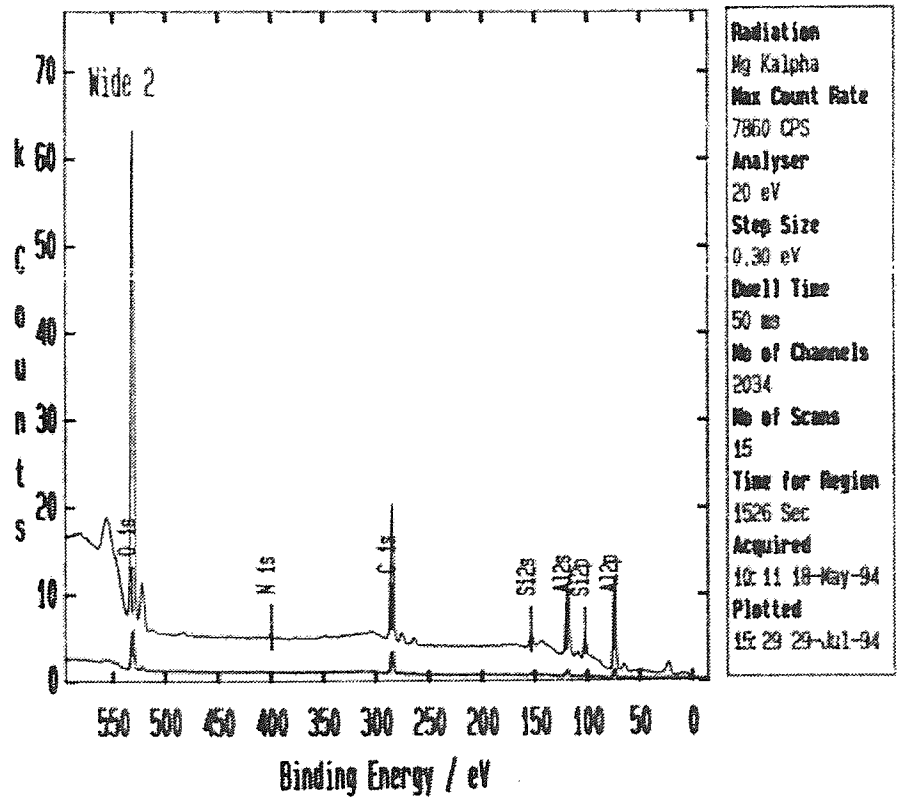

(b)

Fig. 4.3.10 X-ray photoelectron spectra of alumina ceramic, for (a) normal (0°) and (b) 85° glancing-angle beam incidence

Conversely, the glancing-angle spectrum of Fig 4.3.10(b), which highlights the elemental composition of the ceramic surface-layers, does not show a Ca signal, but instead indicates a stronger Si signal from this analysis of the ceramic surface. This finding appears to confirm the previous observation of Ca as a bulk impurity (Fig 4.3.10(a)), and also suggests a segregation of the silica (SiO_2) glass phase towards the surface-layers of the alumina ceramic.

4.3.5.2 μ-RBS analysis of alumina ceramic A RBS analysis was performed upon the ceramic tubes of assembled alumina modules [207]: this direct observation of the alumina, in the 300μm gap between the metallized electrode-rings, was facilitated by the small spot-size (50μm) of the RBS ion-beam, as described in Section 3.3.3. Reflected ions were collected in a 512 channel detector, with an energy range of 3.108 keV per channel (calculated for an incident beam of 1.5MeV He^4 ions).

RBS data was recorded for 'standard' 94% alumina samples (see Section 3.3.2.1), and also for similar alumina specimens which had been implanted with chromium (Cr) ions, (see Section 3.4.1). Figure 4.3.11 displays RBS spectra for both a standard ceramic specimen (spectra #1 and #2), and also for Cr-implanted alumina.

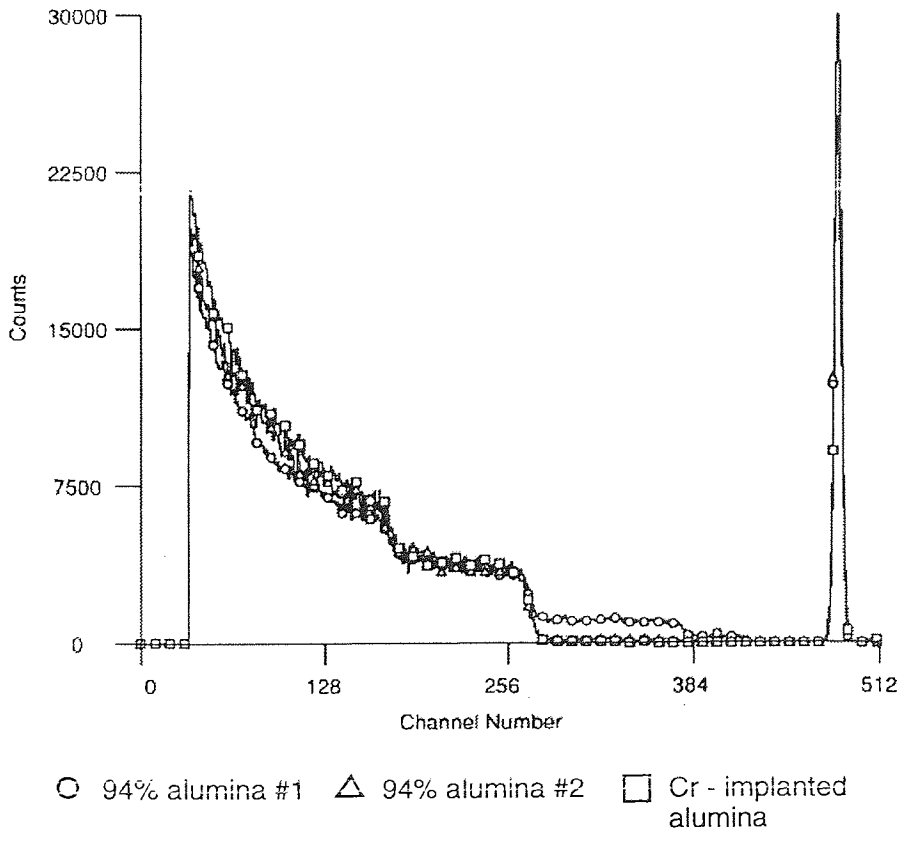

Fig. 4.3.11 RBS spectra of alumina ceramics

Aluminium (Al) and oxygen (O) species within the alumina (Al_2O_3) are clearly shown by RBS spectral edges at channels 177 (O) and 271 (Al). A large high-energy signal was seen to be returned to the detector, indicating some electronic charging of the alumina samples, and consequent space-charge repulsion of the incident ion beam.

Copper (Cu) and silver (Ag) species are indicated by spectral edges at channels 377 and 420 respectively, in the alumina #1 spectrum of Fig 4.3.11. These spectral features may have resulted from the ion-beam striking the brazed copper tag of the alumina module. The 50μm-diameter ion beam spot was therefore stabilised, in order to minimise any impingement upon the brazed copper tag. A further set of normalised RBS spectra were recorded for both the standard and Cr-implanted alumina modules, and are shown in Fig 4.3.12.

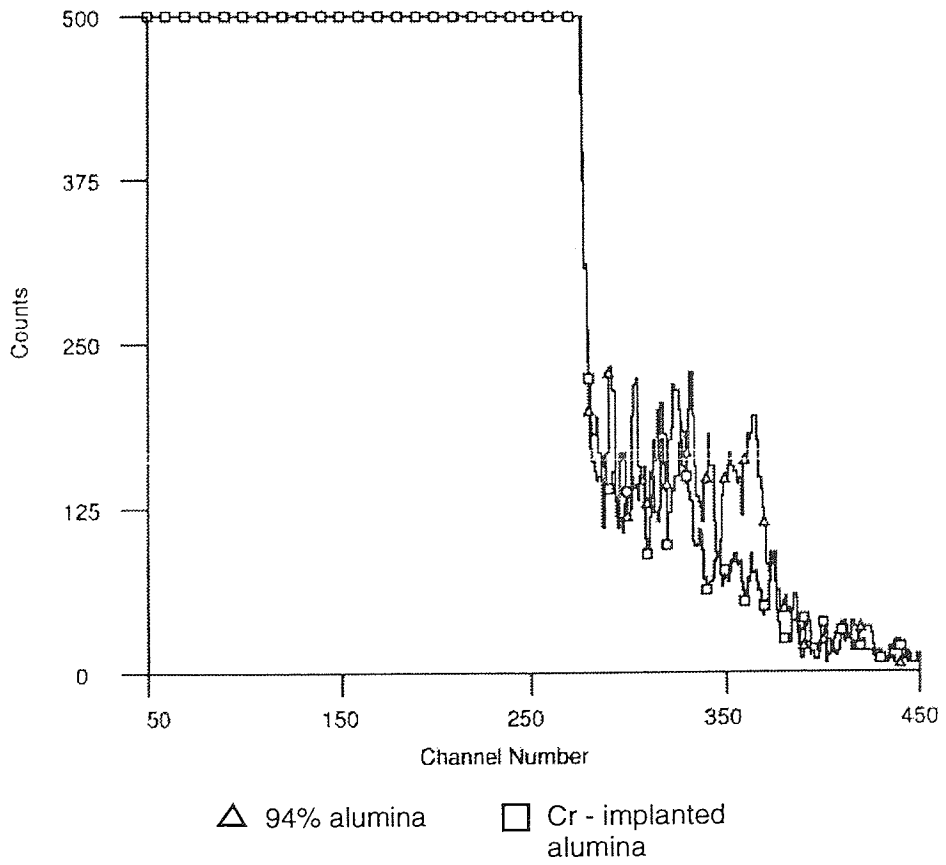

Fig. 4.3.12 Normalised RBS spectra of alumina ceramics

Once again, a large Cu signal (channel 377) is visible in the 94% alumina spectrum of Fig 4.3.12. The spectrum of the implanted sample shows an 'edge' at channel 334 (corresponding atomic mass 41/42 amu), indicating the presence of calcium (Ca) within the alumina matrix.

4.3.6 Collected efflux material from HV (5kV) flashover events

Surface analysis techniques were used in two further investigations to determine the nature of any material emitted from the pulsed breakdown of an alumina module. Niobium foils were used as targets in front of alumina modules, and were exposed to pulsed-field surface-flashover events, which occurred *in vacuo* on the module end-face (see Section 3.3.2.2). The first such investigation looked at high-voltage (HV) surface-flashovers on the metallized alumina, using the 5kV voltage-pulses described in Section 3.2.3.1 (see also Section 4.2.1.1). A second analysis involved *extra*-high voltage (EHV) pulses, and is documented in Section 4.3.7.

4.3.6.1 XPS spectrum of HV Nb foil collector X-ray photoelectron spectroscopy (XPS) [199] of the exposed Nb foil was undertaken to examine the nature and state of any emitted material, or *efflux*, which was collected from pulsed breakdown events on the alumina module. Figure 4.3.13 gives the XPS spectrum of an 'unexposed' region of the niobium foil material, together with that of a target region which was 'exposed' to the pulsed-field flashover events on the alumina specimen.

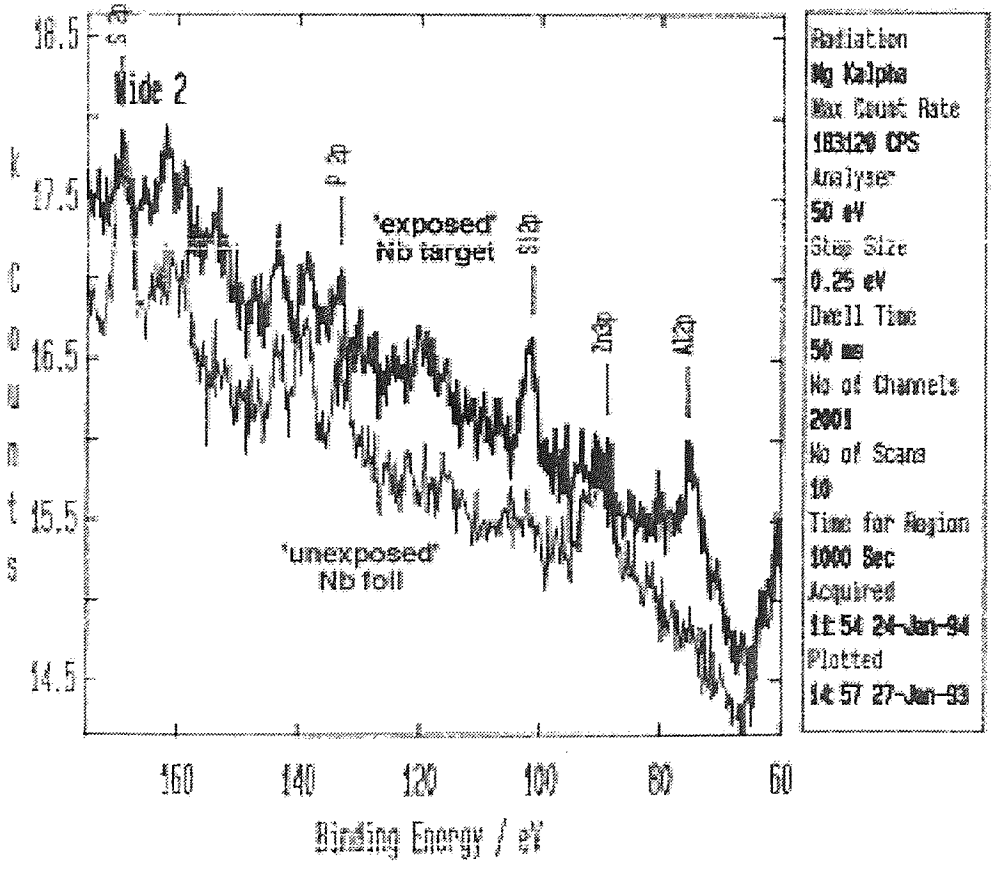

Fig. 4.3.13 X-ray photoelectron spectra of Nb foil collector, and exposed Nb target

The XPS spectrum of the exposed Nb target shows two distinct electron-energy peaks at 105eV and 75eV, corresponding to Si and Al species respectively [199]. Figure 4.3.13 also shows that neither Si nor Al were detected as intrinsic impurities within the unexposed Nb foil material. Tables 4.2.and 4.3 provide a detailed breakdown of the XPS spectra presented in Fig 4.3.13. This data reveals a small deposition of copper (Cu) on the exposed Nb target, in addition to the Al and Si species described above.

Element	Atomic [%]	Atomic ratio	Centre [eV]
Nb 3d	14.964	24.774	206.86
C 1s	41.373	68.494	284.60
O 1s	39.203	64.900	530.55
Ca 2p3	1.096	1.815	347.10
S 2p	1.597	2.643	169.10
Zn 2p3	0.643	1.065	1022.00
P 2p	0.604	1.000	133.35
Na 1s	0.520	0.860	1072.15

Table 4.2 XPS spectrum of niobium foil substrate

Element	Atomic [%]	Atomic ratio	Centre [eV]
Nb 3d	15.020	32.316	206.85
C 1s	43.692	94.009	284.60
O 1s	35.835	77.104	530.30
Ca 2p3	0.917	1.974	347.60
S 2p	1.005	2.163	169.60
Zn 2p3	0.465	1.000	1021.90
P 2p	0.617	1.327	133.85
Na 1s	0.579	1.247	1071.50
Cu 2p3	0.107	0.230	932.70
Al 2p	0.688	1.480	74.35
Si 2p	1.075	2.314	102.60

Table 4.3 XPS spectrum of exposed HV niobium target

4.3.6.2 SEM analysis of HV Nb target Analyses of both unused Nb foils and exposed Nb targets were undertaken in a scanning electron microscope (SEM). These studies revealed a distribution of microparticles on the niobium target surface that were not detected on the unused Nb foil. Figures 4.3.14(a) and 4.3.14(b) present electron micrographs of such a microparticle.

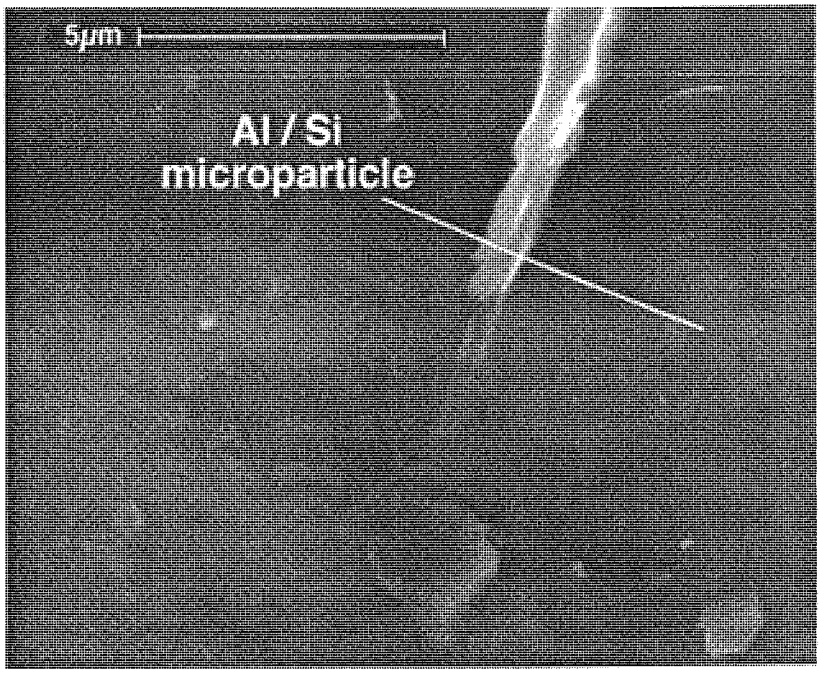

(a)

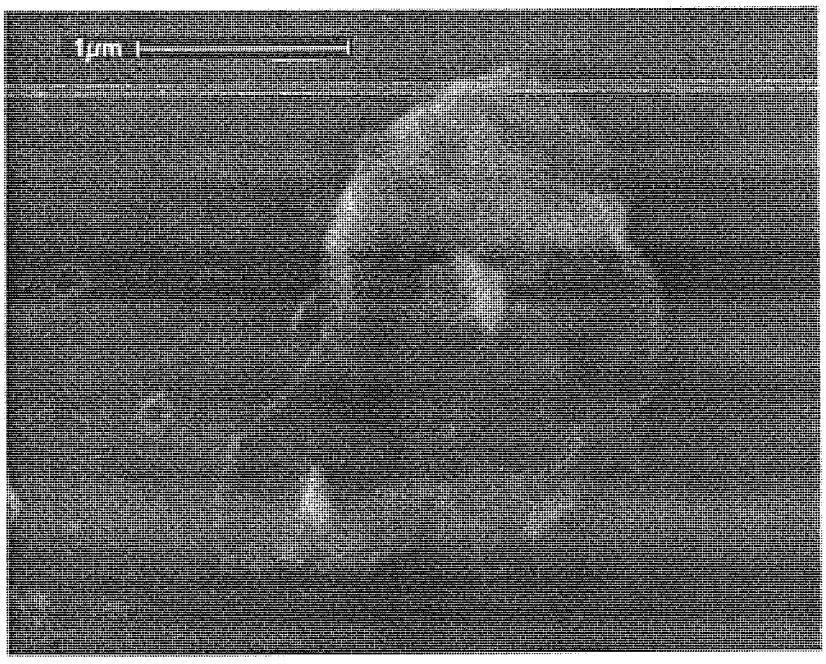

(b)

Fig. 4.3.14 Electron micrographs showing (a) surface of exposed Nb foil, and (b) collected microparticles of Al / Si material

Energy-dispersive X-ray analysis (EDXA) in the SEM showed the scanned microparticles (Fig 4.3.13(b)) to consist of aluminium (Al) and silicon (Si) material species. This finding was consistent with the electron-energy peaks in the XPS spectrum of the exposed niobium foil (Fig 4.3.13), previously described in Section 4.3.6.1.

4.3.7 Collected efflux material from EHV (20kV) flashover events Niobium foil collectors were affixed to further alumina modules, and extra-high voltage (EHV) pulses, of the type described in Section 3.2.3.2, were applied to the inner electrode-ring of the alumina specimen.

4.3.7.1 Analysis of EHV Nb target Following the application of 50 EHV pulses to the alumina module, the Nb target was removed from the experimental system. An annular region on the exposed surface of the target was found to be 'scarred' with a dark region of discoloration. Fig 4.3.15 shows this exposed EHV target alongside an unexposed piece of niobium foil. The outer periphery of this scarred area on the exposed target has been marked with a metal scriber, to provide a reference outline for the subsequent XPS analysis of this region.

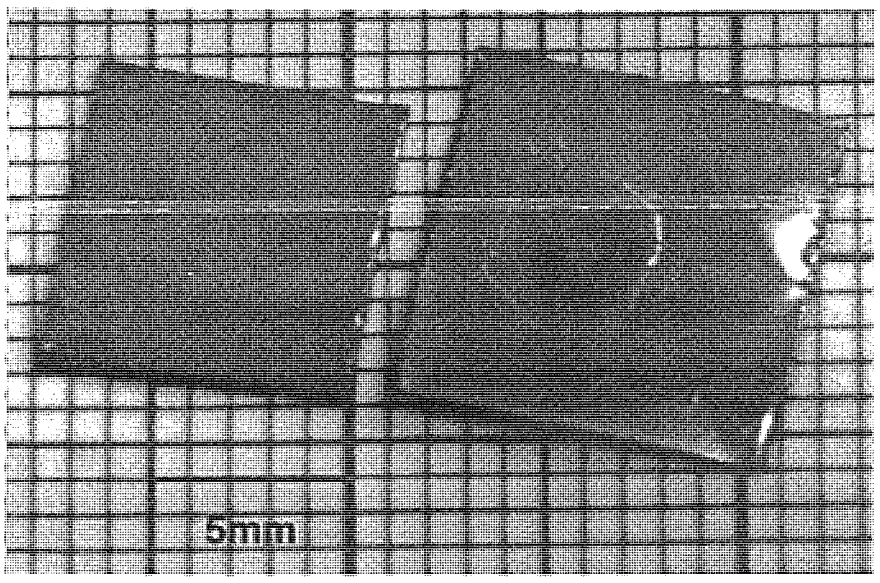

Fig. 4.3.15 Niobium foil {left} and exposed EHV Niobium target {right}

4.3.7.2 XPS spectrum of EHV Nb foil collector The XPS analysis described for the HV target in Section 4.3.6.1 was repeated for the EHV target portrayed in Fig 4.3.15. This analysis was conducted in the scarred area in the centre of the target, and also in the peripheral unscarred regions of the target, away from this scarred area.

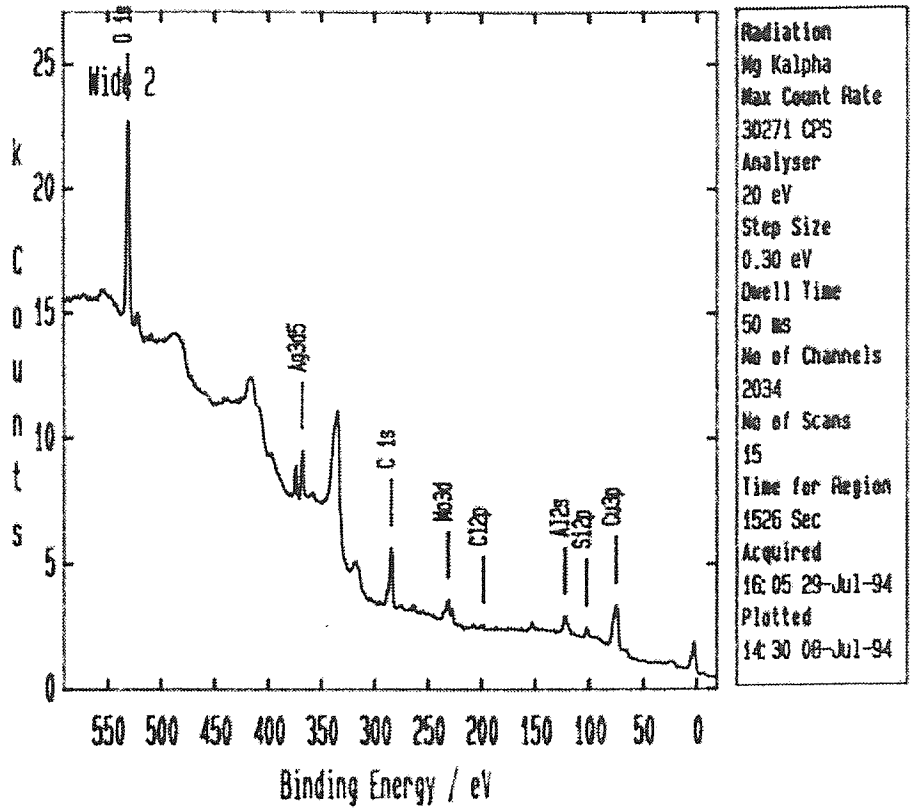

(a)

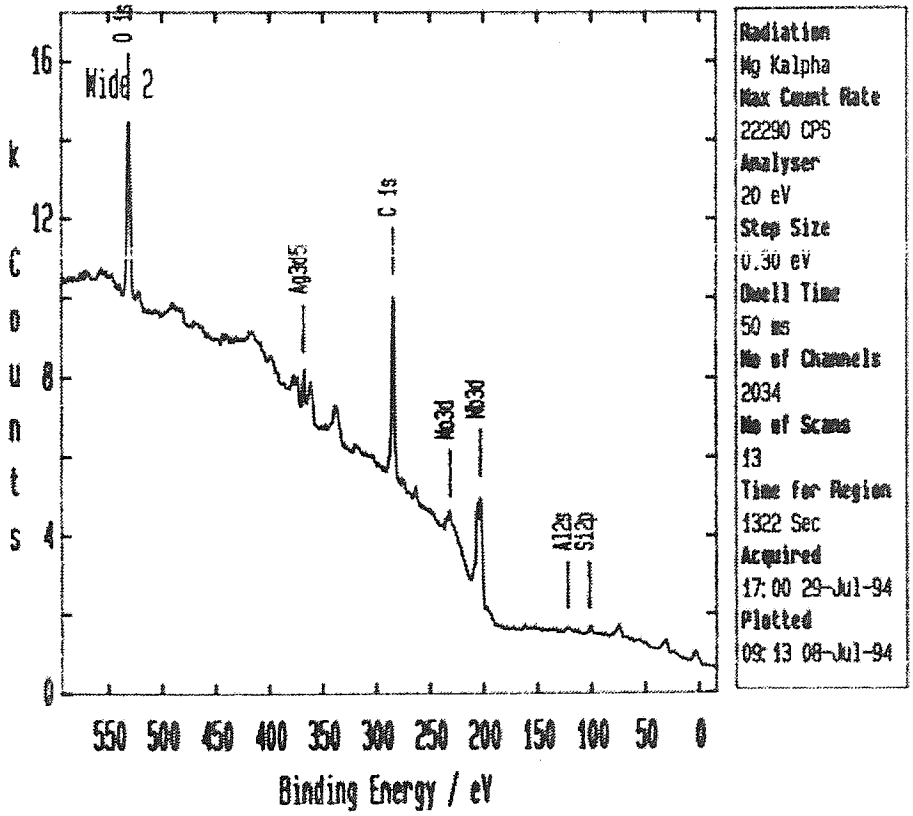

(b)

Fig. 4.3.16 XPS spectra of (a) scarred and (b) unscarred regions of Nb target {binding energy range 0 - 600 eV}

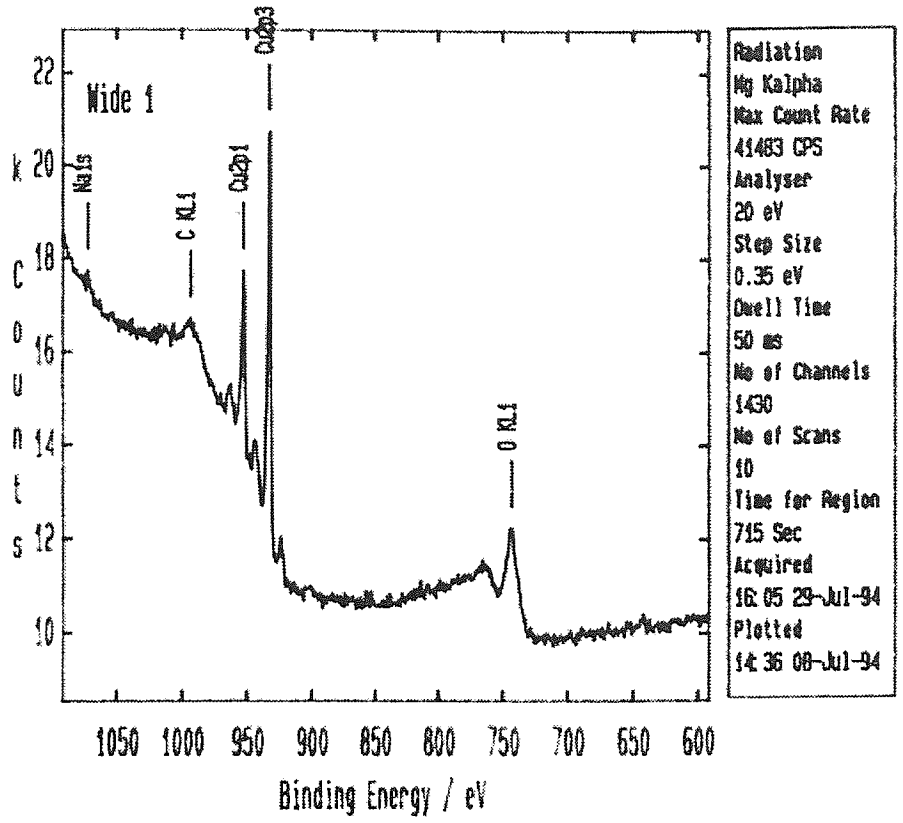

(a)

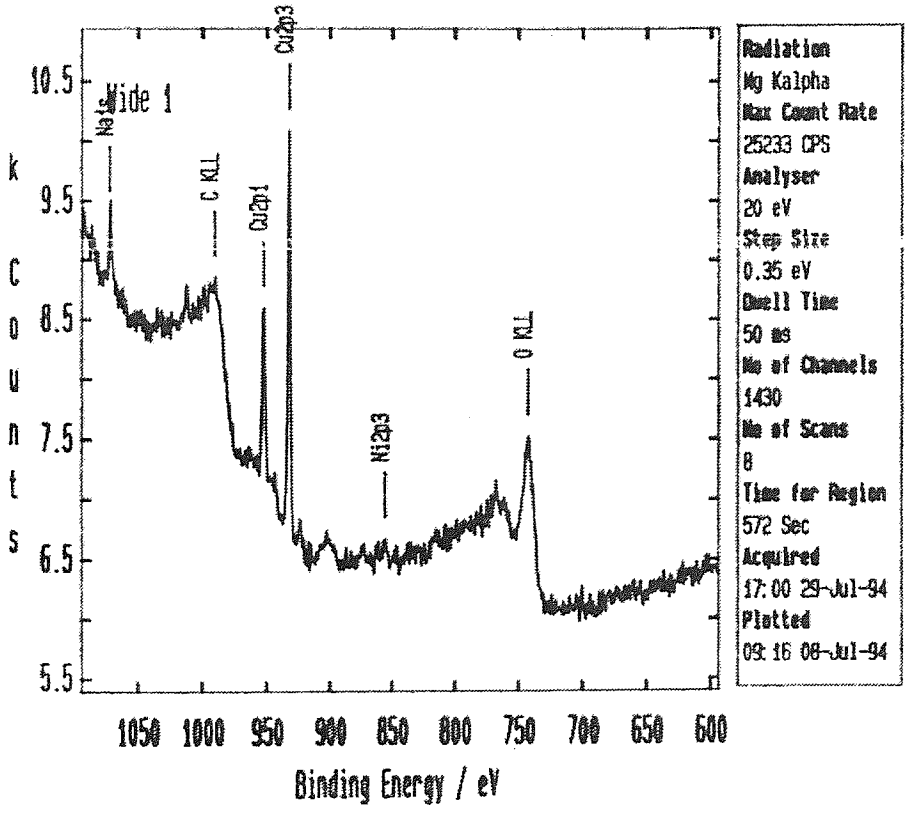

(b)

Fig. 4.3.17 XPS spectra of (a) scarred and (b) unscarred regions of Nb target {binding energy range 600 - 1100 eV}

Figures 4.3.16 and 4.3.17 present plots of the XPS spectra recorded from the scarred and peripheral regions of the EHV target. These spectra are tabulated in Tables 4.4 and 4.5.

Element	Atomic [%]	Atomic ratio	Centre [eV]
Nb 3d	8.068	4.036	203.01
C 1s	54.277	27.150	284.60
O 1s	23.731	11.870	531.50
Mo 3d	1.908	0.955	231.50
Na 1s	1.125	0.563	1072.25
Cu 2p3	3.535	1.768	932.61
Al 2p	4.192	2.097	122.60
Si 2p	1.999	1.000	102.20
Ag 3d5	0.422	0.211	0.124
Ni 2p3	0.740	0.370	855.56

Table 4.4 XPS spectrum of outer region of exposed EHV niobium target

Element	Atomic [%]	Atomic ratio	Centre [eV]
C 1s	33.641	6.780	284.60
O 1s	37.941	7.647	531.50
Mo 3d	2.247	0.453	231.50
Na 1s	1.424	0.287	1072.25
Cu 2p3	11.424	2.302	932.61
Al 2p	5.884	1.186	122.60
Si 2p	4.962	1.000	102.20
Ag 3d5	1.387	0.280	368.30
Cl 2p	1.089	0.220	198.20

Table 4.5 XPS spectrum of scarred region in exposed EHV niobium target

From an inspection of Tables 4.4 and 4.5, it appears that Al and Si have been deposited upon the entire surface of the EHV target; the concentration of these species, which were also observed in the HV target of Section 4.3.6.1, appeared to be higher within the scarred zone of the Nb target. Concentrations of molybdenum

(Mo), copper (Cu), silver (Ag) and sodium (Na) were also detected on the EHV target, and again appeared to be concentrated within the scarred region. Indeed, the deposition of these metallic materials in the scarred zone was such that the underlying Nb substrate was completely obscured from the X-ray beam, as shown by the absence of a Nb peak in the XPS spectra of Fig 4.3.16(a).

4.3.7.3 SEM analysis of EHV alumina modules To further probe the possible origins of the collected material on the EHV niobium target, the corresponding alumina modules were analysed in the SEM, using the BSE microscopy procedure described in Section 3.3.1. Figure 4.3.18 displays an electron micrograph of a "used" alumina module, which had been subjected to 50 extra-high voltage pulses.

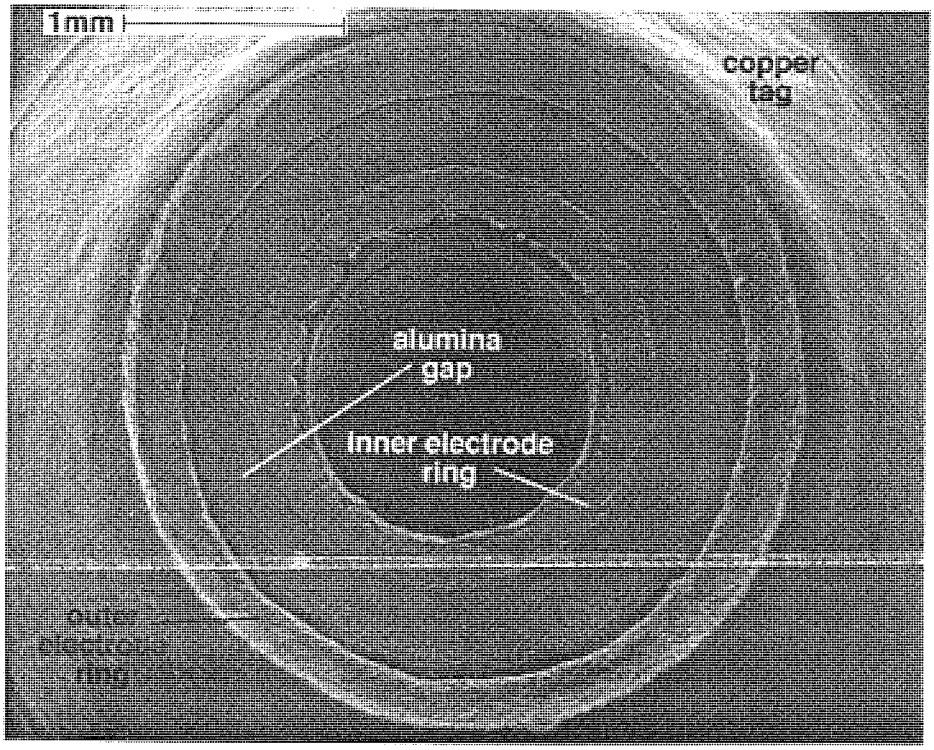

Fig. 4.3.18 Electron micrograph showing front face of "used" alumina module

Considering the form of the unused alumina module depicted in Fig 4.3.1, the 'used' EHV module, shown in Fig 4.3.18, displays several interesting features. Most notably, the molybdenum/manganese metallization, in the region between the inner electrode-ring and the metallized inner bore of the alumina tube, appears to have been eroded as a result of EHV operation of the module in vacuum. This eroded region of the inner electrode-ring is further illustrated in Fig 4.3.19, together with a magnified micrograph showing the inside edge of this metallized electrode.

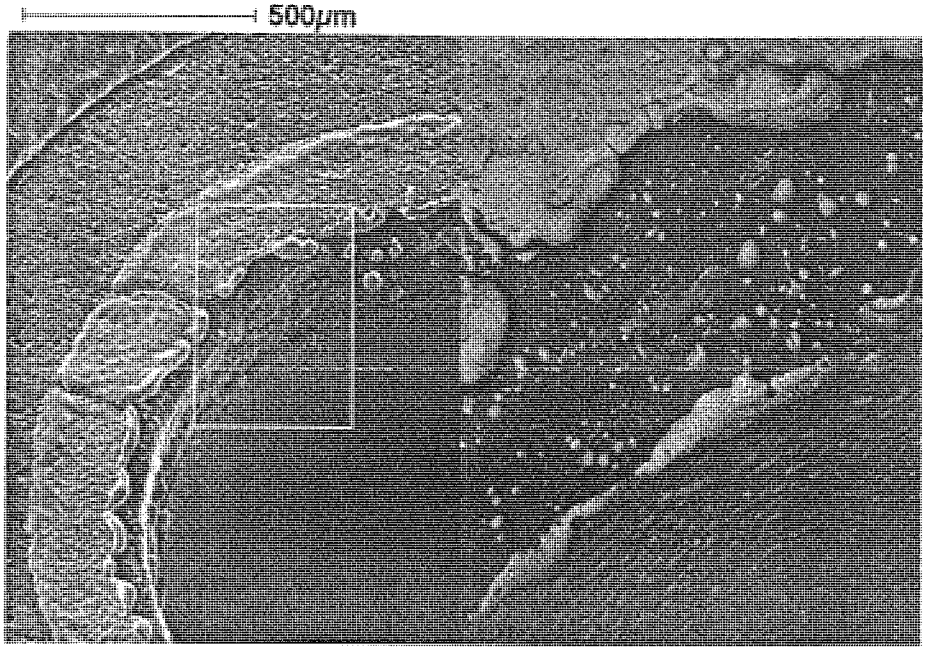

Fig. 4.3.19 Electron micrographs of eroded inner electrode-ring

The metallization on the inside edge of the inner electrode-ring appears to have been largely removed under the influence of the EHV pulses which had been applied to the module. This is particularly apparent in the magnified image of Fig 4.3.19, where the erosion of the metallization has revealed much of the underlying alumina ceramic.

Figures 4.3.18 and 4.3.19 also suggest a modification of the 300µm-wide alumina region, around the edge of the outer electrode-ring, where a change in contrast can be observed in the BSE image of the alumina. This region of the 'used' alumina module is explored in Fig 4.3.20, which presents an oblique view across the alumina region, obtained by viewing from the centre-axis of the alumina tube towards the outer electrode-ring.

Comparing Fig 4.3.20 with a similar region on an unused alumina module (see Fig 4.3.3), severe erosion can be seen to have occurred at the interface of the outer electrode-ring (cathode) with the exposed region of alumina ceramic. The edge of the metallized electrode appears to have been eroded back from the ceramic, leaving few points of contact between the electrode-edge and the underlying alumina. A pronounced "step" is visible on the ceramic surface at this interface, which extends from below the edge of the outer electrode-ring onto the exposed ceramic region. The surface of the alumina region appears 'amorphous' in comparison to that of an

unused alumina specimen (Fig 4.3.3), and there appear to be "globules" of deposited material on the ceramic surface.

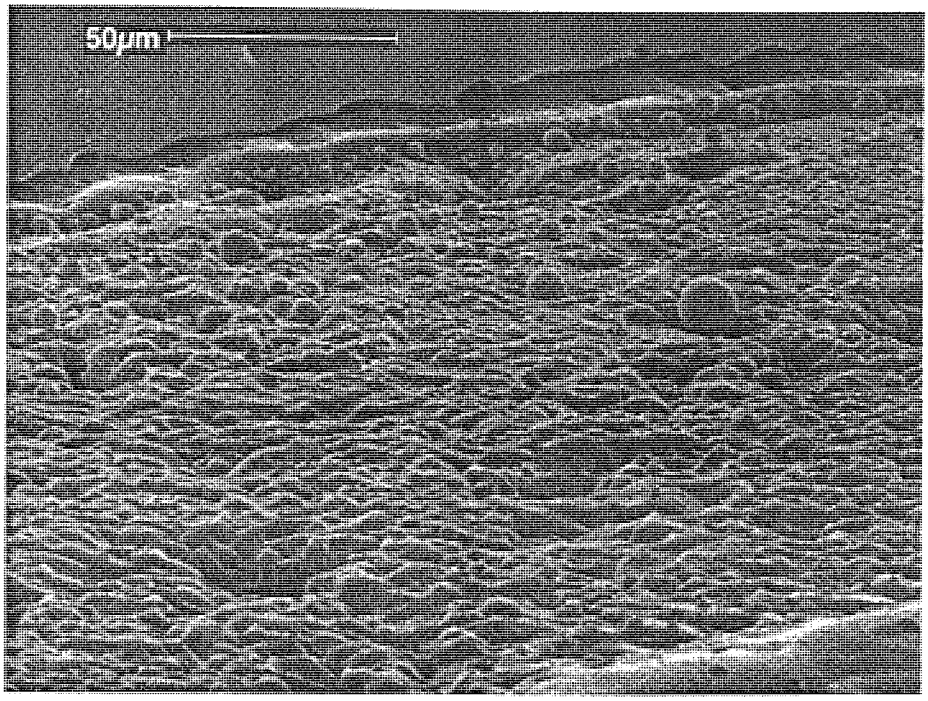

Fig. 4.3.20 Electron micrograph of eroded alumina region near outer electrode-ring

The form of this eroded M-I-M regime is portrayed in the micrograph of Fig 4.3.21, which looks directly down upon the M-I interface region of the alumina and the outer (cathode) electrode-ring:

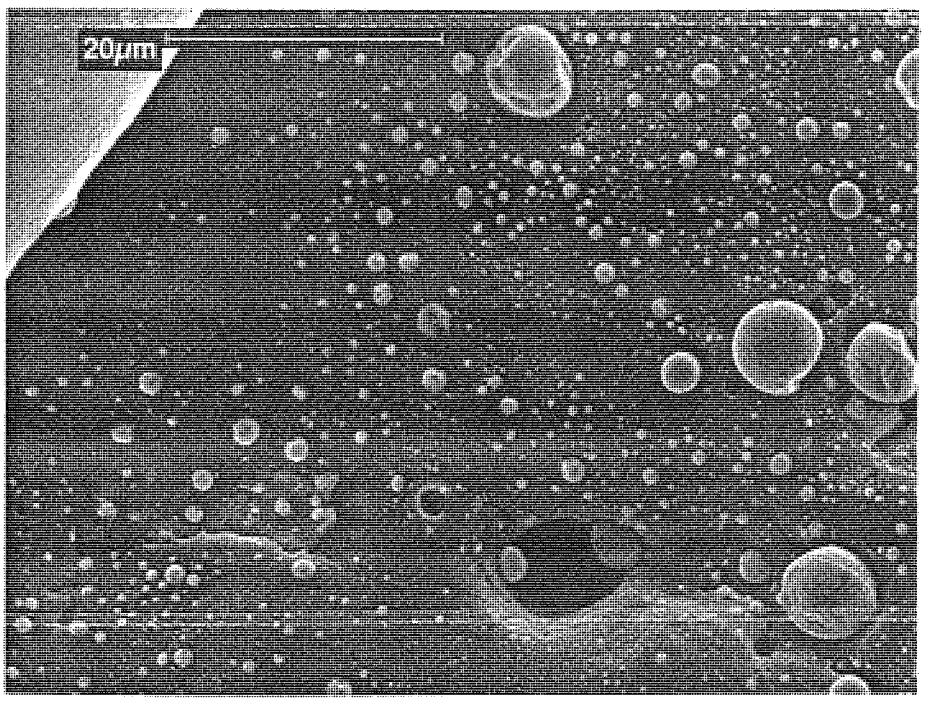

Fig. 4.3.21 Glassy 'step' in eroded alumina region near outer electrode-ring

EDXA analysis of the step region revealed a composition of aluminium and silicon oxides, indicating a silica/alumina mixture similar to that found in the glassy phase of the alumina ceramic. This glassy region also contained small concentrations of molybdenum (Mo) and silver (Ag). A similar analysis of the deposited 'globules' on the surface of this alumina region indicated that these globules were of molybdenum (Mo) metal: the Mo globules appeared to vary in size, measuring from ≈1μm up to 10μm in diameter.

It is worth noting that the glassy step appears almost continuous in its extent, in its protrusion of some 40μm from the outer electrode-ring. Fig 4.3.21 shows this step to appear as a "crust" of glass material, which is occasionally punctured by small pores and fissures.

4.4 Summary of experimental findings

In conclusion, this section presents an *interim* summary of the experimental findings, prior to their discussion in Chapter 5. Thus, analytical studies of the vacuum emission from an alumina dielectric have revealed the following phenomena:

4.4.1 DC prebreakdown luminosity occurs within the alumina insulator module, at electric field strengths of approximately 8kVmm^{-1} (see Section 4.1.1.1). As the applied field-strength exceeded this threshold, a red/pink 'doughnut' discharge was observed in the alumina, with a corresponding emission-spectrum doublet of 692.6nm and 694.0nm wavelengths. With increasing electric field-strengths (≈12kVmm^{-1}) distinct bright-blue 'spots' became visible in the alumina ceramic. Two wave-bands, centred around 325.0nm and 410.0nm, appeared to be associated with these 'spot' phenomena.

4.4.2 DC prebreakdown electron-emission has been observed using a transparent anode technique [37]. Cathode-luminescence on the anode, as a result of impacting electrons, appeared to coincide with the local bright-blue 'spots' of luminosity on the alumina ceramic (see Fig 4.1.13). Furthermore, the initiation of these 'spots' on the ceramic resulted in an enhancement of the main-gap current (I_a) which was collected through the transparent anode (see Sections 4.1.3.1 and 4.1.3.4).

4.4.3 High-voltage pulsed-field optical emission was recorded from alumina ceramic with the application of pulsed field magnitudes of $\approx$10kVmm^{-1}, and consisted of bright 'jets' which were radiated from one or more 'luminous centres' in the alumina (see Fig 4.2.1). The 'jets' were seen to propagate along straight-line trajectories, at velocities in the range of 20 to 100ms^{-1}. Ballistic interactions were observed when the jets struck metallic target surfaces, with a deposition of Al/Si microparticles onto target materials which had been exposed to the pulsed-field surface-flashover events (see Section 4.3.6).

The luminous emission-centres appeared in the same spatial regions as the bright-blue DC spots (Section 4.2.5), with these pulsed-field and DC emission-centres occurring in regions of porosity in the ceramic surface (see Section 4.3.4). Optical emission from the luminous centre appeared to contain a significant deep-red spectral-component, in the wavelength range 678 to 706nm (see Section 4.2.4.1). These luminous centres displayed a logarithmic decay over a time-constant of $\approx$5ms (Fig 4.2.4).

4.4.4 Extra-high voltage pulsed-field optical emission, at field-strengths in excess of 60kVmm^{-1}, again revealed the emission of bright 'jets' from the metallized end-face of the alumina ceramic. Emission of these jets was preceded by a bright 'flash' of luminosity from the ceramic surface, which appeared to originate in the cathode-ceramic interface region (see Figs 4.2.12 and 4.2.21). This initial luminosity appeared to extend outwards from the cathode region with a propagation velocity in the region of $\approx$2x10^{5}ms^{-1} (Fig 4.2.12) to 1x10^{6}ms^{-1} (Fig 4.2.14).

Surface-analysis of target materials which had been exposed to the EHV jets showed a deposition of Al and Si species, together with metallic elements including Mo, Cu, Ag and Na. Scanning electron microscopy of the "used" alumina module showed severe erosion of the metallized inner electrode-ring (Figs 4.3.18 and 4.3.19), and the formation of a "glassy crust" around the M-I regime of the cathode-alumina interface (see Figs 4.3.20 and 4.3.21).

5. DISCUSSION

As a precursor to the discussion of the vacuum emission phenomena observed from an alumina dielectric, it is necessary to have a clear structural description of the metallized alumina regime studied in this work. In the majority of cases, insulating materials have been regarded as *continuous* media, and classified according to *homogeneous* electrical properties [146]. In the present study of a polycrystalline alumina ceramic, it is considered more realistic to view the ceramic as a 'non-ideal', inhomogeneous *'heterosystem'* formed from the alumina grains and the silica glass phase, i.e. as shown in Fig 5.1. In this context, an ionic model has been widely used to describe the electronic conduction behaviour of electroceramic materials that have a high glass content (see Section 2.4.4) [108]. This ionic model corresponds to the near-ohmic characteristics associated with the glassy phase, and proposes charge-transport to occur entirely within the glass fraction of the insulator.

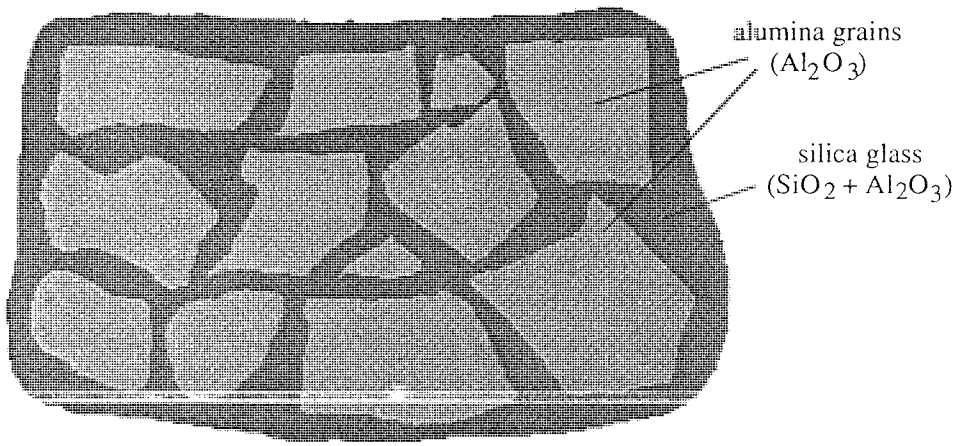

Fig. 5.1 Illustrating the inhomogeneous structure of a polycrystalline alumina ceramic

In the high-alumina materials studied in this work (Al_2O_3 fraction >90%), it will be shown that the electro-optical phenomena observed from the ceramic appeared to be associated with emission processes from *within* the alumina grains. With reference to Chapter 4, there is little experimental evidence to support any significant role of the silica glass-phase in the electronic behaviour of the ceramic. Thus, a discussion on the nature of the emission phenomena observed from the alumina insulator specimens will be based upon solid-state electronic processes within the polycrystalline alumina matrix.

5.1 Planar DC prebreakdown behaviour of alumina in vacuum

Two types of DC prebreakdown photon-emission processes have been recorded from the alumina specimens used in this study; namely, a broad-area, deep-red 'doughnut' emission, and localised bright-blue spots, as shown in Figs 4.1.1(b) and 4.1.1(c) respectively. Furthermore, concurrent measurements of the electrical (I_t-V_t) characteristics of the alumina insulator displayed features associated with the onset of these two optical phenomena (see Fig 4.1.1(a)) .

For clarity of presentation, the prebreakdown optical and electrical characteristics associated with the alumina specimen will be discussed separately, with particular attention being paid to the physical nature of the optical and electrical findings. In a subsequent discussion, conclusions will then be drawn from both of these areas, and a unified model will be presented that describes the optical and electrical phenomena associated with the DC prebreakdown of an alumina insulator in vacuum.

5.1.1 Origin of optical emission Considering first the recorded images depicted in Fig 4.1.1, the corresponding optical spectrum shown in Fig 4.1.9 indicates predominant optical-emission from the alumina in a narrow wavelength-band around 694nm, with additional broad emission-bands centred around 325nm and 410nm, extending into the UV region. The dominant spectral-lines around 694nm are characteristic of the observed deep-red 'doughnut' emission, whilst the emission-bands centred around 325nm and 410nm are believed to be associated with the localised bright-blue spots observed on the alumina specimen (Fig 4.1.1). These optical phenomena represent key findings of this work.

Two possible models may be cited to explain the physical nature of the optical-emission associated with an electrically-stressed alumina insulator. Firstly, the luminosity could stem from the desorption of gas from the insulator surface by 'hopping' electrons [13], and the resulting initiation of a gas-discharge above/over the surface of the insulator. Secondly, it could result from the injection of electrons from the cathode into the surface-layers of the alumina [18], that subsequently give rise to solid-state luminescence processes at defect-sites within the solid dielectric [28], such as will be discussed later in Sections 5.1.1.1 and 5.1.1.2.

With reference to Figs 4.1.8 and 4.1.9, it should be noted that the spectrum of the optical-emission does not indicate any strong atomic spectral lines, and so offers little evidence that the emission was derived from atomic processes associated with

the ionisation of desorbed gas [208]. To consolidate this assumption, an experimental study of the behaviour of the photon-emission in a residual atmosphere of argon gas, described in Section 4.1.2.2, showed no effect of the residual gas upon the optical signature of the photonic emission from the alumina sample.

In composition, the alumina ceramic was of 94% purity (Al_2O_3) by weight, with a mean grain-size of 10μm. A remaining fraction of oxide-glass locked these alumina grains into a ceramic matrix, with this 'glassy phase' consisting of alumina, silica (SiO_2) and CaO, with trace (a few ppm) concentrations of metal-oxides including sodium, titanium and chromium [209]. Scanning-electron microscope (SEM) studies of the surface-topography of the alumina (see Section 4.3.3) illustrate a granular surface structure, together with a broad distribution of pores within the matrix of the ceramic. Thus, the presence of material-impurities and structural-defects in the dielectric will be considered in detail alongside the findings of this work, since these defects are possibly implicated in the optical-emission phenomena observed from the insulator.

5.1.1.1 Nature of 'doughnut' emission (λ=694nm) From a consideration of the expanded high-resolution (0.3nm HPBW) wavelength-plot of the 'doughnut' emission shown in Fig 4.1.10(b), it can be concluded that the doublet form of this spectrum is in close agreement with the emission-spectra of ruby (Al_2O_3:Cr^{3+}), i.e. characterised by a narrow emission-doublet (R_1,R_2) of two closely-spaced spectral lines, centred around 693.5nm [134]. This hypothesis of a ruby-line (R-line) nature of the recorded spectrum indicates a significant luminescence *within* the bulk of the alumina dielectric [44,134], and is associated with optical-emission from chrome (Cr) impurity-centres according to the following radiative electron-transition process:

$$Cr^{4+} + e^{-} \rightarrow \left(Cr^{3+}\right)^{*} \rightarrow Cr^{3+} + h\nu\left(R_1, R_2\right)$$

Figure 4.1.1(b) illustrates that the doughnut emission is a *distributed* phenomenon, involving the entire 300μm alumina region between the metallized ring-electrodes. Correspondingly, Fig 4.1.2 plots the intensity of this emission across the alumina gap, and shows a spatial distribution of detected photon intensities throughout the alumina region. It can therefore be concluded that these findings are consistent with a distributed impurity-population of chrome throughout the *bulk* of the alumina

dielectric: typically, impurity concentrations of Cr in undoped Al_2O_3 are reported to be ≈1ppm [134] to 3ppm [105].

5.1.1.2 Nature of localised bright-blue 'spots' (λ=325nm and λ=410nm) Photon-emission from alumina observed in the broad 410nm band is characteristic of a radiation-transition associated with negative-ion (oxygen (O^{2-})) vacancies, conventionally termed *Farbzentrum* or *F*-centres [29]. This *F*-centre emission process may be represented by the following expression:

$$F^+ + e^- \rightarrow (F)^* \rightarrow F + h\nu(410nm)$$

Similarly, emission from an F^+ -centre (an oxygen-vacancy that has trapped a single electron) has a characteristic emission-band around 327nm [29] described by:

$$F^{++} + e^- \rightarrow \left(F^+\right)^* \rightarrow F^+ + h\nu(325nm)$$

F-centres are associated with defect-sites within the Al_2O_3 crystal-structure [28,29], such as the porosity of the alumina region illustrated in Fig 4.3.4. Figure 5.2 presents an energy-level diagram summarising the characteristics of *F*- and F^+ -centres, together with the substitutional Cr^{3+} centres described in Sections 5.1.1.1.

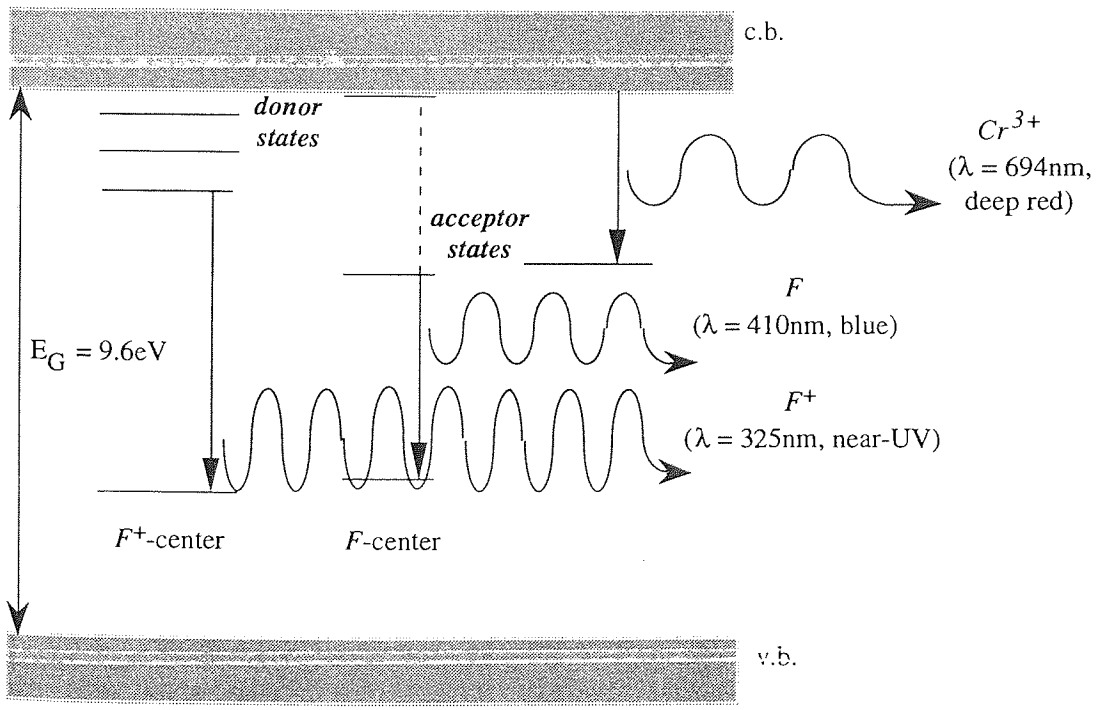

Fig. 5.2 Illustrating the energy levels associated with the photon-emission spectra recorded from a polycrystalline alumina ceramic

Significantly, both porosity and defect-centres in alumina have been found to be concentrated at grain corners and grain edges [210]. Thus, the possible role of *F*-centre emission from the alumina is consistent with the observed local concentration of pores in the alumina specimen, in the spatial vicinity of the observed bright-blue spots. Indeed, a local clustering of pore-defects may constitute a structural precursor to a spot of bright-blue (410nm) *F*-centre photon-emission. This hypothesis appears to be consistent with the spatial coincidence observed between the bright-blue luminescent 'spots' and porous regions on the alumina surface, as described in Section 4.3.4.

5.1.2 Planar prebreakdown electrical characteristics Both the initial and subsequent electrical (I_t-V_t) characteristics of the alumina specimen show measurable current-flow through the insulator. More specifically, the initial electrical characteristic of the alumina specimen (Fig 4.1.1(a)) shows two current thresholds associated with applied DC voltages of 2.5kV and 4.0kV, corresponding to applied electric-field magnitudes of ~8MVm^{-1} and ~13MVm^{-1} respectively. The first threshold (of V_t = +2.5kV) coincided with the initiation of the ruby-red 'doughnut' glow within the 300μm alumina region on the end-face of the alumina specimen, whilst the second threshold marked the appearance of two bright-blue 'spots' between the electrode-rings in the alumina region.

A further feature of the electrical characteristics of the alumina specimen, illustrated in Fig 4.1.1(a), is the non-reversible transformation of the material-behaviour of the alumina following a sustained application of DC voltage across the specimen. Thus, the I_t-V_t characteristic of the alumina is modified, from an initial *semi-insulating* state to a *semi-resistive* condition that is characterised by a near-linear variation of current with applied DC voltage across the alumina specimen.

This apparent decrease in the resistivity of the alumina may be explained by a migration of metal-ions, such as manganese (Mn), from the metallizing material of the inner (anodic) electrode-ring, over the alumina surface and along grain boundaries. Similarly, sodium ions (Na^+) within the glassy-phase of the ceramic may also migrate under comparable DC field conditions [139]. Vacant oxygen sites (*F* centres) may also migrate within the crystalline-phases of the ceramic [139]. These field-induced changes in the ceramic material, where the migration of metal-ions or defects leads to a redistribution of these defects throughout the ceramic matrix, may in turn lead to local variations in the resistivity of the solid insulator and, as a consequence, modify the electrical (I_t-V_t) behaviour of the ceramic.

Figure 5.3 shows a band-diagram representation of the metallized alumina regime. In the 'non-ideal' polycrystalline alumina dielectric, defect trap-centres can present electronic states *within* the band-gap of the alumina. Furthermore, these positively-charged F , F^+ and Cr^{3+} defect centres may migrate towards the cathode [139], as shown in Fig 5.3. Similarly, electrons may 'hop' between defect-centres within the band-gap of the dielectric [51,115], and migrate towards the anode electrode. According to this picture, some electrons may become trapped at defect sites, and emit a photon by radiative recombination with the trap centre. Thus, assuming a concentration of conduction-electrons in the anode region of the dielectric [51], this physical model suggests a higher intensity of photon-radiation from the alumina in the vicinity of the anode. This hypothesis is consistent with the photon-emission intensity-profile of Fig 4.1.2, recorded from an alumina specimen.

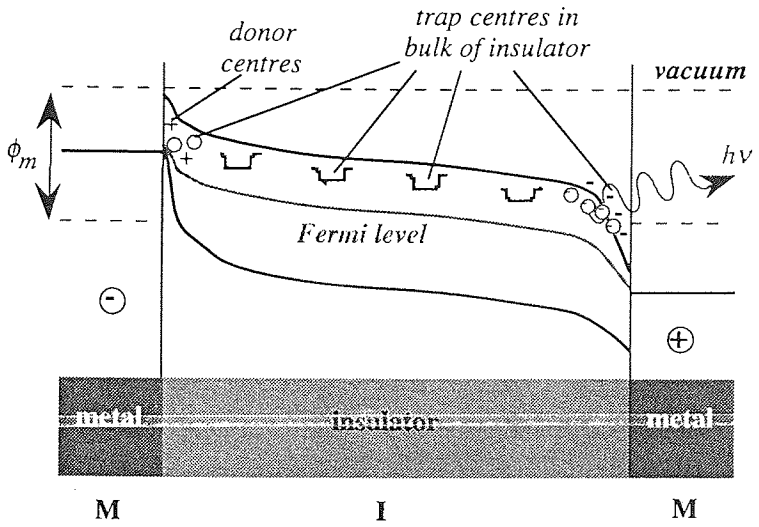

Key: ○ *empty trap centre* ⊙ *filled trap centre* + *donor centre*

Fig. 5.3 Electron energy diagram of the metal-insulator-metal (M-I-M) regime formed by a polycrystalline alumina ceramic bridging two electrodes in vacuum

The approximately *ohmic* form of the planar I-V characteristic {Fig 4.1.1(a)} was unaffected by electrode polarity: i.e. as confirmed by other workers [49]. This observation therefore seems to rule out the possibility of the planar I-V characteristic being controlled by field emission from discrete sites at the cathode triple junction, or indeed by any other electrode-specific process. Otherwise, one would expect *different* I-V characteristics for a reversal of voltage polarity, since the field strength in the cathode region is different for a given potential difference.

Thus, the I-V characteristics appear to be determined by electronic properties associated with the insulator region, either in the bulk or the surface layer.

5.1.3 Physical processes of photon emission Drawing upon the findings and observations described in sections 5.1.1 and 5.1.2, a qualitative account can be given of the physical processes believed to be associated with the observed optical phenomena.

5.1.3.1 Initiation of 'doughnut' emission The initial state of the virgin alumina ceramic may be viewed as a distribution of empty charge-traps, associated with vacancy (*F*- and F^+-centres) and impurity (Cr^{3+}) defects in the alumina [29]. Mobile donor centres and trap centres may migrate towards the cathode under the influence of an applied electric field [139], and form a positive space-charge near to the cathode. Thus, locally enhanced electron-injection may occur at the cathode-insulator junction, where high values of electric field can develop between the cathode and the 'virtual anode' formed by the positive space-charge region [51].

As an increasing field is applied to the specimen, measurable current flow through the ceramic is detected, indicating that significant charge-transport processes are occurring in the alumina. It can therefore be assumed that a proportion of the injected-electrons reach the anodic inner electrode, with a further proportion of injected-charge being trapped at defects in the insulator. This charge-injection process may be accelerated by increasing the applied electric field, such that a threshold field is reached whereby electrons may tunnel from emission-sites on the cathode into the conduction-band of the ceramic insulator (charge-injection may be further assisted by a local enhancement of the electric field across voids at the interface of the cathode and the alumina [51]). At this threshold point, the magnitude of the injected current is markedly increased, as electrons tunnel into the ceramic and occupy vacant traps, allowing a higher proportion of injected-electrons to reach the anode as more traps are filled. The process of filling traps throughout the ceramic increases the mean-free-path associated with the injected electrons [30], and consequently increases the probability of electron-flow from cathode to anode.

This behaviour is consistent with both of the threshold currents shown in the initial I-V characteristic of Fig 4.1.1(a), where the first current-threshold coincided with the initiation of the 'doughnut' emission (illustrated in Fig 4.1.1(b)) as electrons filled the 1.79eV traps at chromium (Cr^{3+}) impurity-sites. With increasing field, a second current-threshold was then reached, at which bright-blue emission was

initiated in localised 'spot' regions (Fig 4.1.1(c)), with electrons filling the deeper 3.0eV and 3.8eV traps of the *F*- and *F*+-centres.

5.1.3.2 Persistence of the doughnut emission The onset of the deep-red 'doughnut' emission may indicate three radiative electron-recombination processes. Thus, the ruby-red component of the observed emission can be described by a radiative electronic transition, through the recombination of a conduction-electron at a chromium impurity site (Cr^{3+} centre), i.e. as shown by process **1** in the simplified band-diagram of Fig 5.4.

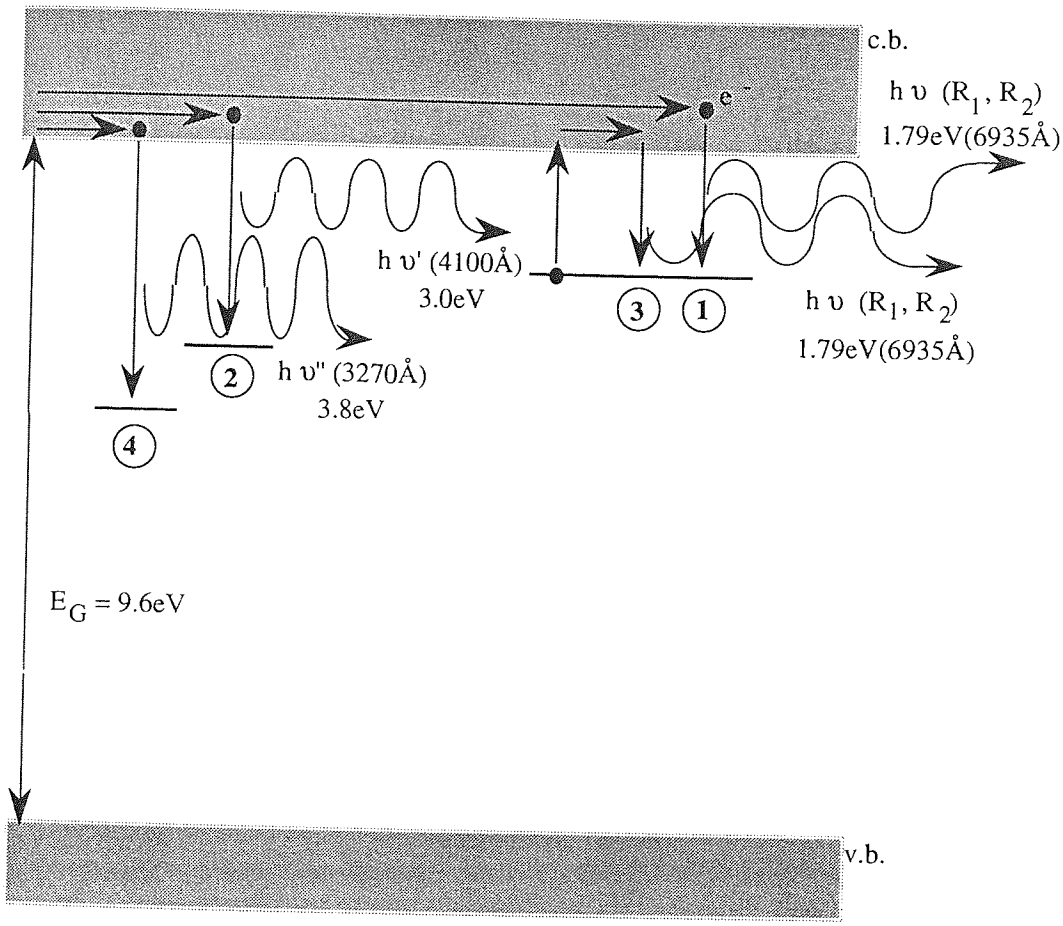

Fig. 5.4 Energy-band diagram, illustrating photon-emission by four solid-state mechanisms at defect-sites within an alumina insulator

A further contribution to the $\{R_1,R_2\}$ line emission can arise from *internal photoluminescence*. Here, the 410nm photons emitted by electron-recombination at oxygen-vacancies (*F*-centres) in the alumina (process **2**) ionise the absorption-band of the Cr^{3+} traps [134], causing the de-trapped electrons to enter the conduction-band of the alumina matrix. These electrons may subsequently recombine at a Cr^{3+} trap (process **3**), thereby releasing a further $\{R_1, R_2\}$ photon.

A quasi-equilibrium current condition can therefore be established, whereby the initial population of electrons that filled the chromium-site traps may subsequently be excited back into the conduction-band of the alumina by *F*-centre photons. Thus, the continued trapping of electrons at chrome impurity-sites may be counter-balanced to some extent by the emptying of these chromium traps by internal photoluminescence, as a result of the excitation of trapped electrons by *F*-centre photons (Fig 5.4 process **3**).

However, it is also necessary to explore the finite *lifetime* observed in the doughnut emission, at a given applied-voltage V_t (see Section 4.1.1). This finding may be explained if it is assumed that the majority of Cr^{3+} traps are eventually filled, where the total *F*-centre emission from the ceramic (and excitation of electrons from Cr^{3+} traps by these 410nm photons) is not sufficient to balance the filling of the chromium traps. According to this picture, only a *quasi*-equilibrium may exist between the excitation of electrons into the conduction-band, and the trapping of electrons at Cr^{3+} defects. Thus, fewer electrons are trapped by Cr^{3+} defects since the majority of these traps may eventually be filled, and so the observed R-line (694nm) emission from the chromium centres is reduced and the ruby-red 'doughnut' emission is seen to diminish. This mechanism would result in an increase in measured current, as shown over a 30-minute time-period in Fig 4.1.1(a).

5.1.3.3 Onset and persistence of bright-blue 'spots' (λ=410nm) Figure 4.1.1(c) shows a co-existence of the distributed doughnut emission with several localised bright-blue spots. However, these spots have also been observed in isolation, without the presence of the doughnut (see Sections 4.1.1.1, 4.1.1.3 and 4.1.3). The filling of the deep (3.0 eV) *F*-centre traps thought to be associated with these spots may be promoted by localised electric-field enhancement, in the vicinity of filled Cr^{3+} traps. In this scenario, the filling of the chrome-defect traps can cause local distortions of the applied DC field, enhancing the local electric field associated with the *F*-centre. A convincing manifestation of such a field-effect is the distinct "switch-on" of the bright-blue spots when the applied voltage, V_t, is increased beyond a second threshold value of +4kV {Fig 4.1.1(a)}. Conversely, the dimming of these spots after several hours of voltage-application [23] may be explained by the eventual filling of all the traps associated with *F*-centre defects, thus leaving too sparse a population of empty traps to promote significant electron-recombination and consequent photon-emission from bright-blue spots on the alumina specimen.

Any increase in measured current-flow, arising from the greater electron mean-free-path created by the macroscopic filling of the *F*-centre traps [30], is likely to be incremental upon the marked current-increase associated with the filling of Cr^{3+} traps (Fig 4.1.1(a)), given the former dominance of these Cr^{3+} traps in the initial electro-optical behaviour of the alumina ceramic. This hypothesis is evidenced on the one hand by the predominance of the 694nm line associated with Cr^{3+} defects (Fig 4.1.9), and the marked increase in measured current (I_t) following the reduction in the intensity of the doughnut for V_t = 5kV (Fig 4.1.1(a)). On the other hand, no noticeable change in I_t has been observed following the extinction of the bright-blue spots [23]. Thus the bright-blue spots appear to be of lesser significance than the doughnut emission in the DC prebreakdown optical behaviour of the alumina ceramic.

5.2 Transverse DC prebreakdown characteristics

The findings from the planar I-V measurements of Section 4.1.1 do not in themselves indicate whether the currents are 'within' or 'above' the insulator surface. However, the investigation of the effect of a *transverse* electric-field upon the planar I-V characteristics has provided valuable experimental evidence relating to this important question. Thus, as shown in Fig 4.1.12(a), only a very low transverse field is needed to establish a significant transverse current across the main-gap from the alumina module to the transparent anode.

Conversely, Fig 4.1.11 also shows that a further substantial increase in transverse field strength, from $5MVm^{-1}$ to $10MVm^{-1}$, does not yield a corresponding increase in transverse (main-gap) current. Significantly, Fig 4.1.12(b) also indicates that the extraction of a transverse current, I_a, is at the expense of a reduction in the planar current, I_t. However, such an increase in transverse field causes only a *limited* depletion of the planar current; i.e. the applied transverse field did not cause a complete switching of the planar current to the main gap. This finding suggests that a major proportion of the planar current is flowing *within* the insulator surface. It may therefore be concluded that the planar current could well have two components, consisting of electrons (a) hopping along the insulator surface, and (b) flowing in the surface layer of the insulator.

5.2.1 Mechanisms of field-stripping of electrons In order to investigate the charge-transport mechanisms responsible for the observed behaviour of the insulator, it is necessary to pursue possible explanations as to how a transverse

field can strip electrons from the 'ambient' planar current. In this context, note should be taken of two important experimental findings presented in Section 4.1.3.2. Firstly, a direct relation may be postulated between the 'electron flares' on the transparent anode and the bright blue spots observed in the planar insulator region. Secondly, a key temporal correlation was established between the initiation and extinction of both the planar spots and the electron-impact 'flares' visible on the transparent anode.

5.2.1.1 Contribution of planar emission to transverse current An association between the transverse current and the bright planar spots is supported by a number of experimental findings. Firstly, the removal of the planar DC voltage (V_t) caused the bright-blue planar spots to disappear, and the main gap current to simultaneously collapse by three orders of magnitude. Secondly, the observed extinction of the planar spots (due to their finite lifetime) also caused the transverse current to collapse, despite the continued flow of planar current (I_t) between the ring electrodes. Thirdly, the migration direction on the transparent anode of the electron impact image with increasing main-gap voltage is further evidence to support the above conclusion. Thus, a strengthening of the transverse component of the main-gap electric field means that the trajectory of the stripped electrons to the transparent anode has an increased vertical field component, and consequently causes the electrons to impact the anode at a decreased radial distance.

5.2.2.2 Nature of electron-emission from planar bright-blue 'spots' A possible interpretation of the optical spots observed near the inner electrode-ring is that they are localised micro-plasmas, initiated by electron emission from the (negative) outer electrode-ring. According to this reasoning, the transverse field would then be assumed to strip electrons from the plasma, and again yield a transverse current which is activated by applying a planar voltage to the inner electrode-ring. This interpretation would then attribute the formation of these micro-plasmas to the planar field acting between the electrode rings, since the optical spots were visible in the absence of any transverse electrical field.

However, the spectroscopic investigation presented in Section 4.1.2 found no evidence of gaseous discharge processes within the optical emission from the alumina insulator. Instead, as discussed in Section 5.1, solid-state defect-centres within the dielectric material appear to give rise to the luminous emission recorded from the alumina ceramic. This hypothesis is reinforced by the observed persistence of the luminosity following the introduction of a background pressure of argon gas (see Section 4.1.2.2). The luminous emission did not appear to be

quenched by the argon, and this observation therefore diminished the likely role of gaseous species in the DC prebreakdown emissions recorded from the planar dielectric regime.

This solid-state picture therefore highlights the possible role of the electronic states associated with the F and F^+ centres, which are believed to be responsible for the blue/UV photon-emissions detected around 410nm and 325nm respectively. The electronic energy-level schemes of these electron-centres are shown in Fig 5.5. In particular, the excited 1p level of the F centre introduces a population of electrons at energies close to the conduction-band of the alumina dielectric. It follows therefore that the excitation of the F centre defects can introduce mobile charges of free-electrons into the alumina dielectric [41,96]. These electrons may be subsequently field-emitted into the vacuum gap under the influence of the transverse electric field, and accelerated by this main-gap field towards the transparent anode. Where F centre electrons remain in an excited energy-state close to the conduction band, a *negative* electron affinity may therefore be associated with such defect centres.

Fig. 5.5 Illustrating electron-energy levels for absorption and photon-emission processes at F and F^+ centres within an alumina insulator (from Lee & Crawford [41])

A transverse electron current may also arise from the 'quasi-thermionic' emission of electrons from the alumina dielectric [68]. In this scenario, local heating of the

alumina may occur due to phonon-heating from non-radiative electronic transitions at F centre defects. The heated electrons may be subsequently excited into higher electronic energy states close to the conduction band of the alumina, as shown in Fig 5.5. The application of a transverse field may then ionise these shallow electron-energy states, leading to a detrapping of the 'thermalised' electrons [68].

5.2.2 Desorbed gas analysis With reference to Table 4.1, the desorbed gas species detected following a planar prebreakdown event appear to be molecular hydrogen (H_2, molecular mass 2 amu), and air [211]. The presence of air can be understood, since it would inevitably have been absorbed during the manufacture of the alumina ceramic when the pressed ceramic powder was kiln-fired in an (oxidising) air atmosphere. On the other hand, hydrogen is thought to have originated from the metallizing process of the ceramic, where the metallizing ink applied to the ceramic was fired in a wet hydrogen atmosphere. Significantly, hydrogen desorption has also been associated with electron emission in a vacuum gap at current levels of $\approx 10^{-4}$ A [49].

5.3 Pulsed-field breakdown behaviour of alumina in vacuum

The experimental findings presented in Section 4.2 have identified two optical phenomena that appear to play a key role in the pulsed-field surface-flashover of an alumina insulator, namely

i) the formation of explosive 'luminous centres' within the surface of the insulator, and

ii) the subsequent emission of bright 'jets' from these same localised regions

In seeking an explanation of the physical origin of these phenomena, the following discussion will review the available experimental evidence in relation to the current theories of solid-insulator surface-flashover, previously reviewed in Section 2.4 [12].

5.3.1 Properties of emitted 'jets' The bright 'jets' were observed to propagate along straight-line trajectories from the surface of the alumina module (Fig 4.2.1). Furthermore, this linear propagation behaviour was observed with electric fields applied to the module regime: in all recorded cases, no evidence of electromagnetic deflection was observed in the propagating jets. From this observation, the visible constituents of the jets may be postulated to consist of electrically *neutral* material, with little indication of any charged material species.

5.3.1.1 Trajectory tracks and propagation velocity Referring to Fig 4.2.1, jet propagation-velocities of approximately $10ms^{-1}$ are indicated from the jet lengths of ≈10mm viewed within 1ms frames. However, this *minimum* estimate of jet velocities is limited by the 1000fps recording-speed of the high-speed video camera, and the maximum time-resolution of 1ms offered by this recording system. From ultra-fast frame images of the jets over consecutive 50μs frames, as shown in Fig 4.2.22, a more precise estimate of the jet velocities appears to be in the range $20ms^{-1}$ to $100ms^{-1}$.

In considering the apparent divergence of the jets, note has to be taken of the limited depth-of-field of the video optics that were used, where the field-depth was significantly constrained by the wide lens apertures required to capture images of pulsed-field surface-flashover events [212]. It therefore has to be recognised that the divergence recorded in some of the emitted jets may in fact be due to the *optical aberration* of non-diverging, collimated jets, as they propagate out of the field-depth of the imaging optics. Such jets would become increasingly defocused, and appear to diverge as they propagate away from the plane of the ceramic surface.

5.3.1.2 Environmental interaction of jets The evidence of Fig 4.2.15 strongly indicates that the jets can exhibit *ballistic* reflections from metallic surfaces, i.e. suggesting a particle-based description for the origin of the jets. This interpretation is supported by the ability of alumina-ceramic surfaces to stop the propagation of jets (see Fig 4.2.6(b), where it is believed that the high surface-area of the 'open', or porous, surface morphology of the 10μm grain-size ceramics used in this work increases the likelihood of jet 'condensation', or trapping, at the ceramic surface.

5.3.1.3 Nature of jet material Referring to Section 4.3.6, the surface analysis of niobium (Nb) target foils, that had previously been exposed to high-voltage (HV) pulsed-field surface-flashovers on the alumina modules, revealed a deposition of aluminium (Al) and silicon (Si) material. An associated SEM analysis of the

exposed Nb target revealed the collected Al and Si material to have a particulate form, with a microparticle size of approximately 2μm (Fig 4.3.14). This material constitution of *particulate* jets is also suggested by the ballistic interactions observed between jets and solid target materials (see Fig 4.2.15), and a velocity-range of more than an order of magnitude below that recorded for ablated alumina vapour [213].

It should also be pointed out that both silicon *and* aluminium are abundant within the glassy alumina / silica phase that forms a glass matrix around the alumina (Al_2O_3) ceramic grains. The micrometric dimensions of these efflux particles also suggests that they may originate in the ceramic glass phase, rather than the crystalline alumina phase where the grain-size is typically larger than 10μm. From the bright luminosity of the jets (Figs 4.2.1 and 4.2.7), it is reasonable to assume the propagating particles of the jet efflux to have a high thermal temperature, and that they are emitting visible blackbody radiation [214]. To evaluate this proposition, the following simplified analysis of a propagating 'hot glass particle' may be considered.

Assuming a high alumina content, as in the bulk of the 94% Al_2O_3 ceramic material, the parameters of the jet particle may be summarised as shown in Fig 5.6. The physical dimensions of the particle are based upon those of the collected efflux particles shown in Fig 4.3.14.

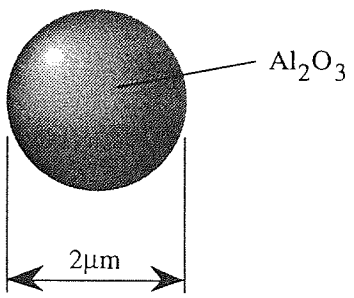

Volume, $V \approx 4\mu m^3$

Surface area, $A \approx 12\mu m^2$

Density, $\rho = 3970\ kg\ m^{-3}$

Melting temperature, $T_m = 2015°C$

Specific heat capacity, $C_p\big|_{T = 2000K} \approx 2000\ J\ kg^{-1}K^{-1}$

Fig. 5.6 The estimated physical parameters of an alumina efflux microparticle

As the emitted efflux particle propagates away from the alumina dielectric, cooling of the particle by radiative energy-loss can be modelled using the Stefan-Boltzmann

equation, where the rate of energy-loss by radiation

$$H = Ae\sigma T^4 \quad [\text{J s}^{-1}]$$

given σ = Stefan-Boltzmann constant = 5.6699 $\text{Wm}^{-2}\text{K}^{-4}$

e = emissivity ≈ 0.5 for polycrystalline alumina

It is worth noting that this approximate calculation neglects the background temperature of the UHV system chamber, and takes no account of conductive energy-losses during ballistic microparticle collisions. From an initial temperature of 2000K, i.e. at approximately 90% of the melting temperature of alumina [215], the cooling of the efflux particle by radiative processes has the form shown in Fig 5.7. In an 'emission lifetime' of approximately 10ms, the alumina microparticle can be seen to cool to approximately 1000K, at which temperature the intensity of the visible blackbody radiation spectrum becomes negligible [214]. This analysis is consistent with optical emission 'lifetimes' of ≈1ms observed in high-speed recordings of jets associated with surface-flashover events (see Section 4.2.1.3).

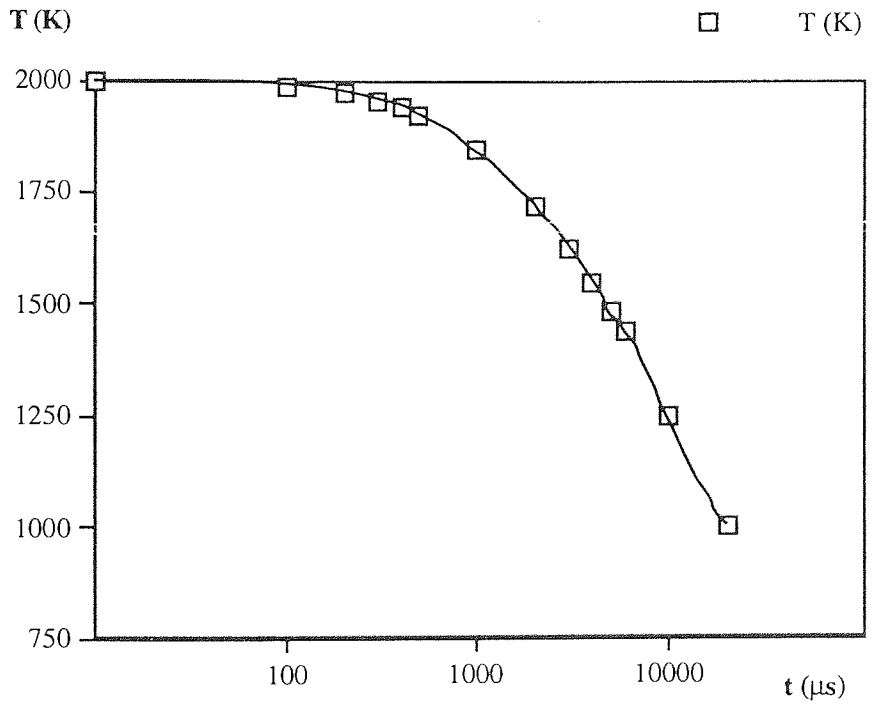

Fig. 5.7 Time-variation of efflux-microparticle temperature owing to radiative energy-loss

Exposure of alumina modules to extra-high voltage (EHV) pulsed-fields caused an increase in the collection of 'metallic' species emitted from the alumina ceramic (see Section 4.3.7.2), together with the Al and Si species previously observed with HV

pulsed fields. These metallic materials were principally molybdenum (Mo) and copper (Cu), which were present in the electrodes of the alumina module. This finding suggests the occurrence of additional 'metallic' jet emission at EHV fields, accompanying the Al/Si type of jets already discussed. In this scenario, electrode material may be heated and vaporised under the influence of high electron currents associated with the high-energy EHV pulse. Significantly, the detection of dielectric material from low-field surface-flashover events, and the subsequent detection of additional electrode material at higher field values, has also been reported by Bugaev and co-workers [216] from a barium titanate dielectric.

5.3.1.4 Nature of 'diffuse' emission phenomena Although the findings discussed in Sections 5.3.1.2 and 5.3.1.3 appear to discount a 'gaseous' constitution of the jets, further images of pulsed-field breakdown events, such as Fig 4.2.21, do show 'diffuse' emission phenomena to emerge from the alumina ceramic at the onset of a surface-flashover event on the insulator, prior to the emission of distinct 'jets' (see Fig 4.2.21).

From analyses of Nb target materials that had been exposed to these events (Sections 4.3.6 and 4.3.7), an extensive coverage of Al and Si, together with several metallic species including Mo and Cu, was seen over the entire surface of the target. The only non-metallic contaminant was chlorine (see Table 4.5), which may be attributed to contamination of the Nb foil sample with human perspiration (H_2O + NaCl). Thus, from the extensive spatial coverage seen in these deposited efflux materials, it may be concluded that the material species detected in discrete form in the jets are also present on a nano-particle scale in the diffuse emissions recorded from the alumina ceramic.

5.3.1.5 Electron exo-emission The negative emission current collected by the auxiliary anode (see Fig. 4.2.23) may in part arise from negative ions (such as O^{n-}) within the jet efflux: any collection of oxygen spectra in the present study was masked by the surface oxides of the niobium (Nb_2O_5). In time-of-flight studies of plasma jets emitted from an alumina-insulated spark plug, Buraczyk *et al* [47] observed ionised species of aluminium (Al^{m+}) and oxygen (O^{n-}) ($1 \leq m,n \leq 6$). Such ions typically propagate at speeds of $\approx 10^4$ ms^{-1} [47], yielding a transit time of ≈200ns across the 2mm gap between the alumina sample and the collecting electrode (Section 2.2.5). However, this order of transit-time delay was not observed in the collected current waveform of Fig. 4.2.23, where negligible time delay was observed within a 50ns resolution. Furthermore, the presence of any

ionised jet species was not suggested by the apparent immunity of the jets to electrical fields, as discussed in Section 5.3.1.1.

Accordingly, the possible presence of free electrons within the jet may also be considered. If emitted, such electrons can reasonably be assumed to be non-relativistic, with low energies around 500eV, propagating at $\approx 10^7$ ms^{-1} with a corresponding transit-time of ≈2ns across the 2mm gap. Apart from electrons generated during the breakdown process, it also has to be recognised that *pre*breakdown electron-emission may further contribute to this negative collected-current. Thus, *pre*breakdown electrons emitted from the alumina may lead to an 'early' collected-current signal, as electrons are emitted *prior to* the surface-flashover event. In fact, such DC prebreakdown electron-emission has been previously reported from alumina ceramics in vacuum, with similar magnitudes of applied electric-field [36], as described in Section 4.1.3.2.

5.3.2 Physical origin of jets From the spatial correlation observed between pulsed-breakdown surface-flashover events and the local clustering of pore-defects within the alumina ceramic (see Section 4.3.4), it may be circumstantially concluded that these pore structures are involved in the initiation of a pulsed-field surface-flashover event, and the associated generation of a luminous centre and emission of jets. As discussed by Chang *et al* [164], the presence of a pore cavity within an alumina insulator causes a local enhancement of the electric-field across the cavity [217]. Thus, for a 20μm pore within the 300μm-wide alumina (ε_r = 10) gap, the maximum field within the pore-cavity may exceed the applied macroscopic field by 50% [164].

In addition to this local field-enhancement at pore cavities, such vacancy defects can also lead to localised concentrations of segregated impurities such as Ca, Na and Ti from the glass-phase of the alumina, and an associated concentration of trapped electronic charges [26]. Therefore, the porous structures observed in the alumina ceramic appear to represent electronic 'weak points' in the insulation of the two-ring test-electrode structures used in this experimental investigation.

5.3.3 Nature of luminous centres within the dielectric The luminous centres that appear to be the source of the 'jet' emissions discussed in Section 5.3.1 may be described both in terms of their optical characteristics, and the electronic signature of the associated surface-flashover event.

5.3.3.1 Nature of luminous centre emission It has been pointed out in Section 5.3.1.5 that the explosive exoemission of electrons from the pulsed-field surface-flashover of the alumina insulator may lead to an emitted electron-current into the vacuum-space above the ceramic. In addition, this exoemission may be accompanied by a significant injection of electrons into the surrounding bulk surface-layers of the alumina dielectric [51]. Observations of the initial luminosity in the cathode-insulator interface region (Fig 4.2.14) show this luminescence to spread from the cathode at a velocity of $\approx 2 \times 10^5 ms^{-1}$. Indeed, other workers [45] have also observed the propagation of electrical-breakdown luminescence on alumina dielectrics with this magnitude of velocity.

With reference to Fig 5.5, the injection of electrons into the conduction-band of the alumina may lead to the population of defect-centre traps within the band-gap of the insulator. As the injected-electrons recombine with the defect-centres, so radiative photon-emission can occur as these traps are filled. In support of this interpretation, strong deep-red (694nm) R-line (ruby) emission has been reported from chromium (Cr) impurity-centres in alumina [96], whilst oxygen lattice-vacancy defects, termed *F* and F^+ centres, emit photons in blue (410nm) and UV (325nm) bands respectively [41,96]. A deep-red line emission from Cr impurity centres is consistent with the observed deep-red glow observed in the luminous centres of surface-flashover events on the alumina sample (see Section 5.1.1.1). Furthermore, the apparent exponential decay of this deep-red afterglow (Fig 4.2.4) is indicative of *solid-state luminescence* at Cr centres within the alumina ceramic [218,219].

5.3.3.2 Electronic characteristics of pulsed-field breakdown events Referring to the oscillograms of the breakdown-voltage waveforms recorded from the alumina modules in Section 4.2, the temporal characteristics of these waveforms appeared to depend upon the physical location of the surface-flashover event. Thus, for the majority of surface-flashover events, which occurred on the front-face of the alumina module between the metallized electrode rings, a waveform such as that shown in Fig 3.2.5(b) was recorded. In contrast, where pulsed-breakdown surface-flashover of the alumina module occurred along the outer-diameter of the ceramic tube, as described in Section 4.2.3.2, a "softer" breakdown voltage waveform was observed, as depicted by Fig 4.2.17(b). These two alternative forms of the pulsed-field voltage-breakdown waveform are illustrated in Fig 5.8. In both the "front-face" {Fig 5.8(a)} and "outer-diameter" {Fig 5.8(b)} surface-flashover regimes, the breakdown voltages, V_t, were of equivalent magnitudes. However, the fall-time of the collapsing planar voltage-pulse was ≈10ns across the

module end-face {Fig 5.8(a)}, whereas fall-times of ≈200ns were associated with breakdown events along the outer diameter of the ceramic {Fig 5.8(b)}.

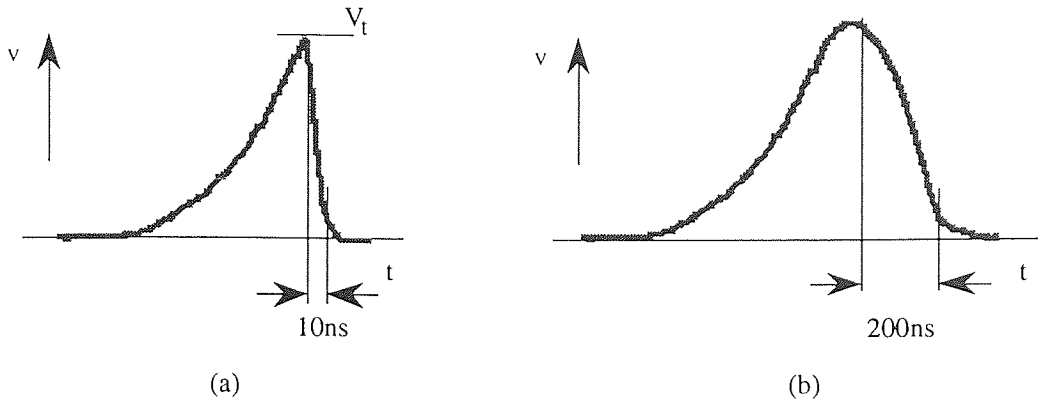

Fig. 5.8 Examples of breakdown voltage-pulses recorded for surface-flashover events (a) on the front-face and (b) along the side of the alumina module (from Figs 4.2.23 and 4.2.17(b) respectively)

Assuming an equivalent breakdown voltage of V_t ≈5kV in both breakdown regimes, the peak electric field magnitude across the 300μm gap on the module end-face, E_h, will be approximately 15 MVm^{-1}, i.e. as shown in Fig 5.9. Similarly, the peak electric field magnitude along the side of the module, E_s, will be ≈ 1MVm^{-1}. In each case, a reasonable estimate may be made of the *apparent* charge-carrier velocity along the dielectric, by dividing the insulator path-length (see Fig 5.9(a)) by the fall-time of the applied voltage pulse. In the metallized insulator regime shown in Fig 5.9, and from the waveform diagrams of Fig 5.8, these propagation velocities appear to be equivalent, i.e. $v_h \approx v_s \approx 3x10^4$ ms^{-1}.

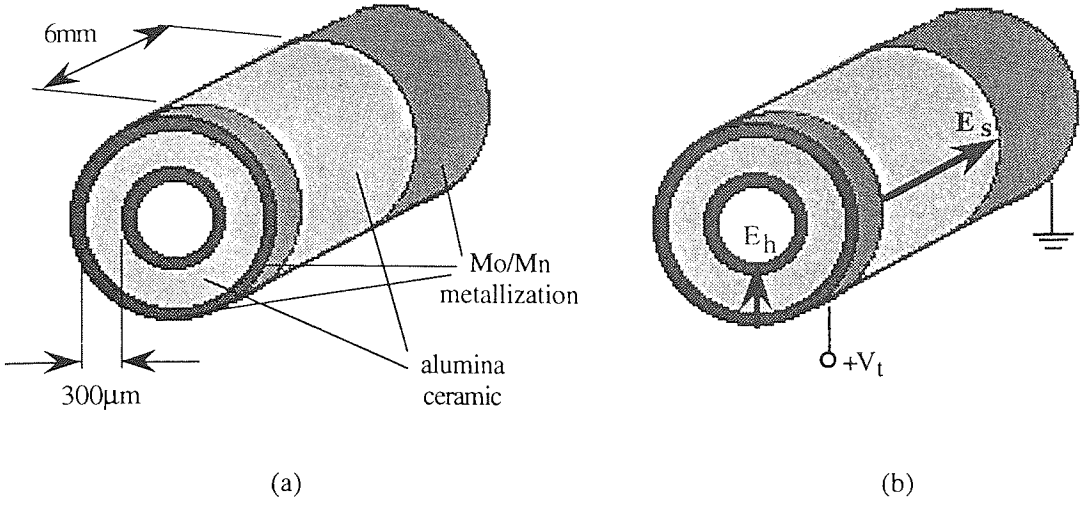

Fig. 5.9 Schematic illustrations of (a) the metallized alumina trigger module, with (b) applied voltages and electric fields (adjacent copper tag and threaded termination not shown)

This value of the propagation velocity may now be used to estimate the charge-carrier mobility, μ, using the relation

$$\mu = \frac{v}{E} \qquad [cm^2V^{-1}s^{-1}]$$

The above expression yields a carrier mobility of $\mu_h \approx 20cm^2V^{-1}s^{-1}$ in the metallized ceramic region on the module end-face. Where breakdown occurs along the outer diameter of the ceramic tube, an increased charge-carrier mobility, $\mu_s \approx 300cm^2V^{-1}s^{-1}$ is observed. Significantly, these carrier-mobility estimates are in reasonable agreement with the $200cm^2V^{-1}s^{-1}$ value reported by Will *et al* [106] for high-purity alumina. Furthermore, it may be concluded that the presence of a higher mobility region on the outer diameter of an alumina sample may promote surface-flashover in this peripheral domain.

According to this picture, high electronic mobility may result from a high concentration of vacancy and impurity defect-centres in the alumina dielectric [105,106]. High densities of these defects may be introduced by the sintering of Mo/Mn onto the end-face of the alumina module, where the metallized Mo/Mn layer sinters with the alumina glassy phase [35]. Thus, the metallized Mo/Mn electrodes may therefore further perturb the structure of the polycrystalline alumina in the M-I junction region on the end-face of the alumina sample.

Conversely, a high-mobility regime may be formed by high concentrations of defects in the outer-diameter of the alumina, with lower concentration-densities present on the metallized end-face of the alumina. In this alternative scenario, defect-concentrations in the surface-layers of the alumina tube periphery may form a 'preferential' surface-flashover discharge path, since this outer-diameter region may present a higher carrier-mobility with respect to that of the interelectrode gap on the module end-face.

5.3.4 Defect-initiated model of surface flashover From the solid-state description of the electro-optical phenomena observed in an alumina insulator, a physical description of the surface-flashover process may be postulated. Thus, as insulator charging takes place around a pore, the alumina grain crystallites become polarised under the influence of the applied field, with significant charge-trapping also occurring at impurity- and vacancy-defect sites within the pore [26]. Trapped electrons may subsequently tunnel out of these defect centres under the influence of the locally enhanced electric field [51]. Upon reaching a threshold value of the local electric-field, explosive relaxation of the polarised dielectric can occur across the pore [51]. Such a process may then give rise to the explosive exoemission of electrons, with local electron-heating and vaporisation of ceramic glass. Detachment of alumina grains [26] and/or glass particles may result from such a micro-discharge event within the pore. This localised micro-discharge process in a porous dielectric is illustrated schematically in Fig 5.10.

Referring to Figs 4.2.1 and 4.2.7, it is also important to note the *collimated* nature of the jets emitted from surface-flashover sites. Collimation of the jet efflux may result from the ejection of ceramic material from within a pore, following some degree of internal reflection as the jet of material emerges from the ceramic. Figure 5.11 gives a schematic illustration of this jet-emission process from a pore-defect in the alumina insulator.

It can be further concluded that a well-collimated emission of jets might be expected from deeper pore structures, i.e. owing to a longer pore-depth and a higher probability of jet-collisions with the pore wall. Conversely, more 'diffuse' jets might be emitted from shallow pores (shallow pore-depth in relation to the pore-diameter), where there is less likelihood of the jet striking the ceramic before it emerges from a pore.

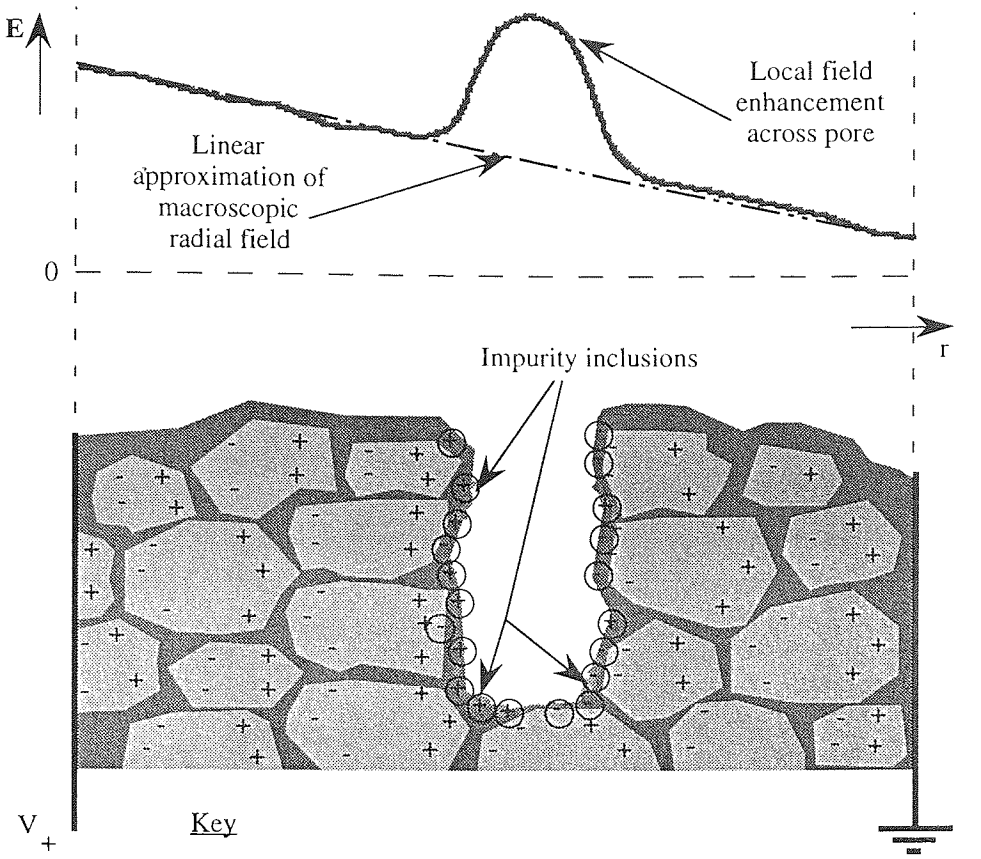

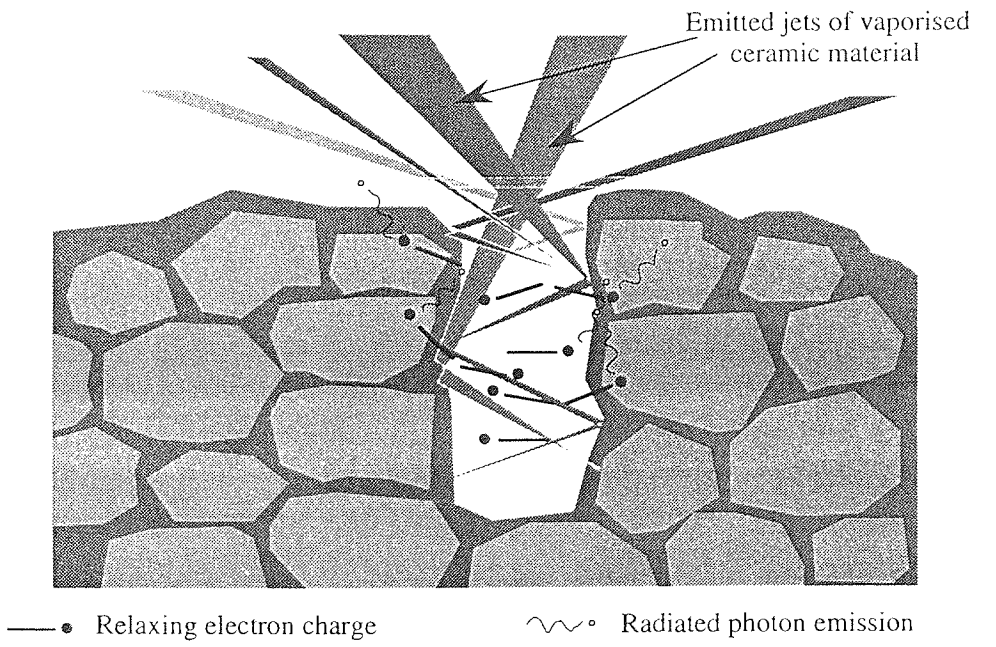

Fig. 5.10 Schematic illustration of enhanced-field polarisation and explosive charge-relaxation at a ceramic pore, leading to the vaporisation of jets of ceramic material

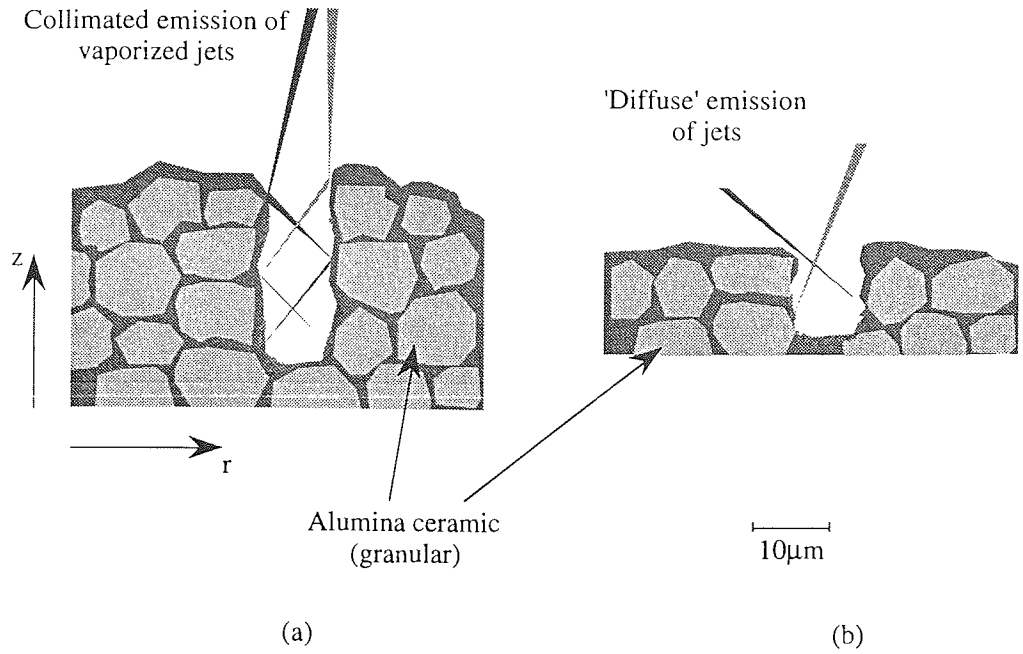

Fig. 5.11 Illustrating jet emission by (a) collimated processes from deep pore structures, and (b) diffuse emission processes from shallow pores

5.4 Surface-discharge initiation of triggered vacuum breakdown

From the electro-optical prebreakdown and breakdown studies of alumina ceramic described in Chapters 3 and 4, the specific behaviour of an alumina trigger dielectric within a triggered vacuum gap (TVG) switch (see Section 2.7.4) may be discussed. This section therefore explores the physical nature of a pulsed-field surface-flashover event across the trigger ceramic, and the role of the trigger-ceramic surface-flashover in the initiation of triggered electrical breakdown within the vacuum gap of the TVG.

Considering the electrical breakdown ("firing") of the TVG, several physical models of vacuum breakdown predict the initial traversal of the interelectrode gap by a population of prebreakdown electrons [67,70,220]. In plane vacuum gaps, the physical electron-emission processes at the cathode have been widely explored [68], as reported in Section 2.2. Within the *three*-electrode structure of the TVG, the erosion of the trigger insulator has been proposed to yield a "trigger plasma" that introduces a population of breakdown-initiating electrons and ions into the vacuum gap [13]. However, it is interesting to note from the present work that the

high-voltage DC and pulsed-field (HV) operation of an alumina trigger-ceramic did not result in any visible erosion of the insulator, as shown by Figs 4.3.7 and 4.3.8. Erosion processes were only evident in the metallized ceramic with the application of extra-high voltage (EHV) pulsed electrical fields in excess of 60 $kVmm^{-1}$, as described in Section 4.3.7.3.

With reference to Section 5.3, pulsed-field surface-flashover events were seen to evolve bright jets from the insulator; the observed behaviour of these jets, and the condensation of ejected efflux material onto Nb target surfaces, suggested the vaporisation of ceramic material from the trigger module. From the temporally-correlated electrical and optical observations shown in Figs 4.2.13 and 4.2.14, the ablated jet material was not seen to emerge from the ceramic until ≈ 50 - 100ns after the collapse of the applied voltage-pulse. This observation may therefore suggest a finite *thermal* time-constant in the heating and vaporisation of the ceramic efflux material. Thus, the development of this pulsed-field emission process, and its possible role in the initiation of a triggered vacuum gap switch, will be discussed in the following sub-sections.

5.4.1 Physical origins of 'Initiating Electrons' The studies of DC prebreakdown phenomena described in Section 4.1.3 have observed the low-field "stripping" of electrons from localised luminous centres in the alumina trigger ceramic. From the apparent solid-state nature of the vacancy defects associated with these emission centres (Sections 5.1.1.2 and 5.2.1), localised populations of trapped electrons may exist at these *F*-centre defect sites, with electron-energies close to the conduction-band of the alumina (see Fig 5.5).

This 'solid-state' model of the alumina dielectric may be expanded to describe the surface-flashover phenomena associated with the application of a time-varying voltage *pulse* to the trigger-ceramic module. Thus, electrons may be detrapped from *F*-centres as these defects become ionised under the influence of an increasing electric field, at field-values approaching ≈10 $kVmm^{-1}$; i.e. as observed in Section 4.1.3.1. A proportion of these electrons may subsequently be scattered into vacuum in the direction of the main-gap field, as shown in Fig 4.1.13. Figure 5.12 illustrates this pulsed *prebreakdown* emission of detrapped electrons from the alumina dielectric. It is important to note the *pre*breakdown nature of this electron-emission process, and the possible emission of electrons *prior* to the collapse of the trigger voltage, V_t {Fig 5.12(a)}.

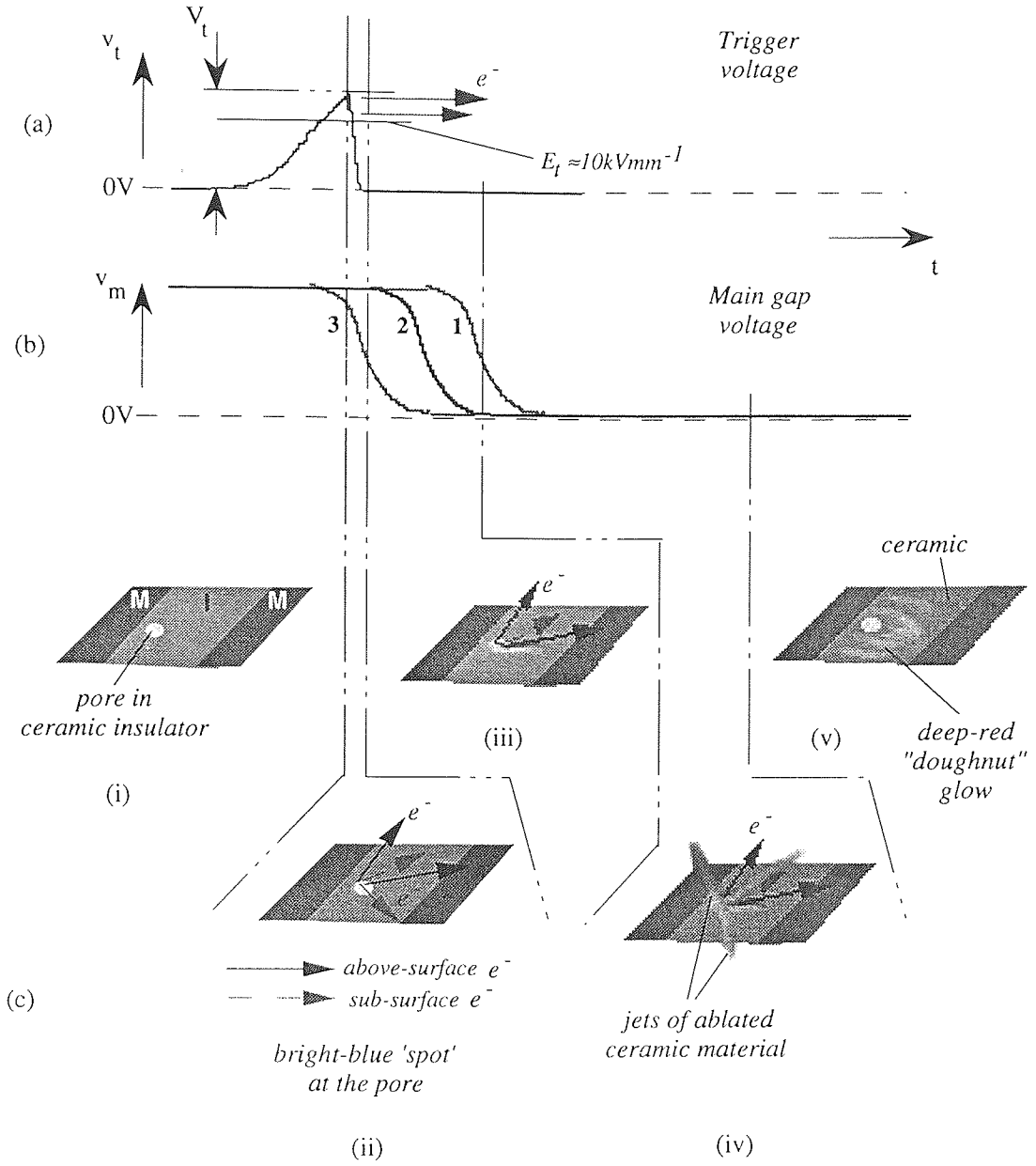

Fig. 5.12 A schematic temporal sequence showing the breakdown of the (a) trigger and (b) main-gap voltages in a TVG, with (c) a proposed cycle of electro-optical emission events from a porous region of the trigger ceramic

With reference to Section 4.2.5 and the spatial correlation observed between DC prebreakdown and pulsed breakdown surface-flashover events, Fig 5.12(c) proposes a schematic sequence of electro-optical events at a porous region in the surface-layers of the alumina trigger-ceramic. As the applied electric field exceeds ≈10 $kVmm^{-1}$, concentrations of *F*-centres at pores in the alumina may become ionised, and emit electrons into the vacuum gap under the influence of the main-gap voltage, V_m {Fig 5.12(b)}. Further electrons may recombine with the ionised *F* and F^+ centres, producing localised spot(s) of near-UV / bright-blue light in the porous alumina region {Fig 5.12(c ii)} [38,39,41]. A further population of "hot"

electrons (Section 5.2.2.2) may also be detrapped from phonon-excited defect-centres in the alumina, under the influence of the applied planar electric field.

This prebreakdown electron-detrapping process may be enhanced as V_t continues to increase, until a threshold population of electrons are detrapped and scattered into the alumina. A corresponding electron-current threshold may then lead to a bridging of the alumina trigger gap, causing V_t to collapse {Fig 5.12(c iii)}.

Thus, the electrical breakdown of the main interelectrode-gap voltage in the TVG (V_m) may be initiated by the emission of prebreakdown electrons from defect centre(s) in the alumina trigger insulator. Main-gap breakdown is often observed to follow the collapse of the trigger voltage, V_t, i.e. breakdown often occurs between regions **1** and **2** of Fig 5.12(b). This observation is consistent with the "trigger erosion" / "trigger plasma" models of TVG firing, such as those conceived by Boxman [13] and Vozdvizhenskii *et al* [5]. The present picture of *pre*trigger-breakdown electron-emission from the trigger ceramic raises the possibility of electron-initiated TVG firing *prior to* the collapse of V_t, i.e. as shown in region **3** of Fig 5.12(b).

5.4.2 Post-breakdown phenomena in the TVG trigger ceramic With reference to the proposed model of prebreakdown exoelectron emission from defect-centres within the alumina, as postulated in Section 5.4.1, further electrons may be scattered into the surface-layers of the alumina dielectric. These electrons may then become trapped at Cr^{3+} substitutional defects, as discussed in Section 5.1. Recombination of electrons at Cr^{3+} sites is associated with the radiation of a deep-red (R_1, R_2) photon-emission line-doublet, described in Section 5.1.1.1.

In the pulsed-field surface-flashover of the ceramic trigger modules studied in this work, a deep-red post-breakdown 'glow' was observed in the ceramic, in the spatial vicinity of a surface-flashover event. As discussed in Section 5.3.3.1, the exponential decay recorded in this glow suggested a solid-state *luminescence* phenomenon. This finding appears to be consistent with the scattering of electrons into the ceramic from ionised defect (*F*) -centres, with a subsequent recombination of these scattered electrons at Cr^{3+} sites within the alumina matrix (see Section 5.1.3.2). Thus, a post-breakdown luminescence may be observed in the trigger insulator, as illustrated by Fig 5.12(c v).

5.4.3 Vaporisation phenomena in the trigger ceramic The scattering of prebreakdown electrons during their transport through the trigger ceramic can lead

to localised ohmic heating of the alumina. Equally, thermal excitation may arise from the phonon-vibrations that are associated with non-radiative electron-transitions at *F*-centre sites in the alumina (see Fig 5.5) [41]. Thus, material from the porous alumina region may subsequently be vaporised, and ejected from the trigger ceramic as a plume, or 'jet' of ablated ceramic material, as discussed in Section 5.3 {see Fig 5.12(c iv)}. It was also noted that the evolution of the jet plume has been recorded to appear ≈100ns after trigger breakdown (see Section 4.2.2.3). Consequently, the emergence of the jet of ablated ceramic material may occur too late to initiate the breakdown of the main vacuum gap, given the short (sub-100ns) delay-times observed in the firing of practical TVG switches [173,216].

However, the apparent 'late' emergence of the jet plume from the trigger ceramic can nevertheless provide a region of plasma in the interelectrode region, following the initial emission of prebreakdown electrons into the main vacuum gap. Considering a plane vacuum gap, the space-charge limited electron current, I_e, that can be sustained through the main vacuum gap may be estimated from the Child-Langmuir equation [170]

$$I_e = 2.3 \times 10^{-6} \cdot \frac{A\, V^{1.5}}{d^2} \qquad [A]$$

where V is the main gap (anode-cathode) potential, d is the interelectrode spacing {Fig 5.13(a)} and A is the cathode area. For the commercial TVG described in Section 2.7.5, having a 6mm diameter cathode and 5mm interelectrode gap, the Child-Langmuir equation predicts a main-gap current $I_e \approx 430$mA, for a main-gap voltage of 3kV.

With the introduction of prebreakdown electrons and a trigger-discharge vapour into the main interelectrode gap, an *effective* gap separation, d', may be postulated, measured between the anode electrode and the propagation front of the trigger plasma. The emergence of the vapour plume from the trigger ceramic may therefore substantially reduce the effective gap spacing, and yield a corresponding increase in the measured value of switched main-gap current, I_a. According to this model, the trigger vapour may not necessarily *initiate* the breakdown of the TVG, but instead emerge as an extension of the adjacent main electrode (see Fig 1.2) [13], as illustrated in Fig 5.13 (b).

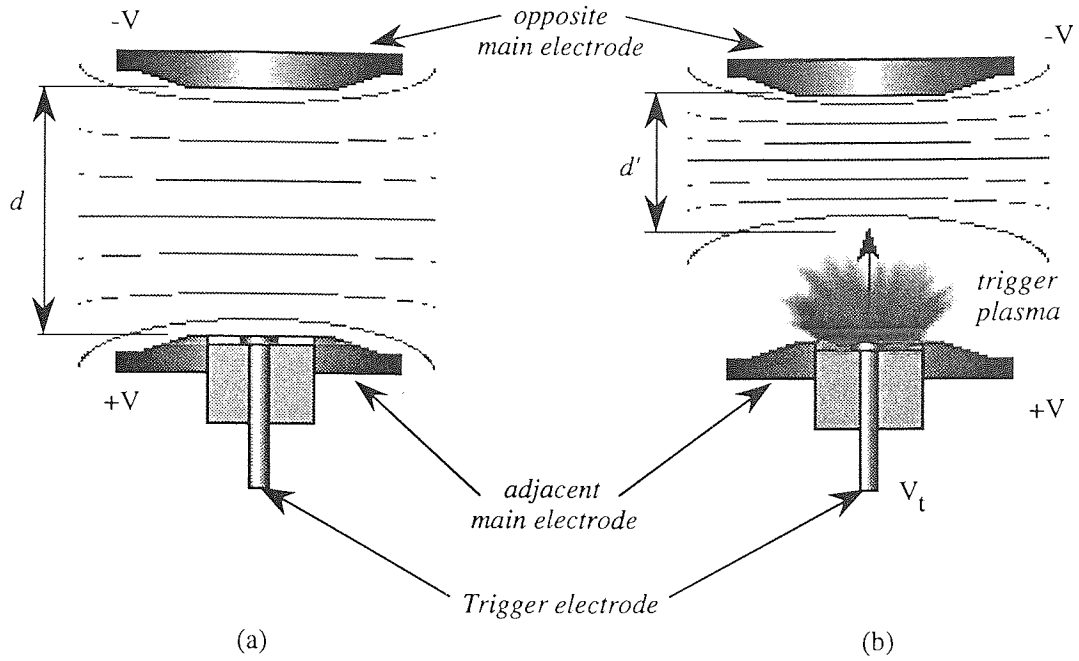

Fig. 5.13 (a) An illustration of the effective shortening of the main interelectrode gap-spacing {d} of a TVG, that may occur as a result of (b) the introduction of a trigger-discharge plasma

Therefore as the trigger vapour emerges as a "virtual electrode" into the main vacuum gap, the resulting close gap-spacing (d') could then support the commutation of high main-gap currents into the kilo-ampère range, as predicted by the Child-Langmuir equation. This hypothesis is supported by the high main-gap currents observed in the commercial TVG outlined in Section 2.7.5, where the measured interelectrode current, $I_a \approx 8kA$ (see Figs 1.6 and 2.7.3).

6. CONCLUSIONS AND RECOMMENDATIONS

The key objectives of the work described in this thesis have been to explore the physical nature of the surface-flashover phenomenon along a solid insulator in vacuum, and to determine the role of such a surface-flashover event in the initiation of a triggered vacuum gap (TVG) switch. In order to investigate existing physical models of surface-flashover, this experimental study has characterised the *in vacuo* electro-optical behaviour of a metallized trigger insulator that formed part of a commercial surface-discharge triggered TVG switch. The metallized ceramic module comprised a 94% alumina (α-Al_2O_3) cylindrical insulator, bridging two planar concentric rings of Mo/Mn metallization. From complementary electrical and optical studies of this planar M-I-M regime, it has been possible to draw the following conclusions.

6.1 DC prebreakdown optical emission

By exploiting the visible access provided by a transparent anode [37] to simulate the anode of a real TVG device, it has been demonstrated for the first time that the prebreakdown phase in the trigger ceramic is characterised by a distributed optical luminosity, termed the "doughnut" effect [37,38]. Furthermore, from the use of high-speed optical spectroscopy techniques [37], it has been shown that this photon-emission associated with the DC prebreakdown of the alumina ceramic is consistent with radiative electron recombination processes at defect-centres within the solid insulator.

Thus, a deep-red prebreakdown luminescence was recorded from the ceramic (R_1, R_2 ruby-line emission: λ_1 = 692.5nm and λ_2 = 694.0nm), that appeared to originate from substitutional chromium impurity-centres (Cr^{3+}) within the alumina lattice [45,134]. In addition, bright-blue and near-UV photon-emissions (λ=410nm and λ=325nm respectively) were also observed, that were consistent with radiative electron-recombination processes at negative-ion (anion) oxygen-vacancy defects (*F* and F^+ centres respectively) within the crystalline alumina phase [41,93]. The apparent 'solid-state' nature of the optical emission spectrum, and its persistence within a partial gas pressure environment, offered no experimental evidence to support the long-established hypothesis of "electron hopping" presented in the electron-stimulated gas desorption (ESD) model of solid-insulator surface-flashover [16,18].

6.2 Prebreakdown DC electronic characteristics

From complementary measurements of the electrical characteristics of virgin insulator samples, it was established that the optical phenomena described above were associated with two electric-field thresholds in the alumina ceramic module. The first of these thresholds was coincident with the initiation of the deep-red "doughnut" effect, and the second with the bright-blue 'spot' optical emissions. The onset of each of these current thresholds was attributed to the filling of charge-traps by injected electrons, giving rise to the observed radiation of photons. Corresponding increases in the measured current over time are thought to indicate a lengthening of the mean-free-path available to injected-electrons as a greater number of trap-sites were filled [29].

Exposure of the alumina specimen to DC voltage stress, over a time-period of several hours, produced an irreversible increase in the measured resistivity of the insulator. Again, this behaviour was consistent with the macroscopic filling of charge-traps associated with defect-centres in the alumina, thereby lengthening the electron mean-free-path, and increasing the proportion of electrons contributing to the DC current measured at the anodic ring-electrode [29]. Such a hypothesis was also evidenced by the observed decrease in the intensity of luminescence detected from the alumina; i.e. since it indicated a reduction in the number of injected-electrons being trapped and thereby radiating photons.

Another mechanism by which the alumina resistivity could be modified is by the migration of defects under the influence of the applied electric field; i.e. since a redistribution of electronic defect-centres can be expected to result in a change in the measured resistivity [139]. The resistivity of the alumina may also be reduced by local heating of the ceramic from phonon-excitations associated with electron-recombination at *F* centre defects [41]. Given the observation of an *irreversible* increase in resistivity in the alumina following the removal of a DC prebreakdown voltage-bias, the possible role of this phonon-heating mechanism remains uncertain.

With the application of an additional transverse electrical field to an auxiliary transparent anode located above the metallized alumina M-I-M regime, electrons were seen to be 'stripped' from the planar metallized-ceramic region with low transverse voltages ($V_a \leq 10kV$) applied to the transparent anode. At low transverse fields ($E_a \approx 5kV\ mm^{-1}$), transverse electron-currents were only measured

in the presence of a DC bias to the planar M-I-M regime, and the accompanying excitation of bright-blue luminescent 'spots' in the alumina dielectric region. This electron-emission behaviour may be explained by the field-induced emptying of shallow electron-traps at oxygen-vacancy defect centres (F^+ and F centres) within the alumina ceramic [41]. Such low-field 'stripping' of electrons from electronic defect centres can be seen to have implications upon the initiating mechanism of surface-discharge initiated TVG switches, whereby *pre*breakdown electrons may be detrapped from the trigger ceramic and scattered into the main interelectrode gap (see Section 6.6.4).

6.3 Optical emission from pulsed-field surface-flashover events

In order to more closely simulate the operational conditions of the metallized alumina trigger structure, the experimental measurements were extended to include *pulsed field* studies. Thus, concurrent real-time high-speed imaging and electronic-monitoring techniques have been used to capture the spatial and optical characteristics of pulsed-field flashover events at the surface of this alumina dielectric structure. Careful spatial analysis of captured surface-flashover images showed firstly that the breakdown process is associated with luminescent centres within the alumina, and secondly that these centres were the source of bright 'jets'. It was also noted that these jets could be explained in terms of a model involving the ballistic ejection of electrically-neutral hot particulate material. This conclusion was further evidenced by the collection of Al and Si material from pulsed-field surface-flashover events on the alumina module: the nature of the collected material suggested an emitted 'efflux' of vaporised silica/alumina glass microparticles within the jet plume, ejected during the surface-flashover of the alumina ceramic. The jets were seen to propagate with straight-line trajectories, with no recorded influence from transverse electric fields. This finding suggested a predominant *vapour* state of jet material, with little evidence to show field-deflection of ionised jet species.

Spectral studies of the luminous centres on the ceramic surface revealed a strong band of photon-emission within the 678nm-706nm wavelength range. This deep-red emission band was characteristic of radiative electron-recombination at substitutional Cr^{3+} impurity centres within the ceramic lattice, as characterised during the DC prebreakdown of the alumina dielectric module (see Section 6.1). Following a surface-flashover event, a logarithmic decay was observed in this luminescence, again suggesting *solid-state* photon emission from the decaying luminous centres in the alumina [218].

6.4 Pulsed-field electronic behaviour

Following the collapse of the applied voltage pulse, negative currents were collected through a transversely-mounted transparent anode: these negative current signals were observed to follow the voltage breakdown of the alumina module within a 50ns period. The temporal characteristics of these current-pulses suggested an exoemission of electrons from the pulsed-field surface-flashover event, accompanying and possibly preceding the emission of any ionised species in the jets. Thus, the *pre*breakdown 'stripping' of electrons has been proposed to occur from ionised defect-centres in the alumina, with electrons scattered into the vacuum gap under the influence of the main-gap electric field, *prior to* the collapse and breakdown of the planar voltage across the alumina dielectric.

Infrequent observations were made of pulsed-field surface-flashover events along the outer-diameter of the cylindrical alumina modules. Such events were characterised by a slow rate of collapse in the applied voltage pulse: i.e. compared to the voltage collapse-times associated with (more typical) surface-flashover events recorded on the metallized end-face of the alumina. This observation was interpreted in terms of the apparent charge-carrier velocity indicated in each of these surface-flashover regimes. Thus, it has been proposed that the local propagation of a surface-flashover event is enhanced by the presence of a high electronic-mobility region in the alumina surface, i.e. such as would result from the presence of local concentrations of defect-centres within the alumina surface-layers [105,106,221].

6.5 Surface topography of flashover sites

In order to determine the physical origin of the 'jet' phenomena observed from the surface-flashover of alumina modules, scanning electron microscopy (SEM) was employed to view the ceramic in the spatial vicinity of recorded surface-flashover events. Thus, SEM mapping of pulsed-field surface-flashover sites on the alumina revealed high local densities of pore defects within pulsed-field surface-flashover regions on the ceramic surface. Similar concentrations of surface-porosity were recorded in the region of luminous bright-blue 'spots' observed during the DC prebreakdown of the alumina module. Localised electric-field enhancement [164] and charge-trapping at these defect-centres [26] have been proposed to lead to explosive microdischarges as a result of dielectric polarisation-relaxation at the

pores [51]. The rapid discharge of this lattice polarisation energy may subsequently vaporise alumina material within the pore, and initiate an explosive surface-flashover event along the ceramic.

6.6 Recommendations for further investigation

Apart from answering a number of important questions, the present study of the physical phenomena associated with the pulsed-field surface-flashover of an alumina insulator has also raised a number of questions that point to possible areas for further investigation. It is believed that these additional studies would provide new experimental findings to complement those of the present work, and facilitate a more comprehensive description of the surface-flashover phenomena on a metallized alumina trigger module.

6.6.1 Temperature monitoring of alumina dielectric In exploring the nature of the photon-emission from the alumina ceramic, thermal *quenching* of DC prebreakdown luminescence at elevated temperatures may occur [219]. This phenomenon might therefore be investigated using concurrent electrical and temperature measurements of the alumina module. Below a given quenching temperature, high-temperature luminescence from the ceramic may also exhibit a broadening of the optical emission bands, owing to the thermal excitation and broadening of the defect-centre electron-energy bands [219]. Furthermore, localised high-resolution temperature probing may confirm phonon-heating of the alumina lattice, associated with non-radiative electronic transitions between F- and F^+ -centre energy-levels in the bright-blue 'spot' regions [41]. Such an investigation might also provide an additional insight into the operation of surface discharge triggered TVG switches at elevated temperatures.

6.6.2 Ultra high-speed optical spectrometry To complement the high-resolution spectroscopy of DC prebreakdown photon-emission presented in this work, similar spectroscopic techniques might be applied to the *pulsed-field* surface-flashover of alumina ceramic. Such an analysis would provide further insights into the nature and state of material species involved in a surface-flashover event [221]. A spectral study of the vapour jets may also be undertaken, in order to confirm the nature of the jet species collected on Nb foils in this work, and to highlight any further constituents in the jet efflux. Thus, whilst ultra-fast optical techniques may be used to characterise the jets [221], laser-induced fluorescence (LIF) could

provide a complementary spectroscopic technique, offering high sensitivity and temporal resolution [222,223].

6.6.3 High sensitivity fast-frame imaging A significant limitation of the fast-framing Imacon camera [194] used in this work was its insensitivity to photon emissions from high-voltage ($E \leq 20kV\ mm^{-1}$) surface-flashover events. The provision of an additional image-intensifier into the lens optics of such a system may permit a more sensitive study of HV surface-flashover events. This arrangement may also reveal further optical phenomena in the initial 100ns "dark period" observed following the application of extra-high voltage pulses ($E \approx 60kV\ mm^{-1}$) to the alumina module.

6.6.4 TVG main gap breakdown development The trigger insulator study detailed in this thesis could clearly be used as the basis for a further programme of research to investigate the triggered breakdown of the main vacuum gap in a TVG switch. Such a scheme would have to probe the interaction of the electrically-stressed main vacuum gap with the surface-flashover vapour material emitted from the trigger insulator. It could be envisaged that such a study would employ a similar experimental regime to that used for the present study. However, as illustrated schematically in Fig 6.1, a fine-mesh metal anode may be employed to form a partially-transparent third electrode. A metallic anode would permit the commutation of pulsed main-gap *breakdown* currents ($I_a \approx$ few kA) between the alumina module and the third electrode, and would therefore replicate the current magnitudes encountered in a TVG.

Careful adjustment of the trigger voltage-pulse magnitude (V_t) could then be used to determine the electric-field threshold across the trigger module that is required to initiate the high-voltage breakdown of the main interelectrode gap. This investigation could therefore explore the *pre*breakdown exoemission of electrons from the trigger ceramic proposed in Section 5.4.1. Significantly, such a study could then consider the possibility of electrical breakdown of the main vacuum gap triggered by a *pre*breakdown electric-field across the trigger ceramic, i.e. the breakdown of the main gap in the absence of a surface-flashover along the trigger insulator.

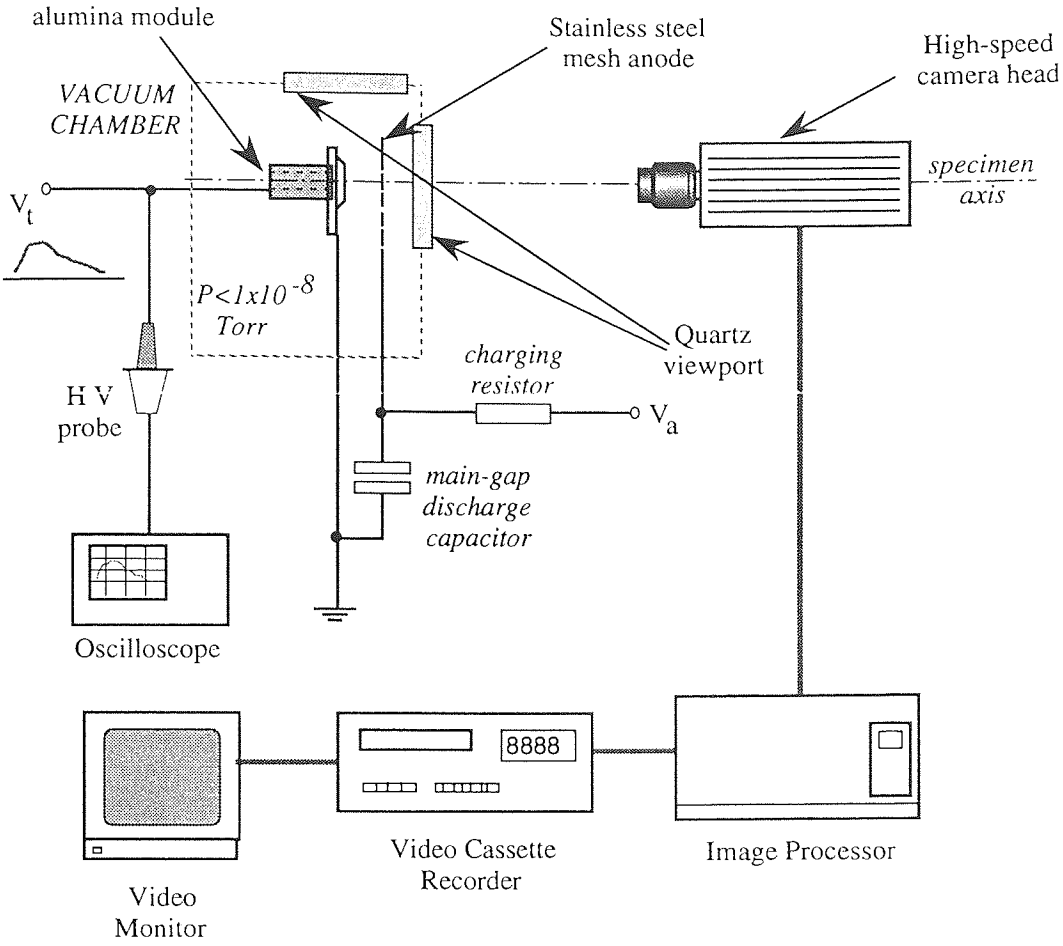

Fig. 6.1 A proposed experimental system for observing the temporal development of a triggered vacuum breakdown event

REFERENCES

[1] J C Kellogg, J R Boller, R J Commisso, D J Jenkins, R D Ford, W H Lupton & J D Shipman, "Triggered vacuum flashover switch for high-power applications", *Rev. Sci. Instrum.*, **62** (11), pp. 2689-2694, 1991

[2] G C Damstra & J A J Pettinga, "Low-vacuum Triggered Gap for Crowbar applications", *Proc. XV International Symposium on Discharges and Electrical Insulation in Vacuum*, Darmstadt, Germany, pp. 433-435, 1992

[3] W Shang & G C Damstra, "Triggerable 250kA/20kV Prevacuum Gaps for Pulsed High Current and Voltage Applications", *Proc. XV International Symposium on Discharges and Electrical Insulation in Vacuum*, Darmstadt, Germany, pp. 508-512, 1992

[4] A N Greenwood, "Vacuum Arc Applications", in *Vacuum Arcs - Theory and Application*, J M Lafferty (editor), New York: Wiley, pp. 321-361, 1980

[5] V A Vozdvizhenskii & V A Sidorov, "RVU-3 Sealed Triggered Vacuum Switch", *Instrum. and Exp. Tech.*, **35** (4), pp. 638-643, 1992

[6] J M Lafferty, "Triggered Vacuum Gaps", *Proc. IEEE*, **54** (1), pp. 23-32, 1966

[7] G A Farrall, "Low Voltage Firing Characteristics of a Triggered Vacuum Gap", *IEEE Trans. Elec. Dev.*, **13** (4), pp. 432-438, 1966

[8] S Kamakshaiah & R S N Rau, "Delay characteristics of a simple triggered vacuum gap", *J. Phys. D: Appl. Phys.*, **8**, pp. 1426-1429, 1975

[9] H Arita, K Suzuki & Y Kurosawa, "Switching Characteristics of the Triggered Vacuum Gap For a High-Repetition-Rate Pulse-Power Source", *IEEE Trans. Plasma Sci.*, **20** (2), pp. 76-79, 1992

[10] F T Warren, J M Wilson, J E Thompson, R L Boxman & T S Sudarshan, "Vacuum Switch Trigger Delay Characteristics", *IEEE Trans. Plasma Sci.*, **PS-10** (4), pp. 298-301, 1982

[11] R A Dougal, G Morris & G D Volakakis, "Low-Loss, High Repetition-Rate Vacuum Switching", *IEEE Trans. Plasma Sci.*, **19** (5), pp. 976-988, 1992

[12] H C Miller, "Flashover of Insulators in Vacuum - Review of the Phenomena and Techniques to Improve Holdoff Voltage", *IEEE Trans. Elec. Insul.*, **28** (4), pp. 512-527, 1993

[13] R L Boxman, "Triggering Mechanisms in Triggered Vacuum Gaps", *IEEE Trans. Elec. Dev.*, **24** (2), pp. 122-128, 1977

[14] G R Govinda Raju, R Hackam & F A Benson, "Breakdown mechanisms and electrical properties of triggered vacuum gaps", *J. Appl. Phys.*, **47** (4), pp. 1310-1317, 1976

[15] K D Bergeron, "Theory of the secondary electron avalanche at electrically stressed insulator-vacuum interfaces", *J. Appl. Phys.*, **48** (7), pp. 3073-3080, 1977

[16] R A Anderson, "Mechanism of fast surface flashover in vacuum", *Appl. Phys. Lett.*, **24** (2), pp. 54-56, 1974

[17] C H de Tourreil & K D Srivastava, "Mechanism of Surface Charging of High-Voltage Insulators in Vacuum", *IEEE Trans. Elec. Insul.*, **EI-8** (1), pp. 17-21, 1973

[18] R A Anderson & J P Brainard, "Mechanism of pulsed surface flashover involving electron-stimulated desorption", *J. Appl. Phys.*, **51** (3), pp. 1414-1421, 1980

[19] E W Gray, "Vacuum surface flashover: A high-pressure phenomenon", *J. Appl. Phys.*, **58** (1), pp. 132-141, 1985

[20] N C Jaitly & T S Sudarshan, "DC surface flashover mechanism along solids in vacuum based on a collision-ionization model", *J. Appl. Phys.*, **64**, (7), pp. 3411-3418, 1988

[21] N C Jaitly & T S Sudarshan, "A collision-ionization model for DC surface flashover across insulator-vacuum interfaces", *Proc. 6th IEEE Pulsed Power Conference*, (Arlington, USA), B H Bernstein & P J Turchi (eds.), IEEE cat. no. 87CH2522-1, (IEEE, New York, 1987), pp. 64-68

[22] R G Bommakanti & T S Sudarshan, "Trap-dominated breakdown processes in an insulator bridged vacuum gap", *J. Appl. Phys.*, **66** (5), pp. 2091-2099, 1989

[23] M J Kofoid, "Phenomena at the Metal-Dielectric Junctions of High-Voltage Insulators in Vacuum and Magnetic Field", *Trans. AIEE III - Power Apparatus and Systems*, **79** , pp. 991-999, 1960

[24] M J Kofoid, "Effect of Metal-Dielectric Junction on High-Voltage Breakdown over Insulators in Vacuum", *Trans. AIEE III - Power Apparatus and Systems*, **79** , pp. 999-1004, 1960

[25] N C Jaitly and T S Sudarshan, "Electrocathodoluminescence in insulator-bridged vacuum gaps under high-voltage stress", *J. Appl. Phys.*, **60** (10), pp. 3711-3719, 1986

[26] G Blaise, "New Approach to Flashover in Dielectrics based on a Polarization Energy Relaxation Mechanism", *IEEE Trans. Elec. Insul.*, **28** (4), pp. 437-443, 1993

[27] C LeGressus, F Valin, M Henriot, M Gautier, J P Duraud, T S Sudarshan, R G Bommakanti & G Blaise, "Flashover in wide-band-gap high-purity insulators: Methodology and mechanisms", *J. Appl. Phys.*, **69** (9), pp. 6325-6333, 1988

[28] G Blaise & C LeGressus, "Charging and flashover induced by surface polarization relaxation process", *J. Appl. Phys.*, **69** (9), pp. 6334-6339, 1991

[29] G Blaise, "Polarization and Relaxation of Dielectrics, the Two Key Points of Breakdown", *Proc. Conférence Interdisciplinaire sur les Dielectriques*, Antibes, France, in *Le Vide, les Couches Minces - Supplément au n° 260*, 1992, pp. 417-426

[30] C LeGressus & G Blaise, "Breakdown Phenomena Related to Trapping /Detrapping Processes in Wide Band Gap Insulators", *IEEE Trans. Elec. Insul.*, **27** (3), pp. 472-481, 1992

[31] G Blaise & C LeGressus, "Flashover in insulators related to the destabilization of a localized space charge", *C.R. Acad. Sci. Paris*, 314 (Série II), pp. 1017-1024, 1992

[32] J E Thompson, "Triggered vacuum switch construction and performance", in *Gas Discharge Closing Switches*, G Shaefer (ed.), (New York: Plenum Press), 1990

[33] S Kamakshaiah & R S N Rau, "Low-voltage and high-current delay characteristics of a simple triggered vacuum gap", *J. Phys. D: Appl. Phys.*, **10**, pp. 1017-1022, 1977

[34] A J Moulson and J M Herbert, *Electroceramics - Materials, Properties, Applications*, (London: Chapman & Hall), pp 212-221, 1990

[35] W. H. Kohl, *Materials and Techniques for Vacuum Devices* , (New York: Reinhold), pp. 458-460, 1967

[36] B M Coaker, N S Xu, F J Jones & R V Latham, "Electrical and Optical DC Vacuum Emission Phenomena from a Ceramic-Insulated Planar Electrode Configuration", *IEEE Trans. Plasma Sci.*, **21** (5), pp. 400-406, 1993

[37] R. V. Latham, K. H. Bayliss and B. M. Cox, "Spatially correlated breakdown events initiated by field electron emission in vacuum and high-pressure SF_6", *J.Phys.D: Appl. Phys.*, **19**, pp. 219-231, 1986

[38] B M Coaker, N S Xu, F J Jones & R V Latham, "DC prebreakdown photon emission from an alumina insulator in vacuum", *Brit. Ceram. Proc.*, **No. 52**, W E Lee & A Bell (eds.), London: The Institute of Materials, 1994

[39] B M Coaker, N S Xu, F J Jones & R V Latham, "Photon emission from an alumina insulator in vacuum subjected to DC electrical fields", *J.Phys.D: Appl. Phys.*, **27**, pp. 1448-1456, 1994

[40] B M Coaker, N S Xu, F J Jones & R V Latham, "High-speed optical imaging of explosive exoemission from an alumina ceramic in vacuum", in *XVI International Symposium on Discharges and Electrical Insulation in Vacuum*, Gennady A Mesyats, Editor, Proc. SPIE 2259, pp. 10-13, 1994

[41] K H Lee and J H Crawford, "Luminescence of the *F* center in sapphire", *Phys. Rev. B*, **19** (6), pp. 3217-3221, 1979

[42] T Asokan and T S Sudarshan, "Spectral Nature of Luminosity Associated with the Surface Flashover Process", *IEEE Trans. Elec. Insul.*, **28** (2), pp. 192-199, 1993

[43] C Jardin, P Durupt, D Robert & C LeGressus, "The Luminescence of Insulating Materials excited by an Electron Beam", *Proc. Conf. on Elec. Ins. and Dielec. Phenom. (CEIDP)*, Annual Report (November 1993), Pocono Manor, PA, USA, pp. 221-226

[44] Y Saito, N Matuda, S Anami, A Kinbara, G Horikoshi & J Tanaka, "Breakdown of Alumina RF windows", *IEEE Trans. Elec. Insul.*, **EI-24** (6), pp. 1029-1032, 1989

[45] Y Saito, S Michizoni, S Anami & S Kobayashi, "Surface Flashover of Alumina rf Windows for High-power Use, *IEEE Trans. Elec. Insul.*, **28** (4), pp. 566-573, 1993

[46] C R Li, R Sundararaman & T S Sudarshan, "Spectroscopic Observations of Surface Flashover across an Insulator in Vacuum under Pulsed Excitation, *IEEE Trans. Plasma Sci.*, **21** (5), pp. 598-604, 1993

[47] D E Buraczyk, G G Edelmon & K W Zieher, "Time-of-flight analysis of a plasma jet from a spark plug in vacuum, *J.Appl.Phys.*, **73** (7), pp. 3169-3171, 1993

[48] N Wild & P Coakley, "Evidence for Discrete Plasma Emission during Dielectric Discharge Events", *IEEE Trans. Nuclear Sci.*, **NS-31** (6), pp. 1591-1593, 1984

[49] A Görtler, J Christiansen, R Dötzer & K Frank, "Investigations of Pulsed Surface Flashovers for the Triggering of Pseudospark High-Power Switches", *IEEE Trans. Plasma Sci.*, **17** (5), pp. 762-765, 1989

[50] T Asokan & T S Sudarshan, "Role of Coulombic Centres on Insulator Surface Breakdown Characteristics", *IEEE Trans. Elec. Insul.*, **27** (5), pp. 1040-1049, 1992

[51] R V Latham, A Abbot, I D Chalmers & N S Xu, "Optical studies of surface flash-over, *J.Phys.D: Appl. Phys.*, **27**, pp. 312-319, 1994

[52] A Roth,*Vacuum Technology*, Amsterdam: North-Holland, 1976, pp. 1-15

[53] F R Fuller & W Brunhart, "A new generation of vacuum tubes for modulator and switch applications", *Int. J. Electronics*, **62** (6), pp. 837-842, 1987

[54] O Gröbner, "General considerations in the design of accelerator vacuum systems", *J. Vac. Sci. Technol. A*, **9** (3), pp. 2074-2080, 1991

[55] D G Armour, "Vacuum aspects of modern surface treatment in analysis",*Vacuum*, **43** (1/2), pp. 117-120, 1992

[56] D T A Blair, "Breakdown in Gases", in *Electrical Insulation*, A Bradwell (ed.), London: Peter Peregrinus, 1983, pp. 1-14

[57] D Kind & H Kärner, *High-Voltage Insulation Technology*, Braunschweig: Vieweg, 1985, pp. 14-30

[58] D Kind & H Kärner, *High-Voltage Insulation Technology*, Braunschweig: Vieweg, 1985, pp. 168-172

[59] R V Latham, *High Voltage Vacuum Insulation: The Physical Basis*, London: Academic Press, 1981, pp. 13-49

[60] P A Redhead, J P Hobson & E V Kornelsen, *The Physical Basis of Ultrahigh Vacuum*, London: Chapman & Hall, 1968, pp. 304-416

[61] R V Latham, "High Voltage Vacuum Insulation: New Horizons", *IEEE Trans. Elec. Insul.*, **23** (5), pp. 881-894, 1988

[62] P A Chatterton, "Vacuum Breakdown", in *Electrical Breakdown of Gases*, J M Meek & J D Craggs (eds.), Chichester: Wiley, 1978, pp. 129-208

[63] R Hawley, "Solid Insulators in Vacuum: A Review",*Vacuum*, **18** (7), pp. 383-390, 1968

[64] P Malkin, "The vacuum arc and vacuum interruption", *J.Phys.D: Appl. Phys.*, **22**, pp. 1005-1019, 1989

[65] T S Sudarshan & J D Cross, "DC Electric Field Modifications Produced by Solid Insulators Bridging a Uniform-Field Vacuum Gap", *IEEE Trans. Elec. Insul.*, **8** (4), pp. 122-128, 1973

[66] P Graneau & H M Scheider, "Vacuum Insulation for Cryocables and its Resistance to Discharges", *IEEE Trans. Elec. Insul.*, **9** (2), pp. 63-68, 1974

[67] J M Lafferty, "Pre-breakdown and Breakdown", *Proc. X International Symposium on Discharges and Electrical Insulation in Vacuum*, Columbia, USA, p. 1, 1982

[68] R V Latham & N S Xu, "Electron pin-holes: the limiting defect for insulating high voltages by vacuum, a basis for new cold cathode electron sources", *Vacuum*, **42** (18), pp. 1173-1181, 1991

[69] R H Fowler & L Nordheim, "Electron Emission in Intense Electric Fields", *Proc. Roy. Soc.*, **A119**, pp. 173-181, 1928

[70] R V Latham, *High Voltage Vacuum Insulation: The Physical Basis*, London: Academic Press, 1981, pp. 51-89

[71] L M J Vries & G C Damstra, "Prebreakdown Emission Current Measurements in a 24kV Vacuum Interrupter with Butt Contacts", *IEEE Trans. Elec. Insul.*, **23** (1), pp. 97-100, 1988

[72] F Schwirzke, M P Hallal & X K Maruyama, "Onset of Breakdown and Formation of Cathode Spots", *IEEE Trans. Plasma Sci.*, **21** (5), pp. 410-415, 1989

[73] B M Cox & R N Bloomer, *Pre-Breakdown Electron Emission Currents in Ultra-High Vacuum and in the Presence of Gases*, Marchwood Engineering Laboratories, Central Electricity Generating Board, report no. RD/M/R.91, 1968

[74] R V Latham, *High Voltage Vacuum Insulation: The Physical Basis*, London: Academic Press, 1981, pp. 211-227

[75] R V Latham, "The insulation of high voltages in an accelerator environment: recent advances", *Nucl. Instrum. Meth. Phys. Res. A*, **287**, pp. 40-47, 1990

[76] V V Blagodarnyy, "Vacuum Breakdown Induced by a Prebreakdown Current from a Nonmetallic Inclusion at the Cathode", *Sov. J. Commun. Technol. Electron. (USA)*, **35** (9), pp. 118-122, 1990

[77] R V Latham, "A New Perspective on the Origin of Prebreakdown Electron Emission Processes", *IEEE Trans. Elec. Insul.*, **23** (1), pp. 9-16, 1988

[78] R V Latham, "The origin of prebreakdown electron emission from vacuum-insulated high voltage electrodes", *Vacuum*, **32** (3), pp. 137-140, 1982

[79] A D Archer, *Spectroscopic Studies of Field-Induced Electron Emission from Isolated Microstructures*, PhD Thesis, University of Aston, 1992

[80] K D Srivastava, *Support Insulators for High Voltage Apparatus in Vacuum*, Rutherford Laboratory Report RHEL/R 124, HMSO: London, 1966

[81] C H de Tourreil, K D Srivastava & U J Woelke, "Experimental Observation of Surface Charging of High-Voltage Insulators for Vacuum Apparatus", *IEEE Trans. Elec. Insul.*, **EI-7** (4), pp. 176-179, 1972

[82] I D Chalmers, J H Lei & J W Bethel, "Dielectric surface charge phenomena in vacuum", *Proc. XIV International Symposium on Discharges and Electrical Insulation in Vacuum*, Santa Fe, USA, pp. 324-327, 1990

[83] I D Chalmers, J H Lei & B Yang, "Surface charging and flashover of insulators in vacuum", in *XVI International Symposium on Discharges and Electrical Insulation in Vacuum*, Gennady A Mesyats, Editor, Proc. SPIE 2259, pp. 332-335, 1994

[84] J Cazaux, "Surface Potential and Electric Field Induced by Electron Bombardment of Insulators", *IEEE Trans. Elec. Insul.*, **24** (6), pp. 995-997, 1989

[85] J P Vigoroux, O Lee-Deacon, C LeGressus, C Juret & C Boiziau, "Surface processes occurring during breakdown of high-voltage devices", *IEEE Trans. Elec. Insul.*, **EI-18** (3), pp. 287-291, 1983

[86] J Cazaux & C LeGressus, "Phenomena relating to charge in insulators: macroscopic effects and microscopic causes", *Scanning Microscopy*, **5** (1), pp. 17-27, 1991

[87] O Yamamoto, T Hara, I Nakanishi & M Hayashi, "Monte Carlo Simulation of Surface Charging on Angled Insulators in Vacuum", *IEEE Trans. Elec. Insul.*, **28** (4), pp. 706-712, 1993

[88] H Takahashi, T Shioiri & K Matsumoto, "Effect of Dielectric Materials on Surface Breakdown in Vacuum and Analysis by Electron Trajectory Simulation", *IEEE Trans. Elec. Insul.*, **EI-20** (4), pp. 769-774, 1985

[89] C L Enloe, "The equilibrium charge distribution and electric field at a vacuum/dielectric interface", *J. Appl. Phys.*, **65** (9), pp. 3329-3334, 1989

[90] J P Shannon, S F Philp & J G Trump, "Insulation of High Voltage across Solid Insulators in Vacuum", *J. Vac. Sci. Technol.*, **2**, pp. 234-239, 1965

[91] T S Sudarshan, "Photonic emissions associated with a dielectric surface under high electric stress", *Proc. Conférence Interdisciplinaire sur les Dielectriques*, Antibes, France, in *Le Vide, les Couches Minces - Supplément au n° 260*, 1992, pp. 224-233

[92] O Milton, "Pulsed Flashover of Insulators in Vacuum", *IEEE Trans. Elec. Insul.*, **EI-7** (1), pp. 9-15, 1972

[93] Y Saito, "Breakdown phenomena in RF windows", *Proc. Conférence Interdisciplinaire sur les Dielectriques*, Antibes, France, in *Le Vide, les Couches Minces - Supplément au n° 260*, 1992, pp. 385-392

[94] C C Klick, "Properties of electron centres", in *Point Defects in Solids, Volume 1 - General and Ionic Crystals*, J H Crawford & L M Slifkin (eds.), New York: Plenum Press, 1972, pp. 291-325

[95] Y Saito, S Yamaguchi, S Anami, S Michizono, A Kinbara & N Matuda, "Breakdown of Alumina RF Windows", *Proc. XIV International Symposium on Discharges and Electrical Insulation in Vacuum*, Santa Fe, USA, pp. 372-376, 1990

[96] Y Saito, "Surface breakdown phenomena in alumina rf windows", in *XVI International Symposium on Discharges and Electrical Insulation in Vacuum*, Gennady A Mesyats, Editor, Proc. SPIE 2259, pp. 512-517, 1994

[97] T Suzuki, "Flashover Voltage over Ceramics in High Vacuum", *Japanese Journal of Applied Physics*, **13** (10), pp. 1541-1546, 1974

[98] T Takuma & T Kawamoto, "Field intensification near various points of contact with a zero contact angle between a solid dielectric and an electrode", *IEEE Trans. Power App. & Systems*, **PAS-103** (9), pp. 2486-2493, 1984

[99] T Takuma, "Field Behavior at a Triple Junction in Composite Dielectric Arrangements", *IEEE Trans. Elec. Insul.*, **26** (3), pp. 500-509, 1991

[100] O Yamamoto, T Hara, H Matsuura, M Hayashi & K Yukimura, "Temporal Behavior of Electric Field at Triple Junction and its Relation to Flashover of Bridged Vacuum Gaps", in *XVI International Symposium on Discharges and Electrical Insulation in Vacuum*, Gennady A Mesyats, Editor, Proc. SPIE 2259, pp.354-357, 1994

[101] J P Brainard & D Jensen, "Electron avalanche and surface charging on alumina insulators during pulsed high-voltage stress", *J. Appl. Phys.*, **45** (8), pp. 3260-3265, 1974

[102] H C Miller, "Flashover of insulators in vacuum: techniques to improve the hold-off voltage", *Proc. XV International Symposium on Discharges and Electrical Insulation in Vacuum*, Darmstadt, Germany, pp. 165-174, 1992

[103] Y Saito, S Michizoni, S Anami & S Kobayashi, "Surface Flashover of Alumina RF Windows for High-Power Use", *Proc. XV International Symposium on Discharges and Electrical Insulation in Vacuum*, Darmstadt, Germany, pp. 227-231, 1992

[104] L Eckertová, "Metal-insulator-metal and metal-insulator structures as electron sources", *Int. J. Electronics*, **69** (1), pp. 65-78, 1990

[105] F G Will, H G deLorentzi & K H Janora, "Conduction Mechanism of Single-Crystal Alumina", *J. Am. Ceram. Soc.*, **75** (2), pp. 295-304, 1992

[106] F G Will, H G deLorentzi & K H Janora, "Effect of Crystal Orientation on Conductivity and Electron Mobility in Single-Crystal Alumina", *J. Am. Ceram. Soc.*, **75** (10), pp. 2790-2794, 1992

[107] K Kitazawa & R L Coble, "Electrical Conduction in Single-Crystal and Polycrystalline Al_2O_3 at High Temperatures", *J. Am. Ceram. Soc.*, **57** (6), pp. 245-250, 1974

[108] A J Moulson and J M Herbert, *Electroceramics - Materials, Properties, Applications*, (London: Chapman & Hall), pp 5-82, 1990

[109] N W Ashcroft & N D Mermin, *Solid State Physics*, (Philadelphia: Saunders), 1976, pp. 615-641

[110] F C Brown, "Conduction by Polarons in Ionic Crystals", in *Point Defects in Solids, Volume 1 - General and Ionic Crystals*, J H Crawford & L M Slifkin (eds.), New York: Plenum Press, 1972, pp. 491-517

[111] N F Mott & E A Davis, *Electronic Processes in Non-Crystalline Materials*, Oxford: Clarendon Press, 1979, pp. 65-95

[112] O T Özkan & A J Moulson, "The electrical conductivity of single-crystal and polycrystalline aluminium oxide", *J.Phys.D: Appl. Phys.*, **3**, pp. 983-987, 1970

[113] J B Goodenough, "Fast Ionic conduction in solids", *Proc. R. Soc. Lond. A*, **393**, pp. 215-234, 1984

[114] A Doi, "Ionic conduction and conduction polarization in oxide glass", *J. Mat. Sci.*, **22**, pp. 761-769, 1987

[115] N F Mott & E A Davis, *Electronic Processes in Non-Crystalline Materials*, Oxford: Clarendon Press, 1979, pp. 1-5

[116] G S Perry. "Dielectric properties of titanate-alumina ceramics", *Proc. Conf. on Diel. Matls., meas. and apps.*, University of Lancaster, 1972, *IEE Conf. Publ. no. 67*, pp. 63-66

[117] P H Gleichauf, "Electrical Breakdown over Insulators in High Vacuum", *J. Appl. Phys.*, **22** (6), pp. 766-771, 1951

[118] H C Miller & R J Ney, "Gases released by surface flashover of insulators", *J. Appl. Phys.*, **63** (3), pp. 668-673, 1988

[119] A Watson, "Pulsed Flashover in Vacuum", *J. Appl. Phys.*, **38** (5), pp. 2019-2023, 1967

[120] R V Latham, *High Voltage Vacuum Insulation: The Physical Basis*, London: Academic Press, 1981, pp. 229-240

[121] T G Akhmatova, G S Kichaeva & P I Shkuropat, "Initiation of pulsed discharge on dielectric surface in high-current vacuum commutators", *Prib. i Tekh. Éksper.*, **3**, pp. 111-114, 1988

[122] R A Anderson, "Propagation velocity of cathode-initiated surface flashover", *J. Appl. Phys.*, **48** (10), pp. 4210-4214, 1977

[123] V A Nevrovsky, "On mechanisms of a surface flashover of dielectrics in a strong electric field", *Proc. XIV International Symposium on Discharges and Electrical Insulation in Vacuum*, Santa Fe, USA, pp. 372-376, 1990

[124] V A Nevrovsky, "Surface and bulk conduction processes in surface flashover", *Proc. XV International Symposium on Discharges and Electrical Insulation in Vacuum*, Darmstadt, Germany, pp. 221-223, 1992

[125] J D Cross & K D Srivastava, "High Speed Photography of Surface Flashover Across a Divided Insulator in Vacuum", *Proc. X International Symposium on Discharges and Electrical Insulation in Vacuum*, Columbia, USA, pp. 286-287, 1982

[126] J D Cross & K D Srivastava, "High Speed Photography of Surface Flashover Across a Divided Insulator in Vacuum", *IEEE Trans. Elec. Insul.*, **EI-18** (3), pp. 277-279, 1983

[127] J K Bhardwaj & P A Chatterton, "Photographic Studies of the Discharge Development in a Low-Trigger-Voltage Vacuum Switch", *IEEE Trans. Elec. Insul.*, **23** (1), pp. 91-96, 1988

[128] K J Caulfield, R Cooper & J F Boas, "Threshold for displacement defect production in electron-irradiated alumina", *J. Nucl. Mat.*, **184**, pp. 150-151, 1991

[129] A Al Ghamdi & P D Townsend, "Ion beam luminescence of sapphire", *Nucl. Instrum. Meth. Phys. Res. B*, **46**, pp. 130-136, 1990

[130] P Kulis, Z Rachko, M Springis, I Tale & J Jansons, "Defect assisted intrinsic luminescence in Al_2O_3 crystals", *Rad. Eff. Def. Solids*, **119-121**, pp. 963-968, 1991

[131] G P Williams, G H Rosenblatt, M J Ferry, R T Williams & Y Chen, "Time resolved luminescence and absorption spectroscopy of defects in MgO and Al_2O_3", *J. Luminescence*, **40 & 41**, pp. 339-340, 1988

[132] E D Aluker, V V Gavrilov & S A Chernov, "Short-Lived Frenkel Defects in α-Al_2O_3", *Phys. stat. sol. (b)*, **171**, pp. 283-288, 1992

[133] M J Springis & J A Valbis, "Visible Luminescence of Colour Centres in Sapphire", *Phys. stat. sol. (b)*, **123**, pp. 335-343, 1984

[134] D Lapraz, P Iacconi, D Daviller & B Guilhot, "Thermostimulated Luminescence and Flourescence of α-Al_2O_3:Cr^{3+} Samples (Ruby)", *Phys. stat. sol. (a)*, **126**, pp. 521-531, 1991

[135] K Kawabata, T Seiyama, S Okuda & Y Shono, "Thermally Stimulated Exo-Electron Emission and Thermally Stimulated Luminescence of Irradiated α-Al_2O_3 powder", *Phys. stat. sol. (a)*, **106**, pp. 181-190, 1988

[136] J J O'Dwyer, "The Effect of Collision-Ionization Space-Charge on High Field Conduction in Solids", *IEEE Trans. Elec. Insul.*, **EI-15** (3), pp. 264-269, 1980

[137] R G Bommakanti & T S Sudarshan, "Time-resolved prebreakdown X-ray emission from polycrystalline alumina-bridged vacuum gaps for impulse stresses", *J. Appl. Phys.*, **71** (5), pp. 2181-2188, 1992

[138] J P Vigoroux, O Lee-Deacon, C LeGressus, C Juret & C Boiziau, "Surface Processes Occurring During Breakdown of High-Voltage Devices", *IEEE Trans. Elec. Insul.*, **EI-18** (3), pp. 287-291, 1983

[139] A J Moulson and J M Herbert, *Electroceramics - Materials, Properties, Applications*, (London: Chapman & Hall), pp 182-194, 1990

[140] H H Zhong, H C Kärner & M Gollor, "Time Characteristics of Fast Pulsed Flashover in Vacuum", *IEEE Trans. Elec. Insul.*, **27** (3), pp. 496-503, 1992

[141] F Hegeler, G Masten, H Krompholz & L L Hatfield, "Current, Luminosity & X-Ray Emission in the Early Phase of Dielectric Surface Flashover in Vacuum", *IEEE Trans. Plasma Sci.*, **21** (2), pp. 223-227, 1993

[142] J P Vigoroux, J P Duraud, A LeMoel, C LeGressus & D L Griscom, "Electron trapping in amorphous SiO2 studied by charge buildup under electron bombardment", *J. Appl. Phys.*, **57** (12), pp. 5139-5144, 1985

[143] K H Oh, C K Ong, B T G Tan, C LeGressus & G Blaise, "Variation of trapping/detrapping parameters as a function of the insulator size", *J. Appl. Phys.*, **74** (3), pp. 1960-1967, 1993

[144] J Fine & M Szymonski, "Electron stimulated desorption mechanisms in insulators", *Proc. Conférence Interdisciplinaire sur les Dielectriques*, Antibes, France, in *Le Vide, les Couches Minces - Supplément au n° 260*, 1992, pp. 69-76

[145] A J Moulson and J M Herbert, *Electroceramics - Materials, Properties, Applications*, (London: Chapman & Hall), pp 1-4, 1990

[146] E Ryshkewitch, Oxide Ceramics - Physical Chemistry and Technology, (New York: Academic Press), pp. 109-205, 1960

[147] S K Mohapatra, S K Tiku & F A Kröger, "The Defect Structure of Unintentionally Doped α-Al_2O_3 Crystals", *J. Am. Ceram. Soc.*, **62** (1-2), pp. 50-57, 1979

[148] N N Greenwood & A Earnshaw, *Chemistry of the elements*, (Oxford: Pergamon), pp. 273-279, 1984

[149] W Zhou, L Zhang & H Fu, "Glassy Phase in Alumina Ceramic Shell Molds", *J. Am. Ceram. Soc.*, **75** (1), pp. 77-81, 1992

[150] E Ya Medvedovskii & F Ya Kharitonov, "Optimizing the properties of electrical-insulating high-alumina ceramic materials", *Glass and Ceramics*, **42** (7-8), pp. 379-382, 1985

[151] L Schachter, J D Ivers, J A Nation & G S Kerslick, "Analysis of a diode with a ferroelectric cathode", *J. Appl. Phys.*, **73** (12), pp. 8097-8110, 1993

[152] A J Moulson and J M Herbert, *Electroceramics - Materials, Properties, Applications*, (London: Chapman & Hall), pp 265-317, 1990

[153] Z W Yin, X Y Song & J W Feng, "Grain Boundary Structures in PLZT Ceramics", *Ferroelectrics*, **94**, pp. 269-273, 1989

[154] J Asano, M Okuyama & Y Hamakawa, "Electron Emission into Vacuum from Lead-Zirconate-Titanate Ferroelectric Ceramics Induced by Polarization Reversal", *Jpn. J. Appl. Phys.*, **32** (1B), pp. 396-398, 1993

[155] J Asano, M Okuyama & Y Hamakawa, "Field-Excited Electron Emission from Ferroelectric Ceramic in Vacuum", *Jpn. J. Appl. Phys.*, **31** (9B), pp. 3098-3101, 1992

[156] H Gundel, H Riege, J Handerek, & K Zioutas, "Low-pressure hollow cathode switch triggered by a pulsed electron beam emitted from ferroelectrics", *Appl. Phys. Lett.*, **54** (21), pp. 2071-2073, 1989

[157] H Gundel, J Handerek & H Riege, "Time -dependent electron emission from ferroelectrics by external pulsed electric fields", *J. Appl. Phys.*, **69** (2), pp. 975-982, 1991

[158] H Gundel, J Handerek, H Riege, E J N Wilson & K Zioutas, "Fast Polarisation Changes in PZT Ceramics by High-Voltage Pulses", *Ferroelectrics*, **94**, pp. 337-342, 1989

[159] P H Gleichauf, "Electrical Breakdown over Insulators in High Vacuum", *J. Appl. Phys.*, **22** (5), pp. 535-541, 1951

[160] J M Wetzer, P A A F Wouters, A J M Pemen, M G Danikas, P C T van der Laan & A J Aldenhoven, "Final Report of the study on high-voltage design aspects of microwave tubes", *ESA contract no. 7186/87/NL/JG(SC)*, 1991

[161] J M Wetzer & P A A F Wouters, "The effect of insulator charging on breakdown and conditioning", *Proc. XV International Symposium on Discharges and Electrical Insulation in Vacuum*, Darmstadt, Germany, pp. 636-640, 1992

[162] J M Wetzer, M G Danikas & P C T van der Laan, "Analysis and Improvement of HV Components for Spacecraft Travelling-wave Tubes", *IEEE Trans. Elec. Insul.*, **25** (6), pp. 1117-1124, 1990

[163] J M Wetzer & P A A F Wouters, "High-Voltage Design of Vacuum Components", in *XVI International Symposium on Discharges and Electrical Insulation in Vacuum*, Gennady A Mesyats, Editor, Proc. SPIE 2259, pp. 382-385, 1994

[164] D D Chang, T S Sudarshan & J E Thompson , "Analysis of Electric Stress Distribution in Cavities Embedded within Dielectric Structures, *IEEE Trans. Elec. Insul.* , **EI-21**, pp. 213-219, 1986

[165] H C Miller, "Improving the voltage holdoff performance of alumina insulators in vacuum by quasimetallizing or doping", *Physica*, **104C**, pp. 183-188, 1981

[166] R. G. Bommakanti and T. S. Sudarshan, "Influence of Mechanical Grinding and Polishing Operations of Brittle Polycrystalline Alumina on the Surface Flashover Performance", *J. Appl. Phys.*, **67** (11), pp. 6991-6997, 1990

[167] N C Jaitly, T S Sudarshan, R A Dougal & H C Miller, "Degredation due to Wet Hydrogen Firing on the High-Voltage Performance of Alumina Insulators in Vacuum", *IEEE Trans. Elec. Insul.* , **22**, pp. 447-452, 1987

[168] D F Alferov, V A Vozdvijemski, N I Korobova, I O Sibiriak and V A Sidorov, "Triggered vacuum switch with subsidiary cathode", *Proc. XV International Symposium on Discharges and Electrical Insulation in Vacuum*, Darmstadt, Germany, pp. 411-415, 1992

[169] K H Bayliss, R V Latham, F Jones & D J Mellor, "A study of the electron emission characteristics of a triggered vacuum switch", *Vacuum*, **34** (7), pp. 705-708, 1984

[170] J K Bhardwaj, *Instabilities in the operation of a low trigger-voltage vacuum gap*, PhD Thesis, University of Liverpool, UK, 1986

[171] V A Vozdvizhenskii & V A Sidorov, "Initial Stage of Discharge Current Growth in a Triggered Vacuum Gap", *IEEE Trans. Plasma Sci.*, **19** (5), pp. 778-781, 1991

[172] V A Sidorov & V A Vozdvizhenskii, "Trigger gap configuration effect on triggered vacuum switch initiating characteristics", *Proc. XV International Symposium on Discharges and Electrical Insulation in Vacuum*, Darmstadt, Germany, pp. 513-517, 1992

[173] A J Green & C Christopolous, "Plasma Build-up and Breakdown Delay in a Triggered Vacuum Gap", *IEEE Trans. Plasma Sci.*, **PS-7** (2), pp. 111-115, 1979

[174] W Shang & G C Damstra, "The Properties of Triggered Vacuum Gaps", *IEEE Trans. Elec. Insul.*, **28** (4), pp. 650-656, 1993

[175] S Kamakshaiah & R S N Rau, "Low voltage firing characteristics of a simple triggered vacuum gap", *IEEE Trans. Plasma Sci.*, **PS-5** (3), pp. 164-170, 1977

[176] S Kamakshaiah & R S N Rau, "Low-voltage and high-current delay characteristics of a simple triggered vacuum gap", *J. Phys. D: Appl. Phys.*, **10**, pp. 1017-1022, 1977

[177] G R Govinda Raju, R Hackam & F A Benson, "Time delay to firing of a triggered vacuum gap with barium titanate in trigger gap", *Proc. IEE*, **124** (9), pp. 828-832, 1977

[178] P J Brannon & D F Cowgill, "Low-jitter laser-triggered vacuum switch using a composite target", *IEEE Trans. Plasma Sci.*, **16** (2), pp. 325-327, 1988

[179] I. M Farley & G L Scott, "Firing characteristics of a low-jitter miniature laser-triggered vacuum switch", *IEEE Trans. Plasma Sci.*, **18** (2), pp. 247-249, 1990

[180] V S Bulygin, V B Lebedev, G A Pryanikova, V V Ryukkert, S S Tsitsiashvili & V A Yakovlev, "Laser-triggered vacuum switch", *Sov. Phys. Tech. Phys.*, **20** (4), pp. 561-563, 1976

[181] R G Fellers, F T Warren & J E Thompson, "A laser triggered vacuum gap for high energy applications", in *South-Easton '80* (April 1980), Nashville, TN, USA, *IEEE pub. no. 4363.06666 1980 80 CH1558-6*, pp. 315-318

[182] A H Guenther & J R Bettis, "The laser triggering of high-voltage switches", *J.Phys.D: Appl. Phys.*, **11**, pp. 1577-1613, 1978

[183] P J Brannon & M E Riley, "A Model for the Operation of a Laser-Triggered Vacuum Low-Inductance Switch", *IEEE Trans. Plasma Sci.*, **17** (6), pp. 859-862, 1989

[184] P H Ron, V K Rohatgi & R S N Rau, "Rise Time of a Vacuum Gap Triggered by an Exploding Wire", *IEEE Trans. Plasma Sci.*, **PS-11** (4), pp. 274-278, 1983

[185] P H Ron, V K Rohatgi & R S N Rau, "Delay time of a vacuum gap triggered by an exploding wire", *J. Phys. D: Appl. Phys.*, **17**, pp. 1369-1379, 1984

[186] T Vijayan & V K Rohatgi, "Characteristics of Exploding-Wire Plasmas", *IEEE Trans. Plasma Sci.*, **PS-13** (4), pp. 197-201, 1985

[187] A Gupta & R S N Rau, "Triggered vacuum gap for initiating electric arcs in vacuum", *J.Phys.E: App. & Tech.*, **5**, pp. 415-416, 1972

[188] N Vidyardhi & R S N Rau, "A simple triggered vacuum gap", *J.Phys.E: App. & Tech.*, **6**, pp. 33-34, 1973

[189] G Banville, A Delmas, N Haddad & C Rioux, "Study of Recovery Phenomena in a High-Current Pulse-Triggered Vacuum Switch", *IEEE Trans. Plasma Sci.*, **17** (5), pp. 781-785, 1989

[190] D F Alferov, V A Sidorov & V A Vozdvijenskii, "Switching characteristics of the submicrosecond triggered vacuum switch", in *XVI International Symposium on Discharges and Electrical Insulation in Vacuum*, Gennady A Mesyats, Editor, Proc. SPIE 2259, pp. 247-250, 1994

[191] G C Damstra & X Zhang, "Series resonance inverter with triggered vacuum gaps", in *XVI International Symposium on Discharges and Electrical Insulation in Vacuum*, Gennady A Mesyats, Editor, Proc. SPIE 2259, pp. 270-272, 1994

[192] A Johnstone, *TVG5 Trigger Unit Users Operating Manual*, EEV Limited, Lincoln, UK, March 1991

[193] *Kodak Ektapro EM Motion Analyzer, Model 1012*, Kodak Ltd. Electronic Vision Systems, 1990

[194] *Operators Manual: Imacon 468 ultra-high speed electronic camera and software*, Hadland Photonics Ltd., April 1994

[195] *6601/6602 Optical Spectrum Analysers Technical Description*, Rees Instruments Ltd. Application Note 10.0

[196] P S Turner, "Electron Microscope Techniques for Surface Characterization", in *Surface Analysis Methods in Materials Science*, D J O'Connor, B A Sexton & R St C Smart (Eds.), (Berlin Heidelberg: Springer-Verlag), pp. 79-96, 1992

[197] N Damaschin & A Damaschin, "History of ceramic samples revealed by SEM images", *Microscopy and Analysis*, **44**, p. 7, 1994

[198] G C Smith, "Quantitative Surface Microanalysis by Auger and X-ray Photoelectron Spectroscopy", *MATERIALS CHARACTERIZATION*, **25**, pp. 37-71, 1990

[199] G E Muilenberg (ed.), *Handbook of X-ray Photoelectron Spectroscopy*, Perkin Elmer Corporation, Eden Prairie, Minnesota, 1979

[200] S H Sie, "Rutherford Backscattering Spectrometry and Nuclear Reaction Analysis", in *Surface Analysis Methods in Materials Science*, D J O'Connor, B A Sexton & R St C Smart (Eds.), (Berlin Heidelberg: Springer-Verlag), pp. 203-219, 1992

[201] J L Cocking & G R Johnston, "Characterization of Oxidized Surfaces", in *Surface Analysis Methods in Materials Science*, D J O'Connor, B A Sexton & R St C Smart (Eds.), (Berlin Heidelberg: Springer-Verlag), pp. 371-386, 1992

[202] N C Jaitly & T S Sudarshan, "Electrocathodoluminescence in insulator-bridged vacuum gaps under high-voltage stress", *J. Appl. Phys.*, **60** (10), pp. 3711-3719, 1976

[203] C J McHargue, "The Mechanical and Tribological Properties of Ion Implanted Ceramics", in *Ion Beam Modification of Insulators*, P Mazzoldi & G W Arnold (eds.), Amsterdam: Elsevier, 1987

[204] J F Ziegler, *TRIM - 91: The Transport of Ions in Matter*, New York: IBM Research, 1991

[205] S Biagi: private communication, University of Liverpool, 1993

[206] G Djogo & J D Cross, "Influence of Injected Plasma on Oscillations of Cathode Luminosity in Triggered Vacuum Breakdown", *Proc. XV International Symposium on Discharges and Electrical Insulation in Vacuum*, Darmstadt, Germany, pp. 51-53, 1992

[207] C Jeynes, "RBS of spark gaps implanted with Cr", *private communication*, University of Surrey, 1994

[208] G R Harrison, *Massachusetts Institute of Technology Wavelength Tables*, (New York: Wiley), 1939

[209] A Duncan, *private communication*, 1993

[210] Y Liu and B R Patterson, "Frequency of Pore Location in Sintered Al_2O_3", *J. Am. Ceram. Soc.*, **75** (10), pp. 2599-2600, 1992

[211] VG Quadrupoles Ltd, *Publication No. AJW-PT 639*

[212] D Lake, "Pictures in Time", *Advanced Imaging*, **9**, pp. 47-51, 1994

[213] P Kovitya, "Thermodynamic and Transport properties of Ablated Vapors of PTFE, Alumina, Perspex, and PVC in the Temperature Range 5000-30000 K", *IEEE Trans. Plasma Sci.*, **PS-12** (1), pp. 38-42, 1984

[214] A H Kitai, *Solid State Luminescence*, (London: Chapman & Hall), 1993, pp. 12-16

[215] G W C Kaye & T H Laby, *Tables of Physical and Chemical Constants*, (London: Longman), 1972, p. 156

[216] S P Bugaev, V V Kremnev, Yu I Terent'ev, V G Shpak & Ya Ya Yurike, "Surface Breakdown in vacuum on Barium Titanate", *Sov. Phys. - Tech. Phys.*, **16** (9), pp. 1547-1551, 1972

[217] C Oatley, *Electric and Magnetic Fields* (Cambridge University Press: Cambridge), pp. 99-119, 1976

[218] A K Jonscher & A de Polignac, "The time dependence of luminescence in solids", *J.Phys.C: Solid State Phys.*, **17**, pp. 6493-6519, 1984

[219] G Blasse, "Luminescent centres in insulators", *Solid State Luminescence* , ed. A H Kitai, (London: Chapman & Hall), pp. 21-51, 1993

[220] A N Greenwood, *Vacuum Switchgear*, A T Johns, J R Platts & D Aubrey (eds.), (London: The Institution of Electrical Engineers), pp. 25-48, 1994

[221] C R Li, R Sundaraman & T S Sudarshan, "Spectroscopic observations of Surface Flashover across an Insulator in Vacuum under Pulsed Excitation", *IEEE Trans. Plasma Sci.*, **25** (5), pp. 598-604, 1993

[222] G Lins, "Measurement of the copper vapour concentration in a pseudospark discharge by laser-induced flourescence", in *Optogalvanic Spectroscopy* (Institute of Physics Conference Series No. 113), R S Stewart & J E Lawler (eds.), Bristol, Philadelphia, New York, 1991, pp. 233-240

[223] G Lins & W Hartmann, "Metal Vapor Densities and Excitation Densities in a Pseudospark Switch", *IEEE Trans. Plasma Sci.*, **25** (5), pp. 511-515, 1993

APPENDIX A

UHV SYSTEM DESIGN

The design criteria for the experimental vacuum system encompassed specific practical requirements, namely (i) evacuation of the system to backing pressure within the run-up time of the turbomolecular pump, and (ii) system pump-down to UHV pressure ($\leq 10^{-8}$ mBar) within 4 hours. This appendix sets out the design calculations and measured vacuum-performance of the UHV system described in Section 3.2.1. The physical arrangement of various *in vacuo* gauges and fixtures are also described.

A.1 Vacuum system operation in viscous flow regime The performance of the experimental vacuum apparatus may be considered in terms of the intermediate evacuation of the system by the rotary pump (Leybold type D4B), with subsequent UHV pumping by the turbomolecular pump unit (Leybold type Turbovac 150V). The operational boundary between these respective *viscous* and *molecular* gas-flow regimes is determined by the onset of a unity ratio of the internal-diameter (D) of the backing-line hose, to the gaseous mean-free-path, λ [A1]; i.e. the *transition* flow regime is over the pressure region

$$1 < \frac{D}{\lambda} < 110 \qquad (A.1)$$

For the 2cm diameter hose used, the corresponding low-vacuum transition pressure is $\approx 10^{-2}$ Torr (see Fig 2.1.1). Taking an approximate internal system volume (V) of 10 litres, the low-vacuum 'roughing' performance of the rotary pump may be estimated using the simplified diagram of the vacuum system shown in Fig A.1.

Considering a vacuum line of circular cross-section, the gas flow-resistance along a given length of line, W_l, may be estimated from the following expression [A1,A2]:

$$W_l = \frac{\vartheta \, x \, 1 \, x \, 10^3}{1.57} \bullet \frac{l}{r^3} \quad [\mathrm{s\,l^{-1}}] \qquad (A.2)$$

where ϑ = coefficient of external friction = 1.6×10^{-5} s cm^{-1} for air at 20°C

and r, l are respectively the radius and length of the vacuum line in cm

and the corresponding vacuum line conductance, L, is given by

$$L = \frac{1}{W_l} \quad [\mathrm{l\,s^{-1}}] \tag{A.3}$$

yielding an effective pumping speed, S_{eff}, at the end of the vacuum line from a pump of nominal pumping speed Sp

$$S_{eff} = \frac{S_p}{1 + \frac{S_p}{L}} \quad [\mathrm{l\,s^{-1}}] \tag{A.4}$$

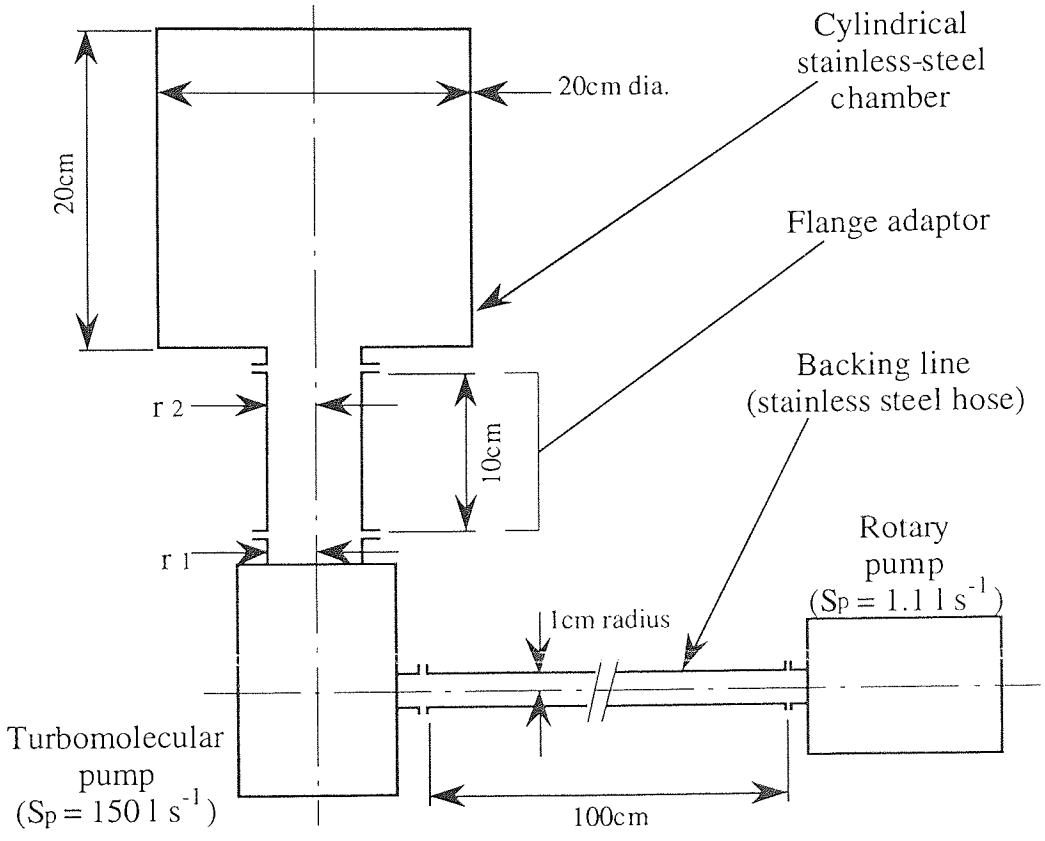

Fig. A.1 Diagrammatic representation of turbomolecular-pumped UHV chamber with rotary backing pump

Thus, for the stainless-steel hose (d = 20cm, l = 100cm) connecting the rotary backing pump to the UHV system, the flow resistance of this backing line (W_{lb}) will be approximately 1 s l^{-1}. Following through expressions A.3 and A.4, the effective backing pump speed, $S_{effb} \approx 0.52$ l s^{-1}. Given this effective pumping speed of the system volume V, an estimate of the system evacuation time in the low vacuum range, t_v, may be made from

$$t_v = \frac{V}{S_{effb}} \bullet \ln\left(\frac{p_a}{p_v}\right) \quad [s] \qquad (A.5)$$

yielding t_V = 220 s ≈ 4 minutes, for an ambient pressure, p_a, of 1000 mBar, and a low-vacuum backing pressure, p_V, of 1x10^{-2} mBar [A1,A2]. Thus, the rotary pump was capable of evacuating the UHV system to a 10^{-2} mBar medium vacuum in a comparable period to the 90s run-up time of the turbomolecular pump [A3].

As the system pressure approached medium vacuum and an intermediate gas-flow regime, the pumping-speed performance of the rotary pump declined owing to the back-streaming of pump-oil along the backing-line hose (see Fig A.2 (a)). The inclusion of a liquid-nitrogen-cooled fore-line trap mitigated against this effect (Fig 3.2.1). At this 'transition' point, the analytical chamber was evacuated by the turbomolecular pump, whose pumping-speed rose to a specified 150 l s^{-1} at system pressures below 10^{-2} mBar (Fig A.2 (b)), with *molecular* gas-flow though the UHV system.

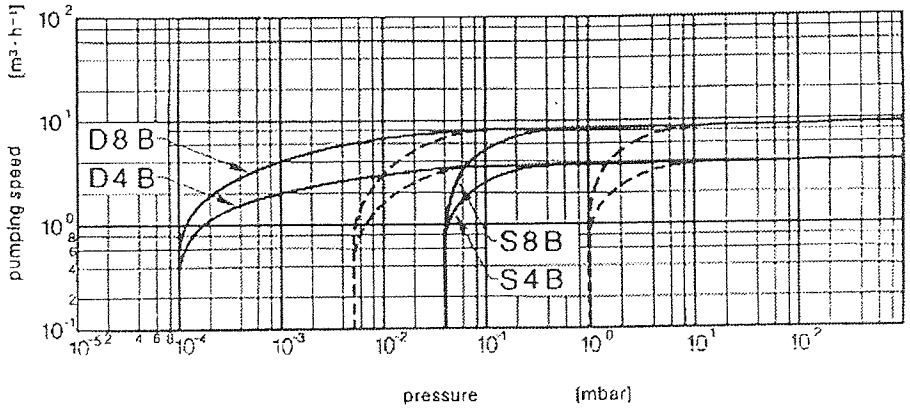

(a)

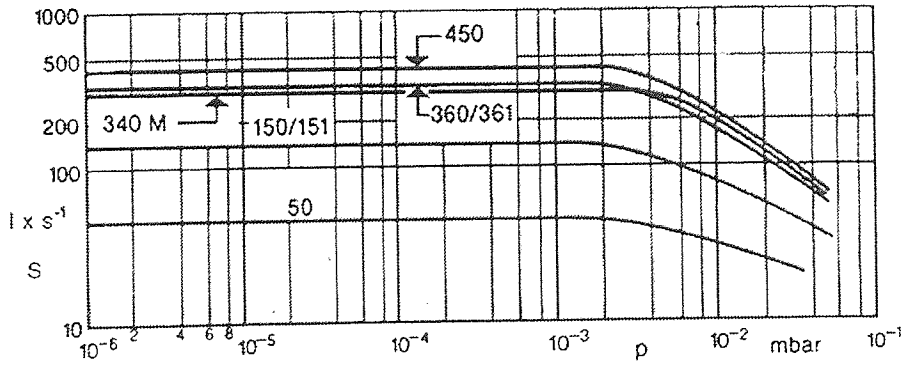

(b)

Fig. A.2 Variation of pumping-speed for air as a function of pressure, for (a) D4B rotary pump, and (b) Turbovac 150V turbomolecular pump (manufacturer's data [A3,A4])

A.2 Vacuum system operation in molecular flow regime In the molecular gas-flow region, at system pressures below 10^{-2} mBar, evacuation of the analytical chamber by the turbomolecular pump was constrained by the vacuum line formed by the flange adapter mating the pump flange to the chamber. With reference to Fig A.1 and eqn A.2, the flow resistance, W_{lv}, over the 100mm length of this adapter, will be approximately 2.8 x 10^{-3} s l^{-1}. Thus, the *total* flow resistance for molecular flow, W, is given by [A2]:

$$W = W_{o_{r1}} - W_{o_{r2}} + W_l \qquad [\text{s l}^{-1}] \qquad (A.6)$$

where W_{or1} and W_{or2} are the opening losses of the pump-header and adapter flanges respectively

For the opening losses W_{or1} and W_{or2}, $r_1 = r_2$ since the turbomolecular pump flange and the flange adapter are of equal internal diameter. Thus, the total flow resistance (W) is given by $W = W_{lv} = 2.8 \times 10^{-3}$ s l^{-1}, with a corresponding UHV line conductance, $L_{UHV} = 353$ l s^{-1}. From eqn A.4, the effective UHV pumping speed at the analytical chamber, $S_{effv} \approx 105$ l s^{-1}. Furthermore, the UHV pumping time, t_{UHV}, may be calculated from [A2]:

$$t_{UHV} = \frac{A \cdot q_{outgas} \cdot t_{outgas}}{S_{effv}\left(p - p_o - \frac{Q_{leak}}{S_{effv}}\right)} \qquad [\text{s}] \qquad (A.7)$$

Considering the stainless-steel vacuum chamber, the exposed area, A, of the internal surfaces is approximately the sum of the areas of the cylindrical wall and the top header flange, i.e.

$$A \approx A_{side-wall} + A_{headerflange} \approx 2\pi r_c h_c + \pi r_{c^2} \qquad [\text{cm}^2] \qquad (A.8)$$

Given a chamber radius, r_c, of 10cm, and a height, h_c, of 20cm, then $A \approx 1000\text{cm}^2$. The specific outgassing rate of stainless steel, q_{outgas}, after 3600 s (1 hour) of pumping is 1.7 x 10-9 l mBar s^{-1} cm^{-2}, and a reasonable leakage-rate, Q_{leak}, for this copper metal-sealed vacuum system would be $Q_{leak} \approx 1 \times 10^{-9}$ mBar l s^{-1}. Thus, from eqn A.7 (given an ultimate pumping pressure, p_o, of $<1 \times 10^{-10}$ mBar [A3]), the UHV pumping time, t_{UHV}, to an operating pressure (p) of 5×10^{-9} mBar will be:

$$t_{UHV} = 1.2\text{x}10^4\text{s} \approx 3.3\text{hrs}$$

The measured performance of the UHV system is summarised in Fig A.3. Figure A.3 plots the time-variation of the system pressure, starting from pump 'switch-on', as measured at the residual gas analyser (RGA) head located in the vacuum chamber beneath the electrode module (see Section A.3).

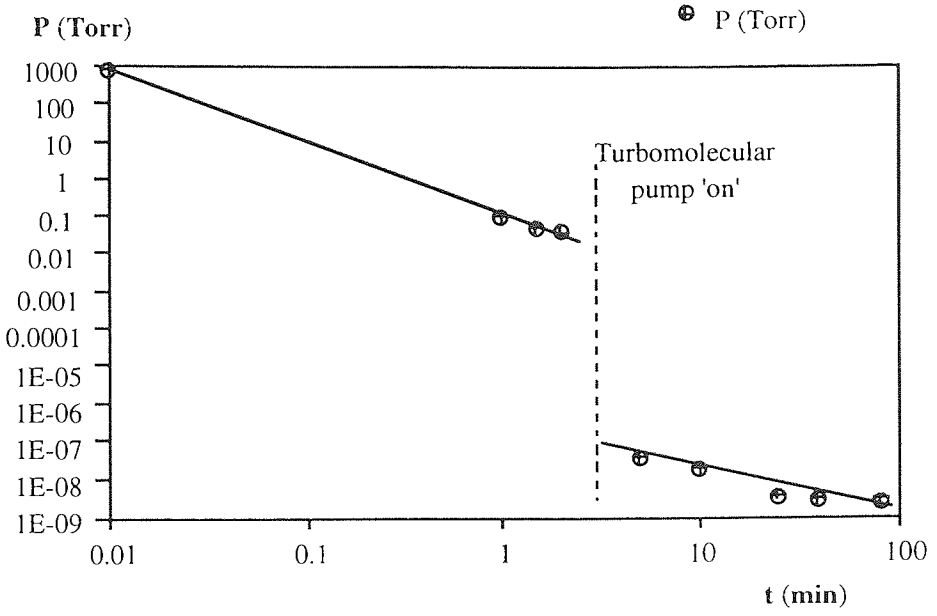

Fig. A.3 Variation of UHV system pressure with time (turbomolecular pump run-up over initial 90 second period)

A.3 Arrangement of analytical vacuum chamber Detailing the *in vacuo* features of the analytical UHV system, Fig A.4 shows a plan view of the interior of the vacuum chamber, together with a front elevation view of the chamber exterior. As described in Section 3.2.2, the electrode module (**H**) was attached to a linear manipulator feed-through (**I**), and aligned along the orthogonal centre-axes of viewports **A** and **B** (labelled as viewports **1** and **2** respectively in Section 3.2.4).

Fused quartz viewports facilitated the observation of optical phenomena at ultra-violet wavelengths approaching 200nm (see Fig A.5). Adjustment of the linear manipulator allowed precise alignment of the electrode module with external diagnostic instruments. Furthermore, these adjustments could be made *in situ*, without an opening the UHV chamber, and no loss of integrity in the evacuated chamber volume.

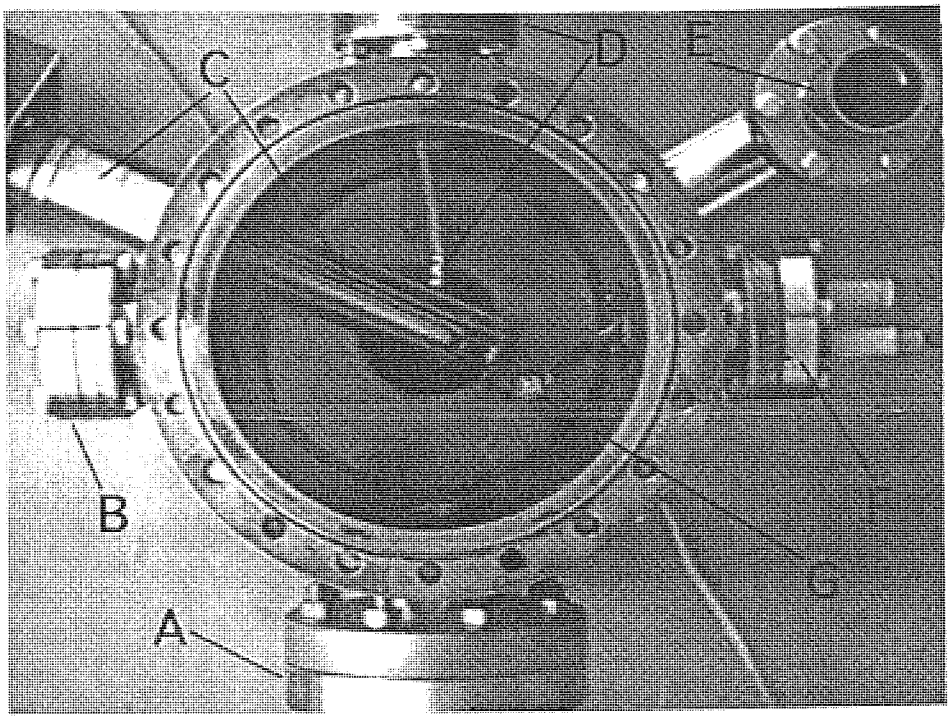

(a)

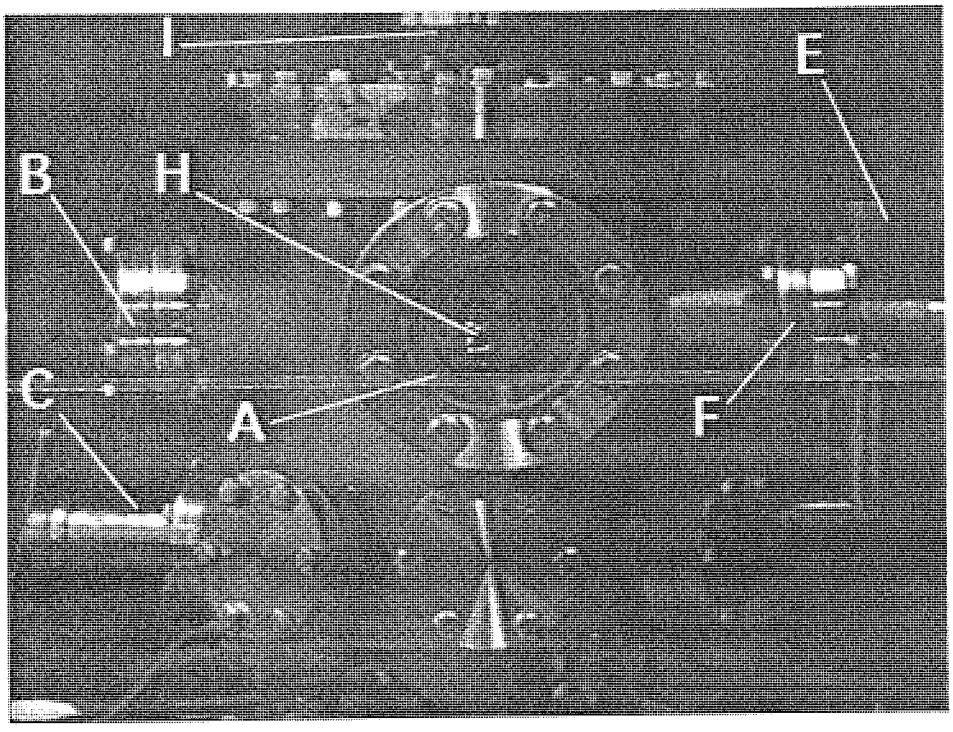

(b)

Fig. A.4 (a) Internal plan view and (b) external side-elevation view of analytical vacuum chamber. Key: (**A**), (**B**) Fused quartz viewports **1** and **2**, (**C**) Residual gas analyzer head, (**D**) High-voltage insulated feed-through, (**E**) Ionization gauge head, (**F**) High-voltage twin feed-through, heater connection, (**G**) 250 W radiant heater, (**H**) Location of experimental electrode module (**I**) Linear manipulator feed-through (50mm vertical traverse)

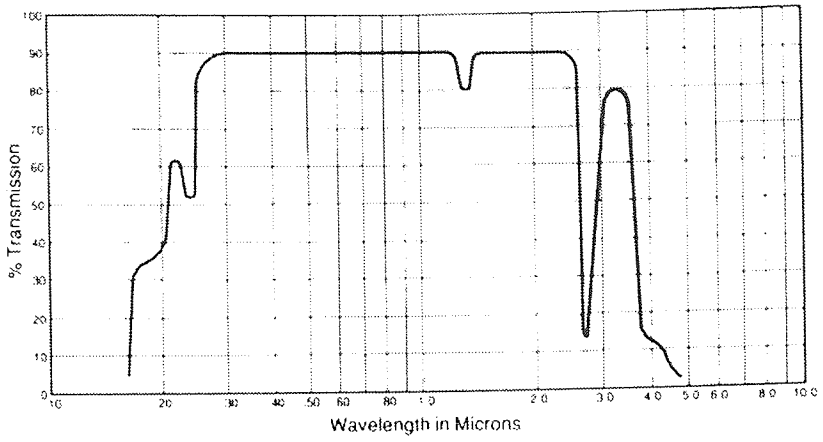

Fig. A.5 Optical transmission curve for fused quartz viewport, 10mm thickness (from manufacturer's data [A5])

Vacuum pressure within the UHV chamber was measured using a calibrated residual gas analyzer (RGA) (**C**), with an ionization gauge (**E**) providing a secondary vacuum-gauge facility. The evacuation of water-vapour could be enhanced by baking the chamber using a 250W radiant heater (**G**). Figure A.6 plots a 2-hour temperature-cycle of a test-specimen electrode module in the vacuum system.

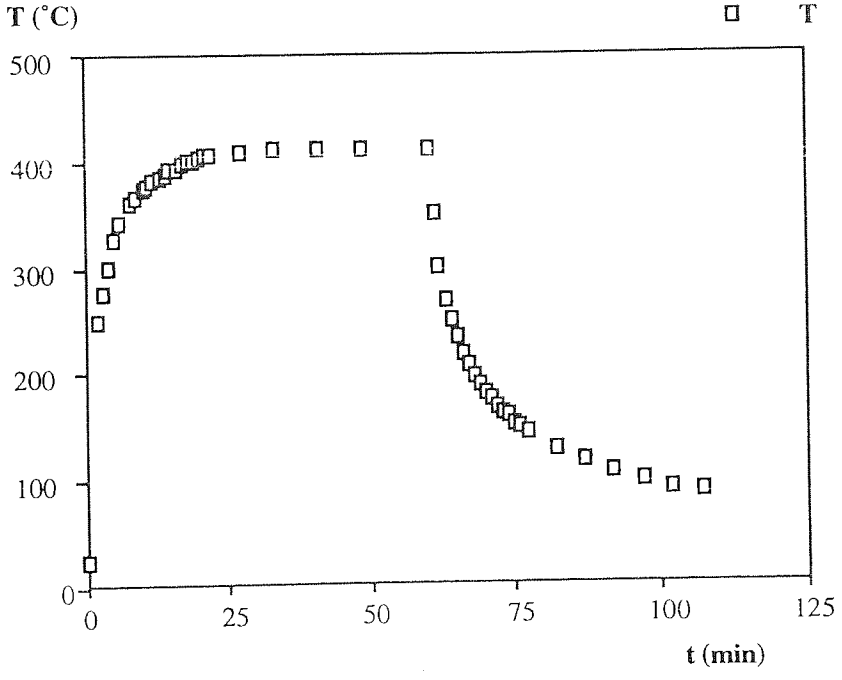

Fig. A.6 Specimen temperature variation with time, for a 60-minute baking cycle

References

[A1] A Roth, *Vacuum Technology*, Amsterdam: North-Holland, 1976, pp. 60-146

[A2] *Vacuum Technology,* (Pfeiffer Balzers: Asslar), Balzers publication n^{o} PM 800 049 PE, 1990

[A3] *Turbomolecular pumps*, (Leybold AG: Cologne), Leybold publication n^{o} 175.01.02, 1991

[A4] *Trivac B*, (Leybold AG: Cologne), Leybold publication n^{o} GA 01.201/5, 1990

[A5] Vacuum Components catalogue, Caburn-MDC Ltd., 1994

APPENDIX B

6kV PULSED POWER SUPPLY DESIGN

B.1 Circuit schematic of pulsed PSU

Figure B.1 provides a circuit diagram of the 0-6kV pulsed PSU, with the operation of the unit described by three modular circuit blocks:

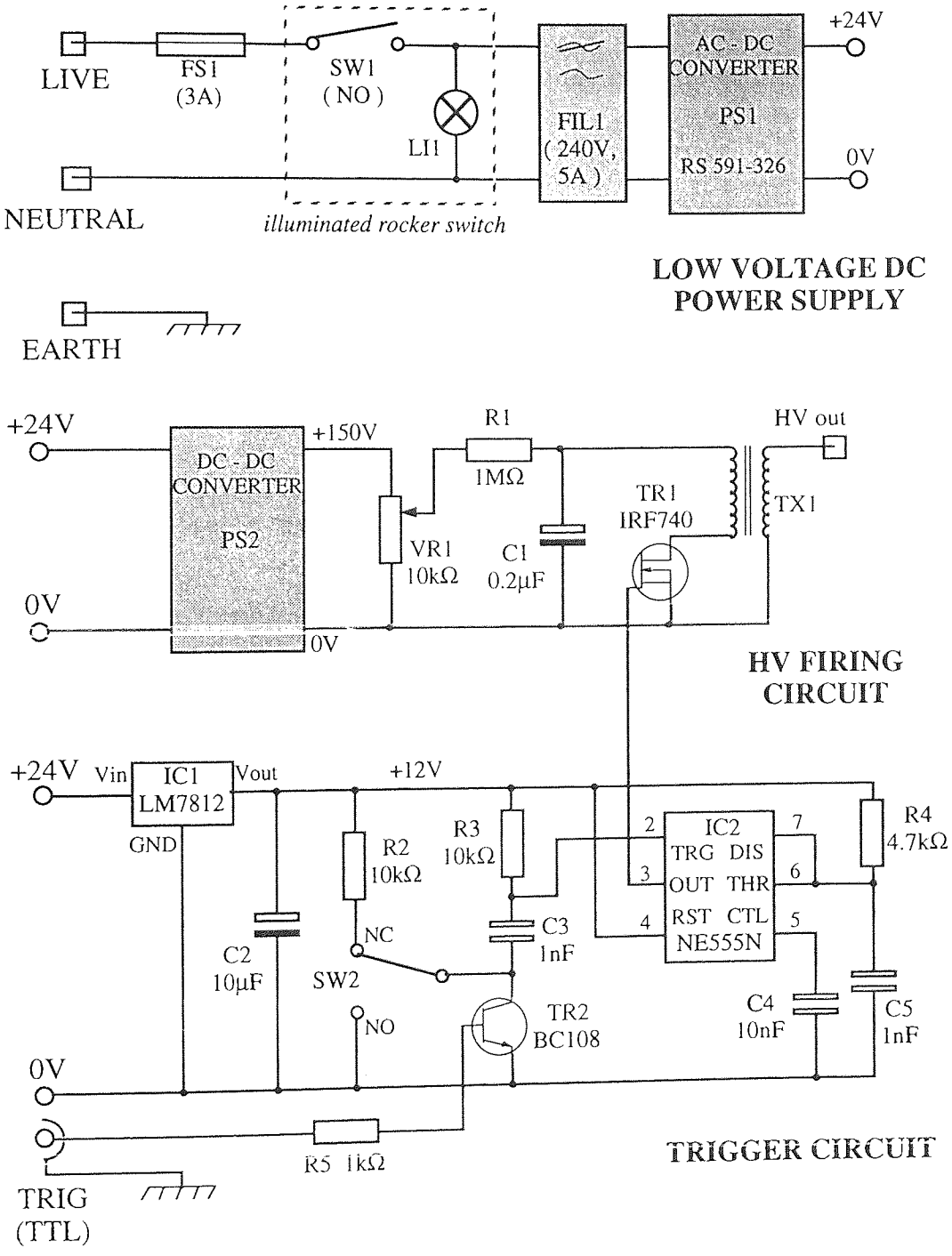

Fig. B.1 Circuit diagram of 0-6kV pulsed PSU

The operation of each 'functional block' of the PSU circuit given in Fig B.1 will be described in the following sub-sections:

B.1.1 Low-voltage DC power supply: mains supply voltage was fed to an illuminated switch (SW1 / LI1) through a 3A fast-blow fuse (FS1); the switched mains voltage was subsequently filtered (FIL 1) before being fed into an AC to DC converter module (PS1). The mains earth feed was bonded to the chassis of the PSU, at a single earth-bonding point.

B.1.2 Trigger circuit: the +24V DC output from PS2 was stepped down to +12V DC by voltage-regulator IC1, with a reservoir capacitor C2 connected across the regulator output. Closure of switch SW2 caused a transient current-flow through R3 as capacitor C3 charged up to +12V. Consequently, this initial flow of current through R3 caused a drop in the potential at the trigger input of the monostable multivibrator IC2, and so the multivibrator 'fired', to give an output square-wave pulse which was applied as gate-bias to the IRF740 FET. The duration of this gate pulse, T_d, was derived from the series combination of R4 and C5, where

$$T_d \approx 1.1\ R_4 \,.\, C_5 \approx 5\mu s$$

Firing of the trigger circuit was also possible by the application of an external TTL-level signal (TRIG), which provided base bias to an NPN transistor (TR2) via a current-limiting resistor, R5. Thus, the biasing-on of TR2 by the external TRIG signal caused a transient flow of current through C3 and R3, providing a negative voltage-edge at the monostable trigger input of IC2.

B.1.3 High-voltage firing circuit: the regulated +24V DC from PS1 was fed into a DC to DC converter module, PS2, which produced a regulated +150V output voltage. A centre-tapping from potentiometer VR1 provided a variable charging-voltage to capacitor C1, with the charging-current limited to below 1mA by resistor R1. Application of a bias-voltage to the gate of the IRF740 FET (TR1) allowed the discharge of C1 through the primary winding of pulse-transformer TX1 (1:50 primary:secondary turns ratio), causing a high-voltage (HV) potential to appear across the secondary winding of TX1.

B.2 General arrangement of 6kV pulsed PSU

A steel enclosure encased the PSU circuit, providing effective electromagnetic screening of the circuit elements. A single earth connection on the case was used to bond the case and PSU circuit to the earth circuit of the experimental system described in Section 3.2 of this thesis. The outline and internal construction of the assembled PSU are illustrated in Fig B.2.

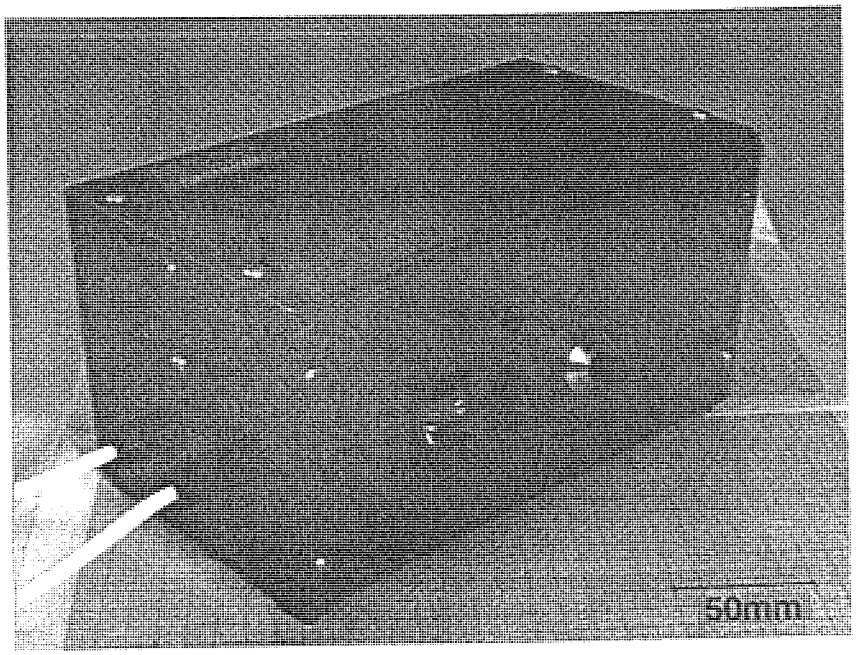

(a)

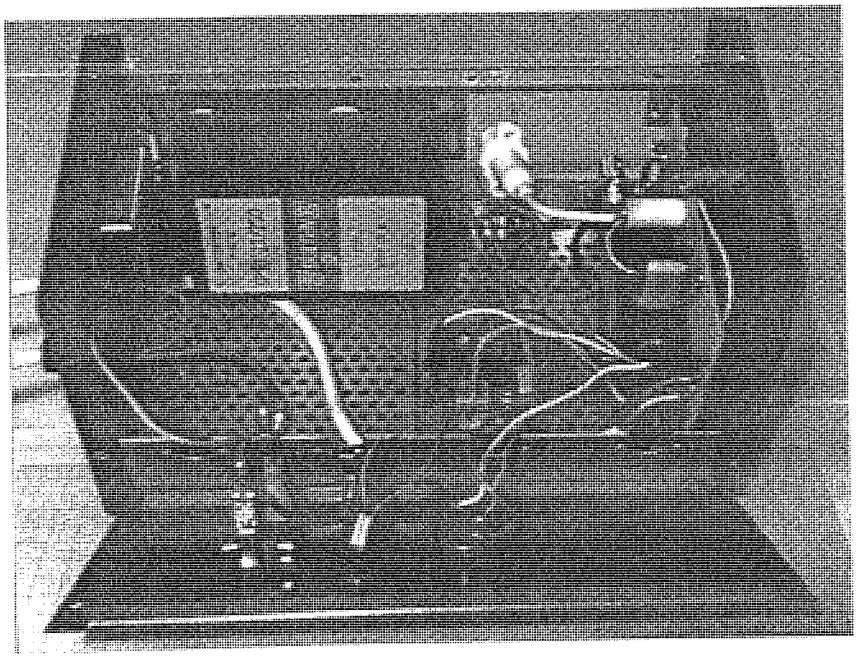

(b)

Fig. B.2 (a) Outline (front view) and (b) internal arrangement of assembled 0-6kV pulsed PSU

APPENDIX C

30kV PULSED POWER SUPPLY DESIGN

C.1 Pulsed PSU performance requirement In addition to the high-voltage (HV) 0-6kV pulsed PSU described in Appendix B, an extra-high voltage (EHV) pulsed power supply was also required, to allow the application of single-shot voltage pulses at magnitudes approaching 30kV. Thus, this EHV pulse facility permitted the study of high-field ($E \approx 100kV\ mm^{-1}$) phenomena in the metallized alumina modules described in the thesis.

C.2 PSU circuit simulation and modelling A simple PSpice circuit model was devised [C1], in order to predict the form of the output pulse available from the pulsed PSU. Figure C.1 displays a schematic diagram of this simple circuit model.

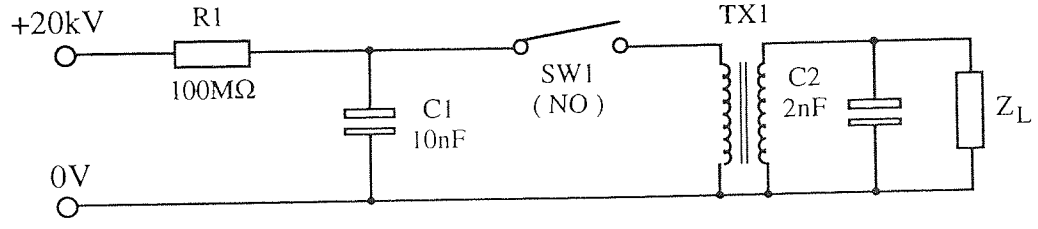

Fig. C.1 PSpice circuit model of 30kV pulsed PSU

In the PSU circuit model, a reservoir capacitor C1 (10nF) is charged to a high-voltage through a 100MΩ current-limiting charging resistor, R1. This C-R combination gives a capacitor charging time-constant $\tau = 1s$, with a capacitor charge-up time of $T \approx 10\tau = 10s$. An electrically-initiated closing switch SW1 then discharges C1 through the primary winding of a unity turns-ratio isolating transformer, TX1.

A rising current is then induced in the secondary winding of TX1, leading to the impulse charging of capacitor C2. Thus, a high instantaneous value of output *surge voltage* may be developed across the load impedance, Z_L. Figure C.2 presents a simulated output-voltage waveform, that was modelled with a resistive load impedance of $Z_L = 0.1\Omega$, and a DC charging voltage of 20kV.

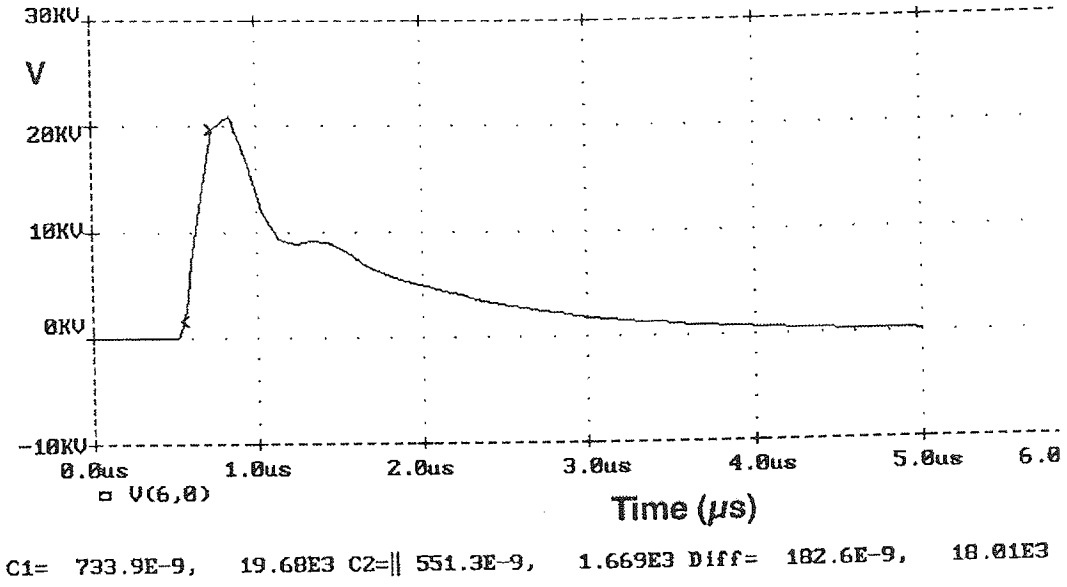

Fig. C.2 PSpice simulated output-voltage waveform from circuit model of 30kV pulsed PSU

C.3 Circuit schematic of pulsed PSU From the simulated circuit model described in Section C.2, a practical pulse firing circuit was realised, as shown in Fig C.3.

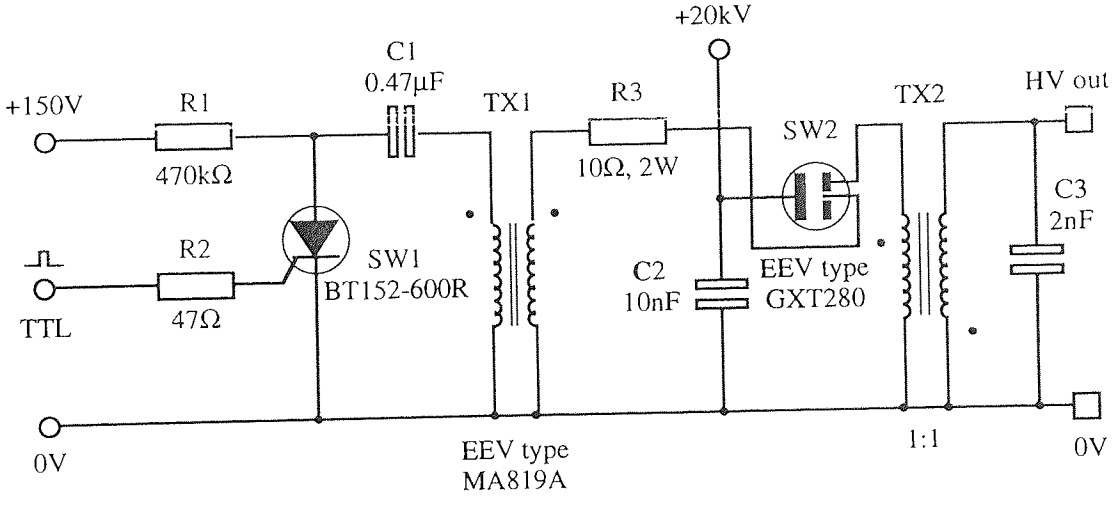

Fig. C.3 Circuit diagram of 30kV pulsed PSU

In the EHV pulse PSU circuit shown in Fig C.3, the 10nF reservoir capacitor (C2) was discharged through a three-electrode triggered spark gap (SW2) into the primary winding of the isolation transformer TX2. Thus, an output voltage was induced across the loaded secondary winding of TX2, that was measured across the

output capacitor C3 as shown in Fig C.4. The form of this output voltage pulse was found to be in agreement with that predicted by Fig C.2.

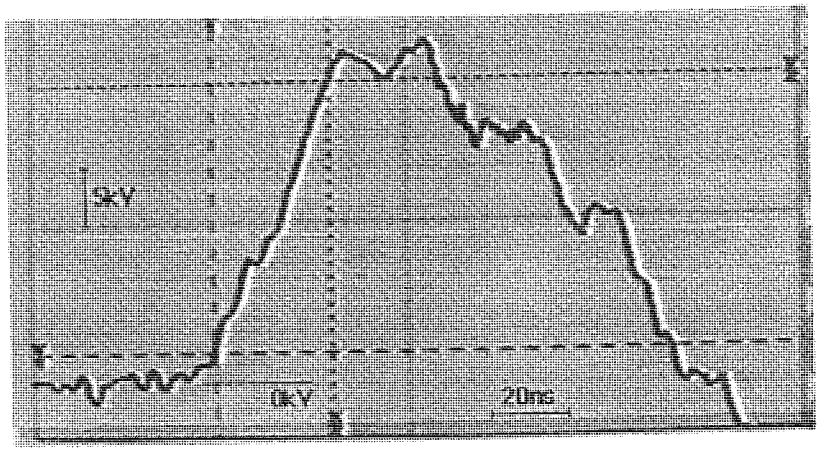

Fig. C.4 Open-circuit output-voltage waveform recorded from 30kV pulsed PSU

The firing of this pulsed PSU was initiated by a single TTL pulse applied to the gate of thyristor SW1. A trigger circuit of the type described in Fig B.1 of Appendix B was used to produce this initiating low-voltage pulse. The thyristor discharged a 470nF capacitor through the primary winding of trigger-transformer TX1, producing a high-voltage trigger pulse to the mode C spark-gap configuration [C2].

C.4 General arrangement of pulsed PSU The complete 30kV pulse PSU unit was assembled in a steel sub-rack case, which was lined with a further thickness of tin-plated steel sheet to provide enhanced electro-magnetic shielding of the PSU circuitry. External views of the assembled PSU are illustrated in Fig C.5. High-voltage line and earth feeds to the rear of the unit are shown in Fig C.5(b). The high-voltage circuitry was housed in the central and lower bays of the three-bay main case, with the trigger circuit located in the upper bay. The low-voltage power supply and control circuitry were mounted within a further screened bay, affixed to the rear of the centre region of the main case.

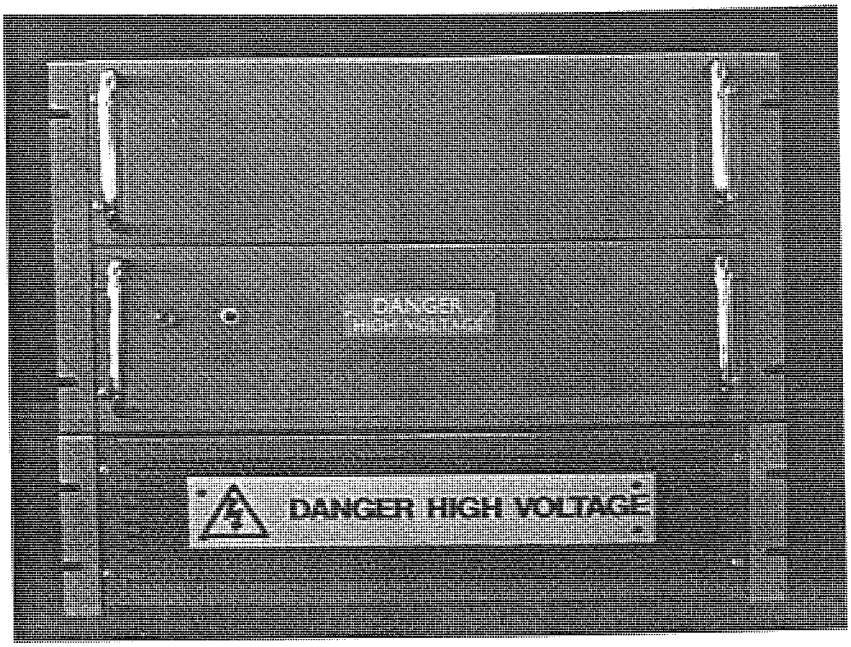

(a)

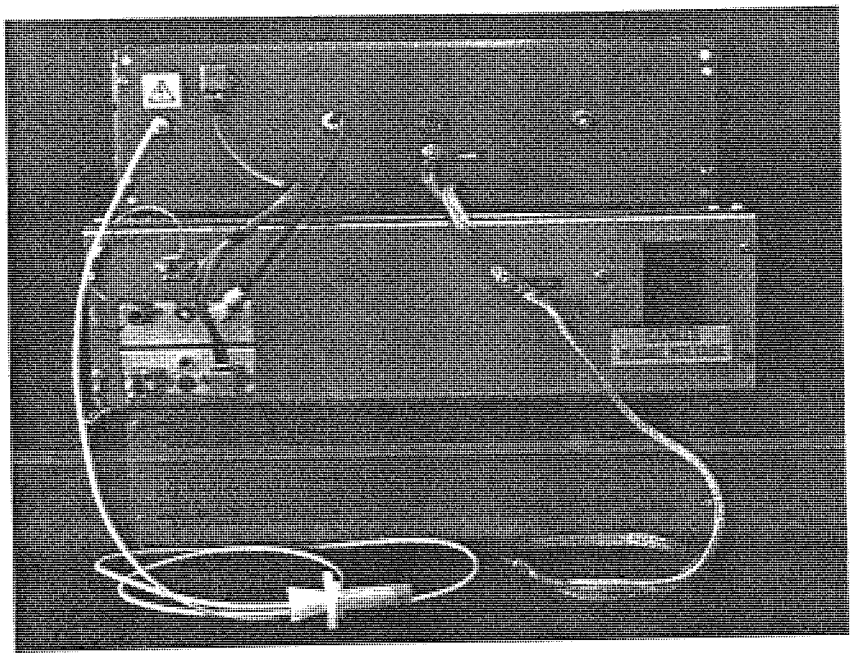

(b)

Fig. C.5 (a) Front and (b) rear views of assembled 30kV pulsed PSU

References

[C1] P W Tuirenga, *Spice: a guide to circuit simulation and analysis using PSpice*, New York: Prentice Hall, 1989

[C2] *Spark Gaps Product Data*, EEV Limited, Lincoln, UK, December 1991

Special Issue Papers

Electrical and Optical DC Vacuum Emission Phenomena from a Ceramic-Insulated Planar Electrode Configuration

Brian M. Coaker, Ning-Sheng Xu, Francis J. Jones, and Rodney V. Latham

Aston University

Content has been removed for copyright reasons

J. Phys. D: Appl. Phys. 27 (1994) 1448–1456 Printed in the UK

Photon emission from an alumina insulator in vacuum subjected to DC electrical fields

B M Coaker†, N S Xu†, F J Jones‡ and R V Latham†

† Surface Science Group, Department of Electronic Engineering and Applied Physics, Aston University, Birmingham B4 7ET, UK
‡ Cold Cathode Engineering, EEV Limited, Carholme Road, Lincoln LN1 1SF, UK

Received 7 February 1994

Aston University

Content has been removed for copyright reasons

gh-speed imaging of explosive exoemission from an alumina ceramic in vacuum

B M Coaker†, N S Xu†, F J Jones‡ and R V Latham†

† Surface Science Group, Department of Electronic Engineering and Applied Physics, Aston University, Birmingham, UK B4 7ET

‡ Cold Cathode Engineering, EEV Limited, Carholme Road, Lincoln, UK LN1 1SF

ABSTRACT

Aston University

Content has been removed for copyright reasons